Geological mapping and structural analysis of Aram Chaos, Mars, with HRSC data

MSc Research

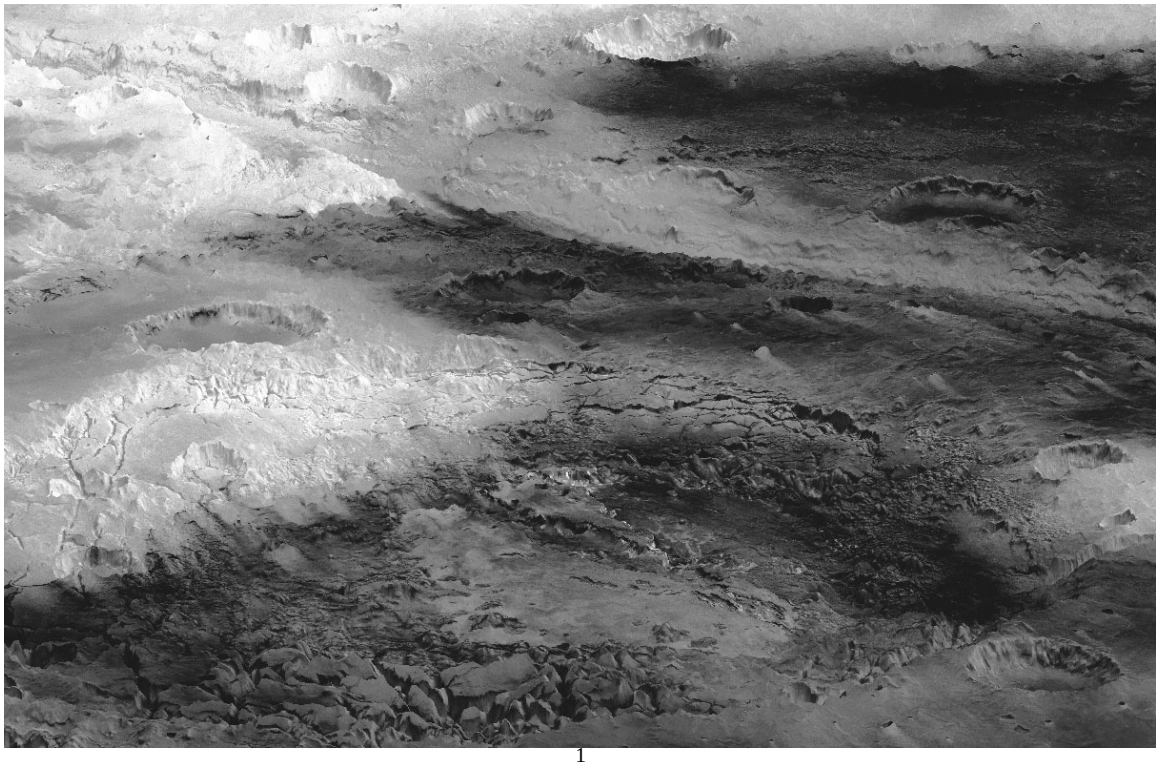

[1]

J.H.P. Oosthoek
0154946
February 2007

Supervisor at ESA ESTEC and Faculty of Earth Sciences, Utrecht University: Dr. T.E. Zegers.

[1] Image caption: A 3D perspective of Aram Chaos (view is towards the North), made in ArcScene, using HRSC nadir image data draped over an HRSC derived DTM (image H401_0000).

Abstract
Aram Chaos is a 280 km in diameter impact crater, located in the equatorial region of Mars. It contains 'chaotic terrain': 10 km-sized tilted and collapsed blocks, and at specific locations km-scale hills, both bounded by fractures. Chaotic terrains are the source regions of outflow channels, which have been interpreted to be formed by water flow. The Aram Chaos chaotic terrain is connected with the ~40 km wide, ~1 km deep Ares Vallis outflow channel via a 15 km wide, 2.5 km deep channel.
The goal of this study is to better understand the processes behind chaotic terrain formation. A 1000x1000 km research area was chosen, surrounding Aram Chaos. A Geographical Information System (GIS) was created, incorporating High Resolution Stereo Camera (HRSC) image data from the ESA Mars Express orbiter and Thermal Emission Imaging System (THEMIS), Mars Orbiter Camera (MOC) and Mars Orbiter Laser Altimeter (MOLA) data from NASA. The research encompassed the structural and lineament analysis of the Aram, Iani, Aureum and Hydaspis Chaos chaotic terrains within the research area. Geological mapping was performed to aid the analysis and to provide a geological framework. The results include 1) (structural) geological and geomorphological maps of Aram Chaos and surrounding region, 2) observation descriptions, 3) stratigraphical columns, 4) cross sections and 5) rose diagrams and concentricity/radiality of lineaments.
The main mapped unit in the study area is the Highland Terrain (HT) unit, which is of Noachian age (4.5 – 4.6 Ga until 3.5 – 3.7 Ga) and at least 1.5 to 2 km thick. The Highland Terrain is interpreted to have been formed by a complex interplay between the processes of volcanism, impact cratering, erosion, deposition and (regional) deformation. The Aram Chaos crater is interpreted to be buried within the HT stratigraphy. After formation of the crater, it was filled with water rich materials. Ongoing HT formation, including deposition, erosion and impact cratering subsequently buried the Aram Chaos crater. More buried craters, with water rich infilling, are interpreted to occur within the HT stratigraphy. During the Noachian these formed water filled 'cavernous systems', which are combined fracture systems of many buried impact craters.
In the Hesperian Period (3.5 – 3.7 Ga until 2.9 – 3.3 Ga) instability of the buried water led to the formation of the Chaotic Terrain (CT), probably triggered by subsurface igneous activity. The following definition of CT is used in this study: CT is considered a lateral unit of the HT, which is observed to have lost coherence with the surrounding HT due to intense fracturing (brecciation). The fracture patterns and morphology of the fractured HT and CT in the study area are interpreted to be caused by fluid assisted brecciation within a hydrothermal system, as well as due to crater related fractures and cavern subsidence. The subsurface water was released catastrophically forming the current brecciated CT morphology of fracture bounded km-scale hills. Water could also have been released through the HT fractures surrounding the CT. No Preferred Orientations (PO's) were observed within the fractured HT and CT lineaments. This suggests that the observed fracture patterns have not been influenced by regional stress. Subsurface faults, related to the Tharsis Bulge volcanic complex could however occur in the study area.
During and/or after the formation of the fractured HT and CT the Aram Chaos Formation (ACF) has been deposited. It is divided into a Lower, Intermediate and Upper ACF. The Lower ACF is further divided into a broken, fractured and smooth subunit. The smooth

subunit is non-fractured and has been interpreted to be a deposit on top of the fractured and broken LACF. The fractured and broken LACF has been deposited during the collapse of the underlying fractured HT and has subsequently been fractured and broken up. The fracturing is 1 km sized compared to the 10 km sized fracturing pattern of the underlying HT. The fractured and broken LACF is contained by the ~150 km in diameter inner ring of the Aram Chaos crater and is therefore interpreted to have been deposited after the formation of this structure. The unit could have been deposited sub-lacustrine within the inner ring.

The non-fractured ACF units form a dome, which does not agree with the previously proposed sub-lacustrine depositional origin for these deposits. Similar looking non-fractured deposits occur within Aureum and Iani Chaos (the Aureum Chaos Deposits and the Iani Chaos Deposits, mapped in this study). The layering sequence of the non-fractured ACF units, from old to young (e.g. smooth LACF, IACF, UACF), is found to be associated with the occurrence of the sulphate kieserite, other hydrated minerals and hematite, respectively. The non-fractured ACF units underwent erosion, after deposition. The erosion morphology of the non-fractured ACF units is interpreted to be caused by the dominant wind direction.

Table of contents

1. Introduction

This thesis describes the research I performed of the Aram Chaos region on the planet Mars. It is my graduation research of my geology Masters programme and included a 4 month internship at ESA ESTEC, Noordwijk.

The research of Mars is possible due to a vast amount of data (images, topography, hyperspectral, subsurface data), currently available from NASA and ESA satellites orbiting Mars or landers, and rovers on the surface, with more data being acquired every day. Since December 2003 the Mars Express satellite from ESA is orbiting Mars. The payload of the Mars Express satellite includes 1) a high resolution stereo camera (HRSC) of which digital terrain models (DTMs) and anaglyphs can be derived and 2) the Observatoire pour la Minéralogie, l'Eau, les Glaces et l'Activité (OMEGA) hyperspectral scanner. This research will focus on the use of the HRSC and OMEGA data covering Aram Chaos. When I started this research a complete HRSC coverage of Aram Chaos had been achieved. Aram Chaos had not before been investigated using HRSC and OMEGA data in a GIS.

The research area is 1000 by 1000 kms and is located in the equatorial region of Mars, between the high elevated southern hemisphere and the low elevated northern hemisphere (Figure 2.1). Aram Chaos is a so called chaotic terrain, containing tilted and collapsed blocks and fractured terrain. Chaotic terrain are the source regions of outflow channels, which have been interpreted to be formed by water flow (e.g. Masson et al., 2001; Baker, 2001). The largest system of chaotic terrain occurs in the Xanthe and Margaritifer Terrain region, including Aram Chaos (Figure 3.1). The research area also includes the Iani Chaos, Hydaspis Chaos and part of the Aureum Chaos chaotic terrain and the Ares Vallis outflow channel. Aram Chaos is a special type of chaotic terrain, completely contained by a 280 km in diameter impact crater (Figure 2.3). Layered deposits occur in Aram Chaos. A small channel connects the chaos with the Ares Vallis outflow channel.

No terrestrial analogues for chaotic terrain are known, and it is unclear which processes formed the observed chaotic terrain morphology and fracture patterns. This research, involving geological mapping and structural analysis, using high resolution HRSC data, aims to understand the processes behind the chaotic terrain formation. In general, investigating Aram Chaos may explain more clearly which processes formed the current Martian surface (e.g. flowing water, tectonics, volcanism, impact cratering). If flowing water occurred, and the Martian climate was once warmer, with a thicker atmosphere, life could possibly have evolved. Investigating the surface of Mars for signs of past or present water may also help to answer this question.

The goals of this research are:

1. Build a planetary GIS with all available image (MOC, THEMIS, HRSC), mineral maps (OMEGA) and elevation (MOLA and HRSC DTMs based on stereopairs) data of Aram Chaos.
2. Perform a geological, morphological, spectral and structural (lineament) analysis of Aram Chaos and surrounding area using a GIS.
3. Unravel the relative time relations of the defined units and geological events.
4. Investigate which processes formed the observed fracture patterns and the chaotic terrain.

2. Mars Background

2.1. Introduction

This section summarizes the current knowledge about Mars. It emphasises the role of water in the formation of chaotic terrains (Figure 2.1) like Aram Chaos.

Mars has been of scientific interest since the advent of the telescope. In the 1960's and 1970's Mariner and Viking spacecraft were sent to Mars and sent back pictures from orbit and from the surface. Viking 1 landed in Chryse Planitia (22.3ºN-311.8ºE), Viking 2 landed in Utopia Planitia (47.7ºN-134.1ºE) (Figure 2.2). From the late 1990's onward a new class of satellites and landers have been sent to Mars. It is mostly their data which I am going to study.

In July 1997 the Mars Pathfinder lander from NASA landed on Mars (at 19.3ºN-326.4ºE), near the mouths of the outflow channel Ares Vallis (Figure 2.2). Ares Vallis is the outflow channel of which Aram Chaos is a source region (Figure 2.3).

In September 1997 the Mars Global Surveyor (MGS) from NASA arrived at Mars and is currently still operational. It's payload includes:

1. The Mars Orbiter Camera (MOC) which consists of a Narrow Angle (NA) high resolution (1.4–1.6 m/pixel) and a Wide Angle (WA) medium resolution (240 m/pixel) camera.
2. The Mars Orbiter Laser Altimeter (MOLA). The derived topography data has a nominal 463 m/pixel (128 pixel/degree) resolution.
3. The Thermal Emission Spectrometer (TES) with a 3 km/pixel resolution. It consists of three parts: (1) a Michelson interferometer measuring the thermal IR wavelength range from 6 to 50 microns, with a 5 and 10 cm^{-1} spectral sampling, (2) a broadband radiance sensor which measures radiance in a single band from 5.5 to 100 microns, and (3) a solar reflectance sensor which measures from 0.3 to 2.7 micron.
4. The Magnetometer/Electron Reflectometer (MAG/ER) and the Radio Science Subsystem (RSS) which have been used to derive the magnetic field and the gravity field, respectively.

In October 2001 the 2001 Mars Odyssey (MO) from NASA arrived at Mars and is currently still operational. Its payload includes:

1. The Thermal Emission Imaging System (THEMIS) which consists of a 5-wavelength visual (VIS) imaging system (18 m/pixel) and a 9-wavelength infrared (IR) imaging system (100 m/pixel).
2. The Gamma Ray Spectrometer (GRS) including neutron detectors to analyze the chemical composition of the Martian surface.

In December 2003 the Mars Express (MEX) from ESA arrived at Mars and is currently still operational. It's payload includes:

1. The High Resolution Stereo Camera (HRSC) (2 and 10 m/pixel) which takes multiple images at different angles, making 3D analysis and the derivation of elevation data possible.
2. The Visible and Infrared Mineralogical Mapping Spectrometer (OMEGA) (100 m/pixel) measuring visible and infrared light in the wavelength range 0.5-5.2 microns.

3. The Sub-surface Sounding Radar Altimeter (MARSIS) to map the sub-surface structure to a depth of a few kilometres. It has recently been found that MARSIS can also be used to measure the local magnetic field strength (Gurnett et al., 2005).
4. Three atmospheric instruments: the Planetary Fourier Spectrometer (PFS), the Ultraviolet and Infrared Atmospheric Spectrometer (SPICAM) and the Energetic Neutral Atoms Analyser (ASPERA).

In Januari 2004 the Mars Exploration Rovers Spirit (MER-A) and Opportunity (MER-B) from NASA landed on Mars (at 1.9ºS-354.5ºE and 14.6ºS-175.5ºE respectively) and are currently still operational. Opportunity landed in Meridiani Planum (Figure 2.2) where, together with Aram Chaos, hematite has been found with TES (Christensen et al., 2001), Spirit landed in the 140 km Gusev Crater (Figure 2.2).

Mars has a complex evolution in which tectonics, impacts, volcanism and erosion played a role. Mars was most active in the Noachian, although episodes of volcanic activity continued until a few Ma ago (Neukum et al., 2004). I will focus on the evolution of Mars relevant to the context of Aram Chaos.

The following sections will describe (1) a chronology system used for Mars, essential to a geological investigation, (2) Global Mars, the global martian features that influence any geological study of Mars and (3) the generalized evolution of Mars using the previously described chronology system.

2.2. Mars stratigraphy and crater chronology

In order to determine the evolution of the Martian geology a means to measure time, a chronology system, is required. Tanaka (1986) proposed a relative chronology system, using a combination of stratigraphic superposition relations and crater counts (Table 2.1). This system divides the surface of Mars, from old to young, in a Noachian, Hesperian and Amazonian Period. The periods were named after the Noachis Terra, Hesperia Planum and Amazonis Planitia type locations. Each period was subsequently divided in an Upper, Middle and Lower epoch (Table 2.2).

An absolute Martian chronology system can only be devised when a sample return mission brings back samples from different type locations on Mars. This has not been undertaken. However, the ages of specific events, which occurred on Mars, have been determined using Martian meteorites found on Earth. They are accepted to have formed on Mars because they contain gasses with the same isotopic signature as the Martian atmosphere (determined by the Viking landers) (Nyquist et al., 2001). The oldest meteorite, named ALH84001, formed ~4.5 Ga ago, providing evidence that the Martian crust had formed at that time (Hartmann, 2005). A group of Martian meteorites, the nakhlites, crystallized 1.3 Ga and show evidence for igneous processes. Some contain evaporate minerals and one nakhlite, named Lafayette, contains weathered minerals and was exposed to liquid water ~670 Ma. Another group, the basaltic shergottites, show evidence for basaltic lava flows hundreds of millions of years ago.

An approximate absolute geochronology system is determined by extrapolating the known cratering flux of the Lunar mare surfaces to Mars. In the 1960's and 1970's Russian robotic and NASA manned and robotic missions landed on the relatively smooth mare surfaces of the Moon and brought back samples. These samples were dated using K-Ar dating and it was determined that the mare surfaces formed ~3.4 billion years ago (Ga). Hartmann and Neukum independently performed crater density counts for these

lunar mare surfaces. They counted craters of specific diameters and plotted their crater densities (craters/km^2) against crater diameter (Figure 2.4). Each subsequently determined a best fit function of the data. This is called the *production function* for cratering, which is the number of craters/km^2 for a certain time period as a function of the crater diameter D (Hartmann and Neukum, 2001). Hartmann fitted a powerlaw and Neukum a polynomial fit (Figure 2.4).

The production function is extrapolated to Mars by using knowledge of asteroid populations in the Solar System to derive a Mars/Moon ratio (Ivanov, 2001). Neukum defined a time dependence of the Lunar cratering rate which is used to extrapolate to different ages (Hartmann and Neukum, 2001). The result, the lunar mare production function scaled to Mars and to a certain time, is called an *isochron*. An isochron diagram shows isochrons of specific ages (Figure 2.5).

The age of surface units on Mars can be determined by plotting their crater counts in an isochron diagram. This results in a *crater retention age*, which is defined as the average time interval during which craters of diameter D are preserved on a given surface (Hartmann and Neukum, 2001). For old surfaces, where there has been enough time for craters to erode or fill, the derived age is D-dependent. Young surfaces on the other hand, will not have lost many craters so the crater retention age is most likely their absolute surface age. Using crater counts from the type localities defined by Tanaka (1986) (Table 2.1, 2.2) Hartmann and Neukum (2001) calculated the epoch boundary ages (Table 2.3). The ages calculated by Hartmann are younger than the Neukum ages (Head et al., 2001).

There are some limitations and uncertainties of the methods described above (Hartmann and Neukum, 2001; Hartmann, 2005):

1. Until ~3.85 Ga both the Moon and Mars suffered a period of intense impact cratering (Figure 2.6) (Strom et al., 2005). Therefore crater count ages before ~3.85 Ga are not reliable (Solomon, personal communication 2005).
2. Mars compared to the Moon:
    a. Extrapolation from the Moon to Mars gives rise to uncertainties.
    b. Mars compared to the Moon has been much more geologically active (and still is).
    c. On a given area on Mars a much larger range in ages is possible.
3. Crater origin:
    a. Small craters on Mars can either be primary or secondary craters. Many smaller secondary craters surround large craters. Determining the secondary crater distribution by using statistics or image observation reduces the primary crater count and thus influences the crater retention age.
    b. Pseudocraters of a possible phreatomagmatic origin have been observed (e.g. Mouginis-Mark, 1985).
4. Mapping:
    a. Recent thin lava flows are difficult to date because observed craters could be situated below or on top of the flows.
    b. More than one definition exists for a given stratigraphical boundary.
5. Statistics:
    a. The isochron method uses least squares statistics which has a 10% error.

b. The derived absolute ages are estimated to have a 1-σ (standard deviation) uncertainty of a factor 2 (Hartmann and Neukum, 2001)
c. A large amount of craters have to be counted for good statistics. Therefore young and/or small units have greater errors.

2.2.1. Crater recognition techniques

Manual crater counting is a painstaking business which is nowadays more and more being automated. A variety of methods and software programs have been developed to recognize crater forms. Plesko et al. (2003a) developed the GENetic Image Exploitation package (GENIE) software which uses a a genetic algorithm to recognize craters. The genetic algorithm is a learning process which results in a crater recognition algorithm to evolve towards a best fit. Earl et al. (2005) developed a so called Radial Consistency algorithm which can detect partially circular features. Magee et al. (2003) used multiple methods to detects craters:

1. For small craters they extracted a template of one small crater from the image and cross-correlated it with each location of the image to find comparable craters.
2. They used edge-detection techniques involving the direction of the sun in the image.
3. They used a Circular Hough Transform. A Hough Transform can identify lines in an image, but can be extended to identify other shapes, like circles and ellipses.

Other methods are being developed to measure the crater shape. Mouginis-Mark et al. (2004) for example developed an interactive software program called IMPACT which can measure the geometry of impact craters. This can be used to compare different regions or analyse degradation of craters. Plesko et al. (2003b) combined the GENIE software with models of the impact process in 3D to investigate the surface response to impacts, which tells something about the underlying geology.

2.3. Global Mars

This section will describe the global martian features, (1) topography, gravity and crustal thickness, (2) surface composition, (3) magnetism, (4) orbital behavior and (5) the atmosphere.

2.3.1. Topography, gravity and crustal thickness

The MOLA instrument on board the MGS was the first to measure the global topography variation of Mars. Mars' topography shows three global scale features, (1) a difference in elevation between the northern and southern hemispheres called the dichotomy, (2) an enormous topographical high called the Tharsis Bulge and (3) The ~2000 km diameter Hellas Basin impact crater (Figure 2.7).

The southern hemisphere of Mars is topographically 2-4 km higher (therefore referred to as the southern highlands) than the northern hemisphere (referred to as the northern lowlands). The southern highlands are mostly Noachian in age with a rugged relief, and saturated by impacts. The northern lowlands are smoother and have less impacts, making them mostly Hesperian in age.

The Tharsis Bulge is a ~10 km high region over 30×10^6 km^2. It started forming in the Noachian and lava flowed probably until a few Ma (Neukum et al., 2004). It formed either by (1) isostatic uplift and flexural loading, (2) magmatic intrusion or (3) volcanic

loading and was possibly caused by one or more mantle plumes (Zuber, 2001) or a combination. The loading of the lithosphere by the Tharsis Bulge created a topographically lower region around it referred to as the Tharsis trough (Phillips et al., 2001).
The Radio Science Subsystems on board the MGS, MO and MEX can be used to derive the gravity field of Mars. According to Smith et al. (1999) the largest free-air gravity anomalies on Mars are more than 10 times larger than terrestrial anomalies of the same scale. They attribute this to the ability of the thicker Martian lithosphere to support larger stresses and prevent isostatic readjustment. They found a smooth gravity signature for the southern highlands which suggests the southern highlands are isostatically compensated. The northern lowlands show more anomalies, and possible buried impact craters.
Phillips et al. (2001) used gravity and topography data and found that loading of the lithosphere by the Tharsis Bulge is able to explain global scale gravity and topography. Tharsis Bulge loading for example explains the Tharsis trough and the Arabia Terra topographic high, opposite to Tharsis. The dichotomy was not included in the loading model.
Combining gravity and topography data the spatial variation of the crustal thickness can be derived (Figure 2.8) (Neumann et al., 2004). The method assumes a specific constant density of the mantle and the crust and a mean crustal thickness. If the mean crustal thickness is chosen to small, negative values would be obtained beneath the large impact basins (Nimmo and Tanaka, 2005). Zuber et al. (2000) used a mean crustal thickness of ~50 km, a constant crustal density of 2900 kg/m^3 and a constant mantle density of 3500 kg/m^3 and derived a crustal thickness variation between 3 and 92 km. Neumann et al. (2004) found mean crustal thicknesses of 32 km in the northern lowlands and 58 km in the southern highlands, indicating the dichotomy is not only a topographical but also a crustal feature. Three hypotheses for the formation of the crustal dichotomy have been postulated (Nimmo and Tanaka, 2005; Head et al., 2001):

1. An endogenic process, f.e. plate tectonics or long wave-length mantle convection.
2. One giant impact.
3. One event of several overlapping large impacts.

Frey (2005) identified Quasi-Circular Depressions (QCDs) in MOLA data from Early Noachian terrain, which he suggests, are buried possibly pre-Noachian impact basins. According to his N(>200) crater chronology the dichotomy formed around 4.08-4.18 Ga or earlier, by multiple impacts which formed the Utopia, Acidalia and Chryse basins in the northern lowlands. Solomon et al. (2005) however argues that the dichotomy, because of its global scale, is 4.5 Gyr in age. Similar in age as when the stable crust formed, evidenced by Martian meteorite ALH84001. They therefore favor an endogenic origin for the dichotomy.
Clifford (1993) proposed that the upper part of the crust is ice-enriched and remains permanently frozen. He estimated this cryosphere to be ~2 km at the equator and ~6 km at the poles.

2.3.2. Surface composition

The global composition of the surface and subsurface of Mars is investigated using different remote sensing techniques. Data from TES on board the MGS for example suggest primarily basaltic compositions for the Martian highlands and more siliceous

andesite-like compositions for the Northern plains (Nimmo and Tanaka, 2005; Head et al., 2001). According to a study by Rogers and Christensen (2003) this is caused by a shift from basaltic volcanism (which formed the southern highlands) to andesitic volcanism (which covered most of the northern lowlands). The andesitic signature could, however, also have been caused by altered basalt (Nimmo and Tanaka, 2005). According to Bibring et al. (2005) preliminary results from OMEGA on board the MEX do not show evidence for this andesitic composition of the northern lowlands. However, they have found olivine concentrations in the floors and ejecta of specific craters in the northern lowlands. The size is these craters suggests they penetrate the ~100 m thick cover (the Vastitas Borealis Formation), exposing an olivine rich layer underneath.

Remote sensing by the Gamma Ray Spectrometer on board the MO and by OMEGA led to the discovery of large amounts of surface and subsurface water ice in the polar regions of Mars (Boynton et al., 2002; Feldman et al., 2002; Mitrofanov et al., 2002; Bibring et al., 2005). The occurrence of rampart craters is also possible evidence for present or past subsurface ice on Mars. Rampart craters have an ejecta blanket with a flow morphology suggesting the impact occurred onto a water or ice-rich surface (Zuber, 2001). Impact simulation experiments at the NASA-Ames Vertical Gun facility resulted in similar morphologies (Masson et al., 2001). OMEGA however did not find enrichment in hydrated minerals in rampart craters (Bibring et al., 2005).

Minerals associated with liquid water are sulfates, carbonates, hematite and phyllosilicates (clay minerals). OMEGA detected sulfates within Valles Marineris, Terra Meridiani, Aram Chaos and in the North Polar Region, but did not observe carbonates (Bibring et al., 2005). Phyllosilicates were also detected by OMEGA, mainly associated with Noachian aged surfaces (Poulet et al., 2005). TES detected small concentrations of carbonates, mostly magnetite, in dust covered regions of Mars (Bandfield et al., 2003). Hematite has been detected by TES in Valles Marineris, Terra Meridiani and Aram Chaos (Christensen et al., 2001).

2.3.3. Magnetism

The MAG/ER instrument on board the MGS measures the magnetic field of Mars and can detect magnetic anomalies larger then ~200 km (Nimmo and Tanaka, 2005). Presently Mars doesn't have an internal magnetic field caused by a core dynamo. MAG/ER however measured a remanent crustal magnetization, caused by iron-bearing minerals in the Martian crust, such as magnetite and hematite (Zuber, 2001). Overall the magnetic anomalies on Mars are 10 times more intense than terrestrial magnetic anomalies (Connerney et al., 2005). A remanent magnetization occurs when magnetic minerals are formed, or cooled below the Curie temperature (580°C for magnetite) in the presence of a prevailing magnetic field (assuming Mars had a geodynamo in the past).

The most recent magnetic field map of Mars, published by Connerney et al. (2005), is derived from two Mars years of observation (Figure 2.9). It shows no, or very low magnetic anomalies at the Utopia, Hellas, Argyre, Chryse and Isidis impact basins which suggests the core dynamo was lost when these impacts formed in the Early Noachian. On Earth the Vredefort meteorite crater in South Africa also shows a lower then usual magnetic intensity when observed using remote sensing (Carporzen et al., 2005). The rocks on the ground however show higher then normal magnetic intensities. These

intensities are randomly oriented and cancel each other out. Therefore the conclusion that the impact basins formed later then the extinction of the geodynamo may be incorrect.
Volcanic regions such as Elysium, Olympus Mons, the Tharsis Montes, and Alba Patera almost completely lack magnetic anomalies. They are observed on the flanks of the Tharsis Bulge which suggests that initial volcanism occurred when the core dynamo was still active (Nimmo and Tanaka, 2005).
The magnetic field map also shows a pattern of magnetic lineations with an alternating positive and negative polarity (Connerney et al., 2005). This has been interpreted as the result of crustal spreading contemporary to a reversing core dynamo, as observed on Earth's ocean floor, although larger in scale. The pattern is strong in the southern highlands but weak in the northern highlands, indicative of a buried Noachian basement. Connerney et al. (2005) also observed offsets of the lineations which they interpret as transform faults. Other interpretations for the lineations are large-scale dike intrusions, accretionary terrains and hydrothermal metamorphism, which is used to explain an apparent correlation between magnetic anomalies and valley networks (Nimmo and Tanaka, 2005; Solomon et al., 2005).

2.3.4. Orbital behavior

The Martian orbit can vary in three ways: (1) eccentricity, which is a measure of the ellipticity of the orbit, (2) obliquity, which is a measure of the tilt of the rotation axis and (3) precession, which is the variation of the rotation axis tilt direction relative to the orbit plane (Figure 2.10).
The current Martian orbit is highly elliptical, with an eccentricity of 0.0935 and a mean radius of 1.52 AU. One complete orbit (a Martian year) lasts 687 Earth days. The obliquity of the Martian rotation axis is 25°. One rotation (a sol) takes 24 hours and 37 minutes. The current high eccentricity and high obliquity causes Mars' seasons to differ in length. The southern summer is 24 sols shorter than the northern summer.
A combination of eccentricity, obliquity and precession cycles (Milankovitch cycles) cause changes in insolation and are known to have influenced the climate on Earth. According to Laskar et al. (2002) these cycles possibly also influenced the deposition of the polar caps on Mars. They found a correlation between calculated insolation parameters and a sequence of bright and dark layers of the northern cap. The 350m thick layer was found to be deposited in 0.9 Myr.
Laskar et al. (2004) calculated the insolation parameters for Mars for the last 250 Ma. Mars' obliquity was found to be highly variable and can vary in time between 0º and more than 60º. A change to a high obliquity (>40°) would influence the climate. Modeling showed that polar ice would sublime and deposit in the equatorial regions. There is evidence that this has happened during the Late Amazonian (300 – 600 Ma until present). Recently multiple stages of glacial activity were discovered at the base of Olympus Mons (18ºN) and east of the Hellas basin (39ºS to 43ºS) (Head et al., 2005; Neukum et al., 2004).
The Gamma Ray Spectrometer on board MO detected large amounts of near surface ice at high latitudes (Levrard et al., 2004). This led Levrard et al. (2004) to propose that during low obliquity (<25°) deposits of equatorial ice, earlier deposited during high obliquity, would sublime and deposit at high latitudes. This cycle of deposition and

sublimation at the Equatorial and Polar Regions could have been active throughout Martian history.
Mars has a fast rotation rate and large-scale topography such as the dichotomy and the Tharsis Bulge. A rotating body is most stable when most mass is farthest away from the rotation pole. Therefore it is possible that true polar wander, a change of the geographic location of the Martian rotation axis, occurred in the past. Sprenke et al. (2005) used gravity data to investigate possible polar wander caused by the emplacement of the Tharsis Bulge. They found that the current pole position would make pre-Tharsis Mars rotationally unstable, which suggests the Tharsis Bulge formation caused a gradual 15º-90º polar wander. The polar radius of Mars is ~22 km smaller than the equatorial radius. This large ellipticity suggests Mars' current geographical orbit orientation is very old (Sprenke, 2004).
There is also geomorphologic evidence for true polar wander, (1) the non-circular morphology of the polar caps of Mars led Murray and Malin (1973) to suggest that a gradual polar wander of 10º–20º occurred in the last 100 Myr, (2) the hiatus between Hesperian aged material and Late Amazonian polar deposits led Fishbaugh and Head (2001) to suggest polar wander brought the poles to their current position and (3) Schultz and Lutz (1987) observed possibly very young anti-podal deposits near the equator, similar to current polar deposits.

2.3.5. The atmosphere

Currently Mars has a surface temperature varying between 300 and 140 K (on average 220 K). Its CO_2 dominated atmosphere (95%) has an average surface pressure of 6.5 mbar. It varies 20% each year by condensation of CO_2 at the poles.
A Hadley type circulation, including trade winds, occurs in the Martian atmosphere (Leovy, 2001). It is stronger during northern winter than during southern winter. This is caused by the current high eccentricity. During the northern winter bright streaks on the surface show the Hadley circulation pattern of the surface winds.
The atmospheric temperature is controlled by suspended dust (Leovy, 2001). The amount of dust in the atmosphere increases during northern winter when the distance to the Sun is smallest. This causes dust storms, mostly occurring at mid latitudes. They can become global dust storms, completely covering the planet surface.

2.4. Mars Global evolution

2.4.1. The Noachian Period

2.4.1.1. Early Mars

Physical modeling and data from Martian meteorites suggest that the core, mantle and crust of Mars formed over a period of ~50-100 My, around 4.5-4.6 Ga (Stevenson, 2001; Solomon et al., 2005). Mars is 6800 km in diameter, about half the size of Earth, with two times the amount of surface area per volume, making it easier to release heat. Therefore Mars probably was most active during its first billion years (Solomon et al., 2005). Numerical modeling by Van Thienen et al. (2005) showed that plate tectonics or flood volcanism could only have occurred during an early episode of rapid cooling (> 200

$K \times Gyr^{-1}$), after which cooling mainly occurred conductively through Mars' lithosphere. From ~4.5 Ga to ~3.85 Ga Mars and Earth suffered a period of intense impact bombardment (Strom et al., 2005). During this period the major impact basins formed, e.g. Isidis, Hellas, Argyre, Chryse, Utopia and the south polar Prometheus Basin. It ended abruptly after a 10 to a 100 Myr final period of cratering called the Late Heavy Bombardment (Strom et al., 2005). The oldest surface unit mapped, the Hellas impact material, is around 4.05-4.13 Ga or older (Frey, 2005).

2.4.1.2. Tectonics and volcanism

According to Nimmo and Tanaka (2005), Head et al. (2001) and Tanaka et al. (1992) most tectonic activity occurred during the Noachian. Mainly extensional, f.e. grabens (fossae) and troughs, although compressional structures (wrinkle ridges) also occurred. Tectonics and volcanism in the Noachian is mostly associated with the construction of the Tharsis Bulge. The Tharsis related extension and compression are perpendicular to each other (Figure 2.11). Parts of the dichotomy boundary also experienced tectonic activity.

2.4.1.3. A Warmer Period?

An important question is if Mars was once warmer with a thicker atmosphere. During the Noachian Tharsis related volcanism probably put a large amount of CO_2 and water in the atmosphere resulting in a thicker atmosphere protected from atmospheric erosion by a global magnetic field (Jakosky and Phillips, 2001; Nimmo and Tanaka, 2005). However, the higher cratering rate during the Noachian also influenced the atmosphere, a 50 – 90% loss of the atmosphere for example occurred in the Early Noachian due to impacts (Jakosky and Phillips, 2001**)**. By correlating magnetic data with crater counts of QCDs, Frey (2005) placed the death of the global magnetic field at 4.10-4.21 Ga or older, occurring earlier than the oldest Noachian surface units. The occurrence of the light gas Xe, trapped in Martian meteorite ALH84001 3.9 Ga, is used to argue that the stripping of the atmosphere of Mars occurred 3.9 Ga or later (Jakosky and Phillips, 2001). An explanation for this difference in time is the presence of enough remanent magnetic anomalies which would have stalled the atmospheric stripping.

According to Baker (2001), Jakosky and Phillips (2001), Head et al. (2001), Masson et al. (2001) and Poulet et al. (2005) there is geological evidence for a warmer period with an active hydrological cycle during the Noachian:

1. The high erosion rates determined for Noachian surfaces (10^2-10^4 mm per 10^6 years) compared to the Hesperian and Amazonian surfaces (10^{-1}–10^{-2} mm per 10^6 years).
2. Thick sequences of layered sediments occur all over the Noachian highlands.
3. Valley network systems, with a dendritic spatial pattern, occur in the Noachian highland (Figure 2.12), with 63% having a Noachian age, 25% a Hesperian age and 12% an Amazonian age, although their small size makes it difficult to derive crater count ages.
4. The recent detection, using OMEGA data, of phyllosilicates, including clays, in outcrops of mainly Noachian age (Poulet et al., 2005).

Currently there are three valley network formation hypotheses, (1) a thicker atmosphere resulting in precipitation and surface runoff, (2) a globally higher heat flow and (3) localized hydrothermal systems (Gulick, 2001; Jakosky and Phillips, 2001).
According to Baker (2001), Gulick (2001) and Masson et al. (2001) the valley network morphology is best explained by groundwater sapping processes from localized hydrothermal systems, releasing subsurface water. This is supported by the lack of bedforms in the valley networks, indicative for surface fluid flow (Masson et al., 2001). However, the groundwater sapping hypothesis does not explain the high amount of recharge necessary to form the valley networks (Craddock and Howard, 2001). According to Jakosky and Phillips (2001) it is generally agreed that in any case a gradual process of water flow, not a catastrophical process is necessary to form the valley networks.
There is increasing evidence pointing in the direction of surface water flow during the Noachian and even Hesperian:

1. A complex of distributary, channelized, meandering flow landforms of Noachian age in the Erythraeum region observed by Malin and Edgett (2003) which they interpret as a fluvial distributary fan (Figure 2.13).
2. Dendritic valleys occurring within Late Hesperian units in the Valles Marineris region are interpreted to be formed by atmospheric precipitation (Mangold, 2004).
3. The MER rover Opportunity in Meridiani Planum found evidence of aqueous subsurface and surface water processes in exposed beds. The Meridiani plains lie on top Middle to Late Noachian material (Squyres et al., 2004; Squyres and Knoll, 2005).

The Noachian Period ended around 3.5 – 3.7 Ga when the cratering rate decreased dramatically (see Figure 2.6) (Hartmann and Neukum, 2001). During this time or early in the Hesperian the formation of valley networks ended abruptly indicating a change to a colder and drier climate (Jakosky and Phillips, 2001).

2.4.2. Hesperian Period

The Hesperian Period is a transition period between the high cratering and volcanic activity in the Noachian and the overall lower cratering and volcanic activity of the Amazonian (Head et al. 2001). It started 3.5 – 3.7 Ga and ended 2.9 – 3.3 Ga (Hartmann and Neukum, 2001).

2.4.2.1. Volcanism and tectonics

During the Early Hesperian there was a peak in volcanic activity (Nimmo and Tanaka, 2005), which resulted in smooth volcanic flood plains, like Hesperia Planum. According to Head et al. (2001) these plains covered more than 40% of the Hesperian surface, including the northern lowlands, where they are now covered by younger material. Frey et al. (2002) interpreted MOLA data and suggested that the volcanic plains in the northern lowlands could be 1-2 km thick. Tanaka et al. (2003) however state that no evidence for volcanic vents and flows have been found in the oldest exposed northern plains material.
According to Head et al. (2001) the volcanic plains were subsequently compressed forming long, sinuous wrinkle ridges. On a regional scale wrinkle ridges in a concentric pattern formed around the Tharsis Bulge. Mangold et al. (2000) found evidence for one

single global event of compressional deformation in the Late Hesperian which created wrinkle ridges in Noachian and Hesperian aged terrain. According to Tanaka et al. (2003) however most highland wrinkle ridges were formed during the Late Noachian to Early Hesperian and most lowland wrinkle ridges are Late Hesperian to Early Amazonian in age.
From the Late Hesperian onwards volcanism was mainly concentrated at the Tharsis Bulge and the Elysium Rise (Nimmo and Tanaka, 2005; Head et al., 2001). According to Neukum et al. (2004) the Martian shield volcanoes erupted episodically. Olympus Mons for example, on the Tharsis Bulge, started forming 3.4 Ga followed by episodes of eruptions, even possibly up to 5 Ma.
The enormous Noctis Labyrinthus-Valles Marineris rift system on the southeast slope of the Tharsis Bulge initiated during the Late Noachian and Early Hesperian and continued rifting during the Late Hesperian (Head et al., 2001; Tanaka, 1986). The opening was probably influenced by tensional stresses associated with Tharsis (Lucchitta et al., 1992). Valles Marineris rifted through thick layers of Noachian aged flood basalts, which were identified in its walls (McEwen et al., 1999). The rifting formed chasmata and troughs, which transitioned into outflow channels towards the east (Lucchitta et al., 1992). Chasmata (singular chasma) are deep, elongated, steep-sided depressions. Unconformably overlying the chasmata floors of Valles Marineris Internal Layered Deposits (ILD) occur. According to Masson et al. (2001) the ILD could be sediments deposited in former lakes. According to Montgomery and Gillespie (2005) the ILD have been eroded and stratigraphically underlie Hesperian aged lava flows. They propose the ILD are evaporite deposits with dewatered after the deposition of the lava. This resulted in catastrophic outflow of water. This hypothesis is strengthened by the detection of hydrated sulfates within the ILD by OMEGA (Gendrin et al., 2005).

2.4.2.2. Outflow channels

During the Hesperian and into the Amazonian episodically outflow channels formed (Masson et al., 2001). These channels are tens of kilometers wide and thousands of kilometers in length with an anastomosing pattern and with almost no tributaries (Figure 2.14). Bedforms include teardrop-shaped islands and scour marks around obstacles (f.e. craters). Terraces in some channels suggest that these channels were active multiple times (Tanaka, 1986).
The outflow channels have been interpreted to be caused by catastrophic outflow of a material behaving as a fluid (Masson et al., 2001, Baker, 2001; Baker et al., 1992). A variety of materials have been suggested to have eroded the channels:

1. Hoffman (2000) proposed a model in which Mars is dominated by CO_2 processes. Catastrophic degassing of liquid CO_2 would then create a ‘cryoclastic flow’, a CO_2 gas-supported density flow, which formed the outflow channels.
2. Nummedal and Prior (1981) and Tanaka (1997) favor mass flows or water floods saturated by sediments.
3. Jakosky and Phillips (2001), Head et al. (2001) and Baker et al. (1992) favor catastrophic outflow of water to explain the observed channel morphology. A terrestrial analog are the Channeled Scablands in the USA which were formed by large-scale erosion due to high velocity turbulent water flow (Baker, 2001; Masson et al., 2001). Kleinhans (2005) modelled water flow and sediment

transport of Martian outflow channels. He suggests that the formation of channels took around ten thousand to ten million years.

4. Other agents include SO_2, lava, glaciers or ice streams, winds and liquid hydrocarbons.

The largest system of outflow channels on Mars occurs around Chryse and Acidalia Planitia, the so-called circum-Chryse channels (Figure 2.15) (Masson et al., 2001; Phillips et al., 2001). Other locations where outflow channels occur are Amazonis, Elyseum and Hellas Planitia (Figure 2.15). Using MOLA data Dohm et al. (2001) discovered possible gigantic outflow channels, 1.2–2.4 km deep and 100–700 km wide. They occur on the west flank of the Tharsis Bulge and are defined as northwestern slope valleys (NSVs) (Figure 2.15). The NSVs flowed into the northern lowlands and are presently covered by volcanic and aeolian deposits. All locations show signs of volcanic activity. The formation of outflow channels was mostly restricted to the Hesperian Period but episodically continues until very recently (see *2.2.6.1. Recent and present day Mars*) (Head et al., 2001).

Three types of outflow channel source regions can be observed: chaotic terrains (such as Aram Chaos), Valles Marineris chasmata and extensional tectonic features (Hanna and Phillips, 2005) (Figure 2.16). Most outflow channels originate from chaotic terrains, of which they emanate 'full born' (Max and Clifford, 2001).

2.4.2.3. Chaotic terrain

According to Sharp (1973) chaotic terrain (Figure 2.1) is an area consisting of up to tens of kilometers sized slumped and collapsed blocks. It has possibly subsided, which could have been caused by the removal of water, magma or sediments (Sharp, 1973; Nummedal and Prior, 1981). Wang et al. (2005) attribute the "checkerboard patterns of gaps between blocks" to lateral spreading and collapse. The blocks form an arcuate fracture pattern which extends into the surrounding undisturbed terrain (Sharp, 1973). Chaotic terrains are generally irregular in shape. In some occasions it is confined by a possible impact crater, as is the case with Aram Chaos (Figure 2.3) (Chapman and Tanaka, 2002). Most chaotic terrains are bounded by a sharp escarpment (Baker et al., 1992) and some form systems of terraces (Tanaka, 1986; Rodríguez et al., 2005a). According to Nummedal and Prior (1981) collapsed blocks tend to be smaller away from the main collapse escarpment.

Most chaotic terrain appears at outflow channel heads (Baker et al., 1992) and are therefore interpreted to be the collapsed source regions for the outflow channels. Aram Chaos for example is one of the possible source regions of the Ares Vallis outflow channel (Figure 2.3). Current consensus is that chaotic terrain subsided after a catastrophic release of water (e.g. Masson et al., 2001; Baker, 2001). The water was possibly released do to pore pressure buildup (Carr, 1979) or liquefaction (Nummedal and Prior, 1981) and fluidization (Komatsu et al., 2000). Liquefaction is the collapse of grains of water-saturated sediment. Fluidization is the fluid like behavior of water-saturated sediment when the grains become suspended in the stream.

The water could have been stored as:

1. Ice.

2. Liquid water in a high-pressure confined aquifer below the cryosphere (Carr, 1979) or in a cavern system of fractures formed by impacts (Rodríguez et al., 2005a)
3. Bounded within evaporite deposits (Montgomery and Gillespie, 2005), methane hydrate (Max and Clifford, 2001) or CO_2 clathrate (Komatsu et al., 2000). When heated these materials would dewater and/or degas resulting in volumetric expansion and subsequent explosive release.

According to Max and Clifford (2001) various triggers for the catastrophic events have been proposed: global or regional warming, subsurface igneous activity, local deposition or erosion, impacts or tectonic activity. Wang et al. (2005) proposed that impacts producing craters larger then 100 km in diameter could trigger liquefaction of water saturated sediments on a global scale, resulting in catastrophic release of ground water. Mouginis-Mark (1985) and Chapman and Tanaka (2002) favor volcano-ice interactions as the trigger for catastrophic outflow. Heat from volcanic activity could melt subsurface or ground ice and thin the cryosphere (Masson et al., 2001) triggering catastrophic release. Catastrophic outflow itself could perhaps also trigger new outflow: according to Coleman (2005) catastrophic outflow from Aromatum Chaos (Figure 2.1) carved into the cryosphere, forming Ravi Vallis. This lowered the overpressure, triggering the formation of secondary chaotic terrain downstream (Iamuna Chaos, Oxia Chaos and an unnamed chaotic terrain).

The location of chaotic terrain could be structurally controlled. According to Schultz et al. (1982) chaotic terrain preferentially occur in concentric weakness zones of multiringed impact basins. Cabrol et al. (1997) proposed that the intersection of Tharsis related concentric wrinkle ridges and radial normal faults caused weakness zones where the cryosphere was penetrated by magmatic material. Aqueous fluids and/or magma are both likely to follow pre-existing fracture systems. Rodríguez et al. (2005a) for example proposed that the hydrogeology of Mars was significantly influenced by impact craters and their associated radial and concentric fracture systems.

Chaotic terrains lie 1−2 km below the surrounding undisturbed terrain (Masson et al., 2001) and could perhaps also have been depositional environments. Ori and Mosangini (1998) for example investigated Hydraotes Chaos (Figure 2.1). They found it first formed as a chaotic terrain but changed into a depositional environment. This occurred when its associated channels were captured by catastrophic water release from the Valles Marineris chasmata.

Not all areas defined as chaotic terrain are favorably formed by subsidence due to catastrophic outflow. Howard and Moore (2004) for example investigated Gorgonum Chaos in Terra Sirenum (Figure 2.1). They found that the, previously as ‘chaos’ defined, flat-topped mesas, originated from a continuous unit. This unit was subsequently preferentially eroded at linear zones of weakness, possibly cracks caused by an overburden of ice.

According to Baker et al. (1992) chaotic terrain cannot account for the amount of material needed to form the outflow channels. An explanation could be the erosion of earlier chaotic terrain by later outflow events. Or perhaps a recharge mechanism was active. Recharge by groundwater flow from a higher topographical region, such as Tharsis (Harrison and Grimm, 2004) or the South Pole (Clifford, 1987; Masson et al., 2001) have been proposed. Rodríguez et al. (2005a,b) proposed a model of enormous

subsurface impact fracture controlled caverns which episodically released water, possibly due to magmatic heating.
For a summary of all the mentioned chaotic terrain hypotheses and their predictions see Table 2.3.

2.4.2.4. A possible ocean and lakes?
According to Masson et al. (2001) calculations show that the catastrophic floods released at least 6×10^6 km^3 of water into the northern lowlands (Figure 2.17). The floods around Chryse Planitia alone carried 6×10^6 km^3 of eroded sediments. Under current conditions it is possibly that the freezing of so much water would form an ice cover, protecting against further evaporation (Masson et al., 2001). It is possible that this water remains as subsurface ice deposits or it sublimed and is now redistributed.
The existence of the outflow channels flowing into the northern lowlands led to the suggestion that an ocean or multiple lakes existed during the Hesperian (Masson et al., 2001). This is evidenced by ridges on the dichotomy boundary, interpreted as possible shorelines (Head et al., 2001). The presence of these possible shorelines is however still under debate, a study of high-resolution MOC images for example did not confirm the shoreline interpretation (Baker, 2001) and Withers and Neumann (2001) studied MOLA data of possible shorelines and interpreted these as wrinkle ridges.
During the Late Hesperian until the Early Amazonian the ~100m thick Vastitas Borealis Formation (VBF) was deposited in the northern lowlands, covering 17.6×10^6 km^2 (12% of the surface of Mars) (Figure 2.18) (Tanaka et al., 2003). The VBF has been interpreted as sediment (deposited in an ocean or by a debris flow) or as lava flows (Nimmo and Tanaka, 2005; Fishbaugh and Head, 2001). On parts of its surface 3 to 20 km sized polygonal patterns occur, which have been explained related to (1) tectonic uplift, perhaps caused by a disappearing load of water or (2) cooling of wet catastrophic flood deposits above frozen ground (Baker, 2001; Masson et al., 2001).
There is evidence for Late Hesperian to Middle Amazonian lakes in a large number of impact craters in the southern highlands, connected to valley networks and channels (Cabrol and Grin, 1999; Baker, 2001; Head et al., 2001). One such possible crater lake lies within Gusev crater, where the MER Spirit landed. Spirit however mostly found basaltic rocks, although one rock provides evidence for water alteration (Haskin et al., 2005).
Recently the MARSIS radar on board MEX identified a 250 km diameter subsurface crater within Chryse Planitia, not visible in satellite images and MOLA data, which has a ~1 km thick water ice deposit (Picardi et al., 2005).

2.4.3. Amazonian Period
The Amazonian Period started 2.9 – 3.3 Ga (Hartmann and Neukum, 2001) and continues until today. Volcanism, tectonics and water flow were active in the Amazonian but on a much more limited scale then during the two previous periods and occurring episodically. Volcanism mainly occurred at the Tharsis Bulge (Alba Patera, the Tharsis Montes, Olympus Mons) and at Elysium Mons (Tanaka et al., 1992). According to Neukum et al. (2004) Olympus Mons for example episodically erupted 900, 400 and 50 Ma. Overall they found evidence for repeated volcanic activity on Mars the last billion years.

Catastrophic outflow channels and some valley networks formed during the Amazonian, mostly associated with volcanic activity (Head et al., 2001).
During the Late Amazonian, which started 0.3 – 0.6 Ga (Hartmann and Neukum, 2001), Polar Layered Deposits formed on top of DAF in the South Polar Region and VBF in the North Polar Region (Head et al., 2001). DAF and VBF are Hesperian aged surfaces, which implies a hiatus of perhaps billions of years. Head et al. (2001) suggest polar deposit formation and destruction occurred multiple times. Fishbaugh and Head (2001) suggest perhaps polar wander brought the poles to their current position.

2.4.3.1. Recent and present day Mars
According to Hartmann (2005) the youngest lava flows, younger then 50 Ma occurred at Elysium Planitia, Olympus Mons on the Tharsis Bulge and Amazonis Planitia. Neukum et al. (2004) found ages as recent as 2.4 Ma for lava flows at Olympus Mons. According to Head et al. (2001) volcanism at Elysium Planitia is associated with recent activity (10 Ma or less) of the Marte and Athabasca Valles outflow channels. At the foot of Athabasca Vallis, Murray et al. (2005) found evidence for a 3-7 Myr old ice-covered lake measuring 72×10^4 km^2 and possibly 45 metres deep. On a smaller scale Malin and Edgett (2000) observed numerous gullies on hillslopes on MOC images. They attribute these to recent groundwater seepage and surface run-off. Hartmann (2001) suggests the gullies result from geothermal heating which melts subsurface ice layers producing aquifers. OMEGA however did not detect hydrated minerals within the gullies (Bibring et al., 2005).
Although volcanism and water flow probably have occurred in the recent past, aeolian activity is currently the dominant process on Mars. This is evidenced by the occurrence of global dust storms, dust devils, wind streaks and numerous dune fields, including an enormous dune sea in the north (Fishbaugh and Head, 2001). The dunes are very recent, less then 1 Myr old (Hartmann, 2005). The surface of Mars today is around 40% Noachian in age and around 50% is of volcanic origin (Solomon et al., 2005; Head et al., 2001).

2.5. Summary
The different events previously discussed have been summarized in Figure 2.19.

3. Regional geology

3.1. Introduction

Aram Chaos is a chaotic terrain (Figure 2.1) located 2.5ºN and 338.5ºE, in the Xanthe and Margaritifer Terrae (XMT) region (Figure 3.1). In the Hesperian and into the Amazonian the XMT region has been dissected by six of the circum-Chryse outflow channels: Shalbatana, Simud, Tiu, Ares and Mawrth Valles (Figure 3.1). This section will describe the regional geological history of XMT and the more detailed geological history of Aram Chaos.

3.2. Regional History

The XMT region has been mapped by Scott et al. (1987) (1:15M scale), Rotto and Tanaka (1995) (1:5M), Tanaka (1997), Nelson and Greeley (1999) (1:2M) using Viking images. Tanaka et al. (2003, 2005) (1:15M to 1:7.5M) used Viking, MOC and THEMIS visible and infrared images, MOLA elevation and TES multispectral data to map part of the XMT region focusing on the evolution of the northern lowlands (Figure 3.2). Tanaka (1997) elaborates on the USGS map by Rotto and Tanaka (1995). For this regional history I will refer mainly to the most recent study, Tanaka et al. (2005).

3.2.1. The Noachian

Tanaka et al. (2005) distinguishes between two Noachian aged units in XMT, the Libya Montes unit (Nl), of Early to Middle Noachian age, and the Noachis Terra unit (Nn), of Middle to Late Noachian age (Figure 3.2). Nn is highly degraded by impacts and is dissected by valley networks. It embays the older higher relief Nl, which is also highly degraded by impacts. Nl completely surrounds Aram Chaos. They interpreted Nn and Nl to be volcanic and sedimentary material.

North of XMT the Chryse Planitia 1 unit ($HNCc_1$) occurs, which is Late Noachian to Early Hesperian (Figure 3.2). It embays Nl and Nn and it is interpreted to be a mass wasting deposit. It is covered by wrinkle ridges.

3.2.2. The Hesperian and Amazonian

Three Late Hesperian aged flooding related units occur around Aram Chaos (Figure 3.2):

1. The Simud Vallis unit (HCs)
2. The Ares Vallis unit (HCa)
3. The Chryse Planitia 4 unit (HCc_4)

HCs is the most widespread in XMT and forms Simud, upper Tiu, Shalbatana Valles and Hydraotes, Hydaspis and Aram Chaos. It cuts into $HNCc_1$ and grades into HCc_4 towards Chryse Planitia (Figure 3.2). HCa forms deposits in Ares and lower Tiu Valles, southern Chryse Planitia and Iani Chaos. Its surface is covered by irregular pits, linear scarps and grooves. HCa is interpreted to be of possible igneous origin, because of its olivine-rich TES signature. The observed pits could be caused by thermokarst processes. HCc_4 also forms part of the Ares Vallis floor where it embays HCa. It is interpreted to be a deposit from Simud and Tiu Valles flows.

The crater floor unit (AHcf) of Early Hesperian to Early Amazonian age covers some crater floors, including Aram Chaos, where it is layered (see *3.4. Geology of Aram Chaos*). According to Glotch et al. (2005) layered deposits similar to Aram Chaos occur

in Aureum, Iani and Arsinoes Chaos. The Early Hesperian to Late Amazonian Crater unit (AHc) forms the ejecta, rim, and floors of craters.

3.3. Regional Igneous Activity and Structural Geology

1. Using MOLA data Rodríguez et al. (2005b) identified a transition from highland terrain to lower elevated chaotic terrain. They attribute this transition to different degrees of ground subsidence due to withdrawal of water from a subsurface linked impact fracture system (Rodríguez et al., 2005a).
2. According to Schultz et al. (1982) Chryse basin is a multiring impact basin which influenced the formation of Valles Marineris and controlled the location of chaotic terrain. These form preferentially at locations concentrically to Chryse and intersecting Valles Marineris and other impact basins (Figure 3.3).
3. Lanz and Jaumann (2001) identified cone-shaped hills in Aram Chaos which are up to 2 km in diameter and several hundreds of meters high. They interpreted these to be possible magmatic intrusions.
4. Rodríguez et al. (2005b) observed 'quasi-circular structures', ~1 km in diameter, in the eastern part of Hydaspis Chaos (around 2.6719°N, 334.5755°E), which they interpret as resembling ring dikes.
5. Olivine was detected on the floor of Ares Vallis, NE of Aram Chaos (Rogers et al., 2005)

3.4. Regional Geophysics

A negative gravity anomaly has been observed at Valles Marineris, Chryse Planitia, into the northern lowlands (Smith et al., 1999) (Figure 3.4). The negative anomaly over Chryse Planitia is interpreted to be caused by the removal of ~2 km of material by outflow channel erosion. According to Smith et al. (1999) Chryse Planitia does not show the same anomaly as other northern hemisphere impact basins. According to Phillips et al. (2001) Chryse Planitia is part of the Tharsis trough, a topographical low surrounding the Tharsis Bulge, caused by the loading of the lithosphere by the Tharsis Bulge.

Chryse Planitia, like the Hellas, Argyre, Isidis and Utopia impact basins doesn't show remanent magnetization. The ridged plains of the Tharsis Bulge near Valles Marineris also do not show magnetization (Connerney et al., 2005). The heavily cratered terrain of XMT however are magnetic.

Recently the MARSIS radar on board MEX identified a 250 km diameter subsurface crater within Chryse Planitia, not visible in satellite images and MOLA data, which may have a ~1 km thick water ice deposit (Picardi et al., 2005).

OMEGA detected phyllosilicates (montmorillonite) in light toned Noachian aged deposits near, and in the flanks of Mawrth Vallis (between elevations -3200 and –2700 m) (Poulet et al., 2005).

3.5. Geology of Aram Chaos

3.5.1. Introduction

Aram Chaos is a 280 km diameter circular chaotic terrain, located within a 550 km in diameter multiringed impact basin, Aram Basin (Schultz et al., 1982). Ori et al. (2004)

observed that the chaotic terrain cut into the crater rim, enlarging the inner depression. They didn't observe a central crater peak.
Aram Chaos is interpreted to be one of the Ares Vallis outflow channel source regions. It is connected to Ares Vallis via a 15 km wide, 2.5 km deep channel (Glotch and Christensen, 2005). Cabrol and Grin (2002) observed a possible sublacustrine delta structure at in the Aram Chaos part of the channel (Figure 3.5).
According to Nelson and Greeley (1999) 1.9×10^5 km^3 material was eroded and removed from Ares Vallis alone and its chaotic terrain, and the floods could have reached a rate of 7×10^7 m^3/s. Mars Pathfinder landed on the mouth of Ares Vallis. Boulders of 7 m in diameter were identified by the Pathfinder Camera Team and possibly conglomerates. Outflow rates at the landing site were estimated between 10^6 and 10^7 m^3/s.

3.5.2. Previous mapping

Schultz et al. (1982) created a simple terrain map of the Aram Chaos region using Viking data (Figure 3.6). Detailed mapping of Aram Chaos, using TES, THEMIS, MOLA and MOC data, was performed by Glotch and Christensen (2005). They distinguish between two classes, disrupted (chaotic) terrain and nondisrupted (layered) terrain. The emphasis of their research is on the evolution of the layered terrain, in which a hematite signature was detected (see *3.4.1. Hematite formation*). The layered terrain are interpreted to be deposited after the formation of the chaotic terrain.
Glotch and Christensen (2005) divide the chaotic terrain into three, possibly lateral units (Figures 3.7 and 3.8):

1. The largest unit, the Fractured Plains unit (C_f), almost completely surrounds the crater rim. It consists of up to tens of kilometers sized slumped blocks forming a curvilinear fracture pattern.
2. The second largest unit, the Knobby Terrain unit (C_k and C_{kh}, containing hematite), occurs in the central part of Aram Chaos and at some locations surrounds the crater rim. It consists of km scale irregular blocks ("knobs").
3. The High Thermal Inertia Chaotic Terrain unit (C_{ht} and C_{hth}, containing hematite) occurs in the central part of Aram Chaos. Using superposition relationships Glotch and Christensen (2005) interpreted it to underlie outcrops of layered material.

The layered terrain are divided into five units, from lowest to highest, which form a dome (Figures 3.6 and 3.7N):

1. The Cap unit (P_c), which has a relatively high thermal inertia. MOC images show it to have an etched surface on which dark sand is trapped. P_c was observed to be ~200 m thick at the top of the dome and it is thinning to the west.
2. The Subdued unit (P_s) and the Primary Hematite unit (P_h), which are possibly laterally connected. They differ in the presence of hematite. The thickness of P_h is 100-150 m. P_h has the highest hematite abundance compared to the other hematite units.
3. The Secondary Hematite unit (P_{h2}), is interpreted to be draped onto older terrain (it occurs within a ~500 m elevation difference), containing transported hematite.
4. The Non-Hematite unit (P_{nh}) lies below P_h and is observed to be geomorphologically the same as P_h. TES however indicates it is mineralogically the same as P_s. It is however thicker then P_s and has more distinct layering.

A sixth non-chaotic unit is the Outflow Plains unit (P_o). This occurs at Aram Chaos side of the 15 km wide channel connecting Aram Chaos with Ares Vallis. It contains 200-300 m deep tributaries.
Using remote sensing a variety of minerals have been detected within the layered material. A ~5000 km^2 deposit of grey crystalline hematite has been detected using TES data (Glotch and Christensen, 2005). Glotch and Christensen (2005) favor an aqueous deposition model for the formation of the hematite. OMEGA did not detect grey crystalline hematite at Aram Chaos, although red particulate hematite has been observed (Combe et al., 2005). OMEGA also detected hydrated minerals and sulfates in the layered deposits (Bibring et al., 2005; Gendrin et al., 2005).

3.5.3. Hematite formation

Crystalline gray hematite (α-Fe_2O_3) has been detected by TES in Aram Chaos, Meridiani Planum, Valles Marineris (associated with its Internal Layered Deposits) and Aureum Chaos (Christensen et al., 2001; Glotch et al., 2005).
According to Christensen et al. (2001) hematite can form by three processes: (1) acqueous or hydrothermal deposition, (2) laterite-style or subareal weathering or (3) thermal oxidation of Fe-rich lavas. Weathering mostly forms red hematite and lava flows have not been observed at the Mars hematite locations. Therefore they favor acqueous or hydrothermal deposition. Catling and Moore (2003) studied Aram Chaos and performed geochemical modelling. They favor formation of the Aram Chaos gray hematite in a hydrothermally charged aquifer with 100ºC or greater temperatures.
The MER rover Opportunity found a large amount of spherical hematite concretions ("blue berries") in an outcrop in Meridiani Planum (Squyres and Knoll, 2005). The outcrop occurs in the walls of the 150 m diameter and 20 m deep Endurance crater. It consists of an at least 7 m thick sedimentary sulfate-rich aeolian sand stone formation (Burns formation). In some units large scale cross bedding occurs, interpreted to be caused by subaqueous deposition. The whole formation is interpreted to be formed in an arid environment. Occasionally surface water flow and pooling occured after which the water evaporated. The formation of the spherical hematite concretions is attributed to ground water alteration after deposition of the sands.

3.6. Scenarios

Two main sources for the fluvial activity within the XMT region have been described:

1. A Vallis Marineris source. Nelson and Greeley (1999) for example identified multiple stages of channel floods in the XMT region, starting with a sheetwash flowing from Valles Marineris into Chryse Planitia. This was possibly triggered by early Vallis Marineris rifting. According to their study Ares Vallis was active during multiple stages with subsequent erosion and redeposition.
2. An Argyre Planitia source. Parker et al. (2000) and Grant and Parker (2002) describe a channel system, starting at Argyre Planitia and flowing towards Chryse Planitia via Ares Vallis (Figure 3.9). According to their study the water ponded in Margaritifer Basin, south of Aram Chaos (Figure 3.10). This water was subsequently released carving Ares Vallis. According to Nelson and Greeley (1999) multiple episodes of Ares Vallis channel formation occurred.

Schultz et al. (1982) devised a typical cross section for multi-ring impact basins on Mars, larger then 300 km in diameter, such as Aram Basin (Figure 3.11 and Table 3.1). They interpreted the Aram Chaos chaotic terrain to be occurring, within a ring graben, in zone D of the cross section (Figure 3.11 and Table 3.1). The fault between zone D and E (Figure 3.11 and Table 3.1) is interpreted to provide a conduit for extrusive and intrusive volcanism and associated hydrothermal activity. According to Schultz et al. (1982) no large-scale extrusive volcanism occurred at Aram Chaos. The hydrothermal activity caused the release of 'hydrothermal slurries', which led to the chaotic terrain collapse, and the formation of outflow channels.
They proposed that impact related concentric weakness zones influenced the spatial pattern and location of Aram Chaos, Ares Vallis and two nearby chaotic terrain: Iani and Hydaspis Chaos. Iani and Hydaspis Chaos both sourced Ares Vallis.
Glotch and Christensen (2005) proposed that Aram Chaos underwent multiple stages of development (Figure 3.12):

1. The chaotic terrain was formed by catastrophic outflow from a subsurface aquifer. The triggering event of the chaotic terrain formation is unknown. Possibly volcanism underneath Aram Chaos triggered the catastrophic outflow. The three chaotic terrain units are interpreted to have a different disturbance, with C_f the least disturbed, then C_{ht} and C_k the most disturbed. According to Glotch and Christensen (2005) this could be caused by:
    a. Differences in the pre-chaotic terrain composition.
    b. Lateral differences in the subsurface water content.
    c. Different chaotic terrain processes in time.
2. The layered material was subsequently deposited in a lacustrine environment.
3. A doming event tilted the chaotic terrain and layered material. This fractured the layered material causing resurfacing of chaotic terrain at some locations.

3.7. Discussion

This section discusses the hypotheses described in **2. Mars Background** and in this section, which are of importance to the formation of Aram Chaos. Table 2.3 summarizes all the chaotic terrain formation hypotheses and their predictions described in the literature. The following predictions can possibly be identified using geological mapping:

1. (Subice) volcanism and/or (dike) intrusion (hypotheses 1, 3, 4, 5, 6, 8, 9 of Table 2.3).
2. Uplift prior to subsidence (2, 3, 5, 7). The fracture patterns of uplift type fractures (f.e. salt domes) and collapse/subsidence type fractures (f.e. calderas) will be compared with the observed chaotic terrain fracture patterns.
3. Chaotic terrain occuring preferentially in low elevations (2, 3, 5, 7). This can be verified using MOLA and/or HRSC DTM data.
4. A gradient in topography causing failure (3).
5. A high water content of sediment (3, 6, 10) can perhaps be identified using OMEGA data and/or geomorphological observations.
6. Chaotic terrain at crossing of perpendicular lineaments (5)
7. Chaotic terrain similar to terrestrial analogs (6, 7). The different fracture patterns will be compared.

8. Dewatering of evaporite deposits (9) can perhaps be identified using OMEGA data.
9. Chaotic terrain within outflow channel (11).
10. Attempting to prove that chaotic terrain formed by impacts causing seismic activity (2, 3, 7, 10) is considered futile due to the occurrence of chaotic terrain in impact saturated Noachian terrain.

4. Methodology

4.1. Introduction

This section will describe the different methods used to map and investigate Aram Chaos. The image data had to be processed before it could be used. This included the georeferencing of the data so that each image pixel correlates with a coordinate. The data was subsequently imported into a Geographical Information System (GIS) created using the software product ESRI ArcGIS. This software was used to perform the mapping and analysis.

4.2. Software

The following software was used for the investigation:

1. Integrated Software for Imagers and Spectrometers (ISIS) v2.1 from the USGS (Linux/Unix) (http://isis.astrogeology.usgs.gov)
2. VICAR routines created by DLR to manage HRSC data (Linux/Unix)
3. IDL routines created by the OMEGA science team to manage OMEGA data (Linux/Unix)
4. IDL/ENVI from RSI (Windows/Unix)
5. ENVI reader for ArcGIS v1.1 (http://www.ittvis.com/download/download_splash .asp?wdiid=548).
6. ESRI ArcGIS (Windows)
7. ImageMagick (http://www.imagemagick.org) to create JPEG2000 files from tiffs (Linux/Unix/Window).
8. PEDR2TAB program (http://pds-geosciences.wustl.edu/missions/mgs/mola software.html#PEDR2TAB) to handle MOLA PEDR files.
9. GEOrient to create Rose Diagrams (Windows)
10. Windows driver to access Linux partition (http://www.fs-driver.org/ download.html)
11. Bzip2 for windows (http://gnuwin32.sourceforge.net/packages/bzip2.htm), to be able to unpack the HRSC data in windows.
12. Wget for windows. This software is standard in Unix/Linux but has to be downloaded for windows (http://www.interlog.com/~tcharron/wgetwin.html).
13. Geospatial Data Abstraction Library (GDAL) included in the FWTools package (http://fwtools.maptools.org/)

4.2.1. ArcGIS arcscripts and addons

1. ArcMap tweaks to enhance your productivity (http://arcscripts.esri.com/ details.asp?dbid=13306)
2. Shapefile Repair Tool (http://arcscripts.esri.com/details.asp?dbid=13733)
3. Create and add shapefile (http://arcscripts.esri.com/details.asp? dbid=11652)
4. Overview window (http://arcscripts.esri.com/details.asp?dbid=11965). It creates a small overview window in the lower left of the ArcMap screen. It uses the lowest layer in the ArcMap table of contents as its background.
5. Bookmarks2Shapefile (http://forums.esri.com/Thread.asp?c=93&f=1730&t=1884 69#558092)

6. Copy & Paste Image Symbology (w/ Nulls) to Images and/or ImageCatalogs (http://arcscripts.esri.com/details.asp?dbid=13128)
7. Geodesic (True) Distance Tool for ArcMap 8 or 9 (http://arcscripts.esri.com/details.asp?dbid=12819)
8. Lon/Lat Readout in Projection ArcMap 8.x or 9.x (http://arcscripts.esri.com/details.asp?dbid=12841)
9. Add X and Y Coordinates (Enhanced) for 9.x (http://arcscripts.esri.com/details.asp?dbid=13618)
10. Add Area and/or Length (http://arcscripts.esri.com/details.asp?dbid=12524)
11. Find Polyline Angle (http://arcscripts.esri.com/details.asp?dbid=14234)
12. Profile Tool v1.1 (http://arcscripts.esri.com/details.asp?dbid=14064)
13. XTools Pro (http://www.xtoolspro.com)
14. List MXD Sources (ver.2) (http://arcscripts.esri.com/details.asp?dbid=13780)
15. Add Points At Crossings (http://arcscripts.esri.com/details.asp?dbid=13208)
16. Circular Regression (http://arcscripts.esri.com/details.asp?dbid=14629)

4.2.2. Adding and using arcscripts in ArcGIS

Acrscript addons for ArcGIS come in the form of Visual Basic for Applications (VBA) macros, .dll files and ArcToolbox scripts. ArcToolbox scripts can be added to the ArcToolbox by right-clicking ArcToolbox and selecting Add Toolbox.

The .dll files can be added to ArcMap, ArcScene or ArcCatalog via Tools > Customize > Add from file... In the Commands tab of the Customize window one or more new commands will appear (if not the appropriate category has to be selected). Each command can now be dragged and dropped to a toolbar, becoming a button. You can choose to save the new configuration in either the normal.mxt template or your current project .mxd file.

VBA macros can be added to the project via Tools > Macros > Visual Basic Editor. In the left part of the VBE window a table of contents is located consisting of normal.mxt and your project .mxd file. Right click on one of them and select Insert > Userform or Insert > Module. Inserting the macro in your normal.mxt file means that the script is always available from ArcMap. The modules are .bas files, the userforms are .frm files. The userforms consist of the windows, buttons and events and the modules consist of the underlying code. The macros can be executed via Tools > Macros > Macros. They can be dragged to a toolbar as a button by choosing the Macros category in the Commands tab of the Tools > Customize window.

4.3. Mars GIS definitions

A GIS coordinate system consists of two parts, a geographic and a projected coordinate system. The geographic coordinate system is the representation used to model the planet. The projected coordinate system is the projection used to represent the data.

4.3.1. Geographic coordinate system

In 1971 the International Astronomical Union (IAU) defined two possible Mars geographic coordinate systems (Duxbury et al., 2002):

1. East positive longitude and planetocentric latitude. Longitude is measured positive eastward, in the direction of Mars' rotation. The planetocentric latitude of

a specific point on the surface is defined as the angle between the equatorial plane and a line from the center of Mars to that point (Figure 4.1).
2. West positive and planetographic latitude. The planetographic latitude of a specific point on the surface is defined as the angle between the equatorial plane and the normal to an elliptical representation of Mars at that point (Figure 4.1).

Two representations of Mars are possible, a sphere or an ellipse. In 2000 the IAU defined the geographic coordinate system for Mars to be a best-fit ellipse with a semi-major axis of 3396.19 km and a semi-minor axis of 3376.20 km. When a spherical representation is chosen planetocentric and planetographic latitude are the same, so planetographic latitude only makes sense when using an elliptical representation of Mars.
The longitude system can be further refined. It can either be defined between 0° and 360° or between –180° and 180°. According to Trent Hare (personal communication) most GIS software prefer a 180° longitude system with a 0° central longitude. ArcGIS works with this combination and with the 360° longitude system, 180° central longitude combination (Figure 4.2) Two types of ArcGIS ready MOLA data for example can be downloaded from the USGS, a version using -180° to 180° and the 0° longitude as central longitude (central meridian) and a version using 0° to 360° and the 180° longitude. The two images are thus shifted 180 degrees. The prime meridian 0° longitude of Mars is defined as the middle of the Airy-0 crater (Malin et al., 2001).

4.3.2. Projected coordinate system

The most common projection type for Mars is 'Simple Cylindrical' (also called 'Equirectangular' or 'Equidistant Cylindrical') and is a cylinder wrapped around Mars. The tangent line chosen here is the equator. An example is the USGS ArcGIS ready MOLA data. It is a Simple Cylindrical projected representation of the surface of Mars from 88N tot 88S (22528x46080 pixels), with a resolution of ~463 m/pixel (128 pix/deg). The geographical representation of Mars used is a sphere of 3396.19 km. It is referred to as the Mars_2000_Sphere model of Mars (the IAU2000 ellipse is referred to as the Mars_2000 model).
With this projected coordinate system the equatorial region has the least latitude distortion and the polar region the most. Therefore special Polar Stereographic projected MOLA data can be downloaded from the USGS. Polar Stereographic projected data is projected on a plane with a normal parallel to the polar axis (Figure 4.3). The Mars Global Surveyor orbiter carrying the MOLA instrument is in a polar orbit and therefore the polar region has the highest data density (the highest resolution data is ~115 m/pixel (512 pix/deg)). The USGS Polar Stereographic projected MOLA data are projected onto a sphere with the Mars polar radius (semi-minor axis) of 3376.20 as radius.

4.3.3. In practice

In practice the IAU2000 elliptical standard is not widely used. This is due to some issues:

1. The raw MOLA data, which has a global coverage, was measured relative to a sphere of 3396 km. Most planetary scientists use this data as the base in their GIS on which they project the other data. The USGS ArcGIS ready MOLA data was created by reprojecting the raw data on the 3396.19 Mars_2000_Sphere model.
2. ISIS, the software used to create ArcGIS ready map projected MOC and THEMIS data only supports a spherical representation of Mars for the Simple Cylindrical

projection equation (see http://isis.astrogeology.usgs.gov/Isis2/isis-bin//pdfs2.cgi?mappars). The VICAR software which was used to project the HRSC data however was able to project the data onto an ellipse.

3. In ArcGIS the Simple Cylindrical projection equation uses a sphere, even if you define an ellipse. Polar Stereographic and Sinusoidal projections however do use the ellipse in their equations

For my research I chose the -180 to 180 east positive longitude system which one version of the USGS MOLA data uses. The data uses the Mars_2000_Sphere model although in the label the Mars_2000 model was mentioned. Therefore I presumed the data used the IAU2000 ellipse. I also assumed the ISIS processed data used the IAU2000 definition. I assigned the IAU2000 projection for these data in ArcMap but because ArcMap only supports a sphere for Simple Cylindrical projected data only the 3396.19 km sphere radius was used, which was in agreement with the actual projection of the data. The VICAR processed HRSC data were reprojected using the IAU2000 definitions and therefore did not correlate well with the MOLA and THEMIS data. Therefore I propose to use the Mars_2000_Sphere model for all data.

4.4. Image processing

4.4.1. THEMIS processing

4.4.1.1. The THEMIS data

The THEMIS imager on board 2001 Mars Odyssey consists of a visual wavelength (VIS) and infrared wavelength (IR) camera. The VIS data has 5 bands and the IR data 9 bands. The data is available online (http://themis-data.asu.edu) as .QUB files, which are three-dimensional data cubes. The first two axes form 2D images and the third axis are the different bands. The .QUB files used have been radiometrically calibrated and are named XooooiiiRDR.QUB. RDR stands for Reduced Data Record. The Xooooiii format makes the image id, with X either V (for VIS) or I (for IR), ooooo the orbit number and iii the image number.

4.4.1.2. Selection and downloading

1. THEMIS footprint shapefiles for ESRI ArcGIS were downloaded from ftp://ftpflag.wr.usgs.gov/dist/pigpen/mars/themis/footprints. They were created by Trent Hare from the USGS. I used the April 2005 release. The zipfile on the ftp site contains a THEMIS IR day, IR night and VIS footprint shapefile.
2. Only the footprints covering the area of interest were selected and saved into new shapefiles.
3. The attribute tables of the shapefiles contain the image numbers. These were extracted into textfile lists.
4. Using a perl script (see Appendix A.1) 'http://themis-data.asu.edu/img/browse/' was added in front of each image number in the textfiles creating an image preview download list.
5. The perl script download.pl (Appendix A.2) was used to download the image previews. It uses wget to download.. The downloaded images are .png images but do not have an extention, so in DOS 'ren *. *.png' was performed.

6. The image previews were visually examined and bad images were deleted.
7. A .QUB file download list of the remaining images was made:
    a. In DOS 'ren *.png *.' and 'dir/b *.>list' was performed creating an image name list of the remaining images.
    b. The perl script thmurl.pl (Appendix A.3) was executed to create the .QUB file download list. These were subsequently downloaded using download.pl.

4.4.1.3. Processing

8. The .QUB files were processed to level 2 (map projected and radiometrically corrected) using Integrated Software for Imagers and Spectrometers (ISIS) version 2.1 from the USGS (http://isis.astrogeology.usgs.gov/Isis2/isis-bin/isis.cgi) which works in Unix/Linux. 8-bit jpg images were created which can be used in ArcMap. For each .QUB file the following procedures were performed (for the script see Appendix A.4):
    a. The thm2isis program from ISIS, which converts the QUB files into an ISIS format. The files were given a .QUB.l1 extention. For KERNLST $ISISM01DATA/thm_kernels_both.def.N (N was at the time 8) was used containing the SPICE kernels (camera pointing data). This specific file uses fake pointing data if real pointing data isn't available for an image. This is explained further in Mars Odyssey THEMIS Geometry Processing With ISIS section 12 (http://isis.astrogeology.usgs.gov/Isis2/isis-bin//themis_processing.cgi). For LONSYS 180 was used and for LATSYS OCENTRIC (which is default).
    b. The dsk2dsk program from ISIS, which was used to extract one band from the multiband .QUB.l1 files. For IR day band 9 was used, for IR night band 2 and for VIS band 3. The resulting files were named .QUB.l1.1b.
    c. The thmirmc (for IR day and night) or the thmvismc (for VIS) programs from ISIS, which creates level 2 map projected files. The filenames have .irmc.cub or .vismc.cub extentions. MAPPARS was set to SIMP:0,OCENTRIC. For KMRES 0.1 was used for IR images and 0.019 for VIS images.
    d. The dform program from ISIS, which was used to convert the 32-bit data to 8-bit .tif images and to extract location information to create .tfw world files.
9. The convert program from ImageMagick was used within a perl script (Appendix A.5) to convert the .tif files to .jpg files with a jpeg2000 compression. The .tfw files were copied to .jgw files.
10. The resulting .jpg and .jgw files were visually examined and divided in 'normal, 'bad' and 'large'. The large images form the base of the mosaic. The 'bad' images were too bright, too dark or broken. They were only included if they covered otherwise uncovered terrain. The normal images were included if they covered otherwise uncovered terrain and if they had better quality then the large images.
11. The images were ordered by location using a perl script (see Appendix A.6).
12. The images were loaded in ArcMap. The best images were put on top and bad images were excluded. Using the arcscript 'List MXD Sources' a text file was

created of the Table of Contents of ArcMap containing the image numbers. A perl script created a list textfile of the irmc.cub or vismc.cub files (mc.lst) (for the script see Appendix A.7)..

13. For IR day mosaicking the following procedures were performed (for the script see Appendix A.8):
    a. The b4equal program from ISIS, which calculates and puts statistical information in the vismc.cub or irmc.cub files. The MODE argument was set to SD, which means standard deviation is used to calculate the mean brightness of the overlap area of overlapping images.
    b. The equalizer program from ISIS, which will attempt to remove seams between images. It uses the information added by b4equal to calculate a best fit for brightness values of two overlapping images.
    c. The corrections are written into an ISIS script, which was executed. This creates new image files with a vismc.cub.l4 or irmc.cub.l4 extension.
    d. Because the files in the mc.lst are in a specific order 'ls –1 *.l4>l4' cannot be used within Unix. A perl script was used to rewrite mc.lst to l4.lst keeping the specific order (Appendix A.9).
    e. The noseam routine from ISIS, which uses a high pass and low pass boxfilter to remove seams of images before mosaicking. The program needs the latitude and longitude range, the boxfilter size in line and sample direction (11 was used for both). The TOP argument was set to NO which means that the first processed image is put on the top of the mosaic and the next image is put below this image, etcetera.
    f. Dform and convert were used to create a .jpg image mosaic and accompanying .jgw file.
14. For IR night mosaicking the following procedures were performed (for the script see Appendix A.10):
    a. For IR night images mosaicking was performed using a perl script (Appendix A.11) which calls for the mosaic program without applying the noseam filters. This way the brightness variation is not distorted.
    b. Dform and convert were used to create a .jpg image mosaic and accompanying .jgw file.
15. The mosaic.jpg file can now be opened in ArcMap.

4.4.1.4. New release of THEMIS data

1. The Januari 2006 release from ftp://ftpflag.wr.usgs.gov/dist/pigpen/mars/themis/ footprints was downloaded and both the April 2005 and Januari 2006 releases were opened in ArcMap. Only the newer footprints were selected by first selecting all the footprints in the new shapefile which were identical to the old shapefile. This was done using the Select By Location window (Selection > Select By Location). By right clicking the new shape file and choosing Selection > Switch Selection the new footprints were selected.
2. The new images were downloaded, examined, processed to level 2 and converted to .jpg using the method described in the two previous sections.

4.4.1.5. Difficulties

1. The computer crashed during b4equal processing. Next attempt halted with error that FILE_STATE=DIRTY. This can be bypassed by setting 'setenv ISIS_IGNORE_INTEGRITY TRUE' in the c shell (http://isis.astrogeology.usgs.gov/Isis2/isis-bin/isis_arch.cgi#9).
2. The amount of THEMIS VIS was too big for selection so the individual map projected images were opened in ArcMap.
3. It was attempted to create a seamed IR night mosaic (using the ISIS noseam routine) but this resulted in a black image. Therefore they were simply mosaicked together to create the THEMIS IR night mosaic.

4.4.2. HRSC processing

4.4.2.1. The HRSC imager

The High Resolution Stereo Camera on board the European Space Agency (ESA) Mars Express (MEX) satellite is active since December 2003. The imager is a stereo camera, which means it contains multiple imagers, creating multiple images from different angles at the same time. These images can be combined to create anaglyphs and DTMs. Especially the possibility to create DTMs is valuable because the results are 1) more detailed then current MOLA DTMs and 2) each pixel is a true measurement, whereas the MOLA data is an interpolation of laser points. The highest resolution images are the nadir images (the imager points directly downwards to the surface). They can achieve a resolution <10 m/pixel.

4.4.2.2. The HRSC data

The HRSC images I used were not all available on the ESA Planetary Science Archive (http://www.rssd.esa.int/psa/). Most images had only just recently been acquired. The PSA on the other hand is updated every 6 months. The non-PSA images were provided internally by ESA. See Table 4.1 for a list of all the HRSC images used.

A complete set of HRSC data consists of a high resolution nadir image, two stereo images, a red, green, blue and infrared wavelength image and two photometry images. The photometry images are no different then the stereo images.

Most orbits I used contain a complete set of images. For some orbits however, due to a limiting data transfer rate, only the nadir and stereo images were taken so at least a DTM can be created.

I used level 4 HRSC data, which is 8-bit and is orthorectified using a derived HRSC DTM. The processing level which is available on the PSA is level 2 and level 3. Level 2 is unprojected 16-bit image data, level 3 is sinusoidal map projected 8-bit image data (and polar stereographic for the polar regions). The DTMs and level 4 data are not available on the PSA.

All the level 2 and level 4 data available from Aram Chaos were acquired. The files have a bzip2 compression (.bz2 extension) and had to be decompressed (for windows 'bzip2 for windows' was used). The level 2 data was used to create anaglyphs (see *4.4.2.4. Anaglyph creation*).

4.4.2.3. HRSC processing for ArcGIS

The specific processing described here is only possible at institutions/organizations where the VICAR routines from DLR are available, such as ESTEC.

1. The VICAR environment was started (see Appendix A.12). The DLR specific routines were loaded by typing 'dlr' in the unix/linux shell.
2. Level 4 infrared images (ir4) were downloaded and used as quick previews, to find out the data coverage. They were reprojected to Simple Cylindrical projection using the VICAR DLR program DLRMAPTRAN. The VICAR program VTIFF2 and the convert program from Imagemagick were used to create tiff (.tif) and jpeg2000 (.jpg) files, respectively (see Appendix A.13). A script was used to create world files for the jpg images (.jgw) (see Appendix A.14).
3. The images were opened and observed in ArcMap. The orbits with a good coverage were selected. Of these orbits the highest resolution nadir (nd4) were acquired. Also the nadir data from orbits where no ir4 was taken were acquired.
4. The images were reprojected and saved as jpg files. Some images resulted in oversized jpg files which could not be opened. For these images the reprojected data was split up in smaller files using DLRMAPTRAN (for the script see Appendix A.15). World files were created for each jpg image.
5. For the easy observation of the PSA HRSC data in ArcGIS a hrsc2arcgis perlscript was created (see Appendix A.16)

4.4.2.4. Anaglyph creation

1. A script was used to create for each level 2 nadir (nd2) and stereo 1 (s12) pair stereo images (Appendix A.17). This script converts the data to 8-bit after which it is processed to level 3. First the s12 data is processed to level 3 (s13). The nd2 data is then fitted to the s13 image during the level 3 processing. The script uses the following VICAR routines: HRFILL, DLRTO8, HRORTHO and VTIFF2. All except VTIFF2 are available in mini-vicar (http://pds-imaging.jpl.nasa.gov/data/mex/mex/hrsc/mexhrsc_0001/software/minivicar.zip) (Linux/Unix). Mini-vicar provides another program to convert to tiff or jpg.
2. The image pair jpg files were opened in PhotoShop. Both images were copied and paste as layers in a new RGB image. Using the Levels window (CTRL-L) the nd2 layer was set to only show green and blue. The s12 layer only showed red. In the Layers window 'normal' was changed to 'screen'.
3. A worldfile was extracted from the level 3 data so the anaglyph could be used within ArcMap.
4. In ArcMap the resulting image has to be rotated 90 degrees to see 3D using red/blue or red/green glasses. The 'Data Frame Tools' toolbar was activated. This makes it possible to rotate the Data Frame so the HRSC anaglyphs can be easily observed.

4.4.2.5. HRSCDTMs

1. Accompanying HRSC DTMs (dt4) were downloaded and decompressed. The hrscdtm2arcgis.pl script was started which extracts header and georeference information and assigns correct elevation values (for the script see Appendix A.18).

4.4.3. MOC processing

4.4.3.1. MOC within ArcGIS

1. MOC footprint shapefiles for ESRI ArcGIS were downloaded from ftp://ftpflag.wr.usgs.gov/dist/pigpen/mars/moc/footprints. They were created by Trent Hare from the USGS. I used the Januari 2006 release, which is a reissue of the October 2005 release, using updated SPICE kernels (camera pointing data).
2. I added the MOC_0_100m_SPICECORRECTED shapefile to ArcMap.
3. In the Display tab of the Layer Properties window I checked 'Support Hyperlinks using field:' selecting 'WEB_LINK' and 'URL'. In the Fields tab all fields but the WEB_LINK field were turned off.
4. The footprint can be clicked upon using the Identify button in the Tools toolbar. This opens a small window which shows the associated URL of the MOC image. By clicking on the URL a new browser window is opened.

4.4.3.2. MOC georeferencing

The attribute table of a selection of MOC footprints was saved to a text file. A perl script was created (see Appendix A.19) which downloads MOC images from www.msss.com and processes them to a map projection. Some MOC images are already processed and available online. Most MOC images however were available only as non map-projected images. Georeference and reprojection information was calculated using the latitude and longitudes of the image corners and the images widths and heights. The reprojection was performed by connecting to the ArcGIS geoprocessor within perl. Also the gdal_translate program from GDAL was used in the processing.

4.4.4. MOLA processing

1. MOLA Precision Experiment Data Records (PEDR) files were downloaded from the Planetary Data System (PDS) website (http://pds-geosciences.wustl.edu/geodata/mgs-m-mola-3-pedr-l1a-v1/mgsl_21xx/data/).
2. The PEDR2TAB program was downloaded and the pedr2tab.prm file was rewritten to contain the correct latitude and longitude extent.
3. The ~22 GB of data was subsequently handled by PEDR2TAB which created a textfile with latitude, longitude and elevation columns.
4. A perl script was written to convert the textfile to a CSV style (comma delimited) text file with X, Y, LON, LAT and Z columns (Appendix A.20). The X and Y are the coordinates of the MOLA points in the Simple Cylindrical projection used.
5. The text file was added to ArcMap via Tools > Add XY Data., and was exported to a point shapefile. The MOLA point data was used to find the best cross section profile locations and to provide an estimate of the accuracy of the cross sections.

4.4.5. OMEGA processing

4.4.5.1. The OMEGA spectrometer

The OMEGA (Observatoire pour la Minéralogie, l'Eau, les Glaces et l'Activité) imaging spectrometer on board the Mars Express is active since Januari 2004. With the OMEGA the identification of the mineralogical and molecular composition of the surface and

atmosphere of Mars is possible (Bibring et al., 2004, 2005). The orbit of Mars Express has a 86º inclination (almost a polar orbit) and an eccentricity of 0.6 (elliptical orbit). Because of this high elliptical orbit the OMEGA spatial resolution varies between 4 km/pixel and 300 m/pixel. The high resolution observations lie close to the periapsis (nearest point) of the Mars Express orbit. OMEGA works only during the daytime.
OMEGA is a hyperspectral scanner and acquires for each pixel 352 spectral channels (spectels) from the visible (0,36 μm) to the Thermal Infrared (TIR) (5,2 μm). This makes it possible to look at absorption features in the solar reflected spectrum and in the planetary thermal emission (4 μm and higher) (Bibring et al., 2005) (Figure 4.4). An increasing amount of spectels are not fully reliable, due to detector degradation by cosmic rays.
OMEGA consists of three parts, a VNIR (Visible and Near Infra Red) and two SWIR (Short Wavelength IR) spectrometers. VNIR observes from 0.36 to 1.07 μm, with a spectral sampling of 7 nm. SWIR uses two spectrometers to observe from 0.93 to 2.7 μm (spectral sampling 14 nm) and from 2.6 to 5.2 μm (spectral sampling 20 nm). To be able to create one continuous spectrum the three different observations overlap.
VNIR uses the pushbroom technique where pixels are acquired line per line, with a 8.8º field of view (FOV). It has 40 operation modes, for example a nominal (spatial × spectral) mode (128×96 with summation of 3×3 pixels), a high spectral resolution mode (64×144) and a high-speed mode (16×96) (Bibring et al., 2004). SWIR uses the whiskbroom technique where a scanning mirror moves crosstrack and can acquire 16 to 128 pixels (1.1º to 8.8º FOV), dependent on the elevation above Mars.

4.4.5.2. The OMEGA data

The OMEGA data available for Aram Chaos was downloaded from the Planetary Science Archive (http://www.rssd.esa.int/index.php? project=PSA) from ESA. It consists of a QUB file and a NAV file. For each orbit on average 4 to 7 QUB and NAV files are generated, which are named ORBNNNN_1, ORBNNNN_2, etcetera, with NNNN the orbit number. The QUB file is a so called data cube, a 3 dimensional array of spatial (x and y) and spectral (λ) data. The spectral data consists of 352 spectral channels, divided in three overlapping parts belonging to the three OMEGA spectrometers, an IR C (128 values), an IR L (128 values) and a VIS (96 values) part (also in this exact order in the QUB file). Each channel is 12-bit, which means it can have a brightness value between 0 and 4095.
The NAV file is also a data cube (geocube) and contains spatial (x and y) and geometry information. It contains for example for each data pixel the longitude, latitude, altitude from Mars' center and altitude above the MOLA elevation. Because the IR C, IR L and VIS parts are measured by three different spectrometers they also have their own positioning information. There is also an offset of a couple pixels between the VIS channel and the IR C channel. This implicates that when the latitude and longitude from the IR C part is used to create a projected hyperspectral image of all the 352 channels the VIS part doesn't have to belong to that pixel, it could be a couple of pixels offset.

4.4.5.3. Atmospheric correction

1. IDL routines (SOFT03) were provided by the OMEGA science team. The routines perform a radiometric calibration, which is the conversion of the digital

numbers (DNs) into radiance ($Wm^{-2}sr^{-1}$) and ground reflectance. This results in "idat" data of which the spectrum looks like the solar irradiance curve (Figure 4.5). The so called "jdat" data results after dividing the "idat" data by the solar irradiance curve. The result is now representative for the radiation at the top of the atmosphere.

2. An atmospheric correction IDL routine was provided by the OMEGA science team. The routine only corrects the IR channels and does not correct for dust in the atmosphere. It only corrects for a small part of the atmospheric column (from the base to the top of the 27 km high Olympus Mons volcanoe on Mars). The purpose of atmospheric correction is to re-scale the "jdat" radiance data to "kdat" reflectance by correcting for atmospheric influences and shifting all spectra to nearly the same albedo. The result is a dataset in which each pixel can be represented by a reflectance spectrum which can be directly compared to reflectance spectra of rocks and minerals acquired either in the field or in the laboratory (Van der Meer and De Jong, 2003).

4.4.5.4. OMEGA to IDL/ENVI

3. The write_envi.pro IDL routine was provided by the OMEGA science team to create ENVI files.
4. The omega_path file was edited to contain the correct location of the QUB and NAV files.
5. The readomega.pro IDL routine was edited to handle command line execution (e.g. readomega.pro,'ORBNNNN_#', to execute the atmospheric correction routine and to execute write_envi.pro to write all the data to ENVI format. This resulted in ORBNNNN_#_kdat files.

4.4.5.5. Splitting OMEGA

6. Only the IR-C part of the data (0.93 to 2.7 μm) was used, which has 128 bands. The first band and last two bands were deleted because they had poor quality. Therefore 125 bands remained. The perl script OMEGAsplit.pl (Appendix A.21) was written to automatically split the OMEGA data in its IR-C, IR-L and VIS parts. Executing the script creates omegasplit.pro which has to be executed in IDL/ENVI. It creates ORBNNNN_#_kdat-IR-C, ORBNNNN_#_kdat-IR-L and ORBNNNN_#_kdat-VIS files.

4.4.5.6. OMEGA Georeferencing

7. A perl script writeOMEGAproj.pl (Appendix A.22) was written and executed which generates for each OMEGA set in the directory an IDL routine to automatically project the data. The projection parameters were set to a Equirectangular projection using a 3396190.0 m sphere.
8. The following line was added to the map_proj.txt file in the IDL<version>\products\envi<version>\map_proj directory: *17, 3396190.0, 0.0, 0.0, 0.0, 0.0, Mars Aram Chaos Equirectangular Sphere*
9. The batch of projection routines were saved by writeOMEGAproj.pl into OMEGAproj.pro which was subsequently executed in IDL (ENVI needs to be started also), creating ORBNNNN_#_PROJ files.

a. It uses ORBNNNN_#_lonlat (C channel footprint) to create ORBNNNN_#_GLT containing a Geographic Lookup Table (GLT) which is a projected 'footprint' of the data. The routine uses an automated version of the ENVI function 'Build GLT' (Map > Georeference from Input Geometry > Build GLT).
b. It uses ORBNNNN_#_kdat and ORBNNNN_#_GLT to create the projected data. The routine uses an automated version of the ENVI function 'Georeference from GLT' (Map > Georeference from Input Geometry > Georeference from GLT).

10. In ENVI via Basic Tools > Mosaicking > Georeferenced all the projected OMEGA data could be merged into one mosaic.

4.4.5.7. OMEGA in ArcGIS

11. ENVI reader for ArcGIS (http://www.ittvis.com/download/download_splash.asp?wdiid=548) was installed which makes it possible to add ENVI data to ArcGIS. The ORBNNNN_#_PROJ files need to have an extension .DAT for ArcGIS to recognize the data.
12. The whole dataset can be loaded into ArcMap, which makes it possible to show an RGB color composite of 3 bands by right clicking the OMEGA data layer > Properties > Symbology. One single band can be loaded into ArcMap by double-clicking the OMEGA data in the Add Data dialog window and selecting the band.
13. Within ArcMap a 'History Equalize', 'Minimum-Maximum' or 'Standard Deviations' stretch needs to be implemented to be able to show the data (otherwise the data is completely black).

4.5. Mapping methodology

4.5.1. Prior to mapping

1. Prior to mapping the 'ArcMap tweaks to enhance your productivity' arcscript was installed. This enabled a variety of handy tools and shortcuts such as the possibility to open a shapefile in the Editor by right clicking the shapefile in the table of contents and selecting 'Start editing this layer'.
2. The 'Create and add shapefile' arcscript was installed so shapefiles could be easily creating within ArcMap.
3. The Overview window arcscript was installed which enabled a small overview window showing the image at the bottom of the table of contents. The window shows the current view screen as a box. This box can be relocated and/or resized.
4. The projection parameters were set to the projection the USGS MOLA data uses.

4.5.2. Mapping

1. Mapping was performed on a variety of line shapefiles. Distinct features were mapped on different shapefiles, e.g. ejecta blankets, fractures, craters and crater remnants, wind indicators, etcetera. Each shapefile had a Notes field in the Attribute Table where remarks and notes were added.

2. Interesting locations were saved using Bookmarks > Create. The Bookmarks2Shapefile arcscript was used to create a shapefile of the acquired bookmarks.
3. The Lon/Lat Readout in Projection ArcMap 8.x or 9.x arcscript was used to easily find the latitude and longitude of a specific location.
4. The boundaries of non disturbed and disturbed terrain and the channel boundaries were drawn. These are mostly escarpment boundaries. When mapping a boundary as an escarpment, the cliff itself belongs to the higher elevated unit. Therefore the boundary is drawn at the bottom of the escarpment. HRSC anaglyphs were used when available (see HRSC coverage). The data frame was rotated 90 degrees using the Data Frame Tools toolbar so that the HRSC anaglyphs could be used within ArcGIS.
5. The HRSC data and THEMIS/MOLA are not aligned very well. The alignment is best in the middle of the map, and the southern and northern parts have the highest offset. Therefore shapefiles specific for HRSC and for THEMIS were used for mapping.
6. Albedo differences occur in the Aram Chaos area. Albedo is possitively correlated with dust content of the surface. Only when albedo correlates well with differences in thermal inertia or with geomorphology it will be used to distinguish units.
7. Thermal inertia is high for rocky surfaces and low for dusty surfaces. Most bright regions in the Aram Chaos area are escarpments, which are suspected to be rocky. Most dark regions are flat, which are suspected to be dusty.
8. When there is no HRSC anaglyph available THEMIS and MOLA were used.
9. Interesting locations were saved as 'spatial bookmarks'. The VBA script Bookmarks2Shapefile was used to create a point shapefile containing the spatial bookmarks locations and their names in the Attribute Table.
10. THEMIS IR day 50% visible above colored MOLA data were used as a means to include 3D information at locations where no HRSC Anaglyphs were available.

4.5.3. Creating polygons

1. The boundary lines were combined in one shapefile which was subsequently converted to a polygon shapefile.
2. In ArcCatalog using ArcToolbox the line shapefile containing all the unit boundaries was converted to a polygon shapefile using 'Data Management Tools' > 'Features' > 'Feature To Polygon'. For Cluster Tolerance 500 m was used.
3. In ArcCatalog the polygon shapefile was given an appropriate name. By right clicking the layer and selecting Properties the Shapefile Properties window was opened. In the Fields tab 'Unit', 'Name', 'Definition' and 'Notes' were added in Field Name with Text as Data Type.
4. The polygon shapefile was opened in ArcMap. The Properties window was opened by right clicking the layer and selecting Properties. In the Symbology tab 'Catagories' was selected in 'Show:'. In 'Value Field' Unit was selected and the 'Add Values' button was clicked. In the Add Values window the numbers 1 to 10 were added. The colors of the different unit numbers were adjusted.

5. The Editor toolbar was started for the polygon layer by right clicking the layer and selecting 'Start editing this later'. In the Editor toolbar the Attributes button was pressed. The 'Edit Tool' was used to select a polygon. In the Attributes window for each polygon 'Unit' was give the appropriate number.

4.5.4. Creating cross sections

1. Simple profiles within ArcMap can be created using the 3D Analyst toolbar and the MOLA elevation data. Within the 3D Analyst toolbar the Interpolate Line button is clicked and a profile line is drawn in the view screen (one click creates a new line segment, double-click finishes the line). The Create Profile Graph button in the 3D Analyst toolbar draws the profile. The minimum and maximum elevation of the profile is needed for the cross section. All North to South cross sections follow MOLA tracks for highest data density.
2. The Profile Tool v1.1 arcscript will be used to create geological cross sections. The downloaded .zip file contains Profile_Tool_v1.1.mxd which was started. This ArcMap project file contains a ProfileTool toolbar. The tool needs a polygon shapefile and elevation raster data. The mapping shapefile and MOLA elevation layer were added to the project and the NewProfile button in the ProfileTool toolbar was clicked.
3. The cross sections are chosen using the MOLA point data such that less MOLA covered locations were avoided. By clicking the beginning and ending of the desired cross section line in the view screen the Profile Exporter window is opened. Division is chosen so that the profile is divided into ~500m parts (the resolution of the MOLA data). Vertical exaggeration is set to 10, 'draw graphic for profile line' is deselected, Map Base Units is set to meters and Build a profile box is selected.
4. In the Setup Profile Box window the maximum and minimum elevation is provided and Use profile length is selected. Vertical and horizontal tick spacing are set to 500 and 5000, respectively (it will create a square box because the vertical exaggeration is set to 10). The Continue button is clicked, closing the Setup Profile Box window and 'next step' is clicked in the Profile Exporter window.
5. The MOLA data, the mapping shapefile and the field indicating the geological units are set, the export folder is set to the desired folder and 'last step' is clicked.
6. In the export folder three shapefiles have been created.
    a. Profile_line contains the lateral profile line and can be added to the project.
    b. Profile_intersection_points contains the points on Profile_line where geological boundaries occur.
    c. Profile_profile is the cross section itself and when added to the project will be visualized using North-South = Z, East-West = cross section line.
7. The Profile_profile and Profile_line shapefiles were added to the project. In the Symbology tab of the Layer Properties window of the Profile_profile layer for Show 'Categories' was selected. For Value Field 'Geology' and 'Add All Values' was clicked.
8. The Fractures line shapefile was added to the project.

9. The Add Points At Crossings macro was added to the project and in the Visual Basic Editor the first lines of the code where changed into:
   Public Sub Example_AddPointsAtCrossings()
   Call AddPoints("Fractures", "Profile_line")
   End Sub
10. A new point shapefile was added to the table of contents and the editor was started using Properties > 'Start editing this layer' by right clicking the point layer in the table of contents. The macro was started and the intersections where added to the point layer.
11. New point shape files were added and points were created manually at the intersections of the line and the Light Toned Deposits and Small Scale Hills shapefiles.
12. By only showing the Profile_line and Profile_box shapefiles in the viewscreen and selecting File > Export Map the cross section was exported to a 300 dpi .pdf file. The profile line and the Fracture intersections were similarly exported to .pdf. Some cross sections were alligned long MOLA tracks, therefore the screen was rotated using the Data Frame Tools toolbar until the cross section was horizontal.
13. In Adobe Illustrator the .pdf files were opened and the intersections were fitted to the cross section. The cross section was further refined in Illustrator.

4.5.5. Crater counting

1. A multipoint shapefile is created in ArcCatalog by right-clicking > New > Shapefile and selecting MultiPoint as Feature Type. The shapefile is loaded into ArcMap and the Editor is started.
2. For each crater 3 points along the rim are created. By double-clicking each third point the 3 point feature is created.
3. The Circular Regression ArcToolbox is started with the shapefile as input and a text file as output.
4. The output text file can be opened in excel as a comma-delimited text file and contains the X, Y and radius of the two centers of the ellipse. Because only three points where used the radii are almost the same and either one is chosen or the mean of both is taken.
5. The resulting data can subsequently be further analysed using the XCage program.

4.5.6. Mapping using OMEGA data

1. OMEGA data covering the Aureum Chaos Deposits (ORB0456_1), the Iani Chaos Deposits (ORB0353_2) and the Aram Chaos Formation (ORB0401_3) were downloaded and processed (see *4.4.5. OMEGA processing*).
2. Because Mars is very dusty it was decided to divide the spectra by a mean dust spectrum. Regions with a bright albedo are high in dust. Therefore for each orbit a ROI of the brightest region was created (Figure 4.6) and a mean spectrum was saved to a library. The IDL function 'Divide_By_Spectrum' was created by Harald van der Werff which divides each pixel spectrum by a mean spectrum (Appendix A.23). To accomplish this the following steps were taken in IDL/ENVI per orbit:

a. In ENVI 'File > Export to IDL Variable' the image cube and the spectral library containing the mean dust spectrum were saved to IDL variables.
b. In IDL the Divide_By_Spectrum function was loaded and compiled.
c. In the IDL command line 'result = Divide_By_Spectrum(image,spectrum)' was executed which created the 'result' IDL variable.
d. In ENVI 'File > Import from IDL Variable' the RESULT was added to the 'Available Bands List' window.

3. The three dust and atmosphere corrected orbits were georeferenced and opened in ArcGIS. Per orbit a shapefile of the outcrops which cover the orbit was created, derived from the mapping (the shapes need to be inside the orbit extent).
4. In IDL/ENVI the shapefiles were converted to ROI (Figure 4.7) and mean spectra were calculated:
    a. The georeferenced orbits were opened one at a time.
    b. Via Vector > Open Vector File > Shapefile the appropriate shapefile was opened.
    c. In the 'Import Shapefile File Parameters' window the output result is set to memory and 'Mars Aram Chaos Equirectangular Sphere' is selected as the projection.
    d. In the 'Available Vectors List' window the vector is loaded into the image display window (most likely Display #1). This opens the 'Vector Parameters: Cursor Query' window. Here the vector is exported to a Region of Interest (ROI) via File > Export Active Layer to ROIs > Convert all vectors to one ROI.
    e. In the image display window Tools > Region of Interest > ROI Tool is selected which opens the ROI Tool window. Here the mean spectrum of the ROI can be derived by clicking 'Mean'.
5. Band ratios of distinct absorption features within the mean spectra were created in IDL/ENVI using Band Math ((b1+b3)/2*b2) (Figure 4.8). The resulting images show high values where the absorption features are strongest. Only if the high value areas correspond with the ROIs you can use the OMEGA data for mapping purposes.

4.6. Lineament Analysis

4.6.1. Lineaments in ArcGIS

1. Lineaments were drawn in ArcMap onto a polyline shapelayer.
2. In ArcCatalog using ArcToolbox the multipart lines were split into single lines using 'Data Management Tools' > 'Features' > 'Split line at Vertices'.
3. The 'Find Polyline Angle' arcscript needs to be altered before it can be used because the current script rounds the angles to whole numbers. In the Visual Basic Editor (Tools > Macros > Visual Basic Editor) the FindPolylineAngle module is selected.
    - *Dim getAngle As Integer, iAriAngle As Integer, iGeoAngle As Integer* is changed into *Dim getAngle As Double, iAriAngle As Double, iGeoAngle As Double*.

- The occurrences of *.Type = esriFieldTypeInteger* are changed into *.Type = esriFieldTypeDouble*

4. The 'Find Polyline Angle' arcscript is started. The Editor needs to be started before this script can be used and all lineaments have to be selected with the 'Edit Tool' button. The script adds an ARIANGLE and GEOANGLE field to the Attribute Table. The GEOANGLE field contains the correct angle. The edit needs to be saved via Editor > Save Edits. Sometimes the angles are not saved, check in the Attribute Table, and repeat the angle creation.
5. The 'Add Area and/or Length' arcscript is started. The Editor needs to be closed. It adds a Length field to the Attribute Table.
6. Using the 'Add Points At Crossings' arcscript the X and Y of the lineament center points were added to the Attribute Table.
7. Lineaments were selected via the 'Edit Tool' and in the Attribute Table the selection was exported to a text file.

4.6.2. Creating Rose Diagrams

1. To create Rose Diagrams the software program GEOrient 9.2 is used.
2. The software is started and the Rose Diagram button was selected.
3. The text file exported by ArcMap is selected which opens the 'File structure and data conventions' window. In the 'Plot as' tab the 'Primary data set' is set to Directions. In the 'Data Formats' tab 'Delimiter' is set to comma and 'First row contains column headings' is selected. The column containing the directions is set to the GEOANGLE column number.
4. In the 'Appended Data' tab 'Numeric value' was selected and set to Length. The column number is set to the Length column number.
5. In the 'Plot as' tab the Lines button is pressed. This opened a new window in which the 'Rose Type' is set to 'Length – Azimuth' and the GO button is pressed. This creates a length-weighted Rose Diagram.

4.6.3. Concentricity / Radiality

1. This method uses the lineament shapefile with the GEOANGLE, Length and X, Y of the midpoint fields from *4.7.1. Lineaments in ArcGIS*.
2. The Concentricity / Radiality (C/R) of a lineament is defined as the angle between the lineament and a line through the lineament mid point and a specific location (f.e. the center of the Aram Chaos crater) (Figure 4.9). When this angle is 90 the lineament is concentric to the location, when this angle is 0 the lineament is radial to the location.
3. A point shapefile is created and using the Editor the location of interest is added as a point. A copy of the fractures shapefile is added to ArcMap and in the Editor all the lineaments are selected. The Select By Location window is opened via Selection > Select By Location and all the lineaments outside a certain radius from the location in the point shapefile are removed from the selection. Via Edit > Cut all the selected lineaments are removed from the shapefile after which the edit is saved.
4. The C/R of lineaments is calculated within ArcMap using a VBA script (Appendix A.24). Within the Attribute Table of the lineament shapefile a new

column is created via Options > Add Field (the Editor needs to be closed). By right clicking on the new field header and selecting Calculate Values the Field Calculator window is opened. 'Advanced' is selected and the script is pasted in the 'Pre-Logic VBA Script Code' textbox. In the lower text box Concentricity is typed. The script has to be altered to contain the correct Xcenter and Ycenter values of the midpoint to which the C/R is relative.

5. The attribute table was exported to a .dbf file and opened in excel. In excel via Tools > Data Analysis > Histogram a histogram was created of the C/R. The Bin Range was set to a column with numbers ranging from 5 to 90, per 5 degrees. This created a new table showing 18 bins (0 to 5, 5 to 10, etcetera) with their respective lineament frequency.
6. A length-weighted C/R histogram was created by multiplying for each bin its frequency with the summed lineament length of the bin divided by the total lineament length.

4.6.4. Fracture Density

1. The fracture density can be calculated using Spatial Analyst via Spatial Analyst > Density. For 'Density Type' simple is chosen. The resulting density raster has units of length per square kilometer. Per pixel the length of all the lineaments within a certain radius is divided by the area of the circle. By default the search radius is 1/30 and the cell size is 1/250 of the layer extent.

4.7. Spatial Analysis

4.7.1. Deriving the thickness of the Intermediate and Upper Aram Chaos Formation

1. Using the MOLA processing method described in *4.4.4. MOLA processing* a text file was generated of all the MOLA points surrounding the Aram Chaos LTD between 0.7 and 5.0 °N and -22.8 and -18.6 °E. The text file was imported in ArcMap via Tools > Add XY Data. The Editor was started and all the MOLA points were selected.
2. The mapping polygon shapefile was added to ArcMap and the ACF polygons were selected (via Select > Select by Attributes).
3. Via Selection > Select By Location the MOLA points contained by the ACF polygons were removed from the selection (Figure 4.10). A buffer of 500 m was applied.
4. The selected MOLA points were exported to a shape file.
5. The data was interpolated using Natural Neighbors, with a pixel size of 450 m/pixel. NN has been used before to interpolate MOLA data (see http://pirlwww.lpl.arizona.edu/~abramovo/MOLA_interpolation/interpolation.html).
6. The polygons of the ACF were saved into a shapefile and the shapefile was subsequently converted to a raster via Spatial Analyst > Convert > Features to Raster.
7. An estimation of the thickness of the ACF was calculated in the Raster Calculator (Spatial Analyst > Raster Calculator) using the following calculation: merge([MOLA] - [InterpolationRaster] – [ACFRaster], [InterpolationRaster] /

[InterpolationRaster]). This creates a raster with only thickness information at the raster pixels covering the ACF, the other pixels have value 1 (caused by [InterpolationRaster] / [InterpolationRaster]). The extent of the raster is the same as InterpolationRaster.

4.7.2. Deriving the volume-loss of Aram Chaos

1. Through visual inspection of profiles a pre-collapse crater depth between -1500m and –2000 was chosen (Figure 5.2.18)
2. Using the Raster Calculator a new raster is created using [MOLA] < -1500.
3. The raster is converted to a polygon shapefile using Spatial Analyst > Conversion > Raster to Features.
4. The resulting shapefile is opened in the Editor and using the Cut Polygon Features Task one polygon is created which overlaps the Aram Chaos crater. The other polygons are deleted from the shapefile.
5. The resulting single polygon shapefile is converted to a raster via Spatial Analyst > Conversion > Features to Raster using a Cell Size of 500m.
6. Using Spatial Analyst > Reclassify the raster is given a value of 0.
7. In the Raster Calculator [MOLA] – [Result of (6)] results in a raster with only MOLA values within the Aram Chaos crater.
8. Via 3D Analyst > Surface Analysis > Area and Volume, using the result of (7) and the volume below -1500 m, an estimate of the volume-loss of Aram Chaos is derived.
9. Via 3D Analyst > Surface Analysis > Area and Volume, using the Aram Chaos LTD thickness raster and the volume above 0 m, an estimate of the volume of the Aram Chaos LTD is derived.

5. Results

5.1. Mapping

5.1.1. Background

Mapping (whether it is geological or geomorphological) is the classification of units. It is the best tool we have to derive a history of events which led to the current observable surface. Geological units are defined as deposited layers of material of the same age (Figure 5.1.1). They could vary in composition laterally. Geomorphology is defined as the surface expression. A depositional feature on the surface (e.g. a dune) is considered geology and geomorphology, an erosive feature (e.g. a channel) is only considered geomorphology (Figure 5.1.1). Mapping was performed using GIS software (ESRI ArcGIS) which makes it possible to integrate observations made using different datasets (images, elevation data, hyperspectral data). See *4.5. Mapping in ArcGIS* for an explanation how mapping was done.

The mapping resulted in a map. Allaby and Allaby (1999) define a geological map as "a map which shows the surface distribution of rock types, including their ages and relationships, and also structural features". A geomorphological map shows different landforms and their relationships. In reality a clear distinction between geology and geomorphology when mapping a planetary surface is difficult. Therefore the resulted map is considered to be a combined (structural) geological and geomorphological map.

5.1.2. Unit naming, classification and coloring

The unit names were either adopted from previous studies (e.g. Highland Terrain, Chaotic Terrain) or new names were devised. The unit naming convention used for the latter encompassed the use of 1) specific locations which encloses the unit (e.g. Aram Chaos Formation) or 2) specific features the unit exhibits (e.g. Small-scale Fractured and Chaotic Terrain). The latter immediately suggests the existence of other units (Fractured Highland Terrain and Chaotic Terrain). The units were mapped as 1) geological, 2) geomorphological and/or 3) structural geological units (Type column in Table 5.1).

The units were mainly distinguished using image data (mainly HRSC nadir and THEMIS VIS). A sense of 3D was created using HRSC anaglyphs (see f.e. Figure 5.2.28) or by combining color-coded MOLA elevation and THEMIS IR day (Figure 5.1.2). OMEGA hyperspectral data was only used in a late stage to verify the occurrence of the LTD (see *5.5.6. Integrating OMEGA data*). Albedo differences are mostly attributed to dust content and were not used to map units. Thermal Inertia can be used to distinguish between rocky (high TI) and dusty (low TI) surfaces. The walls of mesas are mostly rocky whereas the tops are dusty. Two units were mapped using TI, the deposits in the Chaotic Terrain (e.g. Aureum Chaos Deposits, Iani Chaos Deposits, Aram Chaos Formation) and the Ares Vallis Channel Deposits. They show relatively high values. TI can also be used to distinguish between relatively fresh (low TI and dust content) and older (high TI and dust content) surfaces. A possible volcanic deposit was mapped this way, showing a decrease in TI farther away from a possible volcanic construct (Figure 5.1.3).

The unit coloring was an attempt to make the units easily distinguishable. Lateral units have the same color but a different texture (f.e. the smooth, fractured and broken Lower Aram Chaos Formation).

5.1.3. Mapping results

The units described are a combination of (structural) geological and geomorphological units. The results of the mapping:

1. Figure 5.1.4 shows the resulted (structural) geological and geomorphological map of Aram Chaos and surrounding area.
2. Figure 5.1.5 shows the resulted (structural) geological and geomorphological map of Aram Chaos.
3. Figure 5.1.6 and 5.1.7 shows the resulted (structural) geological and geomorphological map of Aureum Chaos and The Iani Chaos, respectively.
4. Figure 5.1.8 shows the occurrence of the Small-scale Hills Terrain unit.
5. Figure 5.1.9 shows the mapped lineaments.
6. Figure 5.1.10 shows the unit type locations.
7. Figure 5.1.11 shows the occurrence of a possible volcanic deposit.
8. Figure 5.1.12 shows mapped highly degraded impact crater remnants.
9. Table 5.1 describes the units.
10. Table 5.2 describes the unit boundaries.
11. Table 5.3 describes the definitions which will be used in the following sections.

5.1.3.1. OMEGA mapping results

The Aureum Chaos Deposits (ACD), Iani Chaos Deposits (ICD) and the Aram Chaos Formation (ACF) were investigated using OMEGA data (orbits ORB0456_1, ORB0353_2 and ORB0401_3, respectively) (see *4.5.6. Mapping using OMEGA data*). The following results were obtained:

1. Figures 5.1.25 to 5.1.29 show the resulting mean spectra for the different outcrops. For each mean spectrum two absorption features (red and blue) and a larger spectral feature (the three green dots) were selected. See Table 5.4 for the wavelengths used for the band ratios.
2. Figures 5.1.30 to 5.1.34 show the band ratio maps belonging to two absorption features and a large spectral feature.

The absorption features are relatively small (3 to 7 times the spectral resolution of 14 nm). The absorption feature band ratio maps show much variation, as much as most bands themselves, and they do not show high values at the different deposit outcrops. Therefore these absorption feature band ratios cannot be used in mapping.

The large spectral features band ratios result in much noisier maps. Only the large spectral features band ratios of the smooth LACF and IACF result in corresponding high values over these deposits. The mean spectra of the smooth LACF and IACF are almost similar which explains why the bright region consists of smooth LACF and IACF. The other deposits do not show up in the resulting band ratio maps.

5.2. Geological observations and interpretations

This section describes the various geological observations gathered during mapping and the resulting interpretations and their significance. The section is divided in a regional and an Aram Chaos part. Figure 5.2.1 shows the observation locations. The numbers in the figure refer to the observation numbers.

5.2.1. Regional

5.2.1.1. Channeling

1. In the Flooded Highland Terrain (FHT) multiple stages of channel outflow can be observed (Figure 5.2.2). This suggests that multiple episodes of outflow from the Chaotic Terrain took place. The outflow terraces, which cross-cutting relationships show to be the oldest features, suggest that prior to the Ares Vallis incision sheet floods occurred.
2. In Northern Iani Chaos HT with a channel morphology has been cross cut by chaotization (Figure 5.2.3). This indicates at least at this locality channeling occurred prior to chaotization. It suggests the chaotization destroyed outflow channels.
3. The Aram Chaos channel links Aram Chaos with Ares Vallis (see the Regional and the Aram Chaos Geological Map, Figures 5.1.4 and 5.1.5). This suggests a sheet flood (see Observation 1) originating from Iani Chaos flowed over the rim into Aram Chaos after which the channel was incised. However, no clear flow patterns were observed. High-resolution MOC images of this location were not available. The sheet flow hypothesis is strengthened by the occurrence of the Aram Ares Channel Deposits (AACD) (see Observation 25) and the occurrence of material with a morphology similar to the AACD on the terraces of Ares Vallis, North of Aram Chaos (compare Figure 5.2.4 with Figure 5.1.10j).

5.2.1.2. Cratering

4. Within the Highland Terrain and Chaotic Terrain different types of craters occur (Figure 5.2.5), 1) unfractured craters within the unflooded HT, 2) unfractured craters within the flooded HT, 3) fractured craters within the HT (e.g. Aram Chaos) and 4) fractured crater remnants within the CT. Most unfractured craters within the flooded and unflooded HT (types 1 and 2) have a relatively flat and smooth crater floor surface, which suggest they were filled with material. The relatively smooth crater floors of the fractured craters and the crater remnants are interpreted to be the result of fracturing and collapsing of the crater floor material. If this smooth surface were a surface representation of a distinct deposit within the crater the following scenario is proposed for types 3 and 4 (Figure 5.2.6): 1) Crater formation, 2) deposition of material within the crater with a high water content, 3) deposition of a cap deposit within the crater, 4) Fracturing, collapse of the cap material and the (explosive) release of water.
5. The Chaotic Terrain are observed to contain fractured impact crater remnants (Figure 5.1.12). See also Cross Section III of Aureum Chaos (Figure 5.3.2). This suggests the Chaotic Terrain fractures are structurally controlled by impact craters. See Figure 5.2.7 for an example of an impact remnant within Aureum Chaos.
6. Figure 5.2.8 shows the depth vs. diameter of 45 craters in my research area (including Aram Chaos). The measured crater depth could be different then the actual crater depth due to deposition within the crater and/or erosion of the surrounding terrain. This most likely affected craters in the Flooded Highland Terrain. The diagram doesn't show a clear distinction between fractured and non-

fractured craters. This indicates the fracturing did not involve subsidence or the subsidence was relatively small (more likely a collapse type of subsidence, see Observation 4). Almost all measurements are considerably lower then the power-law relationships derived by Garvin et al., (1999, 2000). This also suggests crater fill and/or erosion of the surrounding surface occurred.

5.2.1.3. Fracturing

7. In Aureum and Aram Chaos pit crater chains occur along the fault trace (Figure 5.2.9). Only at two locations craters pits were observed. According Ferrill et al. (2004) pit crater chains form by dilational normal faulting and appear to be very young. They could even be actively forming. The rareness of crater pits in my area suggests most fractures are old features with currently practically no new fractures forming.
8. Along the Northern border of Iani Chaos fracture ridges occur in the HT (Figure 5.2.10). These fracture ridges are interpreted to be the result of compression prior to or during chaotization. These specific ridges have only been observed at this location and could 1) never have formed at other locations or 2) have been destroyed in the chaotization.
9. In Iani Chaos a HT region partly bounded by large-scale fractures has a smaller-scale fracture pattern on its surface (Figure 5.2.11). The smaller-scale fractures have a smaller width and subsequent smaller fracture valley depth (visible in MOLA data) compared to the large-scale fractures in the vicinity. The smaller-scale fractures grade into large-scale fractures, which indicates both patterns are connected, and a localization of fracturing occurred. This suggests multiple events of fracturing occurred.
10. Highland Terrain fractures are observed to continue into Chaotic Terrain (Figure 5.2.12 and 5.2.13a). The fractures within the CT are less easily distinguishable. The CT consist of km-scale hills, which are interpreted to be fault bounded. This high amount of fracturing within the CT is interpreted to be analogues to brecciation. Breccia is a rock so fractured it has lost coherence.
11. Two possible fracture offsets have been observed, one in Aureum Chaos and one in Iani Chaos (Figure 5.2.14). The rareness of offsets could be explained by 1) a single event of regional stress, or 2) multiple localized fracturing events with no regional stress.
12. A possible 20 by 30 km strike-slip duplex system has been observed in the HT, south of Aram Chaos, (Figure 5.2.15), connecting two HT fractures. It could be contractional with sinistral movement because it is located on a positive topographical feature (~200 m high). The fractures inside the duplex however are not observed to be thrusts (Figure 5.2.15c). Other observations which contradict the duplex-system hypothesis: 1) The two HT fractures are not observed to offset other fractures. 2) A smaller set of fractures located on a positive topographical feature occurs outside the duplex system (arrow in Figure 5.2.15b).

5.2.1.4. Highland Terrain

13. High-resolution HRSC nadir images show the Highland Terrain surface morphology to be varying (Figure 5.2.16a and b). Especially many crater floor

surfaces have a smoother surface then surrounding HT (for example see 4 in Figure 5.2.16b) which suggest they are the surface representation of a distinct deposit within the crater. However these smooth surfaces also occur within the surrounding HT (3 in Figure 5.2.16b). Within Aram Chaos also more rugged HT surface morphology occurs (7 in Figure 5.2.16c). Therefore the HT surface morphology variability is interpreted to be caused by relatively thin deposits of different age (e.g. volcanism, impact ejecta).

5.2.2. Aram Chaos

5.2.2.1. Large scale

14. Figure 5.2.17 shows the rings of the Aram Chaos multiring crater. The crater consists of three visible (using MOLA data) rings with a ~150 km (inner ring), ~280 km (middle ring) and ~500 km (outer ring) diameter. The rings of crater basins on a number of terrestrial planets are spaced at a constant factor of √2 (Spudis, 1994). This means that the diameter D_n of different rings is related to the basin rim diameter through: $D_n = (\sqrt{2})^N D$, with N an integer (1,2,3,4, etcetera). The rings of Aram Chaos approximately follow this '√2 rule' (280 / 2 = 140 which is ~150 km and 500 / 2 = 250 which is ~280 km). Within the inner ring the Aram Chaos Formation is formed (see Figure 5.1.5, the Geological Map of Aram Chaos). Between the inner ring and middle ring fractured HT and CT occurs. The outer ring consists of 1) Ares Vallis, which bends around Aram Chaos, 2) Hydaspis Chaos, 3) the channel branch linking Hydaspis Chaos to Ares Vallis, 4) the upper part of Iani Chaos and 5) a small fractured crater south of Aram Chaos. This suggests the locations of the channeling, fracturing and chaotization around Aram Chaos were structurally controlled by the Aram Chaos multiring crater (Schultz et al., 1982).
15. When assuming 1) the Highland Terrain within Aram Chaos subsided (see Observation 17) and 2) the pre-subsidence Aram Chaos HT was a relatively flat surface (see Observation 4) the amount of subsidence can be estimated. This estimation can subsequently be used to calculate an estimate of the volume of material which was withdrawn (see *4.7.2. Deriving the volume-loss of Aram Chaos*). A pre-subsidence Aram Chaos HT elevation between –1500 and –2000 m was estimated through image and MOLA elevation analysis (Figure 5.2.18). The volume of subsidence was subsequently 70274 km^3 (for –1500 m) and 40852 km^3 (for –2000 m). This estimation did not take into account the volume of the Aram Chaos Formation (6222 km^3) (see Observation 29). The total subsidence volume estimation is calculated by adding the ACF volume: 76496 km^3 (for –1500 m) and 47074 km^3 (for –2000 m).

5.2.2.2. Aram Chaos Highland Terrain

16. Tearing of Highland Terrain is observed at the Aram Chaos rim (Figure 5.2.13b). This is interpreted to be caused by subsidence of the Aram Chaos HT. The tearing has implications for the strength of the HT material.
17. Highland Terrain is observed to continue into Aram Chaos, where it has a lower elevation and has been fractured (Figure 5.2.13c). This suggests subsidence took

place of the HT material within Aram Chaos. Material must have been withdrawn underneath, resulting in subsidence. The HT is subsequently interpreted to be a thick (perhaps a km thick) deposit which was deposited on top of the Aram Chaos crater and the paleosurface it formed upon. This is also suggested by Observation 16. This leads to the following possible sequence of events (Figure 5.2.19): 1) Aram Chaos crater formation, 2) deposition of material within the crater with a high water content, 3) deposition of the HT material, 4) withdrawal and (explosive) release of the water rich material and 5) Fracturing and subsidence of the HT. This scenario is different then the proposed scenario for the other fractured craters and crater remnants (see Observation 4). Because Aram Chaos is the biggest of the fractured craters in my research area it is also most likely the oldest. This could explain the occurrence of overlying HT deposits.

18. The Aram Chaos HT collapse is varying, showing an undulating topography (Figure 5.2.13). This could be either due to 1) collapse and localized upward movements (popup), 2) collapse of the HT onto a subsurface topography or 3) a combination. In any case the resulting topography is best described as a draping of the fractured HT mesas (Figure 5.2.20b). Whether upward movements caused this, or subsidence or a mix remains unknown. One specific feature is a circular elevated area consisting of HT blocks (Figure 5.2.13d). This could perhaps be caused by 1) part of an Aram Chaos crater ring uplift, 2) volcanism underneath, 3) lateral differences in water content or 4) a popup structure formed by high water pressure underneath.
19. Radial fracture patterns can be observed within the Aram Chaos fracture pattern (Figure 5.2.21). This suggests the Aram Chaos pattern originated from specific areas of high stress within Aram Chaos.
20. Parts of the rim of Aram Chaos consists of small arcs (Figure 5.2.22). This suggests the Aram Chaos HT rim subsidence is influenced by more then one crater. After the Aram Chaos crater formed, smaller craters could have impacted.
21. On the edge of the Aram Chaos Chaotic Terrain a HT mesa occurs with a smaller scale fracture pattern on its surface (A in Figure 5.2.23). Next to it, within the CT a similar sized higher elevated region visible in MOLA occurs (B in Figure 5.2.23). Image data show it consists of small hills (Figure 5.2.23b). It is therefore interpreted to be a chaotisized HT mesa. This suggests the following sequence of events occurred: 1) large scale fracturing resulted in HT mesas, 2) within the current CT region the mesas subsequently underwent fracturing of a smaller scale (see also Observation 9) and 3) erosion related to the fracturing produced the current relief of small hills. Some of the fractured mesas were not chaotisized (f.e. A in Figure 5.2.23).
22. A half crater occurs at the boundary between the fractured HT and the LACF (Figure 5.2.24). This boundary can be observed in MOLA data as the inner ring of the multiring Aram Chaos crater (see Observation 14). The boundary is, at least at this location, interpreted to consist of a normal fault (See cross section in Figure 5.2.24). Broken LACF is observed at the down faulted part of the normal fault. This suggests the following scenario: 1) the HT within the inner ring of the crater has been subsided, 2) the LACF was deposited within the inner ring and 3) ongoing subsidence resulted in the LACF fracturing.

5.2.2.3. The Eastern part of Aram Chaos

23. In the Eastern part of Aram Chaos no concentric crater ring fractures were observed (Figure 5.2.25a). In the North the inner and middle crater ring (see Observation 14) fractures converge and die out. In the South the outer crater ring fracture dies out at the mouth of the channel connecting Aram Chaos and Ares Vallis (the Aram Chaos channel), where a delta-shaped feature (see Observation 25) is located. It is therefore interpreted that no concentric crater ring fractures developed in the Eastern part of Aram Chaos. Overlying deposits, such as the Aram Ares Channel Deposits could not have obscured such a large topographical feature. This suggests no collapse and subsidence has occurred in the Eastern part of Aram Chaos. However, the Eastern part of Aram Chaos could perhaps have bended inward without fracturing.
24. Chaotization occurred at the Eastern part of Aram Chaos (Figure 5.2.25b), with the fractures penetrating ~500 m deep. The ~500 m deep fracturing is inferred from the relatively smooth base on top of which the mesas occur (Profile A in Figure 5.2.25b). The outer parts (relative to the crater center) are best described as Small-scale Fractured and Chaotic Terrain, but the inner parts are best described as Intermediate Chaotic Terrain, suggesting a decrease in fracture penetration depth crater outward.
25. The Aram Ares Channel Deposits have been cut by the Aram Chaos channel (Figure 5.2.25c, see also Cross Section I, Figure 5.3.1). This implies the AACD material was deposited prior to the formation of the main channel. The AACD is observed to cap elongated streamlined HT mesas (Figure 5.2.25c). It forms multiple terraces and a delta-shaped feature at the mouth of the Aram Chaos channel (Figure 5.2.25c). Approximately 100 m AACD layering has been observed in the Aram Chaos channel wall (Figure 5.2.25d). The delta-shaped feature is interpreted to be both erosional (the streamlined HT mesas, the Aram Chaos channel) and depositional (the ACCD). The occurrence of the AACD suggest first deposition occurred crater inward, by incision of the Aram Chaos channel. Subsequently flow occurred crater outward, through the Aram Chaos channel into Ares Vallis, suggested by the streamlined HT mesas and the cross cutting of the AACD by the Aram Chaos channel. The channel could have incised due to the subsidence of the Aram Chaos crater. This leads to the following possible sequence of events (Figure 5.2.26): 1) overflow of Aram Chaos, forming the Aram Chaos channel (see also Observation 3), 2) and 3) deposition of the AACD and continued incision of the Aram Chaos channel (also cutting through AACD) due to Aram Chaos subsidence, and 4) incision of the Aram Chaos channel by crater outward flow forming the streamlined HT mesas and eroding AACD.

5.2.2.4. The Aram Chaos Formation

26. A ~350 m high mesa of fractured Lower Aram Chaos Formation (LACF) is situated on top of a HT window within the LACF (Figure 5.2.27). This observation is used to infer a thickness for the LACF between ~250-500 m (see Cross Sections I and II) (Figure 5.3.1). The window is mapped HT because it is

different in morphology then the surrounding LACF material. However, it contains fractures of the same scale as the LACF fractures. It is still mapped as HT because of its size and HT mesa geometry (it is bounded by valleys, most likely fracture valleys), which corresponds with other fractured HT mesas in Aram Chaos.

27. The smooth LACF is observed to be a draping (Figure 5.2.28, see also Cross Section I, Figure 5.3.1). It is interpreted to drape over underlying fractured Highland Terrain. The Highland Terrain fractured and subsided prior to or during the deposition of the LACF.
28. A window of Highland Terrain located in the LACF has a rim of fractured LACF on its south side (Figure 5.2.29). The HT window is interpreted to be a fracture bounded mesa which has been rotated due to collapse.
29. Using MOLA elevation data it is possible to derive an estimate of the thickness of the Aram Chaos Formation (see *4.7.1. Deriving the thickness of the Intermediate and Upper Aram Chaos Formation*). A Nearest Neighbor interpolation of all MOLA points except those that covered the Intermediate and Upper Aram Chaos Formation, was subtracted from the MOLA data to derive an estimate of the combined IACF and UACF thickness (Figure 5.2.30). The combined volume was calculated using ArcGIS to be 1260 km^3. The volume of the Lower Aram Chaos Formation (4962 km^3) was estimated by multiplying the area of the complete ACF (19848 km^2) by a mean thickness of 250 m (a rough estimate). The total volume of the Aram Chaos Formation is subsequently 6222 km^3.
30. Some LACF fractures have raised rims and some show small thrusts at the base of the rim (Figure 5.2.31). This can either be explained by 1) lateral compression due to subsidence and collapse of HT blocks underneath, 2) localized upward movement of water. The fractures form linear patterns of the same scale as the HT fractures (see the Aram Chaos Geological Map, Figure 5.1.5). This suggests HT blocks influenced the LACF fracture pattern. Upward movement of water using HT fractures as pathways could perhaps explain the raised rims. The broken LACF could be the locations where water was released to the surface, because the LACF is thinnest there (Table 5.2, Boundary 2).

5.3. Cross sections

Cross sections are used to visualize the stratigraphical relations of mapped units and their derived thicknesses. See *4.5.4. Creating cross sections* how they were derived. Four cross sections have been made, two through Aram Chaos, one through Aureum Chaos and one through Iani Chaos. The cross sections were created using unit descriptions and unit boundary descriptions (Tables 5.A and 5.B) and relevant geological observations and subsequent interpretations. The cross section profile lines were chosen to go through the different mapped deposits within the Chaotic Terrain (e.g. Aram Chaos Formation, Aureum Chaos Deposits, Iani Chaos Deposits). The cross sections are 10 times exaggerated in elevsation.

The creation of the cross sections encompassed the following issues:

1. A realistic fault interpretation was attempted. The largest shoulder of a fracture valley was used to define the dip direction. The faults are visualized as black lines. Not observed, but interpreted faults were visualized using a dashed pattern.

The fault scarps have likely been affected by erosion and cannot be simply used as fault orientation indicators. The faults are interpreted to be normal faults and are therefore more then 60° relative to the surface. Because the cross sections are 10 times exaggerated this results in approximately 85° vertical fault orientations in the cross sections.

2. The ICT and CTF are considered HT material which have undergone chaotization, making them geomorphologically and structurally distinct (Boundary 1 in Table 5.2). The boundary between HT, ICT and CTF is visualized using a wave pattern. It was decided not to use a fault boundary because this would imply a distinct boundary whereas the boundary is more transitional (the amount of chaotization).
3. The lower boundary of the cross sections is arbitrarily chosen and does not visualize a geological boundary. The buried crater floor of Aram Chaos is not shown in Cross Sections I & II.
4. The Cross Sections are constructed from geological observations, by using the principle of superposition and by assuming layers are continuous.

5.3.1. Aram Chaos (Cross Sections I & II)

A West to East (Cross Section I) and a North to South (Cross Section II) cross section were created through Aram Chaos (Figure 5.3.1). The following assumptions and observations were used to create Cross Sections I & II:

1. The AACD is observed to cap elongated streamlined HT mesas (Boundary 5 in Table 5.2). See also Observation 25.
2. The fractured LACF thickness was inferred from a ~350m LACF mesa (Observation 26).
3. The occurrence of HT fractured mesas underneath the LACF was inferred from HT windows in the LACF (Observations 26 and 28).
4. The smooth LACF is interpreted to be draped over the HT and/or CT (Boundary 4 in Table 5.2 and Observation 27)
5. The boundary between the fractured LACF and HT is interpreted to be a thinning of the LACF towards the HT, and the occurrence of broken LACF (Boundary 2 in Table 5.2).
6. The smooth LACF and the fractured LACF are mapped as lateral units, although their exact relation is unclear (Boundary 3 in Table 5.2).

5.3.2. Aureum Chaos (Cross Section III)

A South to North (Cross Section III) cross section was created through Aureum Chaos (Figure 5.3.2). The following assumptions and observations were used to create Cross Section III:

1. Two impact remnants in Aureum Chaos are covered (see Observation 5).
2. The ACD are thick deposits on top of the CT in Aureum Chaos, forming distinct hills with escarpments (Boundary 9 in Table 5.2).

5.3.3. Iani Chaos (Cross Section IV)

A South to North (Cross Section IV) cross section was created through Iani Chaos (Figure 5.3.3). The following assumptions and observations were used to create Cross Section IV:

1. The boundaries of the ICD (Boundary 10 in Table 5.2)

5.4. Stratigraphy

Stratigraphy deals with the correlation of stratified rocks from different localities (Allaby and Allaby, 1999). A stratigraphical column shows the layering of rocks at a certain location. Layer thicknesses, composition and possible erosion surfaces are depicted. Fracturing has been depicted by black lines or dotted lines for possible fracturing. The thickness of the layers is a mean thickness. Sets of stratigraphical columns have been created along Cross Sections I to IV:

1. Stratigraphical columns along the W-E and N-S Aram Chaos cross sections (Figure 5.4.1). Location 7 is divided in two possible stratigraphical columns. This refers to the unresolved issue of Boundary 3 of Table 5.2.
2. Stratigraphical columns along the Aureum and Iani Chaos cross sections (Figure 5.4.2).

5.5. Lineament Analysis

Lineament Analysis was performed on the digitized fracture patterns. The width of the fractures was not taken into account. Rose Diagrams (RD) were created to determine the possible presence of preferred orientations. Concentricity was used to determine the structural control by crater structures on the fracture pattern. The Concentricity of a lineament is defined as the angle between the lineament and a line through the lineament mid point and a specific location (f.e. the center of the Aram Chaos crater) (Figure 4.I). When this angle is 90 the lineament is concentric to the location, when this angle is 0 the lineament is radial to the location (for the method see *4.6.3. Concentricity / Radiality*).

5.5.1. The Aram Chaos fracture pattern

The Aram Chaos fracture pattern has been investigated using RDs and the Concentricity method. Major questions are:

1. Is the fracture pattern influenced (structurally controlled) by the crater.
2. Is the fracture pattern controlled by the largest chaotisized area in Aram Chaos.

The following results have been obtained:

1. Figures 5.5.1 and 5.5.2 show length-weighted RDs and Concentricity of different locations in Aram Chaos. The blue lineaments (within Circle 2) in Figure 5.5.1 mostly consist of fractures in the Aram Chaos Formation. The RD shows two faint Preferred Orientations (PO) (NNWSSE and NE-SW). Their Concentricity (relative to the center of the Aram Chaos crater) in Figure 5.5.2 show an almost even distribution. Therefore the inner ring fractures do not seem to be strongly structurally controlled by the crater. The red lineaments occur between the 1st and 2nd ring and mostly consist of Highland and Chaotic Terrain fractures. The RD does not show PO's. The Concentricity shows a relatively high distribution of concentric fractures. This is interpreted to be caused by structural control of the crater. The 4 RD of the N, S, W and E corners of Aram Chaos do show distinct PO's. The N and W corners have their major PO concentric to the crater. The S

corner has a distinct set of PO's. The Concentricty relative to this location (Circle 3) shows a relatively high amount of radial fractures. The S corner of Aram Chaos is the most chaotisized part of Aram Chaos and is interpreted to be a focussed zone of subsidence. The E fractures, compared to the N, S and W fractures are relatively small. The E part of Aram Chaos does not contain a major concentric rim fault (see Observation 23, Figure 5.2.25a).

2. Figure 5.5.3 shows length-weighted RDs and Concentricity of two craters (Craters 1 and 2, 72 km and 48 km in diameter respectively) near Aram Chaos (see Figure 5.5.4). Crater 1 shows three distinct PO's, Crater 2 shows 2 distinct PO's and some smaller ones. Only the ~N-S PO's correspond. Both Concentricity's only show high values near 90 degrees, making both crater fracture patterns highly concentric.

5.5.2. The regional fracture pattern

The regional fracture pattern has been investigated using Rose Diagrams (RD), the Concentricity method and by creating a fracture density map (Figure 5.5.5). The fracture density is used to define structural domains. Major questions are:

1. What are the preferred orientations of the different high fracture density areas? Is there a trend?
2. What are the preferred orientations of the low fracture density surroundings?
3. Are the fracture patterns in the chaotic terrain influenced by crater impacts?

The following results have been obtained:

1. Figure 5.5.6a shows lineament domains of chaotic terrain derived from the lineament density map and their length-weighted Rose Diagrams. It also shows RD's for Small-scale Fractured and Chaotic Terrain (SFCT) (blue), Craters 1 and 2 (purple) and Aram Chaos (orange).
2. Figure 5.5.6b shows all the lineaments in the Highland Terrain between the four Chaotic Terrain in my research area (Aram, Iani, Aureum and Hydaspis Chaos) and the low-fracture density Chaotic Terrain and the resulting RD. The lineaments show a weak PO ~NNW-SSE and a second ~E-W.
3. Figure 5.5.7 shows length-weighted Concentricity of the centers of Hydaspis, Aureum and Iani (East and West) Chaos.

The weak ~NNW-SSE and ~E-W PO's of the lineaments in the Highland Terrain between the four Chaotic Terrain could suggest regional stress was active. The different high density Chaotic Terrain RD's however do not show a clear trend. The PO's seem to be influenced mostly by the shape of the chosen structural domain itself (the orientation of the elongation defines the PO). It is therefore concluded that the Chaotic Terrain fracture pattern was not influenced significantly by regional stress.

The two central SFCT RD's show PO's parallel to the outflow (see Figure 5.5.5b) The left RD is derived from fractures confined to the 130 km in diameter Galilaei crater. The PO is approximately parallel to the small channel connecting the crater to the outflow channel (see the Regional Map Figure 5.1.4). Therefore the PO's are interpreted to be mostly influenced by the direction of the outflow. The right SFCT RD has a PO of NEE-SWW. The area of which the RD was derived is very broken and the orientations of the numerous small mesas where not mapped. A more thorough lineament mapping is needed to define PO's for this area.

Figure 5.5.7 shows four circular areas within the Chaotic Terrain of which the Concentricity was calculated. The radius of each area was chosen arbitrarily by observation. Only area D shows a distinct difference in radial and concentric fracture distribution (high amount of radial fractures). The center points where also chosen arbitrarily, after visual inspection of concentric and radial patterns.

5.5.3. Other lineament patterns.

1. Figure 5.5.8 shows the mapped wind directions and a Rose Diagram. Wind directions were obtained by mapping the directions of wind streaks outside craters. These originate because crater impacts cause relatively easily erodable material to resurface in the crater walls. These materials are subsequently transported by wind (Figure 5.5.9).
2. Figure 5.5.10 shows the mapped wrinkle ridges and a Rose Diagram of all the wrinkle ridges. Some wrinkle ridges inside the Flooded Highland Terrain could be eroded crater ejecta blankets. Almost no wrinkle ridges have been observed within the HT mesas of the Chaotic Terrain (only one has been observed, in Aram Chaos). This is most likely due to the degradation of the HT mesas.

6. Discussion

6.1. Introduction

In this section the results will be discussed and compared with work previously published. Figure 6.1 shows a Space-Time diagram of the discussed sequence of event concerning Aram Chaos. Two major assumptions are used in the discussion:

1. Water carved the outflow channels. A variety of outflow carving hypotheses have been stated (see *2. Mars Background*) but catastrophic release of water is found to be the most convincing. A terrestrial analogue is the Channeled Scablands, formed by the catastrophic release of water when an ice dam broke at the end of the last ice age (Baker, 2001; Masson et al., 2001).
2. Craters were formed by impact events.

6.2. Geological evolution

6.2.1. Regional evolution

In this section the regional evolution of my research area is discussed. The region is mainly composed of the thick (km scale) Highland Terrain material, of Noachian age. The Highland Terrain has been degraded into Chaotic Terrain. Chaotic Terrain are densely fractured regions which are the source regions of outflow channels. These outflow channels incised into the Highland Terrain. The evolutions of the Aram, Iani and Aureum Chaos Chaotic Terrain and deposits therein are discussed in detail in sections 6.2.2 and 6.2.3.

6.2.1.1. Highland Terrain composition and structure

Previous mapping by Tanaka et al. (2005) interpreted the Highland Terrain (mostly their Libya Montes unit) to consist of *"a mixture of impact breccia and melt, volcanic rocks, and clastic sedimentary rocks of aeolian, alluvial, mass-wasting, and other undetermined origins"*. They performed crater counting and estimated the HT to be of Noachian age. My findings agree with this interpretation:

1. The many impact craters covering the HT suggest the HT terrain consists of impact related materials (ejecta, breccia and melt)
2. 100-200m layering can be observed in the Ares Vallis escarpment (Figure 5.1.13),
3. HRSC data show that the current HT surface varies in ruggedness (Observation 13)
4. A possible volcanic deposit occurs south of Aram Chaos (Figure 5.1.11).

Rodríguez et al. (2005a) investigated an area in the Xanthe and Margaritifer Terrae region, including the western part of my research area. They observed crater remnants in different gradations of degradation at the boundary escarpments between the HT and lower elevated outflow channels and CT. I agree with their interpretations:

1. The Highland Terrain is at least 1-2 km thick (see Boundary 1, Table 5.2).
2. Circular features visible in the Ares Vallis escarpment were observed interpreted to be exposed impact crater remnants (Figure 5.1.13).
3. Aureum Chaos is observed to consist of multiple impact crater remnants (Observation 5).

Most of the volcanism and tectonics related to the Tharsis Bulge occurred during the Noachian (see *Mars Background*). This could have caused volcanism (intrusive and extrusive) in the HT (Tanaka et al., 2005). Extensional and compressional Tharsis related fault systems are expected to have formed. No clear extensional faults have been observed on the HT surface in my study area, but could have been buried (see *Regional stress*). Compressional Tharsis related faults however are observed: wrinkle ridges occur on the surface of the HT in my area and their mean orientation is concentric to Tharsis (Figure 6.2). They are believed to be the surface representation of compressional faults (Nimmo and Tanaka, 2005). The thrust faults underneath the wrinkle ridges could have formed early in the HT formation, with older wrinkle ridges now being buried.

Most workers agree the Noachian was a time of 1) intense cratering and 2) increased erosion and deposition suggesting a warmer climate with occasionally at least, flowing surface water (see *Mars Background*). In such an environment, newly formed craters probably contained lakes, or were filled with water rich material (Rodríguez et al., 2005a). Subsequent volcanic, sedimentary and/or impact related deposition buried these water rich bodies. The Chaotic Terrain morphology of subsided and collapsed HT blocks suggests the water was unstable and was released to the surface subsequently carving the outflow channels.

Understanding the formation of Chaotic Terrain can help to unravel the Highland Terrain composition and structure. In my *Mars Background* section multiple Chaotic Terrain formation hypotheses are described (Table 2.3). Sharp (1973) was the first to describe the CT and Carr (1979) first described a model. He hypothesized that underneath the CT high-pressure confined aquifers occurred below a permafrost layer. In the aquifers the pore pressure reached the lithostatic pressure, causing surface release of water. The most recent model of CT formation, using MOC, THEMIS and MOLA observations, is by Rodríguez et al. (2005a). They hypothesized that within the HT 'cavernous systems' occur, which are assumed to be the result of combined fracture systems of many buried impact craters. The networks occur because radial and concentric crater fractures can extend up to 1 crater diameter (D) from the crater rim. Therefore laterally and stratigraphically nearby craters connect and form fracture networks. Water was deposited within the crater basins during HT formation. After the wet period in the Noachian the cryosphere (permanently frozen layer) thickened which confined the buried craters and their water ice deposits. Subsequent episodes of heating by endogenetic processes melted the water, caused hydrothermal circulation and started fluid flow through the fracture networks. Erosion by fluid flow excavated caverns in the high fracture density regions which subsequently filled with water. When the hydrostatic pressure exceeded the lithostatic pressure the caverns became unstable and water was released to the surface. This led to the collapse of the caverns and the formation of the Chaotic Terrain. This model is found to be the most detailed and thorough model yet of the CT formation and agrees with the findings of this study:

1. The occurrence of CT within the Aram Chaos crater.
2. The occurrence of fractured craters within the HT (Observation 4).

Figure 6.3 shows a schematized representation of the HT composition and structure. To summarize, the HT stratigraphy in the studied region is formed by a complex interplay between the processes of volcanism, cratering, erosion, deposition and fracturing. The HT stratigraphy most likely consists of many buried impact craters, which may have

undergone various degrees of erosion prior to burial. Each impact event deposited ejecta, formed impact breccias and produced impact melt. Impact related fracture systems dominate the HT structure. Fracture systems of large impacts will likely have the largest influence. During the Noachian the atmosphere may have been denser, and the climate warmer, resulting in water runoff systems (see *Mars Background*). Therefore it is likely river channels and crater lakes or water rich crater fill are buried within the HT. The formation of the Tharsis Bulge probably produced volcanics and tectonic structures. Therefore magmatic intrusions and layers of lava flows and ash deposits will probably occur within the HT stratigraphy. Also (subsurface) Tharsis related faults are expected. Subsurface structures (impact or tectonic related) could have been reactivated during the formation of the HT.

6.2.1.2. Lineament Analysis

I performed Lineament Analysis of the mapped fractures to determine if they were influenced by regional stress (using Rose Diagrams) and to quantify the influence of cratering on the fracture pattern (using Concentricity). Lineament Analysis has been applied to cratering studies before: Baker (1994) performed Lineament Analysis of lineaments from remote sensing data of the Sudbury crater, Canada. He observed two rings and therefore interpreted Sudbury crater to be a multi-ring crater.

6.2.1.2.1. Regional stress

The main question to be answered with the use of Rose Diagrams (RD's) is if the HT and CT fracture pattern was influenced by regional stress. No Preferred Orientations (PO's) were observed in the bulk of the lineaments and within the CT. The lack of offsets (Observation 11) also suggests regional deformation did not occur when the fractures formed.

Other observations however do suggest the past presence of regional stress:

1. The weak ~NNW-SSE and ~E-W PO's of the lineaments in the HT between the four CT (see *5.5.2. The regional fracture pattern*).
2. According to Öhman et al. (2005) regional deformation controls crater shapes. Two pre-existing perpendicular fracture systems can lead to a hexagonal crater. Aram Chaos is observed to be hexagonal in shape (Figure 5.1.5). This suggests regional deformation of the HT occurred prior to the Aram Chaos impact.
3. The mean orientation of the wrinkle ridges in my research area is concentric to Tharsis (Figure 6.2) and therefore suggests a Tharsis related origin.
4. The possible strike-slip duplex system (Observation 12).

Rodríguez et al. (2005a) interpreted the linear shape of the chasmata in their research area (directly west of my research area) to be the result of structural control by fault systems radial to Tharsis. According to Rodríguez et al. (2005b) the fracture systems within eastern Aureum Chaos are remnants of extensional fracture systems. This suggests Tharsis related extensional fault systems also occur in my research area, although it is farther away from Tharsis. These systems could be subsurface faults, currently covered by later deposits, with no current surface representation.

6.2.1.2.2. Cratering

I devised the Concentricity method to quantify the influence of preexisting crater geometry on the lineament pattern. Radial and concentric faults are observed in impact craters (Rodríguez et al., 2005a). On Earth f.e., the Vredefort crater exhibits radial and concentric impact melt dikes (Grieve and Therriault, 2000). Other processes however can also produce concentric or radial patterns and therefore Concentricity is in general a method to quantify the occurrence of centralizations in the lineament pattern. An example is the relatively high amount of fractures radial to (compared to concentric to) the most chaotisized area within Aram Chaos (Figure 5.5.2c and Circle 3 in Figure 5.5.1). Two fractured craters in my study area showed a high amount of concentric fractures (Figure 5.5.3 and 5.5.4). The HT fractures of Aram Chaos also have a relatively high amount of concentric fractures compared to radial fractures and are likely controlled by the crater structure. I also investigated Hydaspis, Aureum and Iani Chaos using Concentricity (Figure 5.5.7). Only one center, in Iani Chaos (D in Figure 5.5.7) had a relatively high amount of radial fractures compared to concentric fractures. It is concluded that the Concentricity method is a first approach to quantify lineament localizations. It has to be expanded by building an algorithm which automatically finds concentric and/or radial centers within the lineament data.

6.2.1.3. Volcanism

The scale of the ~3 km in diameter and 200 m high possible volcanic construct (see Figure 5.1.11) in my study region is comparable to the scale of possible volcanic structures identified by other workers:

1. 'Quasi-circular structures', ~1 km in diameter, in the eastern part of Hydaspis Chaos (around 2.6719°N, 334.5755°E), observed by Rodríguez et al. (2005b) which they interpret as resembling ring dikes.
2. Cone-shaped hills in Aram Chaos identified by Lanz and Jaumann (2001). They are up to 2 km in diameter and several hundreds of meters high. The hills are interpreted to be possible magmatic intrusions.

This would imply volcanism did occur in my region but of a small scale compared to the Tharsis volcanoes. However, volcanism of a larger scale could have occurred, now being buried within the HT. The age of the possible volcanic construct is unknown, but crater counting of the possible volcanic outflow could be performed.

6.2.1.4. Outflow episodes

According to a mapping study by Nelson and Greeley (1999), using Viking data, multiple episodes of Ares Vallis channel formation occurred. The occurrence of cross-cutting Ares Vallis channels (Observation 1) is consistent with this interpretation. The Flooded Highland Terrain is interpreted to be formed by an early sheet wash from Iani Chaos or upstream, prior to incision. The Aram Ares Channel Deposits and similar looking deposits on an Ares Vallis terrace (Observation 3) could have been deposited in this period. Subsequent flooding and incision likely eroded other occurrences of this deposit.
According to Nelson and Greeley (1999) the first episode in the XMT region flooding history was a sheet wash from Vallis Marineris, also covering my study region (their Early Hesperian Hpls unit, consisting of reworked plateau material). Therefore, what is now mapped as non-flooded Highland Terrain in my area, could have been flooded because it is in the direct path of the Vallis Marineris outflow system (Figure 3.1).

However, no flow related morphology in the non-flooded HT was observed. Still, almost all measured crater depths in my area are considerably lower then power-law crater diameter-depth relationships derived by Garvin et al., (1999, 2000) (Observation 6). This suggests crater fill and/or erosion of the surrounding HT surface occurred, potentially related to such flooding events.

6.2.2. Evolution of Aram Chaos

This section will discuss the evolution of Aram Chaos by comparing the observations to the literature, mainly Glotch and Christensen (2005). They proposed the following sequence of events:

1. Formation of the Aram Chaos crater, in the Noachian.
2. Crater fill of water rich material.
3. Formation of aquifers according to the Carr (1979) model (see *6.2.1.1. Highland Terrain composition and structure*).
4. A first release of water formed their Fractured Plains unit (the HT within the ~280 km in diameter Aram Chaos middle ring).
5. A second release formed their High TI Chaos (part of the LACF in this study), reworking the Fractured Plains.
6. A third and subsequent releases formed their Knobby Terrain (the Chaotic Terrain and parts of the broken LACF in this study) and could have resulted in the deposition of the layered material in a sublacustrine environment.
7. A doming event of the Aram Chaos crater occurred, tilting the layered deposits.
8. Erosion of the layered deposits

The scenario proposed by Glotch and Christensen (2005) partly agrees with the mapping of this study and will be further discussed in the following subsections. Figure 6.1 shows a diagram of the evolution of Aram Chaos and will be referred to in the discussion. Key timing relations shown in Figure 6.1 will be represented by <u>underline</u> in the discussion.

6.2.2.1. Crater formation and early evolution

This subsection will discuss the formation of the Aram Chaos crater and its early evolution, prior to the fracturing, collapse and water outflow. The first to investigate Aram Chaos was Schultz et al. (1982), using Viking data. They interpreted the Aram Chaos crater to be a Noachian aged, 550 km in diameter multi-ringed basin. The current Aram Chaos morphology however is found not to correspond with the general morphology of a multi-ringed basin:

1. The part of Aram Chaos within the middle ring of 280 km diameter has been fractured and has subsided and collapsed (Figure 5.2.17). This created an approximately 2 km deep depression (see Cross Sections I and II, Figure 5.3.1). The middle ring is observed to have an elevated crater rim visible in MOLA data (Figure 5.1.2) which makes the middle ring more likely to represent the actual crater. The elevated crater rim, however, could have been accentuated by subsidence and erosion of the surrounding HT.
2. The outer ring is not formed by mountains (massifs) and higher relief, which is the case with other multi-ringed basins on Mars (Schultz et al., 1982), but by channel morphology and chaotic terrain localities (Observation 14). The massifs

could have been eroded or buried (see *Outflow episodes*). Also other structures, such as a possible center or ring uplift, could have been eroded or buried.

According to Schultz et al. (1982) the post crater formation evolution of the Aram Chaos crater involved erosion, deposition and ongoing cratering. Igneous activity localized at old ring faults could have reactivated crater structures and could have localized hydrothermal activity. This agrees with the model of HT formation by Rodríguez et al. (2005a) and with most of my observations:

1. No Aram Chaos related ejecta has been observed.
2. The HT is observed to continue into Aram Chaos (Observations 16 and 17).
3. Parts of the rim of Aram Chaos consists of small arcs which suggests more craters formed after the formation of the Aram Chaos crater and influenced the fracturing and collapse within Aram Chaos (Observation 20).
4. The Aram Chaos crater, due to its size, likely formed early in the cratering history.
5. If the Aram Chaos crater formed late in the HT evolution it would have disrupted the formation of the water filled caverns proposed by Rodríguez et al. (2005a) (see *Highland Terrain composition and structure*).

There are two observations which could be interpreted contradictory to the scenario of a continued build-up of the HT after the Aram Chaos crater formation:

1. The current morphology of incised channels, including Ares Vallis, forming the outer ring (Observation 14). This suggests the HT morphology was affected by the impact of the Aram Chaos crater, resulting in the incision of the channels concentric to Aram Chaos.
2. The middle ring is observed to have an elevated crater rim visible in MOLA data (Figure 5.1.2). The current HT surface could therefore possibly be the paleosurface in which the crater impacted.

If the interpretation that the Aram Chaos crater is buried within the HT is correct, could the current surface and topography still have inherited the crater structure underneath? Perhaps ongoing crater modification and/or reactivation of crater structures during HT formation, causing the deposited material to inherit subsurface structures, could explain the observation. Perhaps ongoing HT formation encompassed mostly a draping style of deposition (e.g. numerous impact ejecta blankets) which inherited the elevated crater rim? The first episode of Ares Vallis channelling is interpreted to be a sheet wash, after which incision occurred (Observation 1). This sheet wash could perhaps have removed HT material, possibly resurfacing terrain which was affected by the impact. Nevertheless, the scenario of ongoing HT deposition is found to be best in explaining the observations. The key observation in this regard is the observation the HT continues within the Aram Chaos crater (Observations 16 and 17).

Glotch and Christensen (2005) interpreted the Aram Chaos crater to be a filled crater, including water fill. They performed mapping using THEMIS IR, THEMIS VIS (comparable in resolution to the high resolution HRSC), MOC images and MOLA elevation data. The findings in this study agree with their interpretation: the occurrence of fractures and the observed HT subsidence and collapse suggests material has been withdrawn from underneath. Because CT are mostly source areas of outflow channels, this material is interpreted to be water. After its formation the Aram Chaos crater could have been filled up with water or water rich sediment. The HT collapse of Aram Chaos is

confined to the 280 km in diameter middle ring. This also suggests the actual crater size is 280 km in diameter.
By measuring over 1300 Martian craters using MOLA profiles Garvin et al. (1999, 2000) derived relations between crater diameter and depth and crater diameter and volume:

$d = 0.98 \times D^{0.18}$, with d the crater depth and D the crater diameter
$V = 0.01 \times D^{3.03}$ with V the volume of the crater

These relations can be used for the 280 km in diameter Aram Chaos crater to derive a depth of 2.7 km and a volume of 259949 km^3. I estimate between 47074 km^3 and 76496 km^3 material was removed from underneath Aram Chaos (Observation 15). The removed material is subsequently between 18% and 29% of the total crater volume. Modelling of large craters like Aram Chaos, however, is not well constrained yet (Barlow, personal communication).
The 280 km in diameter Aram Chaos crater is defined as a 'proto-basin' because the crater is larger then 90 km in diameter (Garvin et al., 1999). According to Spudis (1994) 'basins' on the Moon are larger then 320 km in diameter. Proto-basin craters can have a ring uplift (peak ring) and/or have multiple rings. MOLA data does not reveal an Aram Chaos crater central or ring uplift (see Cross Sections I & II, Figure 5.3.1). The HT collapse is observed to be varying, showing an undulating topography (Observation 18). This could be due to collapse and localized upward movements (popup) or the collapse of the HT onto a subsurface topography. The latter is found to be the most simple explanation. The origin of the subsurface topography could perhaps be caused by lateral differences in the water content of the HT 'cavernous systems' proposed by Rodríguez et al. (2005a).
The current structure of the 280 km in diameter Aram Chaos crater includes an inner ring of 150 km in diameter. This could perhaps be due to the melt sheet produced by the impact. Grieve and Therriault (2000) discussed the three largest known terrestrial impact basins, Vredefort, Sudbury and Chicxulub, of ~250-300, ~250-300 and ~180 km in diameter, respectively. They state that the thickness of the impact melt sheet is 1/50D and it extends 0.5D, with D the crater diameter. If these relations would also apply for Mars, the melt sheet of the 280 km in diameter Aram Chaos crater would have been 5.6 km thick and 140 km in diameter. This could perhaps have had a significant influence on subsequent crater infilling and could perhaps have structurally controlled the current ~150 km in diameter inner ring structure.
In summary, the crater is most likely 280 km in diameter. When it impacted, in the Noachian, the atmosphere may have been denser, and the climate warmer (see *6.2.1.1. Highland Terrain composition and structure*). This resulted in the crater fill of water rich material, perhaps 18% to 29% of the total crater volume. Ongoing formation of the HT, including cratering, buried the crater and its infill.

6.2.2.2. Aram Chaos fractured and chaotic terrain
This subsection will discuss the fracturing of the Highland Terrain and the formation of the Chaotic Terrain within Aram Chaos. The fracturing and chaotization of the Lower Aram Chaos Formation, within the inner ring of Aram Chaos will be discussed in *6.2.2.3.*

The Lower Aram Chaos Formation subsection. The release of water is discussed in the *6.2.2.4. Water activity in Aram Chaos* subsection.

The following definition of the chaotic terrain is used in this study: Chaotic Terrain (CT) is considered a lateral unit of the HT which is observed to have lost coherence with the surrounding HT, due to fracturing and erosion. This is different from the Glotch and Christensen (2005) definition. They also consider fractured terrain to be chaotic terrain.

The fractured Highland Terrain occurs between the inner and middle ring of Aram Chaos (Observation 14). Glotch and Christensen (2005) mapped the HT within Aram Chaos as Fractured Plains (see Figure 6.4). The fracturing formed 10 km scale HT mesas. Two windows of HT have been observed within the Lower Aram Chaos Formation (LACF) in the inner ring. These windows are interpreted to be fracture bounded HT mesas which indicates fractured HT also occurs within the inner ring, now covered by the Aram Chaos Formation (see Observations 26 and 28 and Cross Sections I & II, Figure 5.3.1). The fracturing included subsidence and collapse (see Cross Sections I & II, Figure 5.3.1).

The fracturing and collapse of Aram Chaos varies in intensity and characteristics. The pattern of the HT fractures is approximately concentric to the crater (Figure 5.5.2a), but can vary at different locations (Figure 5.5.1). In the Eastern quadrant of Aram Chaos f.e. no concentric ring fractures are observed and no collapse occurred; perhaps only bending of the HT inwards due to the collapse of the central region (Observation 23). The fracture pattern in the Eastern quadrant consists of relatively small fractures (see Figure 5.1.5, the Geological Map of Aram Chaos) compared to the other quadrants. The Principal Orientations (Figure 5.5.1) of the fractures differ from the other quadrants, which is mainly due to the lack of concentric ring fractures. The fractures occur in at maximum ~500 m high mesas and hills, mapped as Highland Terrain (the mesas) and Chaotic Terrain. They are based on relatively smooth terrain (mapped as Highland Terrain), which is covered by AACD (Observation 24). It is therefore inferred that the fractures extend to ~500 m depth. The chaotization subsequently degraded and eroded the HT until the ~500 m base. If the AACD was deposited on top of the HT base (see the *6.2.2.4. Water activity in Aram Chaos* subsection) this would make the Eastern quadrant chaotization older then the AACD deposition.

In the south of Aram Chaos Chaotic Terrain occurs (see Figure 5.1.5, the Geological Map of Aram Chaos), which is mapped as Knobby Terrain by Glotch and Christensen (2005). The Principal Orientations of this region (Figure 5.5.1) are not concentric to the crater. A broken up HT mesa within the Aram Chaos southern CT (Observation 21), suggests two different fracturing processes occurred within Aram Chaos: 1) large scale fracturing forming the ~10 km HT mesas, 2) smaller scale fracturing forming the ~1 km sized CT hills. The latter process involved intense fracturing, e.g. brecciation. The brecciation forming the southern CT most likely occurred prior to or during the large scale fracturing because the surrounding fractured HT contains a relatively high amount of fractures radial to the southern CT (Figure 5.5.2c). This suggests the fracturing of the surrounding HT has been influenced by the southern CT region. Possible water release from the Southern CT will be discussed in the *6.2.2.4. Water activity in Aram Chaos* subsection.

Other radial fracture patterns can be observed within the fractured HT (Observation 19), suggesting localized processes occurred at more locations. The possible processes behind the fracturing and chaotization will be discussed in *6.2.4. Chaotic terrain formation*. Fracturing may be active in Aram Chaos until today (Observation 7).

6.2.2.3. The Lower Aram Chaos Formation

This section will discuss the deposition and fracturing of the Lower Aram Chaos Formation. Its relation to the possible release of water will be discussed in the *6.2.2.4. Water activity in Aram Chaos* subsection. Spectral mapping of the smooth LACF will be discussed in the *6.2.2.5. Spectral mapping of the layered deposits* subsection.

The Lower Aram Chaos Formation (LACF) is divided in three lateral units, the fractured, broken and smooth LACF, and has been deposited on top of the fractured HT within the inner ring of the Aram Chaos crater. It is therefore interpreted to have been deposited after the inner ring, consisting of subsided HT, formed (see Observation 22). Multiple HT and CT windows can be observed within the LACF (see Figure 5.1.5, the Geological Map of Aram Chaos).

The extent of the fractured Lower Aram Chaos Formation approximately agrees with the combined extent of the Subdued Terrain and the High TI (Thermal Inertia) Chaos, mapped by Glotch and Christensen (2005) (see Figure 6.4). They interpreted the High TI Chaos to be chaotic terrain formed by reworking their Fractured Plains unit (the HT). They observed "muted fractures" within the Subdued Terrain but did not discuss them. Their mapping does not agree with the findings of this study:

1. The fractured LACF is defined by its fracture pattern and its distinct 'glossy' morphology (see Table 5.1). The fracture pattern and morphology of the Subdued Terrain and High TI Chaos is observed to be similar (see Figure 5.1.5, the Geological Map of Aram Chaos).
2. The fractured LACF is observed to be a deposit on top of the HT, approximately ~350 m thick (Observation 26).
3. The high thermal inertia (TI) of the High TI Chaos is interpreted to be caused by the intense fracturing (see Figures 6.4 and 6.5).

The extent of the broken LACF does not agree with the mapping by Glotch and Christensen (2005) (see Figure 6.4). It mainly consists of the Knobby Terrain and High TI Chaos units, mapped by Glotch and Christensen (2005), which they interpret as lateral units, varying in the amount of disturbance. Also the CT in the south of Aram Chaos is mapped as Knobby Terrain by Glotch and Christensen (2005). This does not agree with my findings: the broken LACF consists of km scale mesas and smaller hills, whereas the CT consists of broken up HT mesas forming km scale rounded and sharp hills (Observation 21).

The extent of the smooth LACF does not agree with the mapping by Glotch and Christensen (2005) (see Figure 6.4). It consists of the Primary and Secondary Hematite Units and the Non-Hematite Layered Unit, mapped by Glotch and Christensen (2005). Within the smooth LACF the mineral hematite, the sulphate kieserite and other hydrated minerals have been detected by TES and OMEGA. This is discussed in the *6.2.2.5. Spectral mapping of the layered deposits* subsection. The smooth LACF is interpreted to be a drape over underlying HT (Observation 27). This suggests the smooth LACF was deposited after the HT fracturing, subsidence and collapse had started.

The fractured, broken and smooth LACF were mapped as lateral units, because: 1) they are observed to be deposited on top of the HT and CT and underlying the Intermediate Aram Chaos Formation (see Cross Sections I & II, Figure 5.3.1) and 2) the broken and fractured LACF show a gradual transition boundary (Boundary 2, Table 5.2). The smooth

LACF however could also be a thin deposit on top of the fractured LACF (Boundary 3 in Table 5.2). There are arguments for and against this interpretation of the smooth LACF:

1. A HT-scale fracturing pattern can be observed within the fractured LACF (see Figure 5.1.5, the Aram Chaos Geological Map) suggesting the fracture pattern is (partly) controlled by HT blocks underneath. If the smooth LACF is a lateral unit perhaps no HT collapse occurred underneath these locations. This however is considered to be unlikely, making the smooth LACF a distinct unit.
2. The mineral hematite, the sulphate kieserite and other hydrated minerals, detected by TES and OMEGA (see *6.2.2.5. Spectral mapping of the layered deposits*), were not detected in the broken and fractured LACF. This could be used to argue that the smooth LACF is indeed a distinct unit, although the mineral detection could perhaps also be caused by a thin cover (see *6.2.2.5. Spectral mapping of the layered deposits*).
3. Some fractures within the LACF have raised rims and some show small thrusts at the base of the rim (Observation 30). This could have been caused by: 1) lateral compression due to subsidence and collapse of HT blocks underneath and/or 2) localized release of water from underneath the deposited LACF, forming the LACF fractures. The latter suggests the smooth LACF is a lateral unit. The possible release of water will be discussed in the *6.2.2.4. Water activity in Aram Chaos* subsection. Lateral compression can be explained by the inward dip of the concentric rim faults of multi-ring craters like Aram Chaos (Figure 3.11): subsiding material cannot be easily accommodated and the subsidence causes inward compression. The weak NNW-SSE and NE-SW Preferred Orientations could be indicative of the dominating compressive directions (normal to the two Principal Orientations: NEE-SWW, NW-SE).
4. The most southern window of fractured LACF within the smooth LACF is located at the boundary of the LACF and the CT and Rounded Chaotic and Highland Terrain (RCHT) (Boundary 3 of Table 5.2, Figure 5.1.20). The fracturing pattern is observed to continue within the CT. This suggests the LACF is a drape, deposited after the formation of the CT. The fracturing of the LACF could have formed after localized activity occurred (e.g. water release), suggesting a lateral unit explanation. The observation that the fractured LACF formed after the CT formation would indicate the CT in the Eastern quadrant of Aram Chaos formed prior to the deposition of the Aram Chaos Formation.

Considering the different arguments, the interpretation of the smooth LACF as a distinct unit, covering the fractured LACF, is found to be the most convincing. This suggests the fractured LACF extended at least as far East as the most Eastern fractured LACF window within the smooth LACF (see the Geological Map of Aram Chaos, Figure 5.1.5), which still indicates a deposition of the LACF within the inner ring of Aram Chaos. After deposition the LACF became fractured and broken. The broken LACF could be the locations where water was released to the surface. This is further discussed in the *6.2.2.4. Water activity in Aram Chaos* subsection. The smooth LACF was subsequently deposited as the first unit of the non-fractured part of the Aram Chaos Formation. This was followed by the deposition of the Intermediate Aram Chaos Formation and the Upper Aram Chaos Formation, which subsequently underwent erosion.

6.2.2.4. Water activity in Aram Chaos

This section will discuss the possible 1) in and outflow of water though the Aram Chaos channel, 2) release of water from the Aram Chaos subsurface, 3) ponding within Aram Chaos. This is not a sequence of events.

The occurrence of the Aram Chaos channel connecting Aram Chaos with Ares Vallis suggests in and outflow of water occurred. It is reasonable to assume the channel formed by either crater inward or crater outward flow over the Aram Chaos rim, after which the channel incised. The depth of the channel relates to the depth of Aram Chaos subsidence which suggests the incision occurred during ongoing subsidence. On the Aram Chaos crater rim the Aram Ares Channel Deposits (AACD) have been mapped. The AACD has a distinct morphology of lineations and small elongated hills, which is interpreted to be caused by water flow after deposition. Glotch and Christensen (2005) mapped the AACD as the more extensive Outflow Plains Unit (Figure 6.4).

Cabrol and Grin (2002) identified a possible sub-lacustrine delta structure at the Aram Chaos part of the Aram Chaos channel (Figure 3.5), indicating inward flow. This structure is interpreted in this study, using high-resolution HRSC data, to consist of streamlined HT mesas, which are capped by the AACD (Observation 25). The streamlined mesas were formed by crater outward flow. This indicates the AACD is deposited on top of the HT, after which both have been incised by crater outward flow through the Aram Chaos channel. This observation, and the fact that the AACD occurs on the crater rim would suggest the AACD has been deposited early in the evolution of Aram Chaos as a result of crater inward flow. Glotch and Christensen (2005) do not discuss how the Outflow Plains Unit relates to the other deposits in Aram Chaos. In this study the smooth LACF is observed to embay the AACD capped streamlined mesas (Figure 6.6), which suggests the smooth LACF is younger then the AACD. A deposit looking similar to the AACD has been observed on a terrace of Ares Vallis, North of Aram Chaos (Observation 3, compare Figure 5.2.4 with Figure 5.1.10j).

The AACD morphology is also observed in the Aram Chaos channel wall, forming linear ridges (Observation 25, Figure 5.2.25d). Two scenarios could explain this observation (Figure 6.7):

1. The AACD forms layering within the Aram Chaos channel wall (Figure 6.7a).
2. The AACD is draped over the Aram Chaos channel wall (Figure 6.7b).

The first scenario suggests the AACD was deposited in a basin because it has a thickness of at least 1 km (the Aram Chaos channel wall height). Perhaps the AACD was deposited after the subsidence and collapse? This does not agree with the observations: the Aram Chaos channel incised the non-subsided Eastern quadrant in which the AACD occurs. Perhaps the AACD obscures faults? If this is not the case it suggests the AACD forms part of the HT stratigraphy, which has now been resurfaced. The AACD could be resurfaced deltaic deposits which formed after the Aram Chaos crater impact, in the Noachian, during the HT formation when the water rich crater fill occurred (see *6.2.2.1. Crater formation and early evolution*).

The second scenario would make the start of the Aram Chaos channel incision older then the AACD. The AACD capped streamlined HT mesas would then indicate at least one episode of crater outward water flow occurred after the AACD draping. The AACD draping most likely originated from crater inward flow over the rim. The depth of the Aram Chaos channel at that time would most likely have been comparable with the depth

of incision of Ares Vallis. It would therefore be unlikely that water originating from Iani Chaos flowed over the, 2 km higher in elevation, Aram Chaos rim. It is therefore most likely the AACD forms layering. In any case, a more detailed study of the Aram Chaos channel region is needed to confirm one of the proposed scenarios, using f.e. HiRISE images and HRSC DTMs.

Crater outward flow through the Aram Chaos channel could have occurred after subsurface water release within Aram Chaos. The water could have migrated through the HT fractures to the surface (Glotch and Christensen, 2005), perhaps resulting in ponding and/or flowing through the Aram Chaos channel. The CT in the south of Aram Chaos, which is interpreted to be brecciated HT (see *6.2.2.2. Aram Chaos fractured and chaotic terrain*), could have resulted in the, most likely explosive, release of water. This water could have ponded within Aram Chaos or could have flowed through the Aram Chaos channel. Rotto and Tanaka (1995) f.e. interpreted the Aram Chaos channel to be larger, connecting the CT in the south of Aram Chaos with Ares Vallis (Figure 6.8). The mapping of this study however did not detect channel morphology within the Aram Chaos part of this possible channel: it is mapped as CT (see the Geological Map of Aram Chaos, Figure 5.1.5). Flooding from the southern CT could still have chosen this path and water could also have been released from the subsurface. If the Aram Chaos Formation had already been deposited it would most likely have been affected by the water release from the southern CT. This is however not observed, which would make the outflow from the southern CT having occurred prior to the deposition of the Aram Chaos Formation.

The fractured and broken LACF could have been deposited, prior to fracturing, after ponding of water within the inner ring of Aram Chaos. The LACF could have subsequently been fractured and been broken due to ongoing water release from HT fractures underneath. This is strengthened by the observation of a HT-scale fracturing pattern within the fractured LACF (see Figure 5.1.5, the Aram Chaos Geological Map). It is however also possible that the material forming the fractured and broken LACF was transported into Aram Chaos through the Aram Chaos channel.

Glotch and Christensen (2005) interpret all the layered deposits to have formed in a sub-lacustrine environment. This is not found to be likely because the Intermediate and Upper Aram Chaos Formation form a dome shape (see Cross Sections I & II, Figure 5.3.1) which cannot be easily explained by a sub-lacustrine environment. The detection of hematite, kieserite and other hydrates minerals within the smooth LACF and the IACF (see *6.2.2.5. Spectral mapping of the layered deposits*) in any case suggest water was involved in the formation of the deposits. More layered deposits with the characteristic dome shape have been observed on Mars (see f.e. Fueten et al., 2006), but none are capped by material with an 'icing' texture as is the case with the ACF. Rossi et al. (2007) interpret dome shaped layered deposits to be the result of inclined deposition of layered deposits in long lasting spring deposits.

To conclude, no clear chronological episodes of water release, proposed by Glotch and Christensen (2005), can be observed, although the differences in chaotization within Aram Chaos suggest different events of water release occurred.

6.2.2.5. Spectral mapping of the layered deposits

Spectral mapping of Aram Chaos was performed using TES (Glotch and Christensen, 2005) and OMEGA (Gendrin et al., 2005; Combe et al., 2005). Glotch and Christensen (2005) detected grey crystalline hematite and Gendrin et al. (2005) detected the sulphate kieserite and other hydrated minerals, within what was mapped in this study as the smooth LACF and the IACF. Analysis of Aram Chaos spectra from OMEGA suggests red particulate hematite is present (Combe et al., 2005). They did not provide a map of the abundance. Grey crystalline hematite can be produced in an aqueous or hydrothermal depositional environment. Red particulate hematite is generally produced by leaching and weathering processes (Glotch and Christensen, 2005).

The mapping of the layered deposits by Glotch and Christensen (2005) was largely based on TES hematite distribution data (compare Figure 3.7 with Figure 6.9). They mapped a Primary and Secondary Hematite Unit and a Non Hematite Layered Unit. The extent of the Intermediate Aram Chaos Formation (IACF) and the smooth Lower Aram Chaos Formation (LACF) together is largely the same as the combined extent of these three units (see Figure 6.4). The Primary Hematite Unit covers the three highest hematite abundance patches. According to Glotch and Christensen it contains basaltic sand with a hematite abundance between 10% and 15%. The Secondary Hematite Unit, which surrounds the Primary Hematite Unit and contains less hematite, is interpreted by Glotch and Christensen (2005) to be eroded Primary Hematite Unit material which was transported downhill. The Non-Hematite Layered Unit doesn't contain hematite and is interpreted to be morphologically identical to and stratigraphically below the Primary Hematite Unit. It is mineralogically similar to the Subdued Terrain. This does not agree with my mapping:

1. HRSC data shows that the highest hematite abundance patches do not correlate with a distinct morphology (Figure 6.10). The morphology of the patches also differs among each other: one patch is being located in the smooth LACF, the other patches occur in the rougher IACF (Figure 6.10). However, hematite has also been detected in Aureum Chaos by Glotch et al. (2005), occurring near the Aureum Chaos Deposits (ACD). These deposits exhibit the same 'icing' texture as the UACF. This indicates the hematite could be associated with this morphology. However, no hematite has been detected within the UACF and ACD.
2. Some of the Primary Hematite Unit locations, mapped in this study as the smooth LACF, are observed to stratigraphically underlie the deposits with high hematite, the IACF (see Cross Sections I & II, Figure 5.3.1).
3. The locations mapped as the Non-Hematite Layered Unit are observed to be morphologically different, either smooth (the smooth LACF) or more rugged (IACF).

This suggests the hematite is uncorrelated to the morphology. It could however be associated with the UACF and ACD. The hematite could perhaps be present within a lag deposit formed by deflation of the UACF and the ACD. The occurrence of UACF mesas within the IACF indeed suggests the deposit was once more extensive (see Figure 5.1.5, the Geological Map of Aram Chaos).

Using OMEGA data Gendrin et al. (2005) detected the sulphate kieserite and other hydrated minerals within Aram Chaos (Figure 6.11). These findings approximately correlate with the mapping of this study (Figure 6.11): most smooth LACF is observed to

be kieserite rich (red) and most IACF is observed to be rich in other hydrated minerals (pink). Only the most eastern outcrop of the smooth LACF does not correlate with a high amount of kieserite (Figure 6.11). This suggests the mapping of this study is wrong and the most eastern outcrop of the smooth LACF is in fact IACF. If this apparent correlation with morphology is correct it indicates water was involved in the formation of the smooth LACF and IACF.
The analysis of the OMEGA data in this study did not result in the detection of minerals (see *5.1.3.1. OMEGA mapping results*). The combined extent of the smooth LACF and IACF was visible only for the 'large spectral feature' (see Figures 5.1.32 and 5.1.33). This feature however cannot be used to distinguish between mineralogy. It was observed within the mean spectra (see Figures 5.1.27 and 5.1.28) and is not an absorption feature, which are used to detect minerals. To conclude, the OMEGA results by Gendrin et al. (2005) could not be reproduced.

6.2.2.6. Late-stage evolution
This subsection will discuss the late-stage development of the layered deposits within Aram Chaos. The current morphology of the Aram Chaos Formation, consisting of multiple mesas, suggests erosion took place after the formation of the ACF. Flow morphology occurs in the Intermediate Aram Chaos Formation (IACF) (Figure 5.1.10h), which are parallel to the dominant wind direction (Figure 5.5.8). This suggests a wind related origin. The release of water through broken and fractured LACF could perhaps have caused weakening of the overlying ACF layers, after which surface erosion processes exposed the fractured LACF windows. This would indicate water release was active after the formation of, at least part of, the non-fractured ACF
Small patches of the Upper Aram Chaos Formation (UACF), mapped by Glotch and Christensen (2005) as the Cap Unit, are located around the main deposit (see Figure 5.1.5, the Aram Chaos Map). Glotch and Christensen (2005) therefore interpret the deposit was once more extensive and has been eroded, which agrees with the interpretation of this study. The mapping extent of both UACF and Cap Unit agree because on THEMIS VIS, MOC and HRSC images the UACF material highly contrasts with the surrounding units (see Figure 6.4).
No fracturing is visible within the UACF outcrops, although sharp linear escarpments of the UACF mesas (see Figure 5.1.5, the Geological Map of Aram Chaos) occur. The general trend of this erosion morphology (the trend of the ACF mesa escarpments) is parallel to the general wind direction (compare Figure 5.1.5 with Figure 5.5.8). However, the trend is also parallel to one of the fractured LACF fracture Principal Orientations (Figure 5.5.1). This suggests both wind and fracturing have played a role in shaping the current erosion morphology. According to Glotch and Christensen (2005) a crater related doming event occurred which tilted the layered deposits (Figure 3.12). This is one possibility; another being that the IACF and UACF were deposited prior or during the LACF fracturing event, caused by ongoing HT subsidence and collapse. Smooth LACF, which occurs stratigraphically below the IACF and UACF, has not been extensively fractured. Therefore the current erosion morphology of the smooth LACF, the IACF and the UACF is interpreted to be caused by the dominant wind direction.

6.2.2.7. Summary

This section describes the summarized sequence of events and will summarize the differences between the mapping of this study and the mapping by Glotch and Christensen (2005).

The following sequence of events for Aram Chaos are proposed (see Figure 6.1):

1. HT formation during the Noachian including formation of the Aram Chaos 280 km in diameter crater. Tharsis related regional deformation was active. The AACD could have formed as a deltaic deposit when the crater was filled with water rich material. This would imply the Noachian climate was warmer and the atmosphere was thicker compared to the current situation.
2. In the Hesperian the climate became colder and the water became ice. Subsequent pulses of endogenic heat could have melted the ice. This would have caused an unstable situation after which the overlying HT collapsed. This resulted in decompression vaporization which led to the brecciation of the southern CT (see *6.2.4. Chaotic terrain formation*).
3. Ongoing fracturing, subsidence and collapse of the HT in Aram Chaos, possibly resulting in water release through the fractures. Ongoing channel incision. Formation of the Eastern quadrant CT.
4. Formation of the 150 km in diameter inner ring of Aram Chaos by HT subsidence and collapse.
5. Water ponding within the inner ring and the subsequent deposition of the LACF (except the smooth LACF). The water could have originated from the HT fractures or CT within Aram Chaos or from outside Aram Chaos through the Aram Chaos channel.
6. Fracturing and chaotization of the LACF due to ongoing HT fracturing, subsidence, collapse and possibly water release.
7. The possible draping of the AACD.
8. Formation of the smooth LACF, IACF and UACF on top of the fractured and broken LACF. The detection of hematite, kieserite and other hydrated minerals suggests water was involved in the formation of the units.
9. Erosion and possibly deflation of the UACF, IACF and smooth LACF by wind.

The mapping performed by Glotch and Christensen (2005) shows some major differences with the mapping of this research:

1. Mapping of the layered deposits by Glotch and Christensen (2005) is based on TES hematite abundances, but it is observed not to correlate with morphologically defined units in this study. It could perhaps be a thin cover, although controlled by outcrops.
2. The structural and morphological similarity between Subdued Terrain and the High TI Chaos (both mapped in this study as the fractured LACF) is not recognized by Glotch and Christensen (2005).
3. The morphological difference between broken LACF and CT is not recognized by Glotch and Christensen (2005).
4. The resulted map (Figure 3 in Glotch and Christensen, 2005) is of a lower resolution then the mapping of this study.

The differences are not due to differences in data coverage, but, as said before, by their incorporation of TES data and the incorporation of HRSC anaglyphs in this study to

allow 3D mapping. The mapping in this study is mostly based on morphology and structure visible in high resolution HRSC and THEMIS VIS.

6.2.3. Evolution of Aureum and Iani Chaos

This section will discuss the evolution of the Aureum and Iani Chaos regions within my study area. Both regions are mapped as Chaotic Terrain (CT), surrounded by fractured HT (mesas), and have undergone subsidence and collapse. Subsequently deposits formed on top of the CT.

The part of Aureum Chaos in my study area is not connected to Ares Vallis, it is one of the source areas of the Simud and Tiu Vallis systems, of which Valles Marineris is also a source area (Figure 3.1). Numerous impact crater remnants can be observed within Aureum Chaos (see f.e. Figure 5.2.7 and Cross Section III, Figure 5.3.2). Fracturing may be active in Aureum Chaos until today (Observation 7). Deposits, mapped as Aureum Chaos Deposits (ACD), occur on top of the CT (see the Geological map of Aureum Chaos, Figure 5.1.6). The ACD morphology is similar to the UACF, exhibiting sharp escarpments and an 'icing' texture (Figure 5.1.17c and 5.1.18). Glotch et al. (2005) observed hematite within the CT near the ACD. This indicates the hematite could be associated with this morphology. However, no hematite has been detected within the UACF and ACD. It could perhaps be present in the stratigraphy of both units. The hematite could be lag deposits formed after deflation of the UACF and ACD. This suggests both units were once more extensive (for UACF see *6.2.2.6. Late-stage evolution*).

Iani Chaos lies within an outflow channel system connecting Margaritifer Valles in the south with Ares Valles in the north (Figure 3.9). It has therefore also been flooded. The incision by water flow from Margaritifer Valles could perhaps have lowered the overpressure of buried water rich deposits triggering the formation of Iani Chaos (e.g. Coleman, 2005). Channel morphology remnants, surrounded by chaotic terrain occur within the northern part of Iani Chaos (Figure 5.2.3). This suggests that the chaotization progressed downstream, destroying channels. The CT farthest away from the current start of the outflow channel would then subsequently be the oldest, although chaotization could also have progressed upstream, fracturing and eroding the surrounding HT.

No clear crater remnants have been observed within Iani Chaos. The northern part of Iani Chaos is interpreted to be part of the Aram Chaos outer ring. This suggests structural control of at least the Aram Chaos crater is present (Schultz et al., 1982). Within the northern part of Iani Chaos ridges occur which have been interpreted to be caused by compression (Observation 7). The compression ridges are fractured and are subsequently interpreted to have formed before the fracturing. They could perhaps have formed by upward stresses due to the instability of subsurface water.

The Iani Chaos Deposits (ICD) occur on top of the Iani Chaos CT (Cross Section IV, Figure 5.3.3 and the Geological map of Iani Chaos, Figure 5.1.7). The ICD have been divided into five types on the basis of morphology. They occur in patches and are not connected, except for type 3, which is non-horizontally layered (see 9 in Figure 5.4.2) and lies stratigraphically on top of type 4. The brightest deposits (types 2 and 4) have been influenced by wind erosion. Type 4 is morphologically similar to the smooth LACF and type 5 is morphologically similar to the UACF. Because of the possible association

of the UACF and ACD with hematite (see *6.2.2.5. Spectral mapping of the layered deposits*) it would be expected that hematite occurs around the type 5 deposits.
Activity within the CT of Aureum and Iani Chaos would have destroyed the ACD and ICD. The ACD and ICD are therefore interpreted to have formed during or after the final stage of water release from the CT. The similarity in morphologies between the ACF, ACD and ICD suggest that (parts of) the ICD and ACD have a similar origin as the Aram Chaos Formation deposits.

6.2.4. Chaotic terrain formation
Rodríguez et al. (2005a) did not discuss the origin of the HT and CT fracture patterns. Following their model it is likely the HT and CT fracture patterns (Figure 5.1.9) were formed by 1) crater related fractures and 2) cavern subsidence and collapse related fractures (see f.e. Cross Sections I & II, Figure 5.3.1). I propose a third process which could explain the observed fracture pattern and could explain the CT morphology: fluid assisted brecciation. This process occurs on Earth and is associated with temporal variations in fluid pressure (e.g. pulses) in a hydrothermal system (Jébrak, 1997). According to Jébrak (1997) this occurs in two steps:

1. Hydraulic fracturing, which occurs when the fluid pressure increases causing fracture propagation. Most hydraulic fracturing on Earth occurs during an extensional stress.
2. Critical fracturing occurs when the equilibrium between the fluid pressure and the lithostatic pressure is destroyed. A sudden opening (f.e. due to faulting) causes the fluid pressure to decrease resulting in decompression and brecciation. The intersection line of growing fractures are commonly zones of increased brecciation.

In this proposed scenario the hydrostatic pressure of the water in a hydrothermal system resulted in fracture propagation (hydraulic fracturing). The fracturing destabilized the overlying HT causing it to collapse. This could subsequently have resulted in decompression of the water and brecciation of the overlying HT (critical fracturing). The decompression could have caused the liquid water to turn into vapour (Figure 6.12) after which it was released to the surface. This most probably was an instantaneous and catastrophic event. The resulting decrease in water volume probably caused more instability of the overlying HT, resulting in more collapse and an increase in the pore pressure. If the hydrothermal system remained unconfined, fluid assisted brecciation probably did not occur anymore. HT collapse could however also have caused the formation of confined spaces in the hydrothermal system. This could have resulted in renewed fluid assisted brecciation.
The following observations are interpreted to be consistent with the process of fluid assisted brecciation:

1. The current CT morphology consists of km-scale hills which are interpreted to be fracture bounded. The fracture density within the CT is higher than within the HT (Observation 10). The CT are interpreted to be the locations where groundwater emerged (Newsom, 2001). The surface release of water was likely an explosive event causing brecciation of the HT.
2. In the southern CT of Aram Chaos a broken up HT mesa is observed (Observation 21). This suggests two different fracturing processes occurred within Aram

Chaos: 1) large scale fracturing forming the ~10 km HT mesas, 2) smaller scale fracturing forming the ~1 km sized CT hills. The latter process involved intense fracturing, e.g. brecciation.

3. Within the fractured HT zones of intense fracturing are observed (Observation 9) which are interpreted to be zones where 1) hydrothermal activity was greater compared to other locations but 2) where the water did not reach the surface as was the case with the CT.
4. The build-up of the fluid pressure could have resulted in upward stresses of the HT above and subsequent lateral compression of the HT. This could explain compression related ridges in the North of Iani Chaos (Observation 8).
5. A radial fracture pattern is observed around the center of the CT in the south of Aram Chaos (Figure 6.6). The fractures could be 1) crater fractures or 2) fractures propagating radial outward from the Aram Chaos CT center. Other radial fracture patterns (e.g. Observation 19) can be observed in Aram Chaos.

Crater counts suggest the outflow channelling occurred in episodes in the Hesperian and into the Amazonian (Masson et al., 2001). If the climate during the Hesperian and Amazonian was similar to the current climate, the buried water was most likely in the form of ice. If fluid assisted brecciation occurred the water must therefore have been liquid and under high temperature in a hydrothermal system. Only subsurface igneous activity could have created such an environment.

7. Implications and conclusions

This section will describe the implications and conclusions of this research. The goals of this research (see **1. Introduction**) have mostly been achieved: only the creation of minerals maps from OMEGA data was not successful. HRSC DTMs were available but were of the same resolution as the MOLA data and consequently only MOLA elevation was used.

The following implications and conclusions can be made about the regional evolution and geology:

1. Rodriquez et al. (2005a) proposed the stratigraphy of the Highland Terrain contains many buried impact craters, filled with water rich material, indicating a warmer climate during the Noachian. I propose the HT is formed by a complex interplay between the processes of volcanism, cratering, erosion, deposition and (regional) deformation (see *6.2.1.1. Highland Terrain composition and structure* and Figure 6.3). This has implications for the rheology and density estimation of the, multiple kms thick, HT stratigraphy.
2. I agree with the model of chaotic terrain formation by Rodríguez et al. (2005a). They proposed the HT consists of water filled 'cavernous systems', which are combined fracture systems of many buried impact craters. According to this model crater related fractures and cavern subsidence will explain the observed surface fracture patterns. I propose a third process, which could have been responsible for the observed fracture pattern and the formation of the CT: fluid assisted brecciation. This involved two steps: 1) fracture propagation due to an increase in hydrostatic pressure (hydraulic fracturing) and 2) subsequent destabilization and collapse of the overlying HT resulting in decompression of the water and brecciation (critical fracturing). The decompression most likely resulted in the vaporization of the water, which was catastrophically released to the surface. If the proposed process of fluid assisted brecciation is correct it indicates hydrothermal systems were present, already proposed by Rodríguez et al. (2005a). This implies subsurface igneous activity was the main trigger for chaotic terrain formation.
3. Regional deformation most likely did not occur during the formation of the fractures in the HT and CT. Buried and subsurface deformation structures, most likely related to Tharsis, could however be present in the HT stratigraphy.

The following implications and conclusions can be made about the geology and evolution of Aram Chaos:

1. The Aram Chaos crater is most likely a 280 km in diameter crater formed in the Noachian and buried in the HT stratigraphy. After formation it was filled with water rich materials, as proposed by Glotch and Christensen (2005). Ongoing HT formation, including deposition, erosion and cratering buried the crater.
2. The Aram Chaos channel most likely formed after crater inward or crater outward flow over the Aram Chaos rim. Subsequently incision occurred during ongoing subsidence of Aram Chaos. The final flow was most likely crater outward.
3. The Aram Ares Channel Deposits (AACD) are interpreted to be at least 1 km thick deposits within the HT stratigraphy. This implies the AACD are Noachian aged and formed as deltaic deposits when the Aram Chaos crater was filled with crater rich material.

4. The Lower Aram Chaos Formation (except the smooth LACF) is considered to be a deposited within the 150 km in diameter inner ring of Aram Chaos. It was subsequently fractured and broken by either ongoing subsidence and collapse of the underlying HT or water release from the HT fractures. The unit could have been deposited in a sub-lacustrine environment indicating ponding occurred within the inner ring of Aram Chaos.
5. The mapping of this study approximately agrees with the OMEGA mapping of kieserite and other hydrated minerals: most smooth LACF outcrops contain kieserite and most IACF outcrops contain other hydrated minerals. Hematite is proposed to be associated with the UACF, forming deflation related lag deposits in the smooth LACF and IACF. This would imply that water was involved in the formation of smooth LACF, IACF and UACF, the non-fractured part of the Aram Chaos Formation. The doming morphology of these deposits is not corresponding with a sub-lacustrine deposition environment, as proposed by Glotch and Christensen (2005). They could perhaps be spring deposits, as proposed by Rossi et al. (2007). More research, including crater counting, needs to be undertaken to better understand the dome shaped morphology, the thickness variations, the stratigraphical relations and the relative age of the non-fractured ACF units.

The following conclusions can be made about the mapping and analysis in general:

1. The mapping performed by Glotch and Christensen (2005) is found to be different then the mapping of this research. This is mainly due to their incorporation of TES data and the incorporation of HRSC anaglyphs in this study to allow 3D mapping. The mapping in this study is mostly based on morphology and structure visible in high resolution HRSC and THEMIS VIS images.
2. The Concentricity lineament analysis technique designed in this study is a first approach to quantify lineament localizations. It has to be expanded by building an algorithm which automatically finds concentric and/or radial centers within the lineament data.

Proposed future research:

1. A more detailed investigation of the non-fractured Aram Chaos Formation deposits, using high resolution HRSC data and HRSC derived DTMs. The Orion software could be used to measure strike and dips of the layering. Do the layer orientations of the different mesas connect? Or did the layers rotate due to subsidence and collapse of underlying HT?
2. A more detailed investigation of the Aram Ares Channel Deposits (AACD), using high resolution HRSC data and HRSC derived DTMs, to investigate the influence of the Aram Chaos channel incision and subsidence and collapse related faulting in the formation of the AACD. Is the observed AACD morphology in the Aram Chaos channel wall layering? Is the AACD part of the HT stratigraphy?

Acknowledgements
I would like to thank Tanja Zegers for her supervision, ESA ESTEC for the internship, in particular Angelo Rossi for his help with the methodology, and Bernard Foing. I would also like to thank the International Institute for Geo-Information Science and Earth Observation (ITC) and in particular Harald van der Werff and Frank van Ruitenbeek for the week I could spend there getting familiar with hyperspectral analysis and OMEGA data. Additional thanks to Maarten Kleinhans, Erin Kraal, Hans de Bresser and Bart Meijninger, from the Faculty of Geosciences, University Utrecht, for fruitful discussions and Trent Hare, from the USGS, for his help with the data processing.

References

Allaby, A., Allaby, M., 1999. Dictionary of Earth Sciences, Oxford University Press.

Baker, V.R., Carr, M.H., Gulick, V.C., Williams, C.R., Marley, M.S. (1992) in Mars, eds. Kieffer, H., Jakosky, B. M., Snyder, C. W., Matthews, M. S. (Univ. of Arizona Press, Tucson), pp. 493-522.

Baker, V.R. (2001), Water and the martian landscape, Nature insight, 412, 228-236.

Bandfield, J. L., et al. (2003), Spectroscopic Identification of Carbonate Minerals in the Martian Dust, Science, 301, 1084-1087.

Banerdt, W.B., Golembek, M.P., Tanaka, K. L. (1992) in Mars, eds. Kieffer, H., Jakosky, B. M., Snyder, C. W., Matthews, M. S. (Univ. of Arizona Press, Tucson), pp. 249-297.

Bibring, J.-P., et al. (2004), OMEGA: Observatoire pour la Minéralogie, l'Eau, les Glaces et l'Activité, http://www.ias.u-psud.fr/data/document/03/BibringWeb.pdf.

Bibring, J.-P., et al. (2005), Mars Surface Diversity as Revealed by the OMEGA/Mars Express Observations, Science, 307, 1576-1581.

Boynton, W. V., et al. (2002), Distribution of Hydrogen in the Near Surface of Mars: Evidence for Subsurface Ice Deposits, Science, 297, 81-85.

Cabrol, N. A., Grin, E.A., Dawidowicz, G. (1997), A Model of Outflow Generation by Hydrothermal Underpressure Drainage in Volcano–Tectonic Environment, Shalbatana Vallis (Mars), Icarus, 125, 455-464.

Cabrol, N. A., Grin, E.A. (1999), Distribution, Classification, and Ages of Martian Impact Crater Lakes, Icarus, 142, 160–172.

Cabrol, N. A., Grin, E.A. (2002), Overview on the formation of paleolakes and ponds on Mars, Global and Planetary Change, 35, 199–219.

Carporzen, L., et al. (2005), Palaeomagnetism of the Vredefort meteorite crater and implications for craters on Mars, Nature, 435, 198-201.

Carr, M.H. (1996), Water on Mars, Oxford University Press.

Catling, D. C., Moore, J.M. (2003), The nature of coarse-grained crystalline hematite and its implications for the early environment of Mars, Icarus, 165, 277–300.

Chapman, M.G., Tanaka, K.L. (2002), Related Magma–Ice Interactions: Possible Origins of Chasmata, Chaos, and Surface Materials in Xanthe, Margaritifer, and Meridiani Terrae, Mars, Icarus, 155, 324–339.

Christensen, P.R., et al. (2001), Global mapping of Martian hematite mineral deposits: Remnants of water-driven processes on early Mars, Journal of Geophysical Research, 106, 23.873–23.885.

Christensen, P.R., N.S. Gorelick, G.L. Mehall, and K.C. Murray, THEMIS Public Data Releases, Planetary Data System node, Arizona State University, <http://themis-data.asu.edu>.

Coleman, N.M. (2005), Martian megaflood-triggered chaos formation, revealing groundwater depth, cryosphere thickness, and crustal heat flux, Journal of Geophysical Research, 110, doi:10.1029/2005JE002419.

Combe, J-Ph., Sotin, C., Le Mouélic, S., Launeau, P., Mustard, J., Gendrin, A., Bibring, J-P., Gondet, B., Langevin, Y., and the OMEGA Science team (2005), Methodology of hyperspectral reflectance data analysis for mineralogical mapping of planetary surfaces: application to OMEGA/Mars-Express images, Lunar and Planetary Science XXXVI, Abstract 1633.

Connerney, J.E.P., et al. (2005), Tectonic implications of Mars crustal magnetism, PNAS, 102, 14970–14975.
Costard, F., Baker, V.R. (2001), Thermokarst landforms and processes in Ares Vallis, Mars, Geomorphology, 37, 289-301.
Craddock, R. A., Howard, A.D. (2002), The case for rainfall on a warm, wet early Mars, Journal of Geophysical Research, 107, doi:10.1029/2001JE001505.
Dohm, J. M., Anderson, C., Baker, V.R., et al. (2001), Latent outflow activity for western Tharsis, Mars: Significant flood record exposed, Journal of Geophysical Research, 106, 12,301–312,314.
Duxbury, T.C., Kirk, R.L., Archinal, B.A., Neumann, G.A. (2002), Mars Geodesy/Cartography Working Group recommendations on Mars constants and coordinate systems, http://www.isprs.org/commission4/proceedings02/pdfpapers/521.pdf
Earl, J., et al. (2005), Automatic recognition of crater-like structures in terrestrial and planetary images, Lunar and Planetary Science XXXVI, Abstract 1319.
Feldman, W. V., et al. (2002), Global Distribution of Neutrons from Mars: Results from Mars Odyssey, Science, 297, 75-78.
Ferrill, D.A., Wyrick, D.Y., Morris, A.P., Sims, D.W., Franklin, N.M. (2004), Dilational fault slip and pit chain formation on Mars, GSA Today, v.14, no. 10, 4-12.
Fishbaugh, K. E., Head, J.W. (2001), Comparison of the North and South Polar Caps of Mars: New Observations from MOLA Data and Discussion of Some Outstanding Questions, Icarus, 154, 145–161.
Frey, H. V., et al. (2002), Ancient lowlands on Mars, Geophysical Research Letters, 29, doi:10.1029/2001GL013832.
Frey, H.V., et al. (2003), Evidence for buried "Pre-Noachian" crust pre-dating the oldest observed surface units on Mars, Lunar Planet. Sci., XXXXIV, Abstract 1848.
Frey, H.V. (2004), A timescale for major events in early Mars crustal evolution, Lunar and Planetary Science, XXXV, Abstract 1382.
Frey, H.V. (2005), Impact constraints on, and a chronology for, major events in early Mars history, Journal of Geophysical Research, in press.
Fueten, F., Stesky, R., MacKinnon, P., et al. (2006), A structural study of an interior layered deposit in southwestern Candor Chasma, Valles Marineris, Mars, using high resolution stereo camera data from Mars Express, Geophysical Research Letters, Volume 33, L07202, doi:10.1029/2005GL025035.
Garvin, J.B., Sakimoto, S.E.H., Schnetzler, C., Frawley, J.J., (1999), Global geometric properties of martian impact craters: A preliminary assessment using Mars Orbiter Laser Altimeter (MOLA) topography, Proceedings of the 5th International Conference on Mars, Abstract 6163.
Garvin, J.B., Sakimoto, S.E.H., Frawley, J.J., Schnetzler, C. (2000), North Polar Region Craterforms on Mars: Geometric Characteristics from the Mars Orbiter Laser Altimeter, Icarus 144, 329-352.
Gendrin, A., et al. (2005), Sulfates in Martian Layered Terrains: The OMEGA/Mars Express View, Science, 307, 1587-1591.
Glotch, T. D., Rogers, D., Christensen, P.R. (2005), A Newly Discovered Hematite-Rich Unit in Aureum Chaos: Comparison of Hematite and Associated Units With Those in Aram Chaos., Lunar and Planetary Science, XXXVI, Abstract 2159.

Glotch, T.D., Christensen, P.R. (2005), Geologic and mineralogic mapping of Aram Chaos: Evidence for a water-rich history, Journal of Geophysical Research, 110, doi:10.1029/2004JE002389.
Grieve, R., Therriault, A. (2000), VREDEFORT, SUDBURY, CHICXULUB: Three of a Kind?, Annu. Rev. Earth Planet. Sci. 28, 305-38.
Gulick, V.C. (2001), Origin of the valley networks on Mars: a hydrological perspective, Geomorphology, 37, 241–268.
Gurnett, D.A., Kirchner, D.L., Huff, R.L., et al. (2005), Radar Soundings of the Ionosphere of Mars, Science, 310, 1929 - 1933.
Hanna, J. C., Phillips, R.J. (2005), Tectonic pressurization of aquifers in the formation of Mangala and Athabasca Valles, Mars, Journal of Geophysical Research, in press.
Haskin, L.A., et al. (2005), Water alteration of rocks and soils on Mars at the Spirit rover site in Gusev crater, Nature, 436, 66-69.
Harrison, K.P., Grimm, R.E. (2004), Tharsis recharge: A source of groundwater for Martian outflow channels, Geophysical Research Letters, 31, doi:10.1029/2004GL020502.
Hartmann, W.K. (2001), Martian seeps and their relation to youthful geothermal activity, Space Science Reviews, 96, 405-410.
Hartmann, W.K., Neukum, G. (2001), Cratering Chronology and the Evolution of Mars, Space Science Reviews, 96, 165-194.
Hartmann, W.K. (2005), Martian cratering 8: Isochron refinement and the chronology of Mars, Icarus, 174, 294–320.
Head, J.W., et al. (2001), Geological Processes and Evolution, Space Science Reviews, 96, 263-292.
Head, J.W., et al. (2005), Tropical to mid-latitude snow and ice accumulation, flow and glaciation on Mars, Nature, 434, 436-351.
Hoffman, N. (2000), White Mars: A New Model for Mars' Surface and Atmosphere Based on CO_2, Icarus, 146, 326–342.
Howard, A.D., Moore, J.M. (2004), Scarp-bounded benches in Gorgonum Chaos, Mars: Formed beneath an ice-covered lake? Geophysical Research Letters, 31, doi:10.1029/2003GL018925.
Jakosky, B.M., Phillips, R.J. (2001), Mars' volatile and climate history, Nature insight, 412, 237-244.
Jébrak, M. (1997), Hydrothermal breccias in vein-type ore deposits: A review of mechanics, morphology and size distribution, Ore Geology Reviews 12, 111-134.
Kim, J.R., et al. (2003), Impact crater detection on optical images and DEMs, ISPRS WG IV/9: Extraterrestrial Mapping Workshop: "Advances in Planetary Mapping 2003", Lunar and Planetary Institute, Houston, Texas, USA.
Kleinhans, M. G. (2005), Flow discharge and sediment transport models for estimating a minimum time scale of hydrological activity and channel and delta formation on Mars, Journal of Geophysical Research, in press.
Komatsu, G., et al. (2000), A chaotic terrain formation hypothesis: explosive outgas and outlow by dissociation of clathrate on Mars, Lunar and Planetary Science, XXXI, Abstract 1434.

Lanz, J. K., Jaumann, R. (2001), Possible volcanic constructs in Aram Chaos revealed by MOC and their impact on outflow channel genesis, Lunar and Planetary Science, XXXII, Abstract 1574.
Laskar, J., et al. (2002), Orbital forcing of the martian polar layered deposits, Nature, 419, 375-377.
Laskar, J., et al. (2004), Long term evolution and chaotic diffusion of the insolation quantities of Mars, Icarus, 170, 343–364.
Leovy, C. (2001), Weather and climate on Mars, Nature insight, 412, 245-249.
Levrard, B., et al. (2004), Recent ice-rich deposits formed at high latitudes on Mars by sublimation of unstable equatorial ice during low obliquity, Nature, 431, 1072-1075.
Lucchitta, B.K., McEwen, A.S., Clow, G.D., Geissler, P.E., Singer, R.B., Schultz, R.A., Squyres, S.W. (1992) in Mars, eds. Kieffer, H., Jakosky, B. M., Snyder, C. W., Matthews, M. S. (Univ. of Arizona Press, Tucson), pp. 453-492.
Magee, M., et al. (2003), Automated identification of martian craters using image processing. Lunar and Planetary Science XXXIV, Abstract 1756.
Malin, M.C., Carr, M.H., Danielson, G.E., Davies, M.E., Hartmann, W.K., Ingersoll, A.P., James, P.B., Masursky, H., McEwen, A.S., Soderblom, L.A., Thomas, P., Veverka, J., Caplinger, M.A., Ravine, M.A., Soulanille, T.A., Warren, J.L. (1998), Early Views of the Martian Surface from the Mars Orbiter Camera of Mars Global Surveyor, Science, 279, 1681-1685.
Malin, M.C., Edgett, K.S. (2000), Evidence for recent ground water seepage and surface runoff on Mars, Science, 288, 2330-2335.
Malin, M.C., et al. (2001), The Martian Prime Meridian -- Longitude "Zero", http://www.msss.com/mars_images/moc/01_31_01_releases/airy0/
Malin, M. C., Edgett, K.S. (2003), Evidence for Persistent Flow and Aqueous Sedimentation on Early Mars, Science, 302, 1931-1934.
Mangold, N., et al. (2000), Chronology of compressional deformation on Mars: evidence for a single and global origin, Planetary and Space Science, 48, 1201-1211.
Mangold, N., et al. (2004), Evidence for Precipitation on Mars from Dendritic Valleys in the Valles Marineris Area, Science, 305, 78-81.
Masson, P. L. (1991), The Martian Stratigraphy - Short Review and Perspectives, Space Science Reviews, 56, 9 -12.
Masson, P., et al. (2001), Geomorphologic evidence for liquid water, Space Science Reviews, 96, 333-364.
Matsumoto, N., et al. (2005), Automatic crater recognition on digital terrain model, Lunar and Planetary Science XXXVI, Abstract 1995.
Max, M. D., Clifford, S.M. (2001), Initiation of Martian Outflow Channels: Related to the Dissociation of Gas Hydrate? Geophysical Research Letters, 28, 1787-1790.
McEwen, A. S., et al. (1999), Voluminous volcanism on early Mars revealed in Valles Marineris, Nature, 397, 584-586.
Mitrofanov, I., et al. (2002), Maps of Subsurface Hydrogen from the High Energy Neutron Detector, Mars Odyssey, Science, 297, 78-81.
Montgomery, D. R., Gillespie, A. (2005), Formation of Martian outflow channels by catastrophic dewatering of evaporite deposits, Geology, 33, 625–628.
Mouginis-Mark, P. J. (1985), Volcano-Ground Ice Interactions in Elysium Planitia, Mars, Icarus, 64, 265-284.

Mouginis-Mark, P.J., et al. (2004), Geometry of Martian impact craters: First results from an interactive software package, Journal of Geophysical Research, 109, doi:10.1029/2003JE002147.
Murray, B.C., Malin, M.C. (1973), Polar wandering on Mars?, Science, 197, 997– 1000.
Murray, J.B., et al. (2005), Evidence from the Mars Express High Resolution Stereo Camera for a frozen sea close to Mars' equator, Nature, 434, 352-356.
Nelson, D.M., Greeley, R. (1999), Geology of Xanthe Terra outflow channels and the Mars Pathfinder landing site, Journal of Geophysical Research, 104, 8653-8669.
Neukum, G., et al. (2004), Recent and episodic volcanic and glacial activity on Mars revealed by the High Resolution Stereo Camera, Nature, 432, 971-979.
Neumann, G.A., et al. (2004), Crustal structure of Mars from gravity and topography, Journal of Geophysical Research, 109, doi:10.1029/2004JE002262.
Newsom, H.E. (2001), Central remnant craters on Mars – Localization of hydrothermal alteration at the edge of crater floors, Lunar and Planetary Science Conference XXXII, Abstract 1402.
Nimmo, F., Tanaka, K. (2005), Early Crustal Evolution of Mars, Annual Reviews of Earth and Planetary Sciences, 33, 133-194.
Nummedal, D., Prior, D.B. (1981), Generation of Martian Chaos and Channels by Debris Flows, Icarus, 45, 77-86.
Nyquist, L. E., et al. (2001), Ages and Geologic Histories of Martian Meteorites, Space Science Reviews, 96, 105 - 164.
Oberst, J., Roatsch, T., Giese, B., et al. (2004), The Mapping performance of the HRSC / SRC in Mars orbit, http://www.isprs.org/istanbul2004/comm4/papers/546.pdf.
Öhman, T., Aittola, M., Kostama, V-P., Raitala, J. (2005), The Preliminary Analysis of Polygonal Impact Craters within Greater Hellas Region, Mars, In: Impact Tectonics, Editors: Koeberl, C., Henkel, H., Springer-Verlag, 131-160.
Ori, G. G., Mosangini, C. (1998), Complex depositional systems in Hydraotes Chaos, Mars: An example of sedimentary process interactions in the Martian hydrological cycle, Journal of Geophysical Research, 103, 22713-22723.
Picardi, G., Plaut, J.J., Biccari, D., et al. (2005), Radar Soundings of the Subsurface of Mars, Science, 310, 1925-1928.
Phillips, R.J., et al. (2001), Ancient Geodynamics and Global-Scale Hydrology on Mars, Science, 291, 2587-2591.
Plesko, C., et al. (2003a), Automated development of feature extraction tools for planetary science image datasets, Lunar and Planetary Science XXXIV, Abstract 1758.
Plesko, C.S., et al. (2003b), Automated Feature Extraction and Hydrocode Modeling of Impact Related Structures on Mars: Preliminary Report, Sixth International Conference on Mars, Abstract 3227.
Poulet, F., et al. (2005), Phyllosilicates on Mars and implications for early martian climate, Nature, 438, doi:10.1038/nature04274.
Rodríguez, J. A. P., et al. (2005a), Control of impact crater fracture systems on subsurface hydrology, ground subsidence, and collapse, Mars, Journal of Geophysical Research, 110, doi:10.1029/2004JE002365.
Rodríguez, J.A.P. et al. (2005b), Outflow channel sources, reactivation, and chaos formation, Xanthe Terra, Mars, Icarus, 175, 36–57.

Rogers, D., Christensen, P.R. (2003), Age relationship of basaltic and andesitic surface compositions on Mars: Analysis of high-resolution TES observations of the northern hemisphere, Journal of Geophysical Research, 108, doi:10.1029/2002JE001913.

Rogers, A.D., Christensen, P.R., Bandfield, J.L., (2005), Compositional heterogeneity of the ancient Martian crust: Analysis of Ares Vallis bedrock with THEMIS and TES data, Journal of Geophysical Research, 110, E05010, doi:10.1029/2005JE002399.

Rossi, A.P., Neukum, G., Pondrelli, M., et al. (2007), The case for large-scale spring deposits on Mars: Light-Toned Deposits in crater bulges, Valles Marineris and Chaos, Lunar and Planetary Science Conference 38, in preparation.

Rotto, S., Tanaka, K.L. (1995), Geologic/geomorphologic map of the Chryse Planitia region of Mars, U.S. Geol. Surv. Misc. Inv. Serv. Map, I-2441.

Schultz, P. H., Schultz, R.A., Rogers, J. (1982), The Structure and Evolution of Ancient Impact Basins on Mars, Journal of Geophysical Research, 87, 9803-9820.

Scott, D.H., Tanaka, K.L., Greeley, R., and Guest, J.E. (1987), Geologic Maps of the Western Equatorial, Eastern Equatorial and Polar Regions of Mars, Maps. I-1802-A, B and C, Miscellaneous Investigation Series, 1986-1987, U.S. Geological Survey, Flagstaff.

Sharp, R.P. (1973), Mars: Fretted and chaotic terrains, Journal of Geophysical Research, 78, 4073-4083.

Smith, D.E., Sjogren, W.L., Tyler, G.L., Balmino, G., Lemoine, F.G., Konopliv, A.S. (1999), The Gravity Field of Mars: Results from Mars Global Surveyor, Science, 286, 94-97.

Solomon, C. S., et al. (2005), New Perspectives on Ancient Mars, Science, 307, 1214-1220.

Sprenke, K.F. (2004), Geodetic evidence for Polar Wander on Mars, Geological Society of America Abstracts with Programs, Vol. 36, No. 4, p. 79, Abstract 72455.

Sprenke, K. F., Baker, L.L., Williams, A.F. (2005), Polar wander on Mars: Evidence in the geoid, Icarus, 175, 486–489.

Spudis, P.D. (1994), The large impact process inferred from the geology of lunar multiring basins. In: Large Meteorite Impacts and Planetary Evolution, Special Paper 293, Edited by Dressler, B.O., Grieve, R.A.F., Sharpton, V.L., Geological Society of America, 1-10.

Squyres S.W., et al. (2004), The Opportunity Rover's Athena Science Investigation at Meridiani Planum, Mars, Science, 306, 1698-1703.

Squyres, S. W., Knoll, A.H. (2005), Sedimentary rocks at Meridiani Planum: Origin, diagenesis, and implications for life on Mars, Icarus, In press.

Stepinski, T. F., et al. (2004), Martian geomorphology from fractal analysis of drainage networks, Journal of Geophysical Research, 109, doi:10.1029/2003JE002098.

Stevenson, D. J. (2001), Mars' core and magnetism, Nature insight, 412, 214-219.

Strom, R. G., et al. (2005), The Origin of Planetary Impactors in the Inner Solar System, Science, 309, 1847-1850.

Tanaka, K.L. (1986), The Stratigraphy of Mars, (Lunar and Planetary Institute, NASA, AAS, et al., Lunar and Planetary Science Conference, 17th, Houston, TX, Mar. 17-21, 1986) Journal of Geophysical Research, vol. 91, p. E139-E158.

Tanaka, K. L., Scott, D. H., Greeley, R. (1992) in Mars, eds. Kieffer, H., Jakosky, B. M., Snyder, C. W., Matthews, M. S. (Univ. of Arizona Press, Tucson), pp. 345-382.

Tanaka, K.L. (1997), Sedimentary history and mass flow structures of Chryse and Acidalia Planitia, Mars, Journal of Geophysical Research, 102, 4131-4149.
Tanaka, K. L., et al. (2003), Resurfacing history of the northern plains of Mars based on geologic mapping of Mars Global Surveyor data, Journal of Geophysical Research, 108, doi:10.1029/2002JE001908.
Tanaka, K.L., Skinner Jr., J.A., Hare, T.M. (2005), Geologic Map of the Northern Plains of Mars, Scientific Investigations Map 2888, U.S. Geological Survey, Flagstaff.
Van der Meer, F.D., De Jong, S.M. (2003), Imaging Spectrometry: Basic Principles and Prospective Applications, Kluwer Academic Publishers.
Van der Meer, F.D., De Jong, S.M. (2004), Remote Sensing Image Analysis: Including the Spatial Domain, Kluwer Academic Publishers.
Van Thienen, P., Vlaar, N.J., Van den Berg, A.P. (2005), Assessment of the cooling capacity of plate tectonics and flood volcanism in the evolution of Earth, Mars and Venus, Physics of the Earth and Planetary Interiors, 150, 287–315.
Wang, C., Manga, M., Wong, A. (2005), Floods on Mars released from groundwater by impact, Icarus, 175, 551–555.
Williams, D.R. (2004), Mars Fact Sheet, NASA, http://nssdc.gsfc.nasa.gov/planetary/factsheet/marsfact.html.
Withers, P., Neumann, G.A. (2001), Enigmatic northern plains of Mars, Nature, 410, 651.
Zhang, X., Jeffrey, R.G., Thiercelin, M. (2006), Deflection and propagation of fluid-driven fractures at frictional bedding interfaces: A numerical investigation, Journal of Structural Geology, in press.
Zuber, M.T., et al. (2000), Internal Structure and Early Thermal Evolution of Mars from Mars Global Surveyor Topography and Gravity, Science, 287, 1788-1793.
Zuber, M.T. (2001), The crust and mantle of Mars, Nature insight, 412, 220-227.

Internet References

USGS Astrogeology: Gazetteer of Planetary Nomenclature. Mars System Nomenclature. http://planetarynames.wr.usgs.gov/jsp/SystemSearch2.jsp?System=Mars

Tables

Epoch	N(1)	N(2)	N(5)	N(16)
Late Amazonian	<160	<40		
Middle Amazonian	160-600	40-150	<25	
Early Amazonian	600-1600	150-400	25-67	
Late Hesperian	1600-3000	400-750	67-125	
Early Hesperian	3000-4800	750-1200	125-200	<25
Late Noachian			200-400	25-100
Middle Noachian			>400	100-200
Early Noachian				>200

Table 2.1. Crater counts for Martian epochs, after Tanaka (1986). N(Diameter) is the crater density, the number of craters, of diameter D or larger, per area times 10^6 km^2. N(1) is only possible since MOC and THEMIS.

Epoch	Type location
Upper Amazonian	Flood plains material, southern Elysium Planitia
Middle Amazonian	Lava flows, Amazonis Planitia
Lower Amazonian	Smooth plains material, Acidalia Planitia
Upper Hesperian	Complex plains material, Vasistas Borealis
Lower Hesperian	Ridged plains material, Hesperia Planum
Upper Noachian	Intercrater plains material, east of Argyre Planitia
Middle Noachian	Cratered terrain material, west of Hellas Planitia
Lower Noachian	Basement material, Charitum and Nereidum Montes

Table 2.2. Epoch and type locations for Mars (Tanaka, 1986).

Reference	Location	Trigger	Event and fluid	Prediction
Sharp (1973)	All chaotic terrain	- Dissolution of rock material - Deterioration of ground ice - Removal of magma - Combination of last 2.	- Subsidence due to removal of material. - Deterioration of ground ice could cause escarpment recession and development and breakup of blocks.	- Soluble rocks and solvent - What caused deterioration? - Volcanism
Carr (1979)	All chaotic terrain	- Pore pressure reaching the lithostatic pressure, caused by (1) an artesian aquifer system under high hydrostatic head or (2) growth of the permafrost base due to colder temperatures. - Impact	Catastrophic: Instability of confined aquifer below permafrost layer leading to uplift and fracturing of overlying terrain and eventually breakout and outflow of water.	- Uplift and fracturing prior to chaotic terrain formation should be visible in surrounding terrain. - Chaotic terrain in low lying regions. - Groundwater system extending from chaotic terrain to higher ground causing high hydrostatic head.
Nummedal and Prior (1981) Referring to Carr (1979)	Circum-Chryse	- Seismic event causing liquefaction. - Pore pressure reaching the lithostatic pressure in confined aquifer (Carr, 1979)	Catastrophic: - Subsurface material fails - Collapse due to removal of solid material and/or water. - Slumping of material - Fracturing of surrounding area due to collapse and slumping	- Impacts and volcanism (seismic) - Gradient in topography (failure) - High water content of sediment - See Carr (1979)
Mouginis-Mark (1985) and Chapman and Tanaka (2002)	Elysium Planitia and Circum-Chryse	Rise of magmatic material	Catastrophic: Interaction between layer of subsurface volatiles and volcanism (phreatomagmatic activity).	- Subice volcanism morphology (which was not identified in Elysium, except pseudo craters).
(Figure 4 from) Cabrol et al. (1997) Referring to Carr (1979)	Shalbatana Vallis and Ma'adim Vallis.	Rise of magmatic material through cylindrical lava chimney.	Catastrophic: Rising of magma breaks through cryosphere. Release of liquid water and water vapor from aquifer (Carr, 1979).	- See Carr (1979) - Subice volcanism morphology - Round chaos depressions. - Chaos formation, spatially controlled by weakpoints where radial and

				concentric Tharsis associated faults cross. - Dike intrusion
(Figure 2 from) Komatsu et al. (2000)	Chaotic terrain related to outflow channels	Magmatic heating	Catastrophic: 1. Melting of ice and dissociation of CO_2 and/or methane clathrate. 2. Liquefaction and fluidization. 3. Explosion due to high gas pressure. 4. Outflow of water-sediment mix	- Volcanism - Similarity to seabed pockmarks in continental shelves formed by dissociation of clathrate.
Max and Clifford (2001) Referring to Carr (1979)	Chaotic terrain related to outflow channels	- Global or regional warming - Subsurface igneous activity - Local deposition or erosion - Impacts - Tectonic activity	Catastrophic: Dissociation of methane hydrate in subpermafrost aquifer (Carr, 1979) resulting in explosive eruption of water and methane gas.	- See Carr (1979) - Formation of methane hydrate. - Methane in atmosphere? - Methane indication for past or present life? - Similarity to expulsion and collapse features on Earth, formed by methane hydrate dissociation.
Rodríguez et al. (2005a,b)	Circum-Chryse	High heat flow	Catastrophic and non catastrophic: subsidence due to removal of water from caverns	- Caverns controlled by impact fracture system - Volcanism
Montgomery and Gillespie (2005)	Outflows emanating from Valles Marineris.	Magmatic heating due to Tharsis Bulge.	Catastrophic: Dewatering of evaporite deposits.	- Volcanism - Presence of large amounts of evaporite deposits (such as possibly the Internally Layered Deposits on the floors of Valles Marineris chasmata).
Wang et al. (2005)	Chaotic terrain related to outflow channels	- Impact larger then 100 km in diameter. Favorably occurring during Late Noachian until Early Hesperian when cryosphere was thinner.	Catastrophic: Liquefaction of aquifers on a global scale, resulting in catastrophic release of ground water	- Thinner cryosphere - No necessary spatial correlation between craters and chaotic terrain - Liquefaction morphology (evidence for lateral spreading and collapse) - High fluid content of material
Coleman (2005)	Catastrophic outflow from	Catastrophic outflow from Aromatum	The carving by the water flow lowered the overpressure triggering the formation	- Chaotic terrain occurring within outflow channel.

	Aromatum Chaos	Chaos carved into the cryosphere, forming Ravi Vallis	of secondary chaotic terrain downstream.	- Magmatic heating not necessary to explain the secondary chaotic terrain.

Table 2.3. Chaotic terrain formation hypotheses and predictions.

Region	Interpretation
A. Central hummocky zone.	Uplifted basement controlled by maximum projectile penetration.
B. Peripheral unstable zone.	Geothermal melting of ice saturated deposits above ring intrusions.
C. Stable, fractured zone.	Uplifted basement.
D. Moat of chaotic terrain.	Geothermal melting above ring intrusions.
E. Stable zone.	Ejecta-covered megaterrace.
F. Ring arrangement of chaotic terrains.	Intrusions localized along outer ring fracture.
G. Smooth-floored canyons.	Eroded ejecta facies.
H. Outer concentric arrangement of chaotic terrains, rilles.	Poorly expressed outer fracture.

Table 3.1. Explanation of zones A to H of Figure 3.11, after Schultz et al. (1982).

Orbit #	Available on the PSA?
h0103_0009	Yes
h0401_0001	Yes
h0456_0000	Yes
h0890_0000	Yes
h0901_0000	Yes
h0912_0000	Yes
h0923_0000	Yes
h0934_0000	Yes
h0945_0000	Yes
h0967_0000	Yes
h1000_0000	Yes
h1011_0000	Yes
h1022_0000	Yes
h1055_0000	Yes
h1337_0009	Yes
h1925_0000	No
h1936_0000	No
h1947_0001	No
h2196_0001	No

Table 4.1. HRSC images used for mapping Aram Chaos.

Table 5.1

Unit name	Type*	Description
Highland Terrain (HT)	G	Highland Terrain is the largest mapped unit of my research area. It has been degraded by large-scale impacts. Wrinkle ridges (Figure 5.5.10) and relatively shallow fractures occur on its surface. It is at least 1.5 to 2 km thick (the difference between the mean HT elevation and the Chaotic Terrain Floor elevation). Small-scale variation of surface morphology has been ignored (see Observation 13). 100-200 m scale layering of HT is visible in the Ares Vallis main channel wall (Figure 5.1.13). Fractured Highland Terrain occurs near the Chaotic Terrain. The fractures are 10-100 km scale. They are also visible in the MOLA elevation data with fracture valley depths around 250 – 750m. Mesas (flat topped hills) of Highland Terrain occur within the Chaotic Terrain. Some mesas can reach the elevation of the lower elevated Chaotic Terrain Floor and are therefore interpreted to be collapse/subsidence features. **Type location***:* Figure 5.1.10a and b
Chaotic Terrain (CT)	S/M	Chaotic Terrain (CT) is a degraded lateral unit of HT. The CT unit consists of two types, varying in the amount of degradation: *Intermediate Chaotic Terrain (ICT):* A type of Chaotic Terrain, intermediate in degradation between Fractured Highland Terrain and Chaotic Terrain Floor. The ICT consists of either sharp or rounded km-scale hills (Figure 5.1.14) and shows the gradual loss of coherence due to degradation by fracturing and chaotization. Highly chaotisized areas do not clearly show fractures. Mapping difficulties: It can grade into Small-scale Fractured and Chaotic Terrain (SFCT). **Type location:** Figure 5.1.10a and c *Chaotic Terrain Floor (CTF):* CTF is relatively low in elevation. It consists of knobs and rounded hills. The low elevation of the CTF is interpreted to be due to subsidence and erosion. **Type location:** Figure 5.1.10a and d
Lower Aram Chaos Formation (LACF)	S/M/G?	The Lower Aram Chaos Formation is interpreted to be a distinct unit deposited on top of the HT within the inner ring of Aram Chaos. It consists of three lateral units: *Fractured:* This unit exhibits a distinct 'glossy' morphology visible on THEMIS VIS. It is cross-cut by, compared to the HT fractures, relatively small-scale fractures (1-2 km scale). Some fractures have raised rims and some show small thrusts at the base of the rim (see Observation 30, Figure 5.2.31). Some HT fractures can be followed within the LACF. The relatively small-scale fracture pattern is either caused by the properties of the LACF material with larger-scale HT fractures underneath or due to a smaller-scale fracturization of the HT underlying the LACF. **Type location:** Figure 5.1.10a and e *Broken:* This part of the LACF is highly fractured and broken up considerably, forming ~1 km scale 100-200m high irregular mesas. It always occurs at the boundary of the Fractured Highland Terrain (see Figure 5.1.5, the Aram Chaos Geological Map). The fractures could penetrate to the Fractured Highland Terrain underneath.

		Type location: Figure 5.1.10a and f *Smooth:* Mapped as the non-fractured part of the LACF. It consists of meter scale layering and is observed to be a drape (Observation 27). **Type location:** Figure 5.1.10a and g
Intermediate Aram Chaos Formation (IACF)	G/M	The Intermediate Aram Chaos Formation has a rugged morphology with at some parts 1 km scale 'flow features' on its surface (see type location). The flow features could be wind generated (they are oriented in the direction of the mean wind direction) but could also be resurfaced fluid flow features. Windows of underlying Lower Aram Chaos Formation occur within the IACF. The IACF is at maximum ~250 m thick (see Figure 5.3.1, Cross Sections I and II) and consists of meter scale layering. The 'flow features' can either be caused by wind erosion (they are parallel to the general wind direction (Figure 5.5.8)) or they could be caused by water erosion. **Type location:** Figure 5.1.10a and h
Upper Aram Chaos Formation (UACF)	G/M	Mapped as the upper part of the ACF. It consists of a ~10-100 m light toned cap material, which is relatively strong, with dark less strong material underneath. The cap material exhibits a specific 'icing' texture (Figure 5.1.15) and forms very sharp arcuate 'razor blade-like' escarpments (see Figure 5.1.5, the Aram Chaos Geological Map). In the W the cap overlies the LACF, in the S the cap overlies the Fractured HT. The darker, softer material of the UACF underneath the cap thickens towards the NW (see Figure 5.3.1, Cross Sections I and II). The unit is at maximum around ~300 m thick. Wind eroded lineations occur in the North (Figure 5.1.16). **Type location:** Figure 5.1.10a and i
Aram Ares Channel Deposits (AACD)	G/M	The Aram Ares Channel Deposits has a distinct morphology of lineations and small elongated hills. It is observed to cap elongated streamlined Highland Terrain mesas (see Observation 25 and Figure 5.2.25c). The Aram Chaos channel incised the AACD and 100 meter scale layering can be observed in the channel wall, which is 1 km high (see Observation 25 and Figure 5.2.25d). **Type location:** Figure 5.1.10a and j
Small-scale Fractured and Chaotic Terrain (SFCT)	S/M	SFCT is fractured terrain mostly occurring in (flooded) highland terrain. It doesn't exhibit the same elevation variation between HT and CTF as the larger scale chaotic terrain. It occurs in patches consisting of 100-500 m high mesas and hills. The smaller mesa height implies the fractures are also less deep rooted as HT and CT fractures. **Type location:** Figure 5.1.10a and k
Light Toned Channel Deposits (LTCD)	G/M	Deposits within the Ares Vallis outflow channel system showing a high thermal inertia in THEMIS IR night images. At one location the unit has been eroded suggesting a thickness of 200 – 300 m. **Type location:** Figure 5.1.10a and l
Small-scale Hills Terrain (SHT)	M	SHT is defined as a surface with ~1 km scale hills (see Figure 5.1.8 for the mapped occurrences). The hills occur on HT (mesas). The same scale hills also occur within the Intermediate Chaotic Terrain and Chaotic Terrain Floor units. It is interpreted to be formed by a secondary process, either prior to or post fracturing and chaotization. Difficulty: distinction between small hills in Chaotic Terrain and SHT. **Type location:** Figure 5.1.10a and m
Aureum Chaos Deposits (ACD)	G/M	These deposits occur in Aureum Chaos. Most outcrops exhibit the same sharp arcuate escarpments (at maximum ~ 300 m thick) as the UACF, but of a smaller scale. The top surface exhibits patches of 'icing'

		texture material (Figure 5.1.17c and 5.1.18) also observed in the Upper ACF (Figure 5.1.15). Laterally a variation in brightness can be observed. The two brightest outcrops are also relatively thick (~600 m) and do not exhibit the 'icing' texture (Figure 5.1.17a and b). One of these deposits exhibits flow morphology (Figure 5.1.17b). **Type location:** Figure 5.1.10a and n
Iani Chaos Deposits (ICD)	G/M	These deposits occur in Iani Chaos. Five distinct morphological types of deposits can be distinguished: *Iani Chaos Deposit type 1:* This deposit consists of multiple 10 meter scale layers and is oriented parallel to the Ares Vallis outflow. Flow morphology is visible oriented parallel to the Ares Vallis outflow (see type location). It is observed to be at maximum approximately 500 m thick. **Type location:** Figure 5.1.10a and o. The smaller deposit in the upper left of the image is of type 2. *Iani Chaos Deposit type 2:* This deposit has a smooth curving relief. The deposit has linear grooves and linear dark dune deposits on its surface which are approximately parallel to the mean wind direction (Figure 5.5.8). Flow morphology can be observed (Figure 5.1.19). The occurrence of windows of underlying CTF mesas suggest the material was deposited after the formation of the CTF. It is interpreted to have been eroded by a flow after deposition. Subsequently wind erosion formed the linear grooves. **Type location:** Figure 5.1.10a and p *Iani Chaos Deposit type 3:* This deposit looks the same morphologically as the E boundary of the smooth LACF (Figure 5.1.20). It is relatively dark but patches of bright material occur on its surface. It consists of 10 meter scale layering. **Type location:** Figure 5.1.10a and q *Iani Chaos Deposit type 4:* This deposit is very bright and consist of 100 meter scale layering, which is observed to be at an angle (see 9 in Figure 5.4.2). The layer morphology is distinct, with linear grooves oriented NE. It is superpositioned on top of the type 3 deposit. The linear grooves are not aligned with the general wind direction, however wind directions of this orientation have been mapped (Figure 5.5.8). **Type location:** Figure 5.1.10a and r *Iani Chaos Deposit type 5:* This deposit is exhibits the same 'icing' texture as the UACF (Figure 5.1.21 and 5.1.15). **Type location:** Figure 5.1.10a and s
Outflow Channel Terrain (OCT)	M	Outflow Channel Terrain is a geomorphological unit which underwent flooding and channelization. The channels have escarpments on each side. The channel floor consists of linear ridges aligned in the paleoflow direction. The channel terrain consists of multiple terraces, suggesting multiple outflow events. The source of the channels is Chaotic Terrain (e.g. Hydaspis, Iani, Aureum and Aram Chaos). Multiple stages of outflow have been observed (Observation 1) **Type location:** Figure 5.1.10a and t

Flooded Highland Terrain (FHT)	M	Flooded terrain is a morphological unit consisting of terrain similar to Highland Terrain (no distinct boundary) but with a lower elevation (decreasing towards the OCT), a flow morphology consisting of linear ridges, tear-shaped islands and the occurrence of Small-scale Fractured and Chaotic Terrain. **Type location:** Figure 5.1.10a and u
Rounded Chaotic and Highland Terrain (RCHT)	M	This unit consists of rounded hills and mesas and has only been observed in Aram Chaos, near the Aram Chaos channel linking Aram Chaos with Ares Vallis. The rounded hills and mesas occur in Highland Terrain and Intermediate Chaotic Terrain. The streamlined HT mesas occurring in the Aram Chaos channel (Figure 5.2.25c) are also mapped as RCHT. The rounded morphology suggests fluid flow. **Type location:** Figure 5.1.10a and v
* Means of definition: S = Structural geological, M = Geomorphological, G = Geological (stratigraphic).		

Table 5.1. Unit definitions.

Table 5.2

#	Boundary between:	Description
1	HT – ICT – CTF	The Highland Terrain grades into Chaotic Terrain through the ICT and the CTF (Figure 5.1.22) in a general decrease of elevation: 1. HT becomes more and more fractured. 2. Intense fracturing causes Highland Terrain mesas to form. 3. The mesas degrade and become rounded or sharp hills. 4. The hills become smaller and less high. 5. The CTF consists of small hills. It is lowest in elevation and in Hydaspis Chaos and Aureum Chaos it grades into outflow channels. The ICT and CTF differ from the HT geologically because the chaotization resurfaced older material. However no clear layering has been observed so stratigraphically the base of the HT is unknown. Therefore the ICT and CTF are considered HT material which have undergone chaotization. This involved intense fracturing (e.g. brecciation) and erosion. The mapping of the ICT and CTF has not been on geological (stratigraphical) but on structural geological and morphological grounds. The minimum stratigraphical thickness of the HT is the difference between the mean HT elevation and the mean CTF elevation (1.5 to 2 km).
2	HT – (broken LACF) – fractured LACF	Mesas of Highland Terrain occur within the LACF. One of the mesas has a ~350 m high fractured LACF mesa on top (see Observation 26 and Figure 5.2.27). Although the fractured LACF and HT are distinct units, no clear stratigraphical relationship was observed at their lateral boundaries. The boundary between the HT and the fractured LACF is gradual and either consists of 1) the broken LACF (see Figure 5.1.5, the Aram Chaos Geological Map) or 2) a gradual transition (Figure 5.1.23). The boundary could be a thinning (dying out) of the LACF material towards the HT. Later fracturing and chaotization formed the current broken up and fractured morphology.

3	Fractured LACF – Smooth LACF	The smooth LACF principally occurs in the E part of Aram Chaos. The fractured LACF mainly occurs in the W, although fractured LACF windows occur within the smooth LACF (Figure 5.1.24 and 5.1.20). This lateral difference in fracturing can be explained by 1) localized subsidence of underlying HT, 2) localized upward movement (f.e. by water release), 3) the smooth LACF is a relatively thin layer on top of the fractured LACF or 4) a combination. No clear stratigraphical relations have been observed to exclude one or more of the explanations. If however the fractured LACF became fractured during a regional event (or localized to the Aram Chaos crater) the third option would be the most logical, whereas it would be unlogical that only the fractured LACF fractured during a deformation event. The smooth LACF is still mapped as a lateral unit of the LACF because it is observed to be deposited on top of the HT/CT and underlying the IACF.
4	Smooth LACF – HT/CT/RCHT	The smooth LACF is interpreted to be draped over underlying HT or CT (see Observation 27 and Figure 5.2.28). The smooth LACF gradually thins towards the boundary with the HT and/or CT or it ends in a sharp escarpment (Figure 5.1.20). The Smooth ACF is observed to overlie RCHT (Figure 5.1.20). This would indicate that the outflow which formed the rounded mesas occurred prior to the deposition of the ACF.
5	HT/CT/RCHT - AACD	The AACD is observed to cap elongated streamlined HT mesas (see Observation 25 and Figure 5.2.25c). The streamlined HT mesas could have formed during the erosional event(s) which eroded the ACCD and formed the channel, making the AACD older then these events. The streamlined HT mesas could not have formed prior to the ACCD deposition. Because this would indicate the channel formed prior to the ACCD terraces it cuts into.
6	AACD – smooth LACF	At one location the AACD seems to grade into the LACF (Figure 5.2.25e). However the smooth LACF could also thin and die out gradually towards the AACD.
7	HT – FHT – OCT	Highland Terrain and Outflow Channel Terrain are either bounded by a channel escarpment or via the Flooded Highland Terrain. The FHT gradually lowers in elevation towards the OCT. The FHT has not been mapped as a clearly bounded polygon, but the area between the clear channel outline and the unclear channel outline (the farthest extent of the channel) on the map is an indicator of FHT. The region N, NE and E of Ares Vallis exhibits flow morphology, small channels and Small-scale Fractured and Chaotic Terrain. Therefore it is interpreted to be FHT. The OCT has not been mapped as a clearly bounded polygon, but the channel outline on the map is an indicator of OCT.
8	CT – SFCT	In Iani Chaos the Chaotic Terrain grades into the Small-scale Fractured and Chaotic Terrain.
9	ACD – CT	The ACD are thick deposits on top of the CT in Aureum Chaos, forming distinct hills with escarpments.
10	ICD – CT	Types 1, 2, 4 are distinct deposits which are clearly superpositioned on top of the CT. Types 3 and 5 do not show a clear boundary and probably thin out gradually.

Table 5.2. Boundary descriptions.

Name	Definition
Chaotization	The process(es) which formed the chaotic terrain: the degradation of HT mesas from fractured HT, via ICT to CTF. The chaotization is a younger event than the deposition of the HT material, but it excavates older material. The chaotization is interpreted to have involved intense fracturing (e.g. brecciation). Breccia is a rock so fractured it has lost coherence. The release of water through the fractures was most likely an explosive event causing destruction of the HT.
Fractures	Linear features visible in image and elevation data (MOC, THEMIS, HRSC, MOLA). Elevation data shows they form a linear valley. The width and depth of this valley says something about the size of the fractures.
Faults	These are fractures with interpreted movement, such as the ring faults of Aram Chaos. An example is a fracture dividing two HT mesas, with one mesa considerably higher in elevation then the other. This is interpreted as subsidence, making the fracture a normal fault.

Table 5.3. Definitions.

Type	B1	B2	B3
ACD af 1	1.1411	1.1555	1.1842
ACD af 2	1.3855	1.4143	1.4430
ACD lsf	1.1124	1.3855	1.5291
ICD af 1	1.2849	1.3424	1.3999
ICD af 2	1.3999	1.4143	1.4430
ICD lsf	1.2130	1.5721	1.7007
Lower ACF af 1	1.3136	1.3424	1.3999
Lower ACF af 2	1.3999	1.4286	1.4861
Lower ACF lsf	1.2561	1.6293	1.8991
Intermediate ACF af 1	1.3136	1.3424	1.3999
Intermediate ACF af 2	1.3999	1.4286	1.4861
Intermediate ACF lsf	1.2273	1.6293	1.9132
Upper ACF af 1	1.2849	1.3424	1.3999
Upper ACF af 2	1.3999	1.4286	1.4430
Upper ACF lsf	1.1986	1.3999	1.7007

Table 5.4. The band wavelengths used for the band ratios (see Figures 5.1.25 to 5.1.29). The absorption feature (af) band ratios were calculated using (B1 + B3)/2*B2, the large spectral feature (lsf) band ratio was calculated using 2*B2/(B1 + B3).

Figures

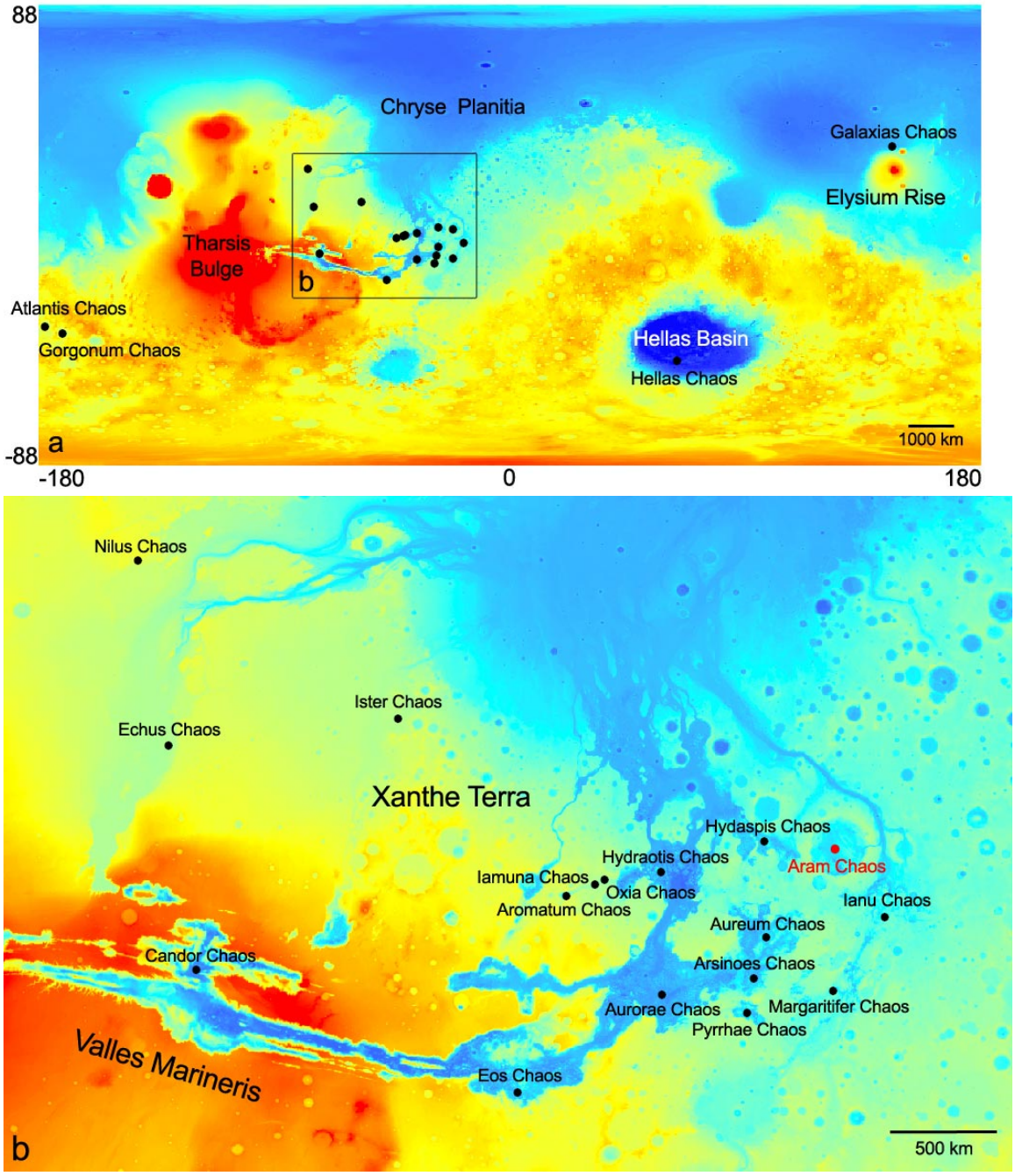

Figure 2.1. Chaotic terrains on Mars (approved by the International Astronomical Union). **a.** Global equirectangular projected 128 pixel/degree MOLA elevation map spanning latitude 88N to 88S and Longitude 180W to 180E. Red is high elevation (maximum: 21249 m) and blue is low elevation (minimum: -8408 m). **b.** Chaotic terrains in the Xanthe Terra region of Mars, including Aram Chaos.

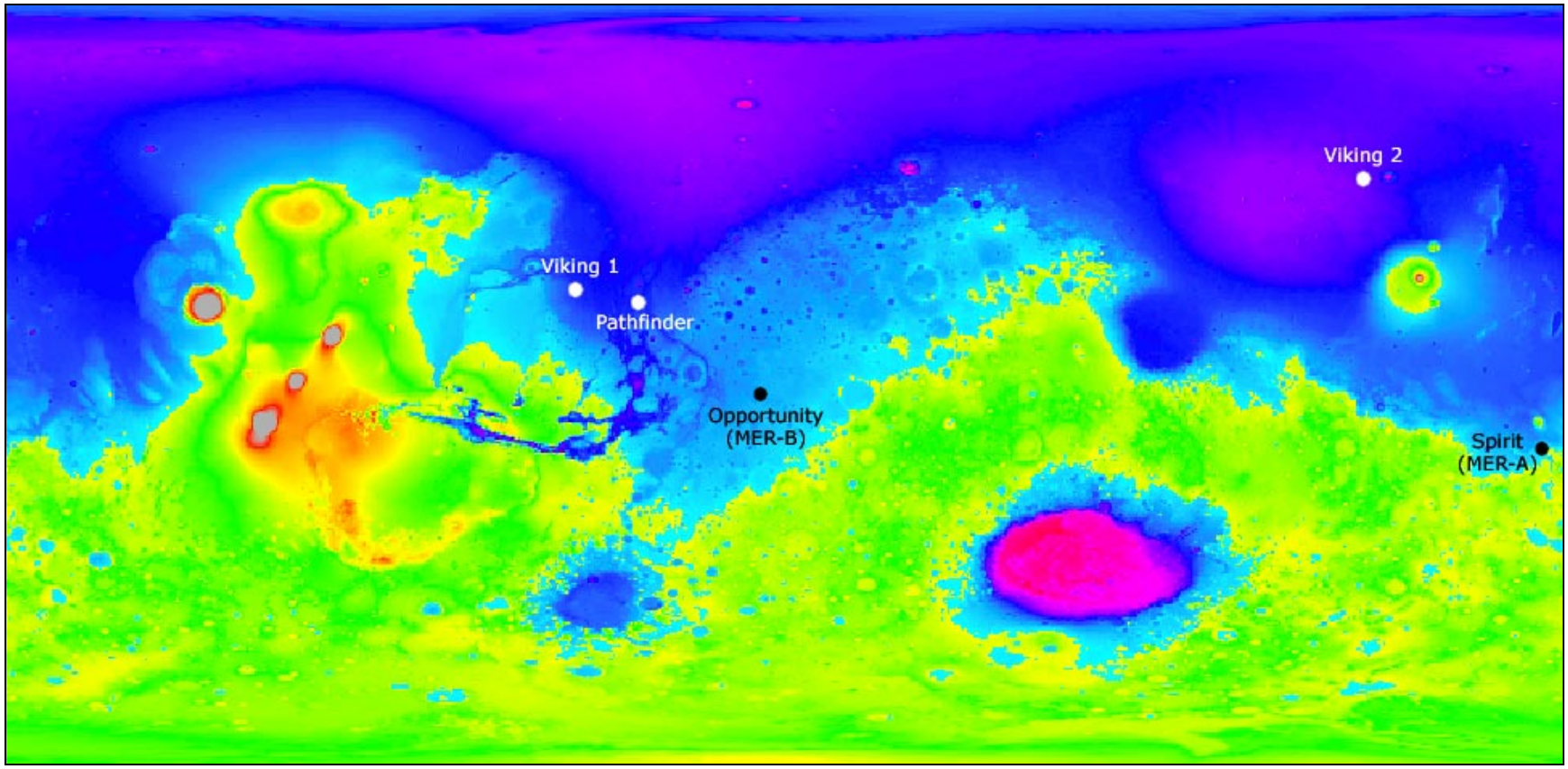

Figure 2.2. The five landing sites of NASA landers.

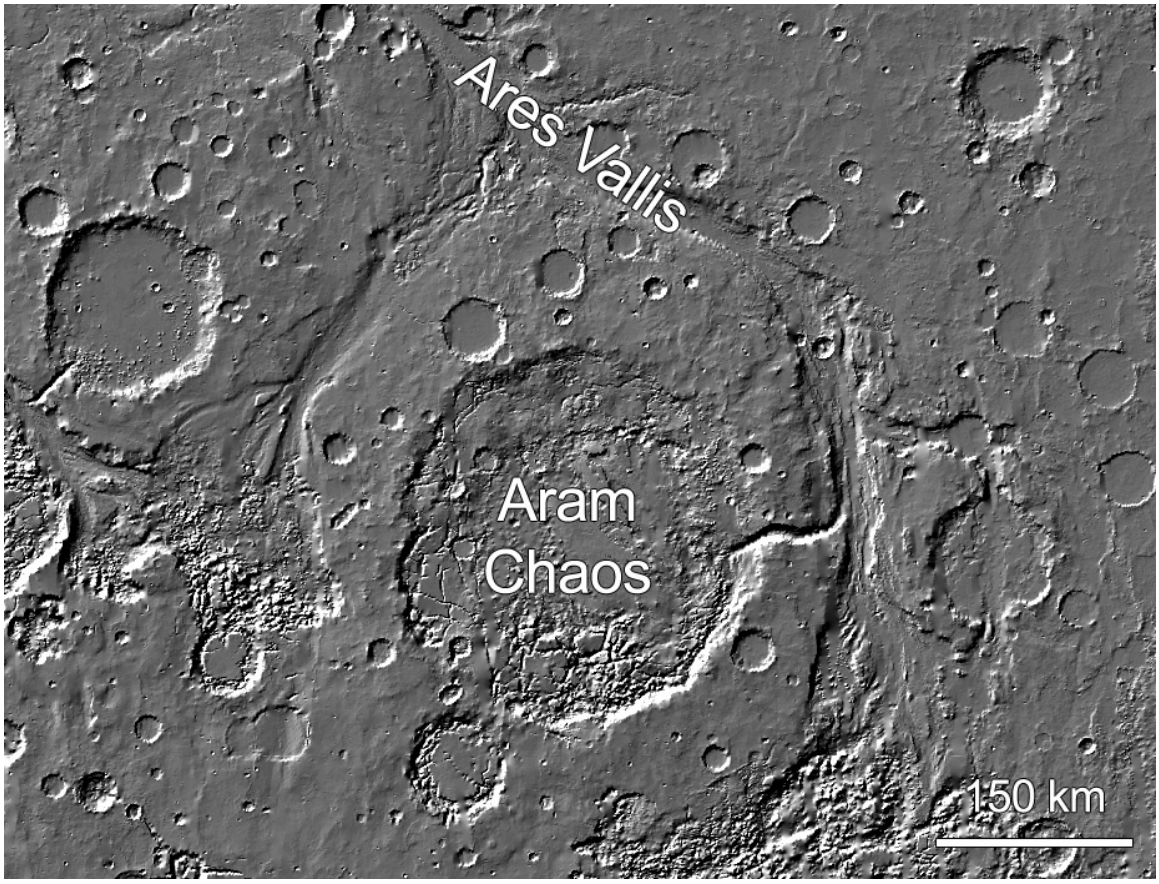

Figure 2.3. MOLA shaded relief image of Aram Chaos and Ares Vallis.

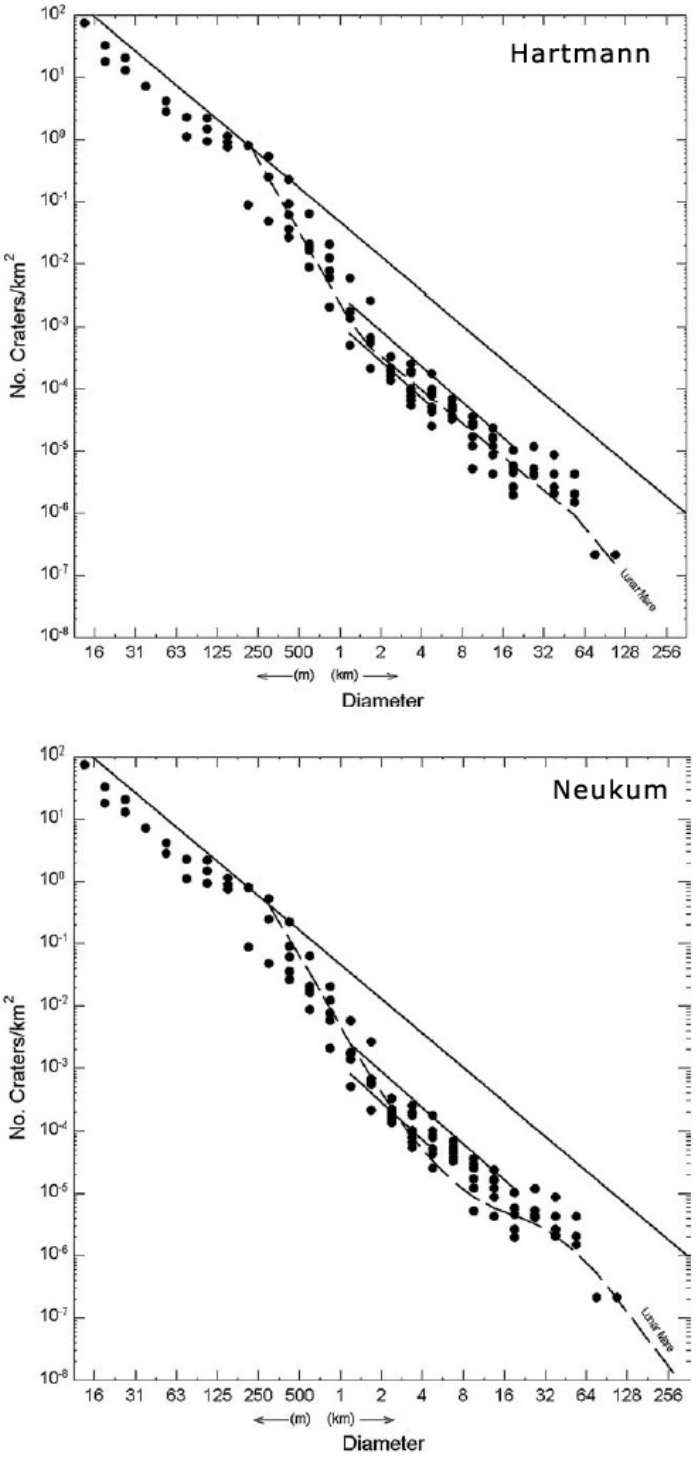

Figure 2.4. Lunar mare crater counts of specific diameters (the black dots) by Hartmann (upper diagram) and Neukum (lower diagram). Hartmann used a powerlaw fit and Neukum a polynomial fit as a production function for cratering. The upper solid line on both diagrams is the saturation equilibrium curve, an empirical upper limit for crater density.

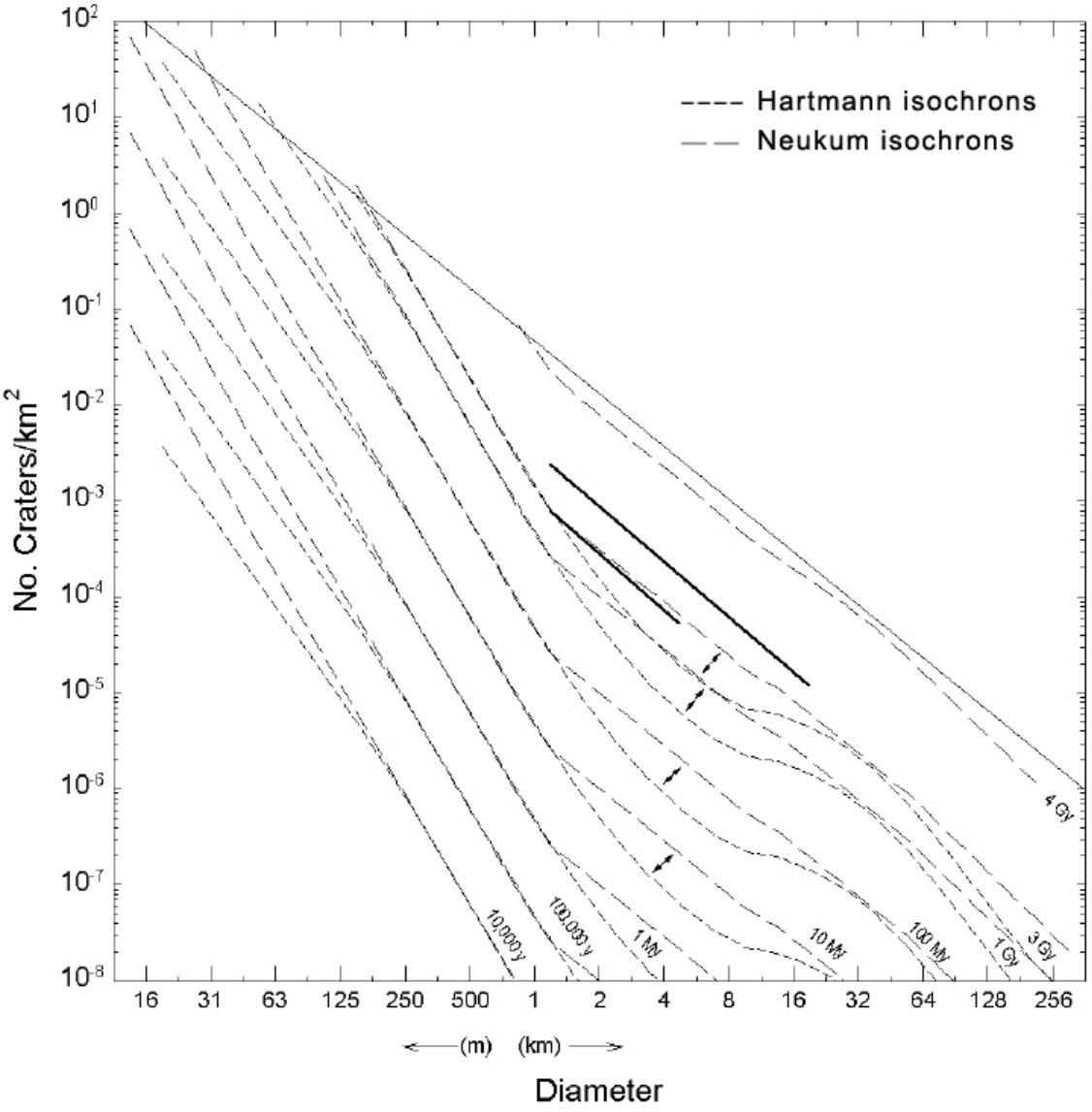

Figure 2.5. A typical isochron diagram redrawn after Hartmann and Neukum (2001). Each set consists of an isochron derived after the Hartmann and Neukum production function. The upper solid line is the saturation equilibrium curve, an empirical upper limit for crater density.

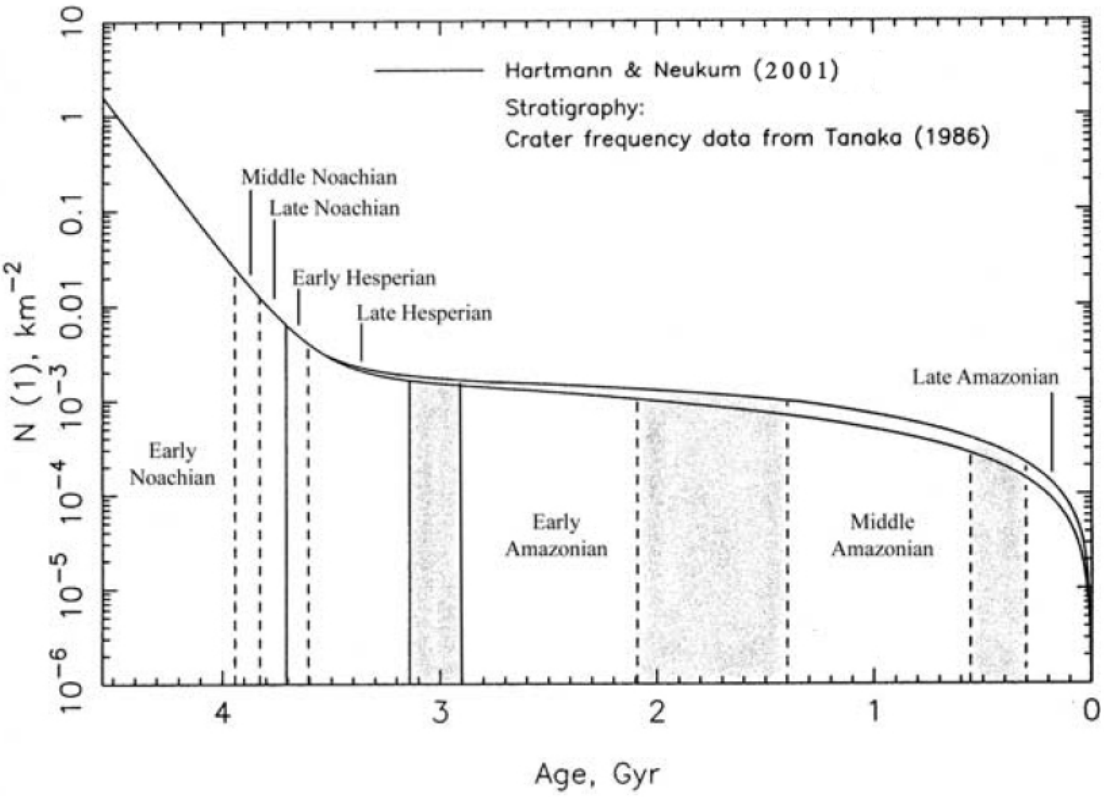

Figure 2.6. A Mars cratering chronology model redrawn after Hartmann and Neukum (2001). The solid curves show the cratering rate in time for Mars.

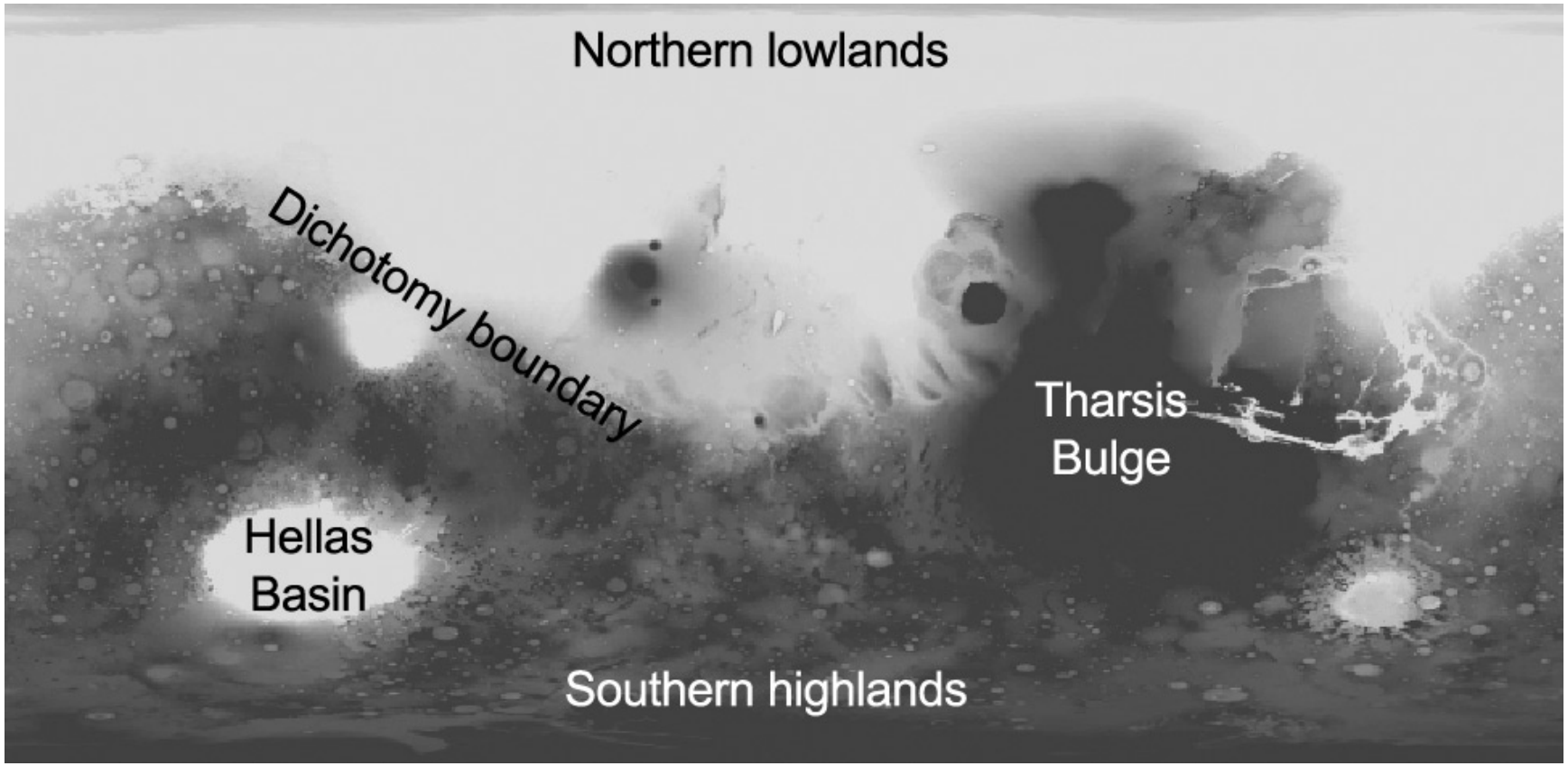

Figure 2.7. Large scale topography of Mars. Global equirectangular projected 128 pixel/degree MOLA elevation map spanning latitude 88N to 88S and Longitude 180W to 180E. Black is high elevation (maximum: 21249 m) and white is low elevation (minimum: -8408 m).

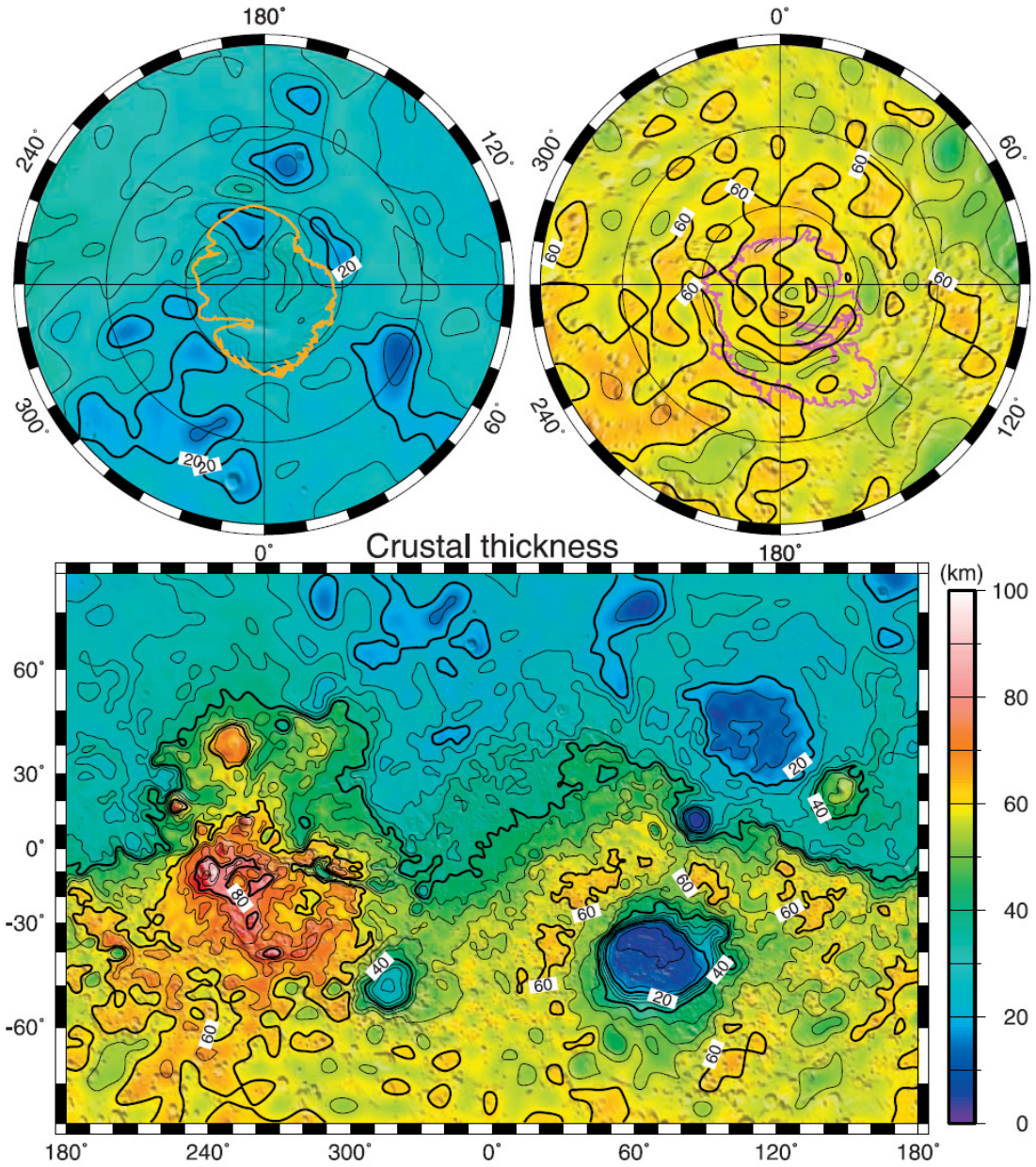

Figure 2.8. Crustal thickness of Mars by Neumann et al. (2004). The lower map has a Mercator (75º to 75º) projection, the upper maps have polar stereographic projection (60º–90ºN for the left map and 60º–90ºS for the right map). The background is a MOLA shaded relief map.

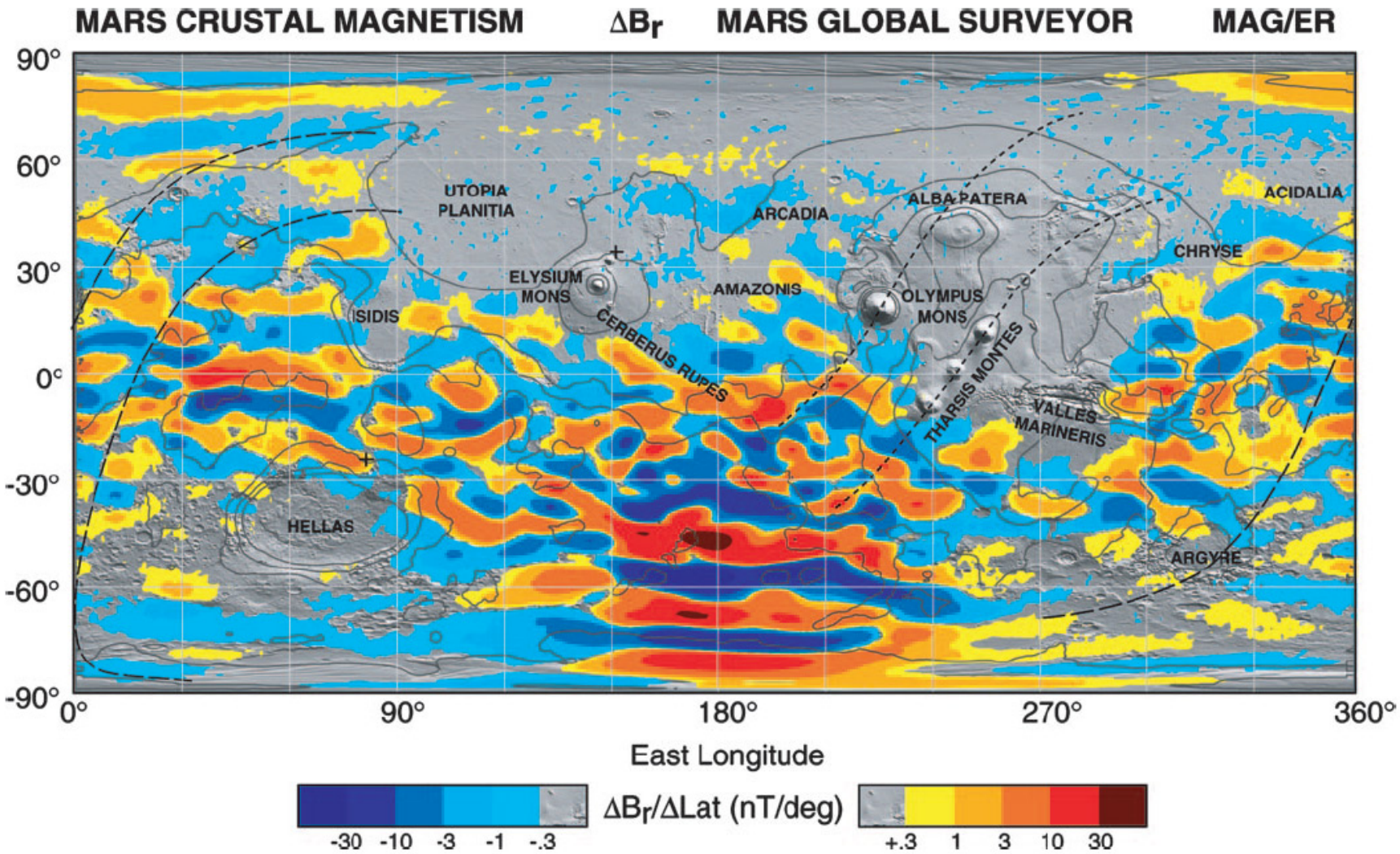

Figure 2.9. Map of the magnetic field of Mars derived from two Mars years of observation by MAG/ER on board the MGS. The background is a MOLA shaded relief map. After Connerney et al. (2005).

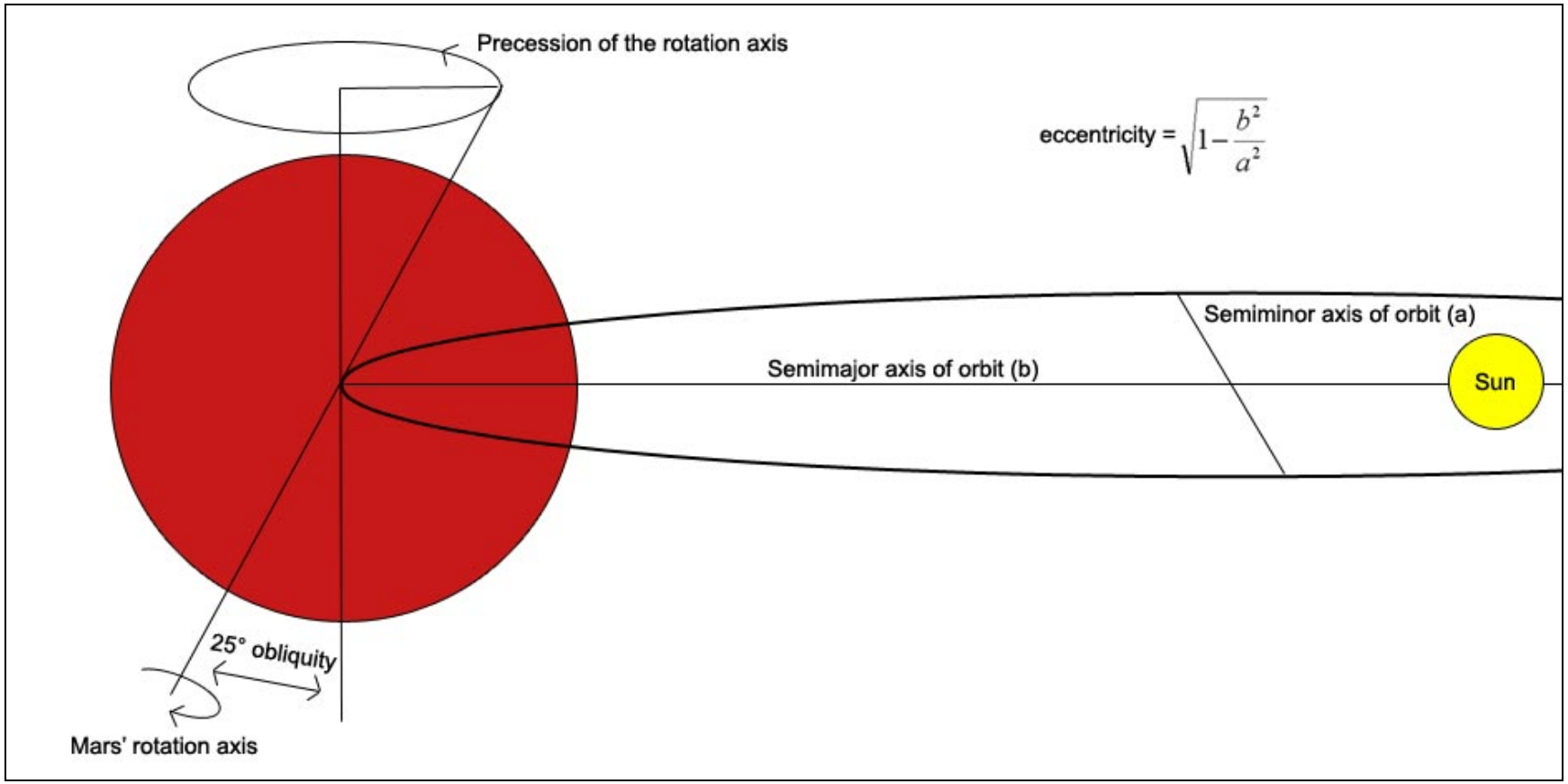

Figure 2.10. Explanation of the Martian orbit parameters, obliquity, eccentricity and precession.

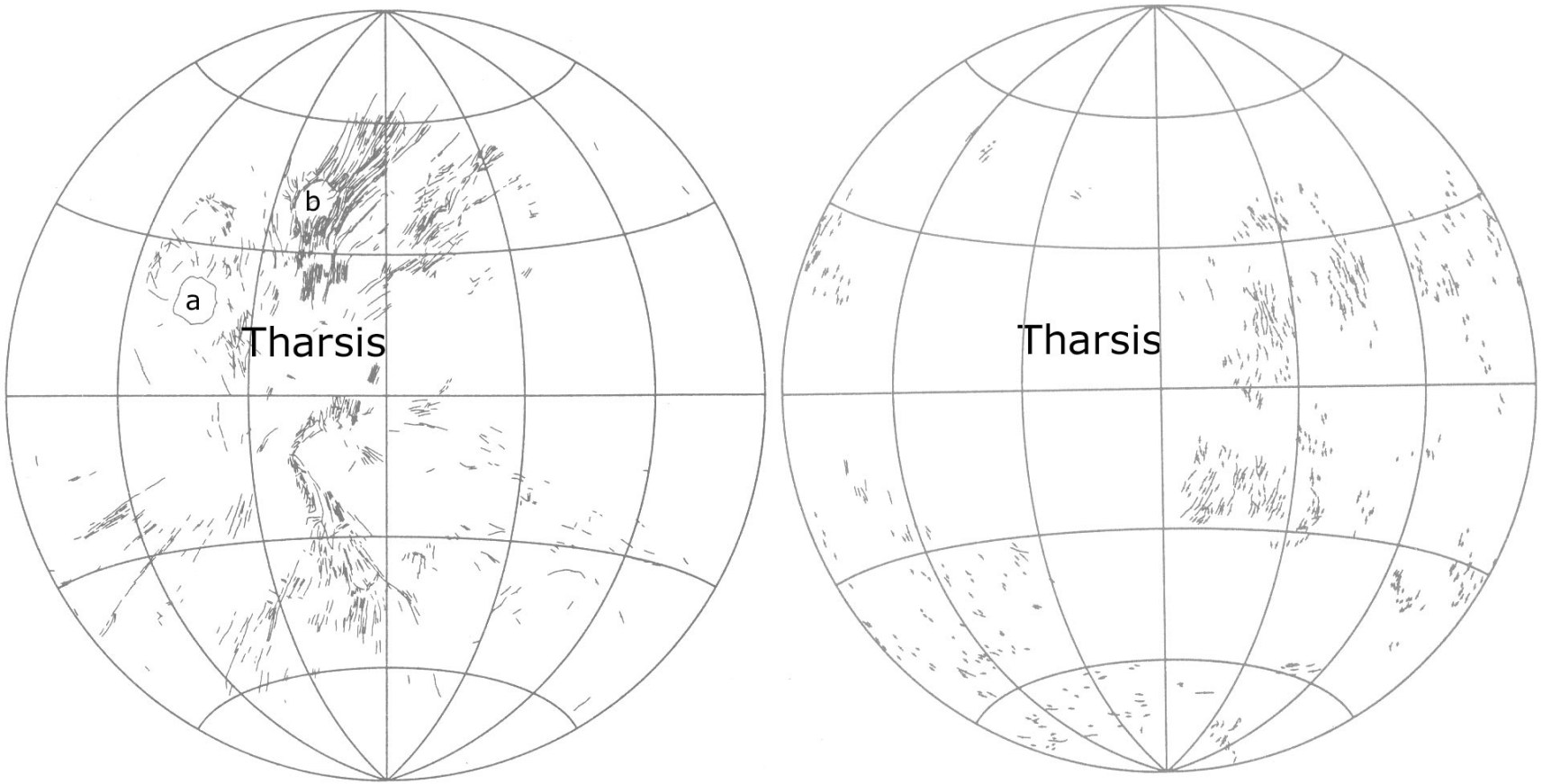

Figure 2.11. Tectonic features of the western hemisphere of Mars. The left image shows extensional features (grabens and fault scarps), the right image shows compressional features (wrinkle ridges). Redrawn after Banerdt et al. (1992).

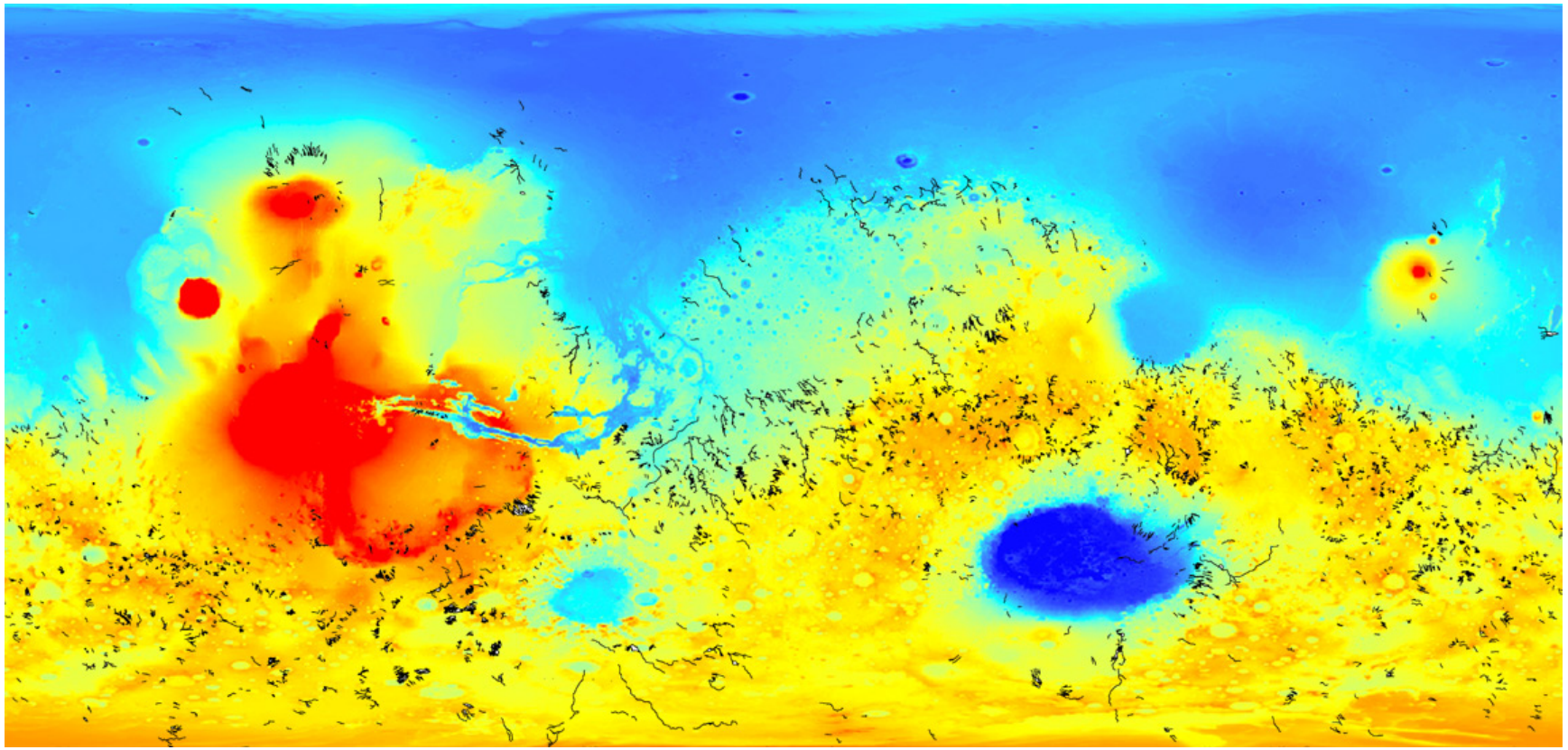

Figure 2.12. Map of valley networks, mapped using Viking and MGS data, on top of MOLA map. Redrawn from a map by Michael Carr.

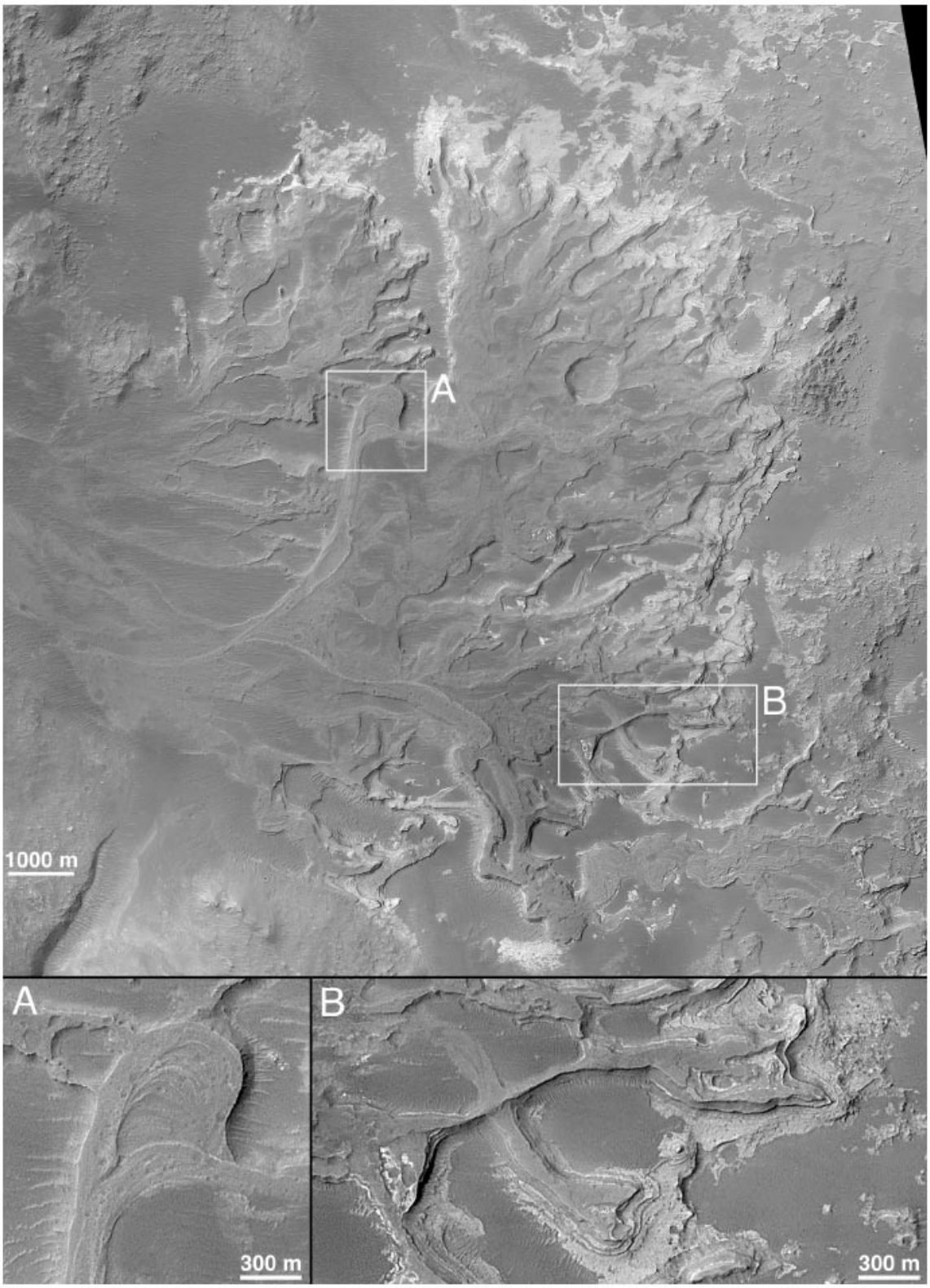

Figure 2.13. A possible fluvial distributary fan. Redrawn after Malin and Edgett (2003).

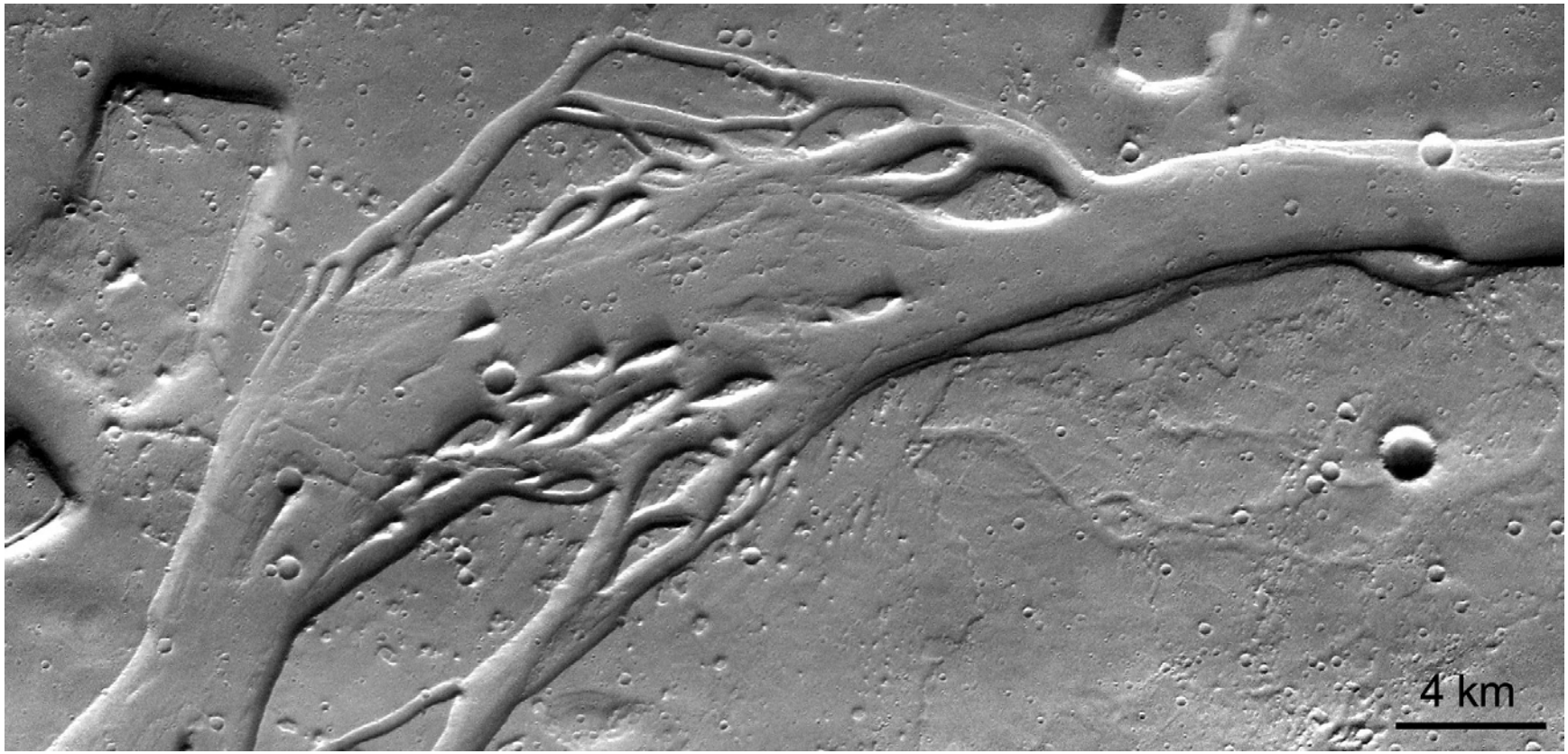

Figure 2.14. Part of outflow channel southwest of the Elysium Mons volcano. Part of THEMIS VIS image 20030620a.

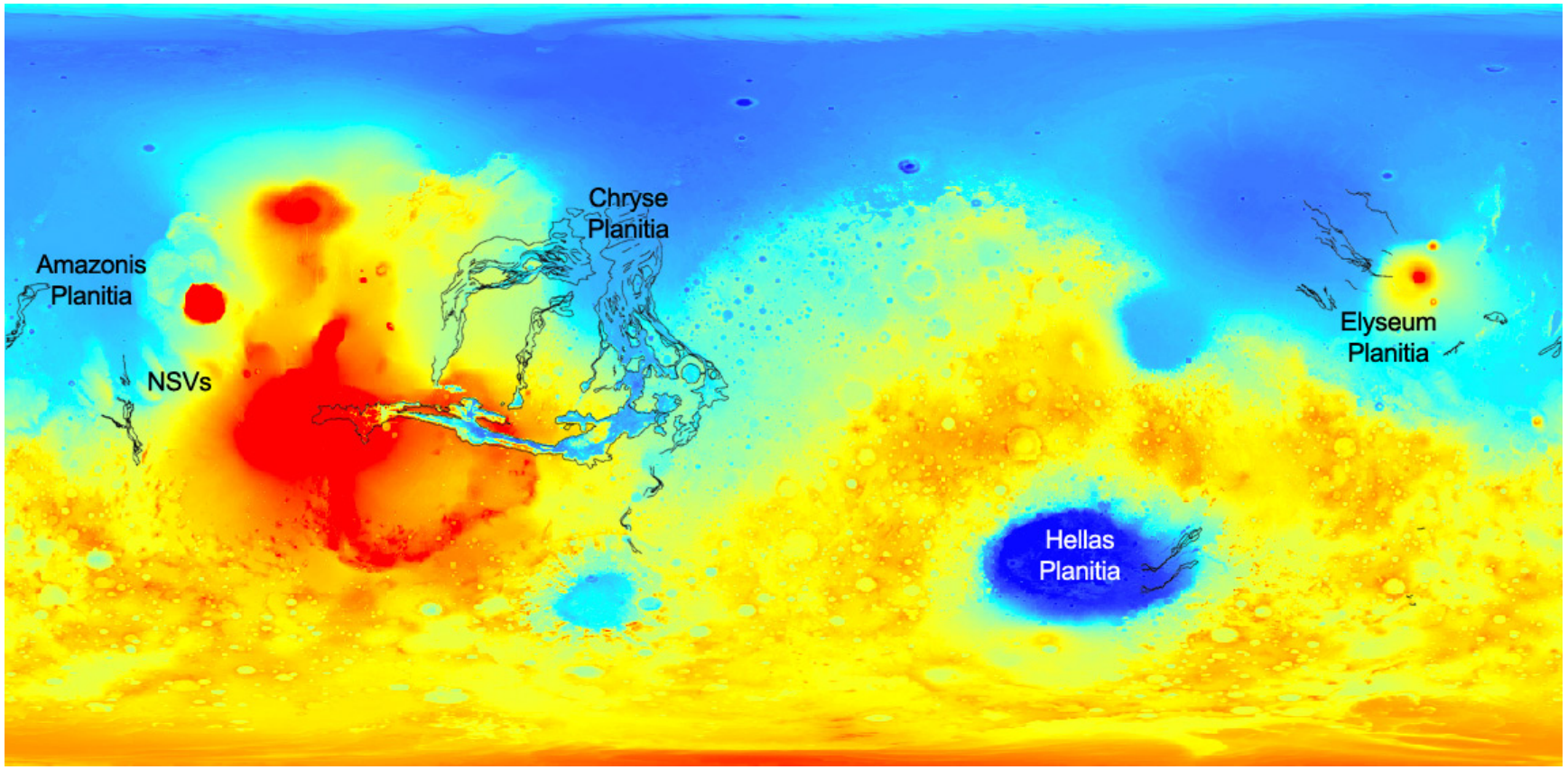

Figure 2.15. Map of outflow channels, mapped using Viking data, on top of MOLA map. Redrawn from a map from Carr (1996).

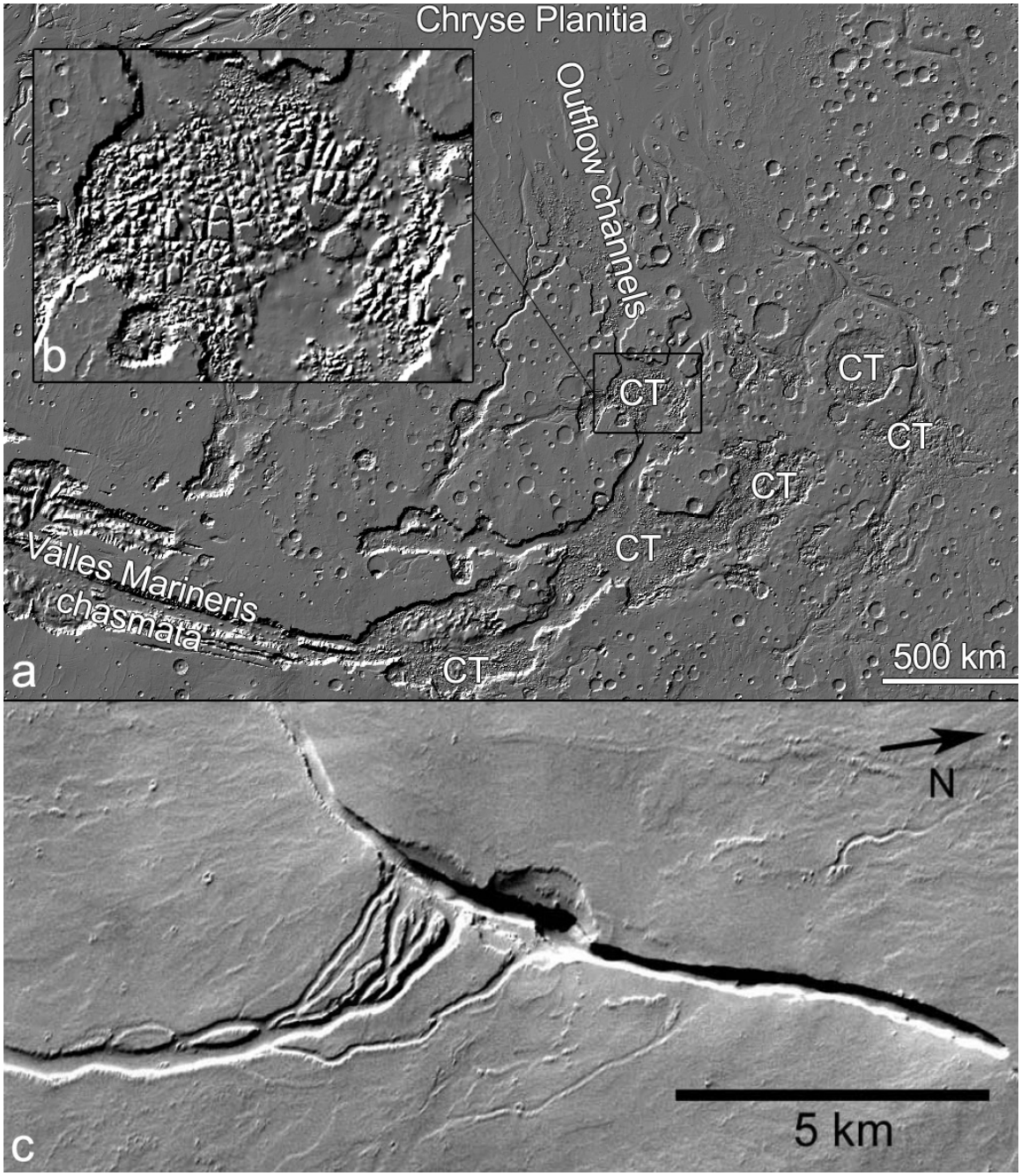

Figure 2.16. Outflow channel source regions. **a.** Circum-Chryse outflow channels with chasmata and chaotic terrain source regions. **b.** Chaotic terrain. **c.** Unnamed channel south of Ascraeus Mons with extensional tectonic feature as source region (Part of THEMIS image V08155020 centered on 6.0°N, 254.5°E). Image after Hanna and Phillips (2005).

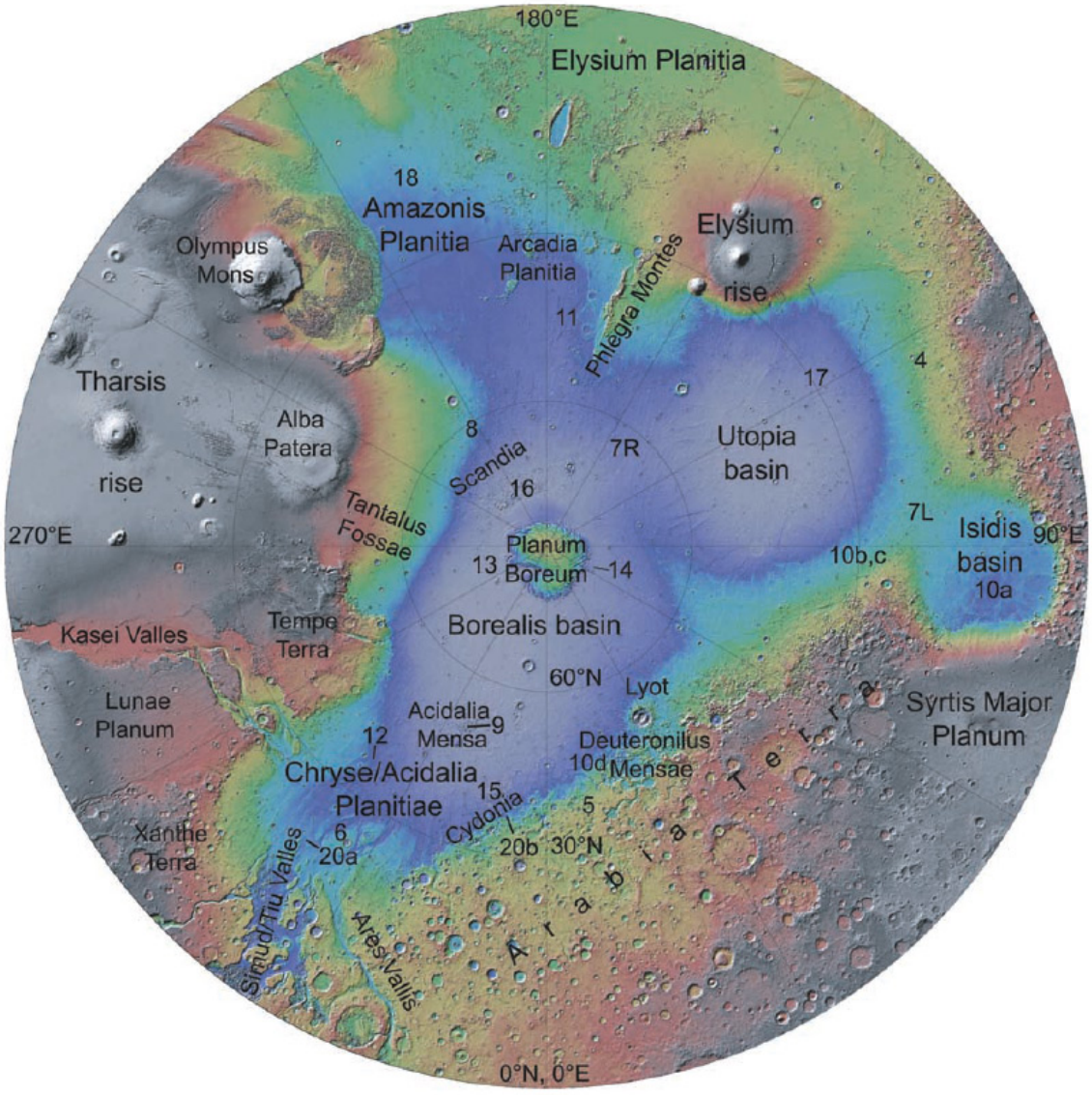

Figure 2.17. Polar stereographic MOLA shaded relief map of the northern hemisphere of Mars, after Tanaka et al. (2003). Blue is low elevation, gray is high elevation.

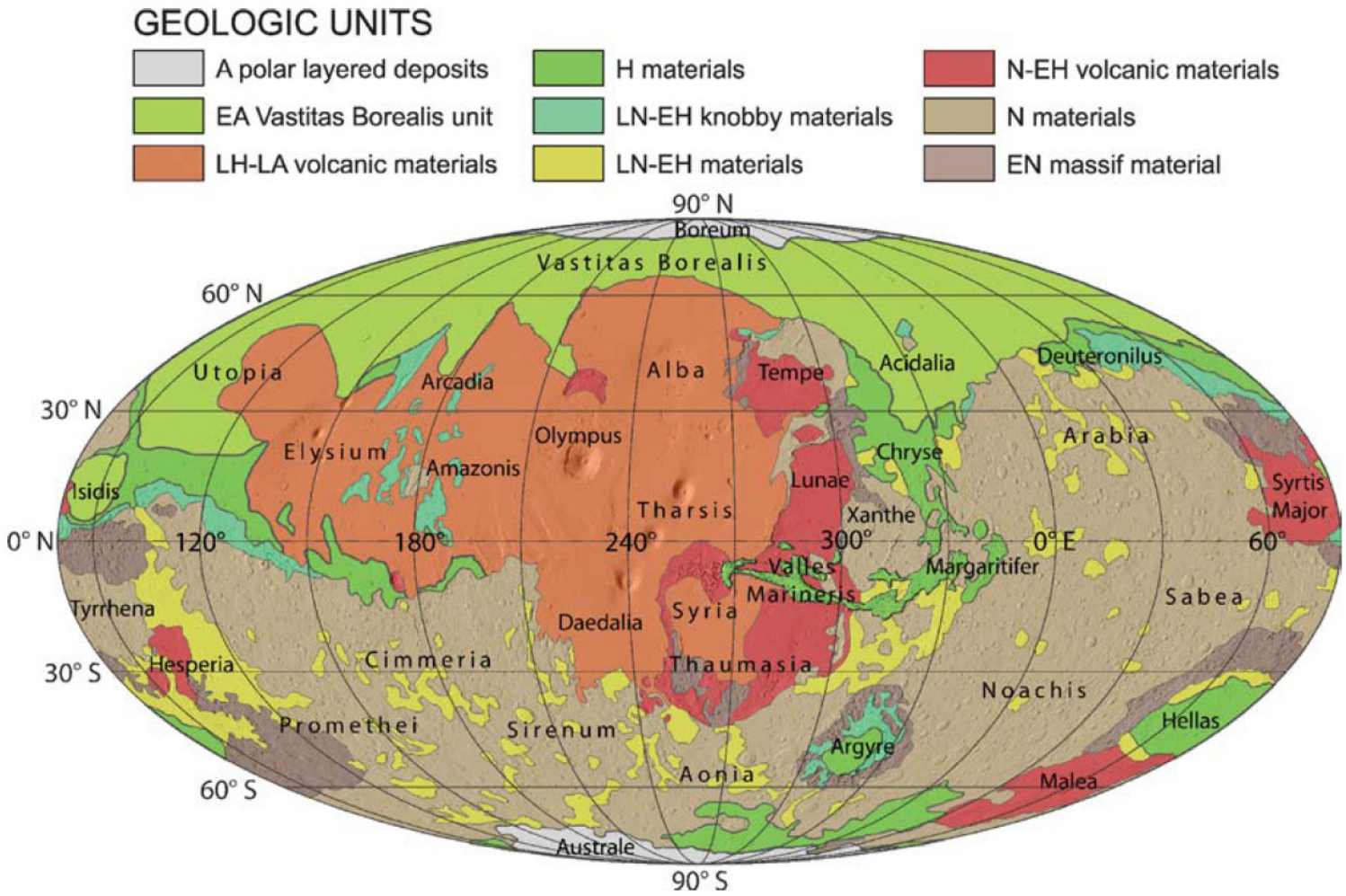

Figure 2.18. Global scale geological map of Mars, using mollweide projection (with east longitude and centered on 260ºE) and MOLA shaded relief as background. N=Noachian, H=Hesperian, A=Amazonian, E=Early, L=Late. Map from Nimmo and Tanaka (2005).

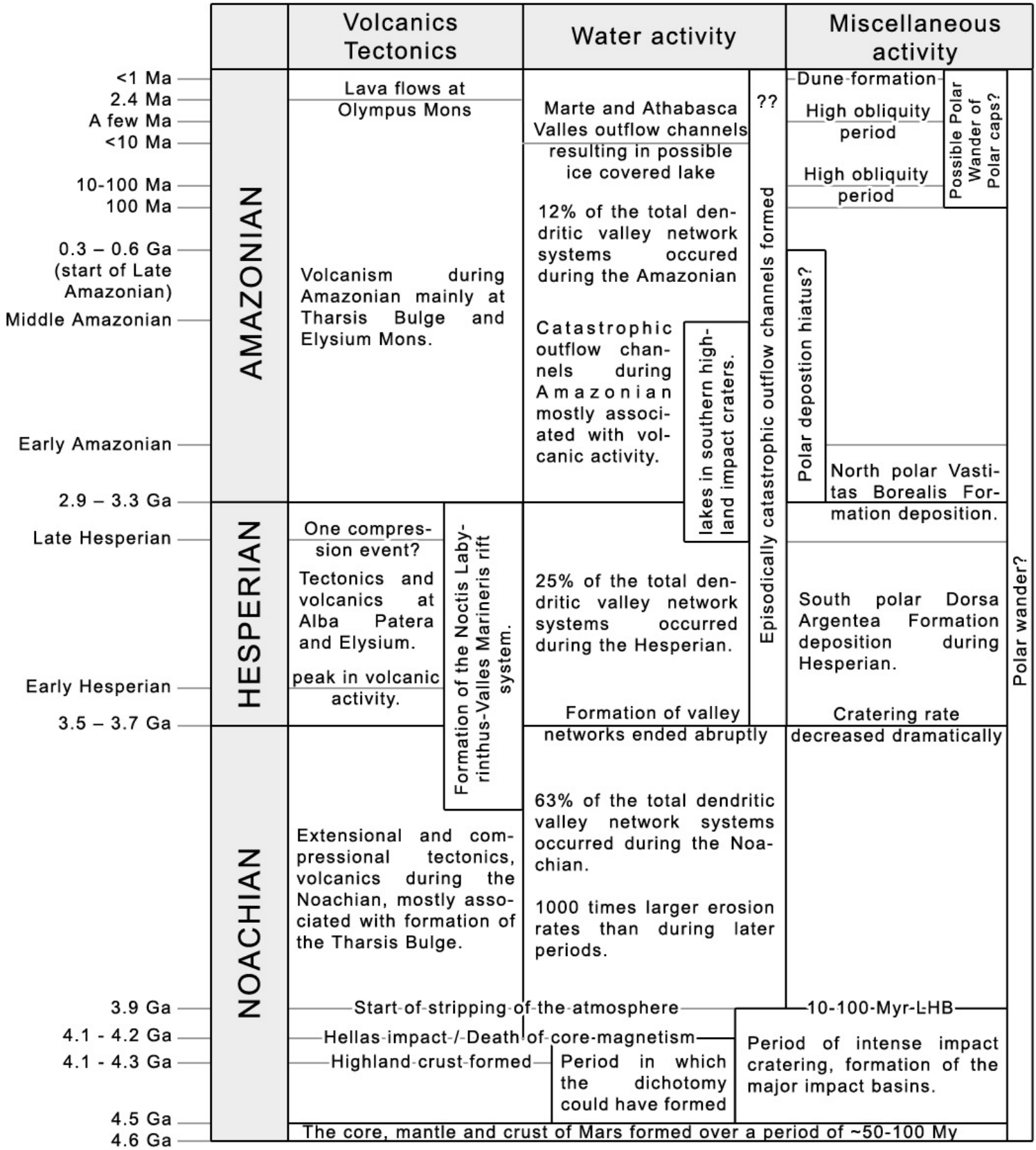

Figure 2.19. Diagram summarizing the evolution of Mars.

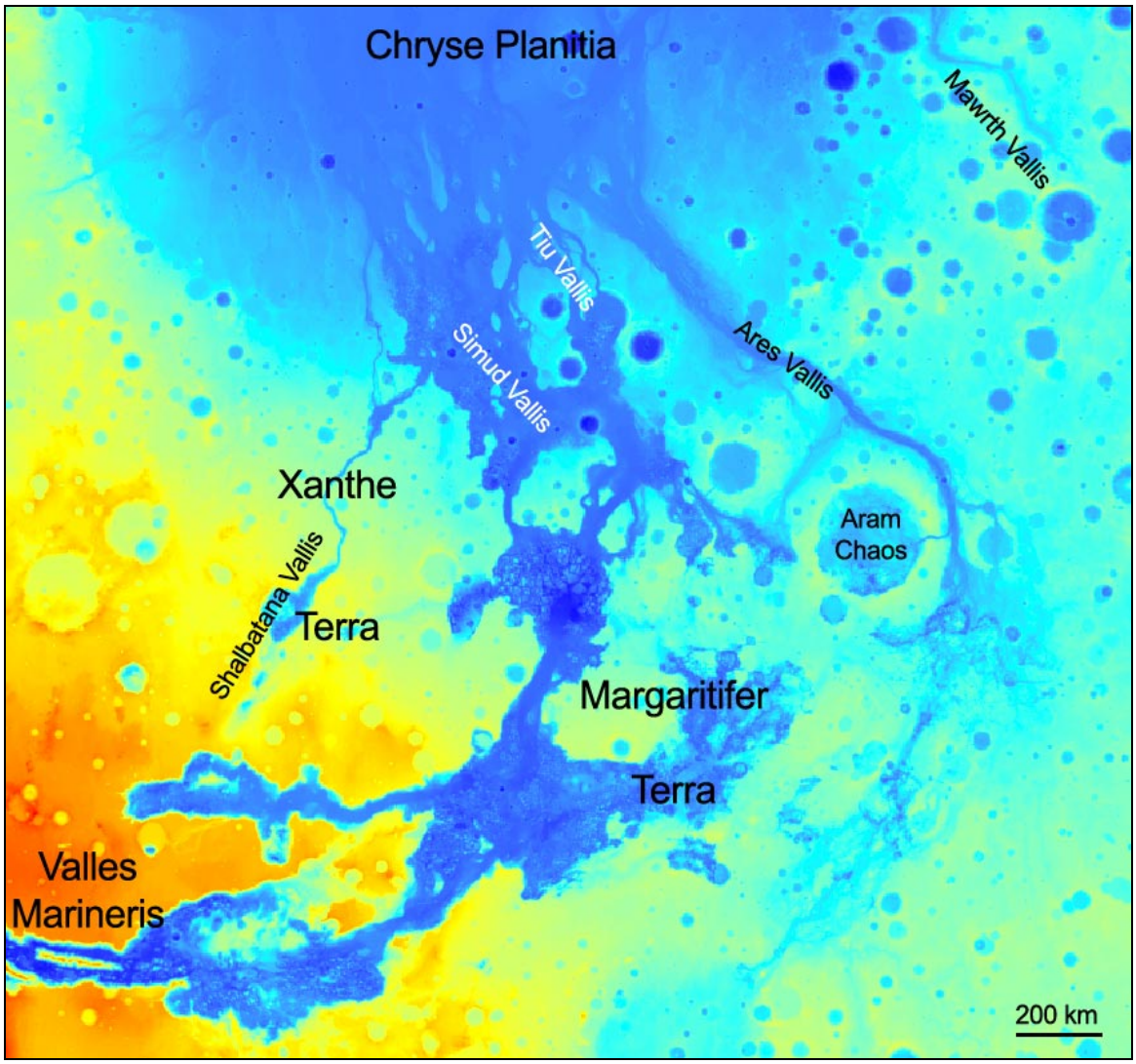

Figure 3.1. MOLA image of Xanthe and Margeritifer Terrae (image center is 4.3°N and -33.1°E).

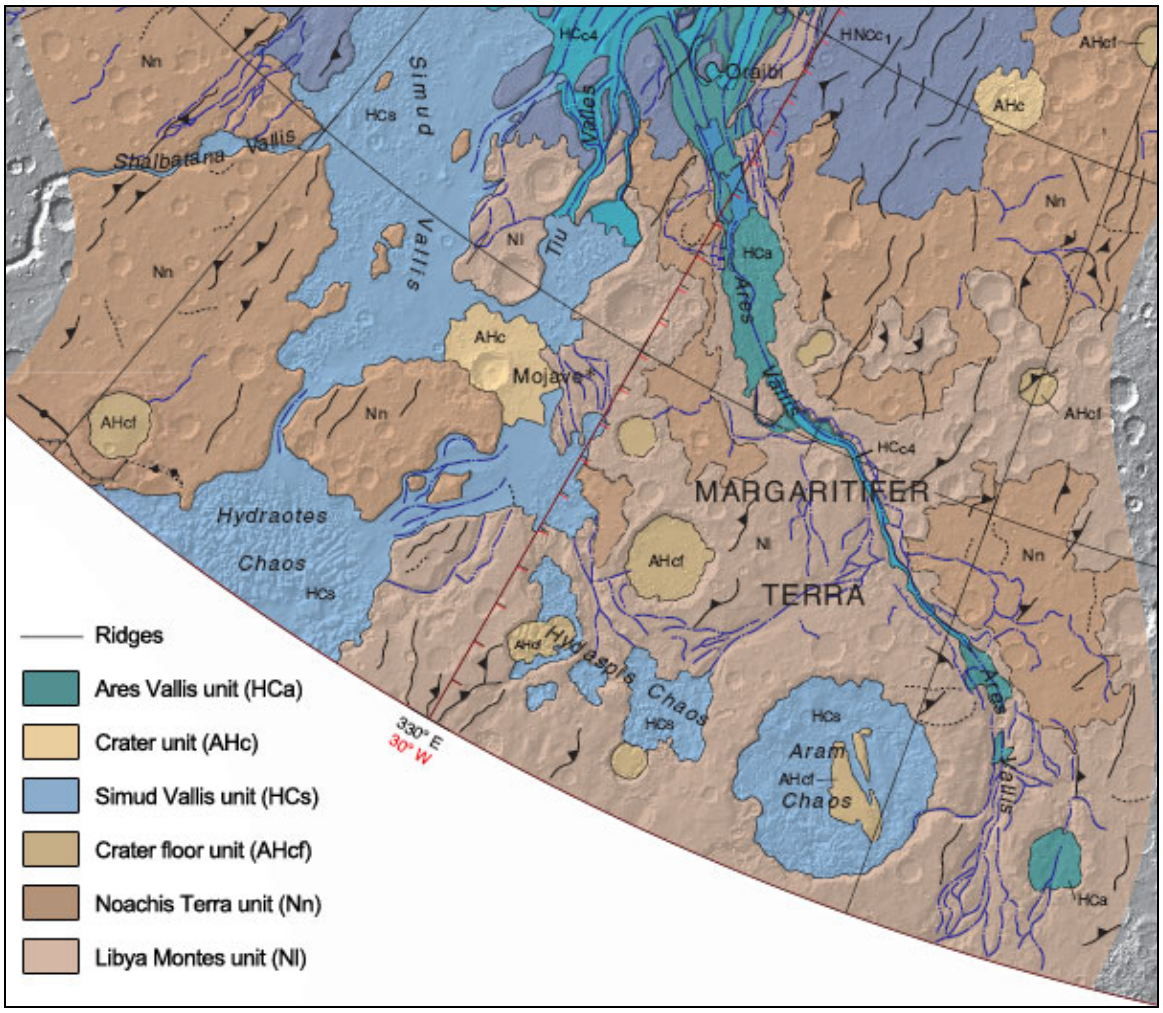

Figure 3.2. Part of polar stereographic northern lowlands geological map showing the Margaritifer Terra Region including Aram Chaos. Redrawn after Tanaka et al. (2005).

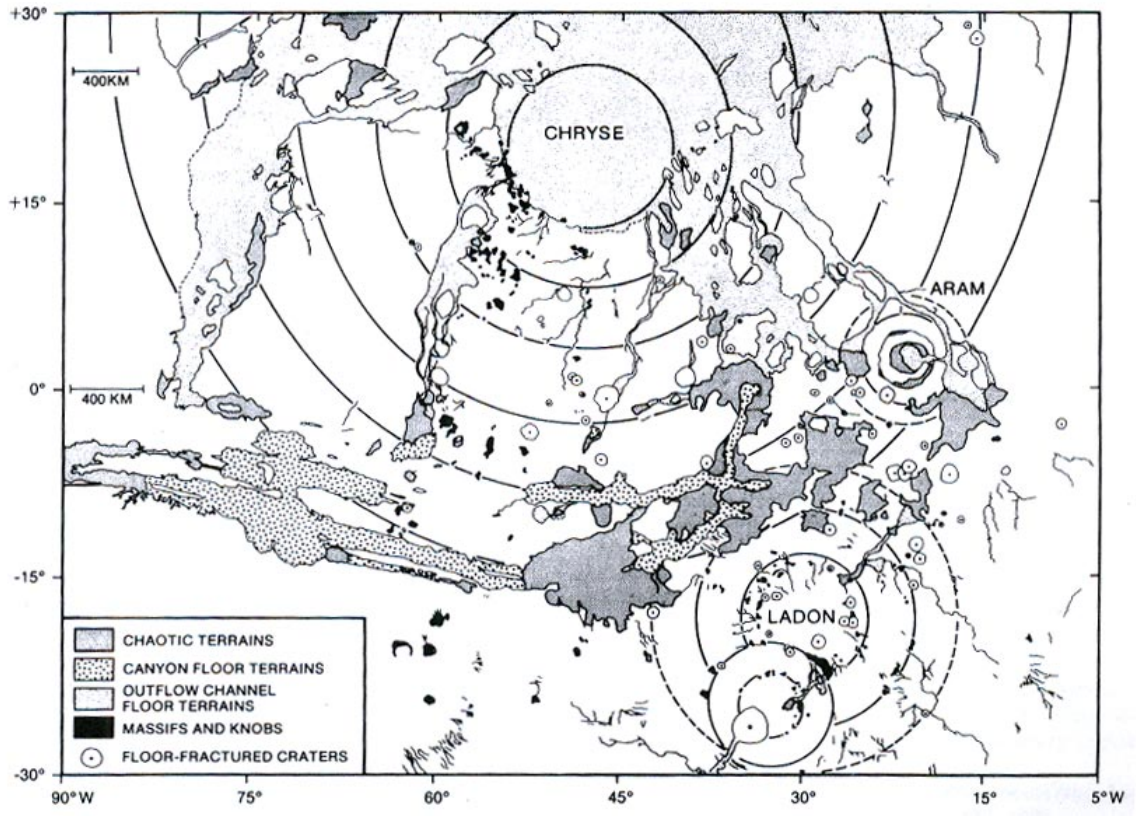

Figure 3.3. Map of Chryse Planitia and Valles Marineris, after Schultz et al. (1982), showing concentric rings of the Chryse and other impacts.

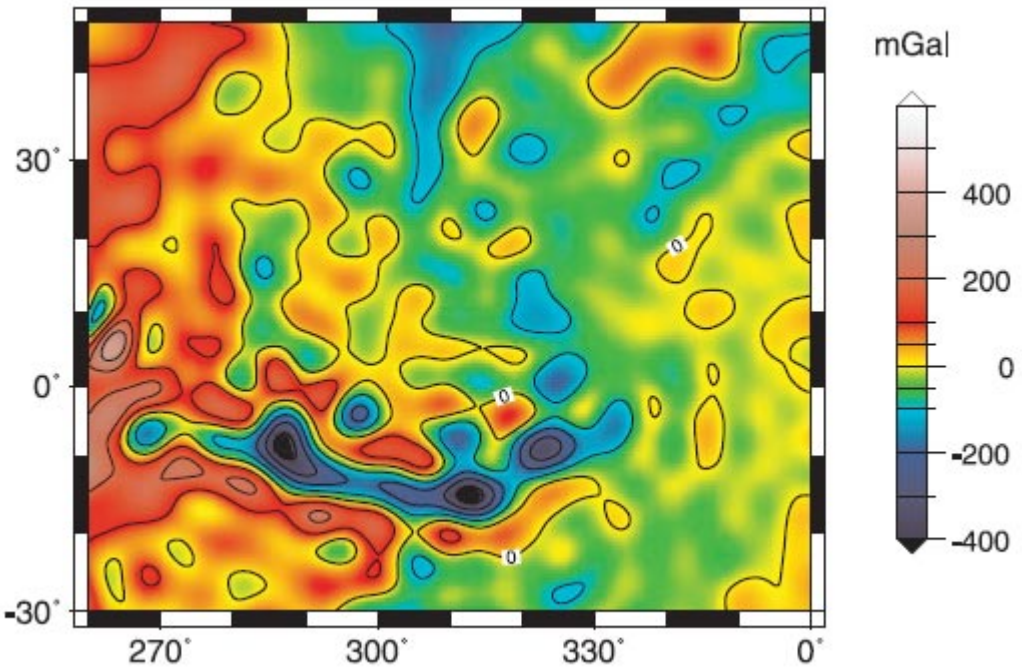

Figure 3.4. Negative Gravity anomalies of Valles Marineris and Chryse Planitia, after Smith et al. (1999).

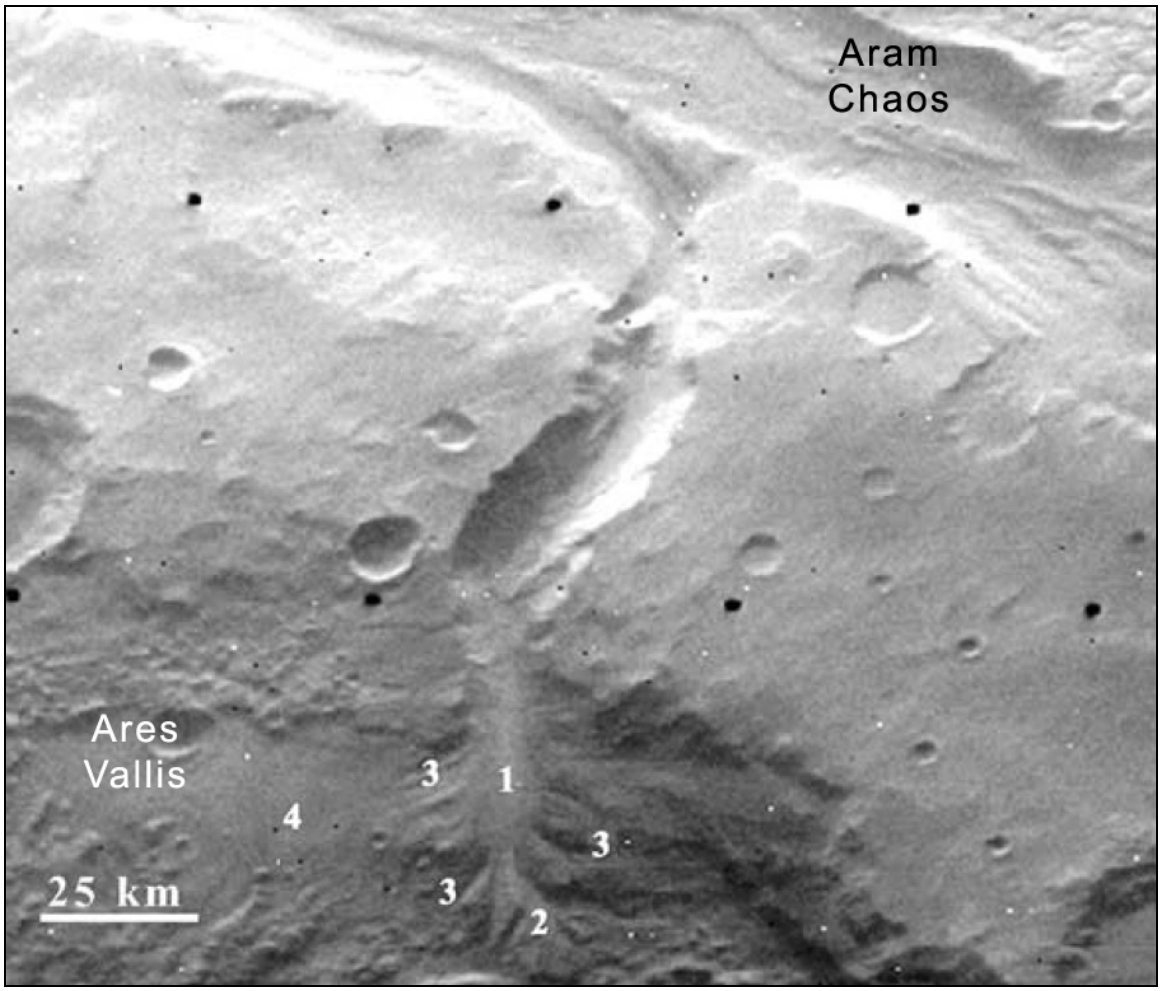

Figure 3.5. Possible delta structure in the Aram Chaos channel. (1) 60 km long and 120 km wide delta platform, (2) prodelta slope, (3) distributary channels, (4) deposit of fine material. Viking image 689A03. Redrawn after Cabrol and Grin (2002).

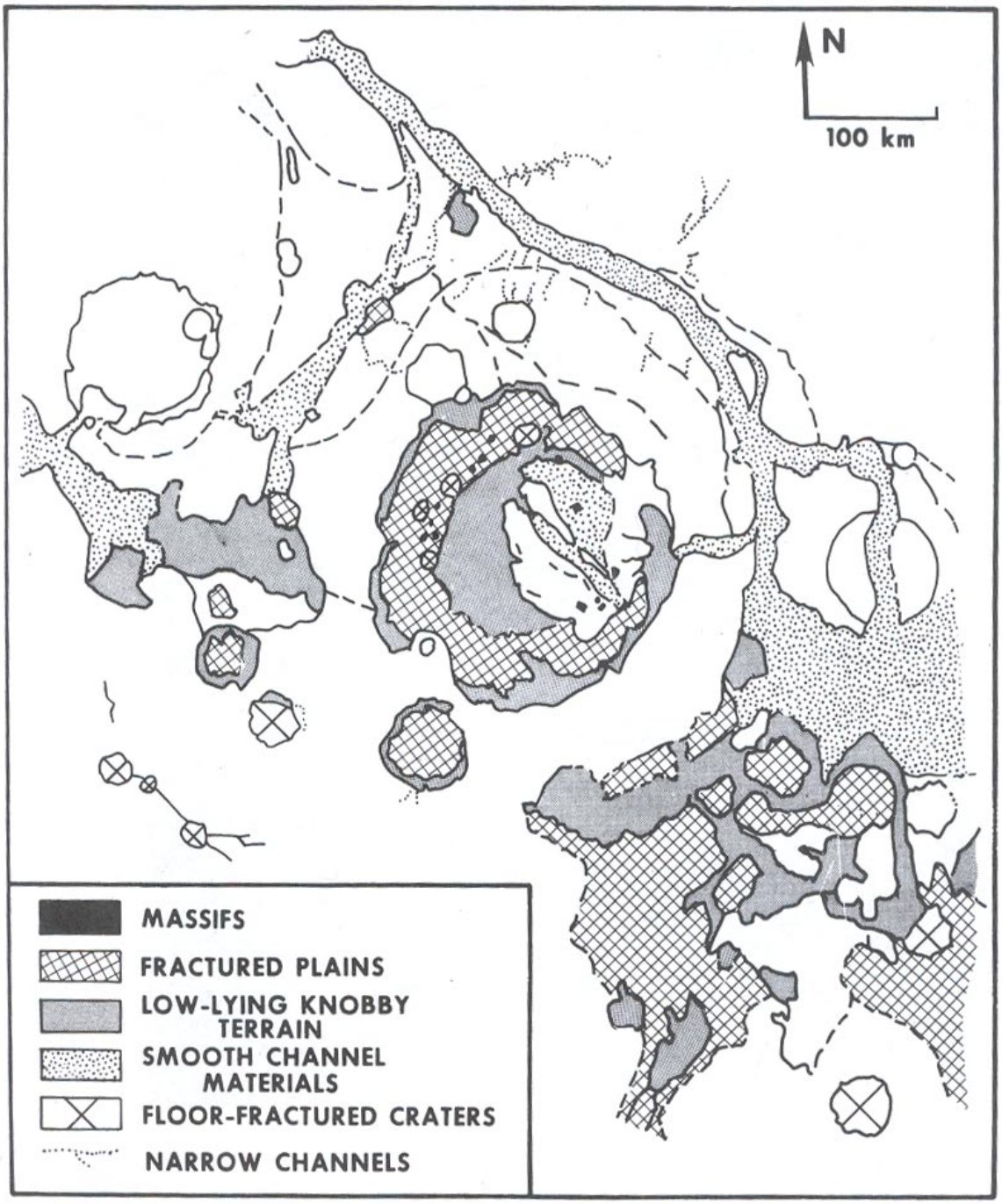

Figure 3.6. A terrain map of Aram Chaos and surrounding area, after Schultz et al. (1982).

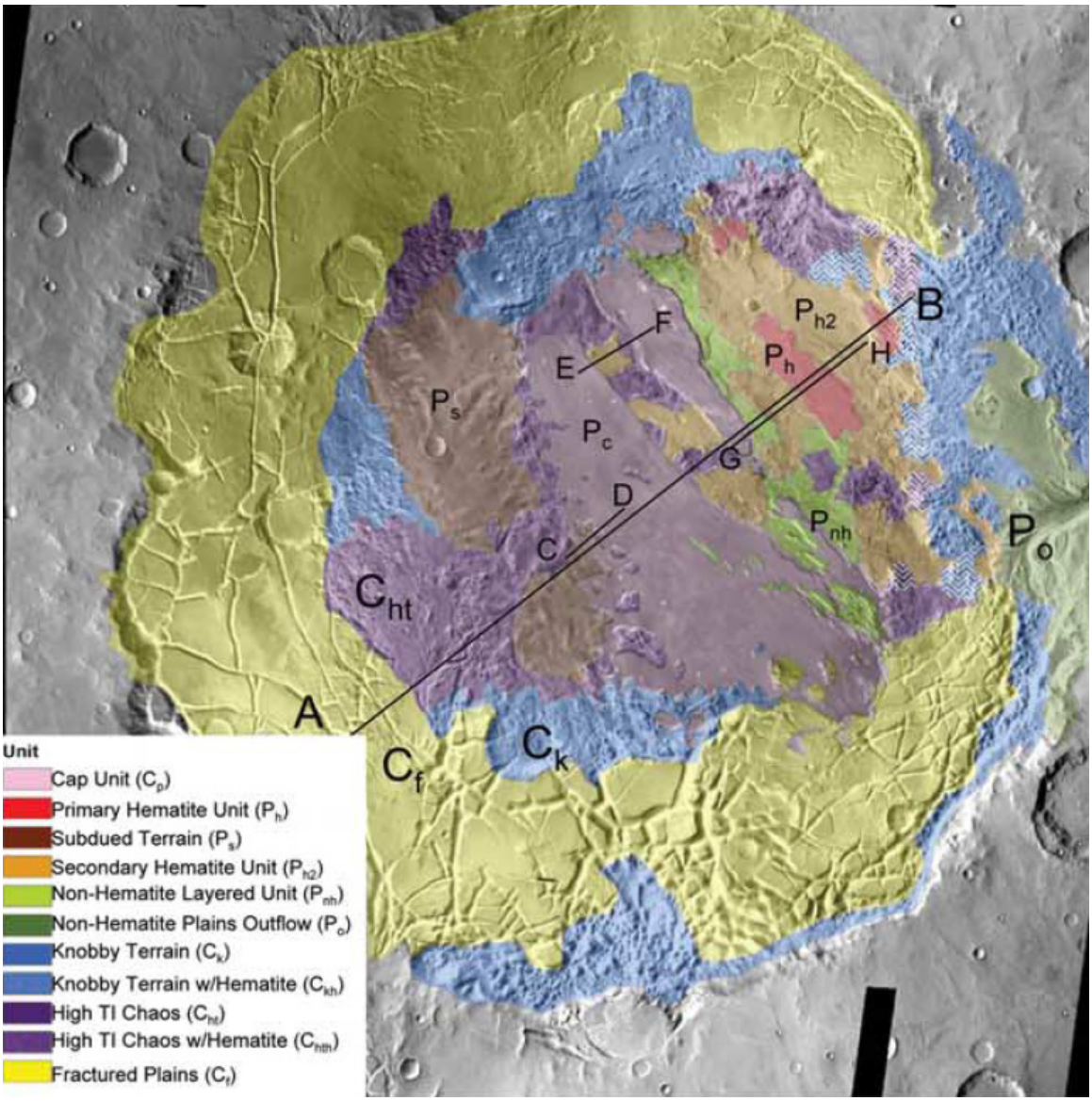

Figure 3.7. Geological map of Aram Chaos, redrawn after Glotch and Christensen (2005).

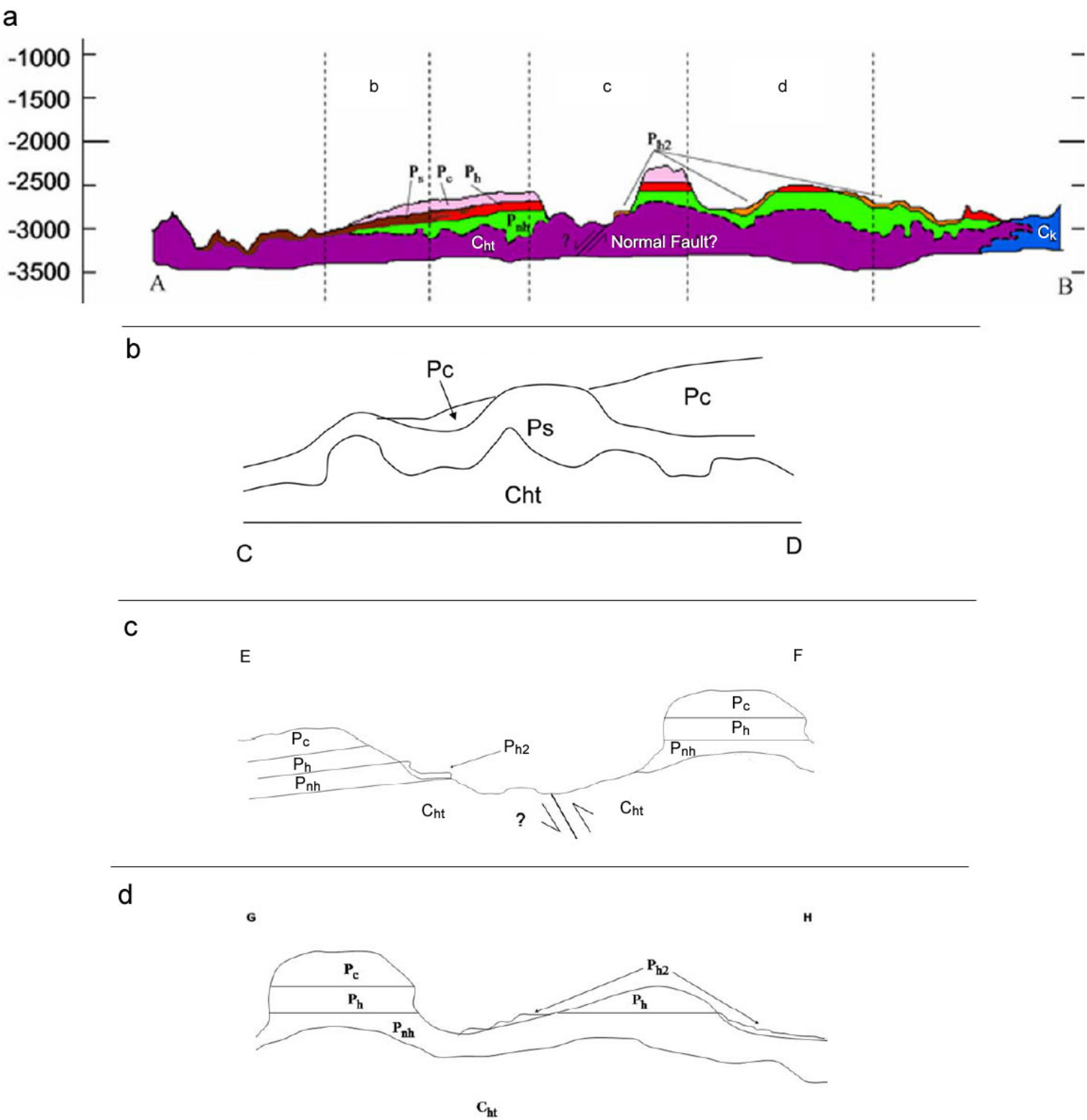

Figure 3.8. Profiles of Aram Chaos chaotic and layered terrain (redrawn after Glotch and Christensen, 2005). The dashed parts in (a) refer to b,c and d. The A-B, C-D, E-F and G-H profile lines are shown on Figure 3.7.

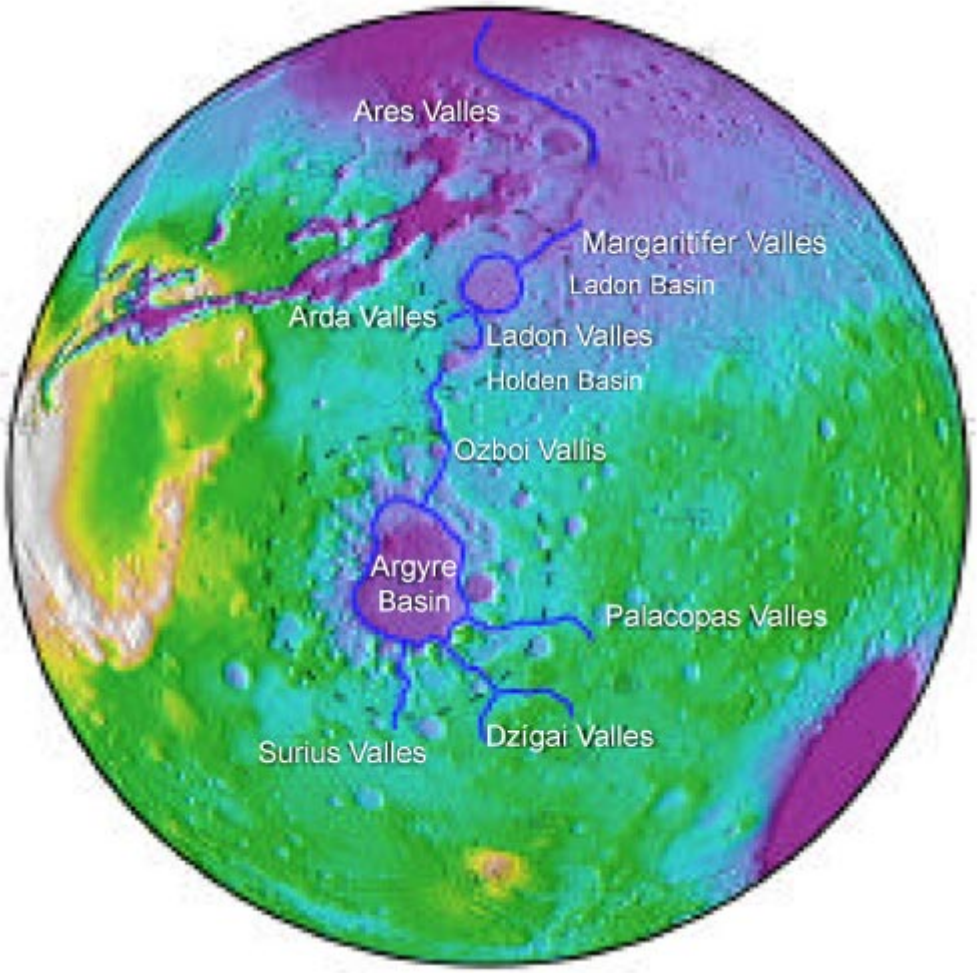

Figure 3.9. Hemisphere view of MOLA elevation data (centered northeast of Argyre Planitia), redrawn after Parker et al. (2000).

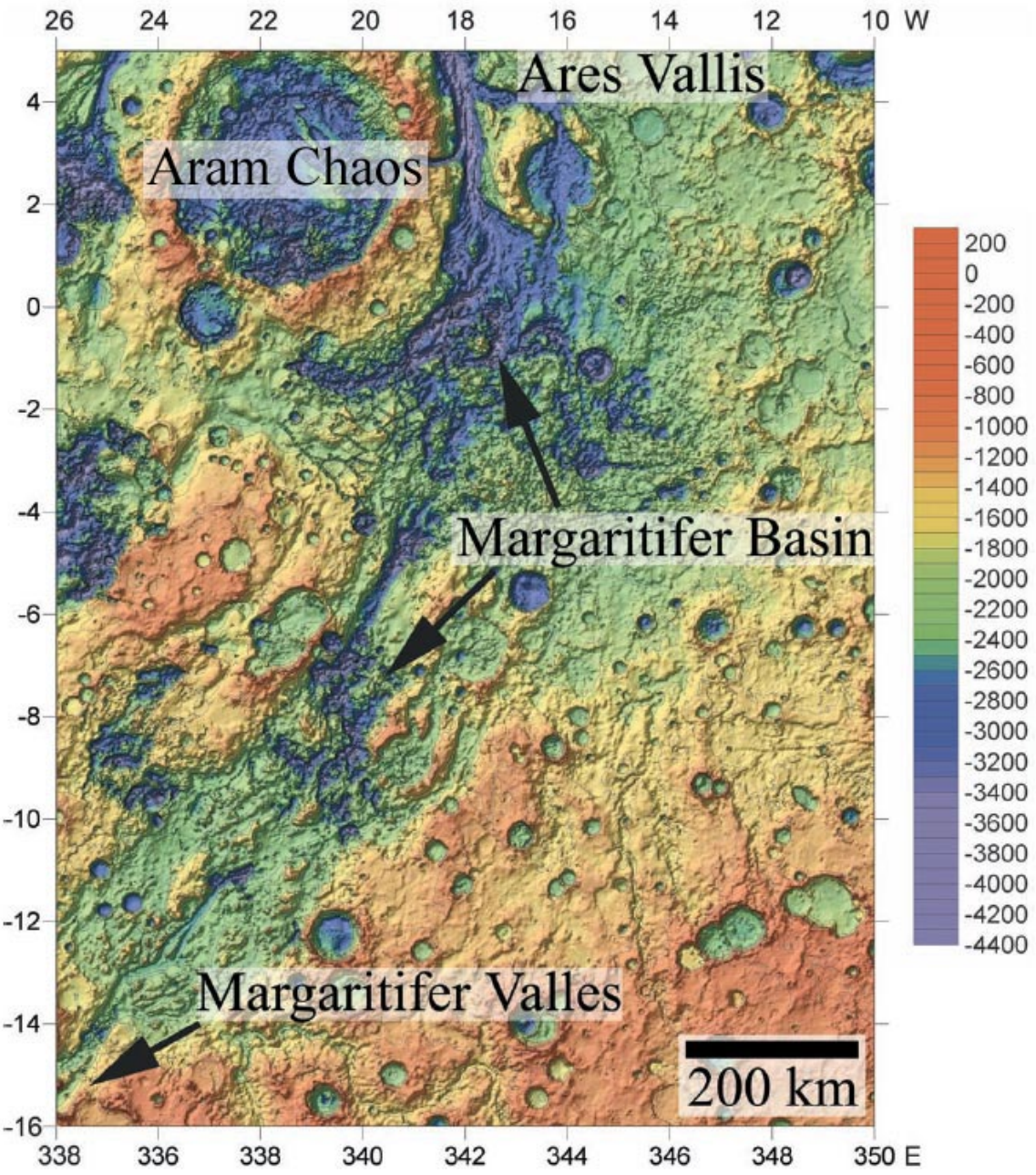

Figure 3.10. MOLA elevation map of Margaritifer Basin, redrawn after Grant and Parker (2002).

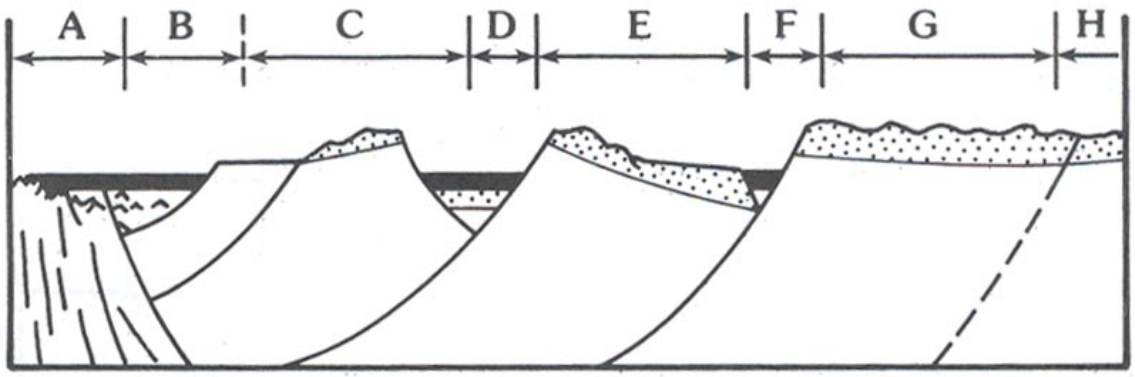

Figure 3.11. Cross section model of typical multi-ring impact basin (>300 km in diameter) on Mars, after Schultz et al. (1982). The zones A to H are explained in Table 3.1.

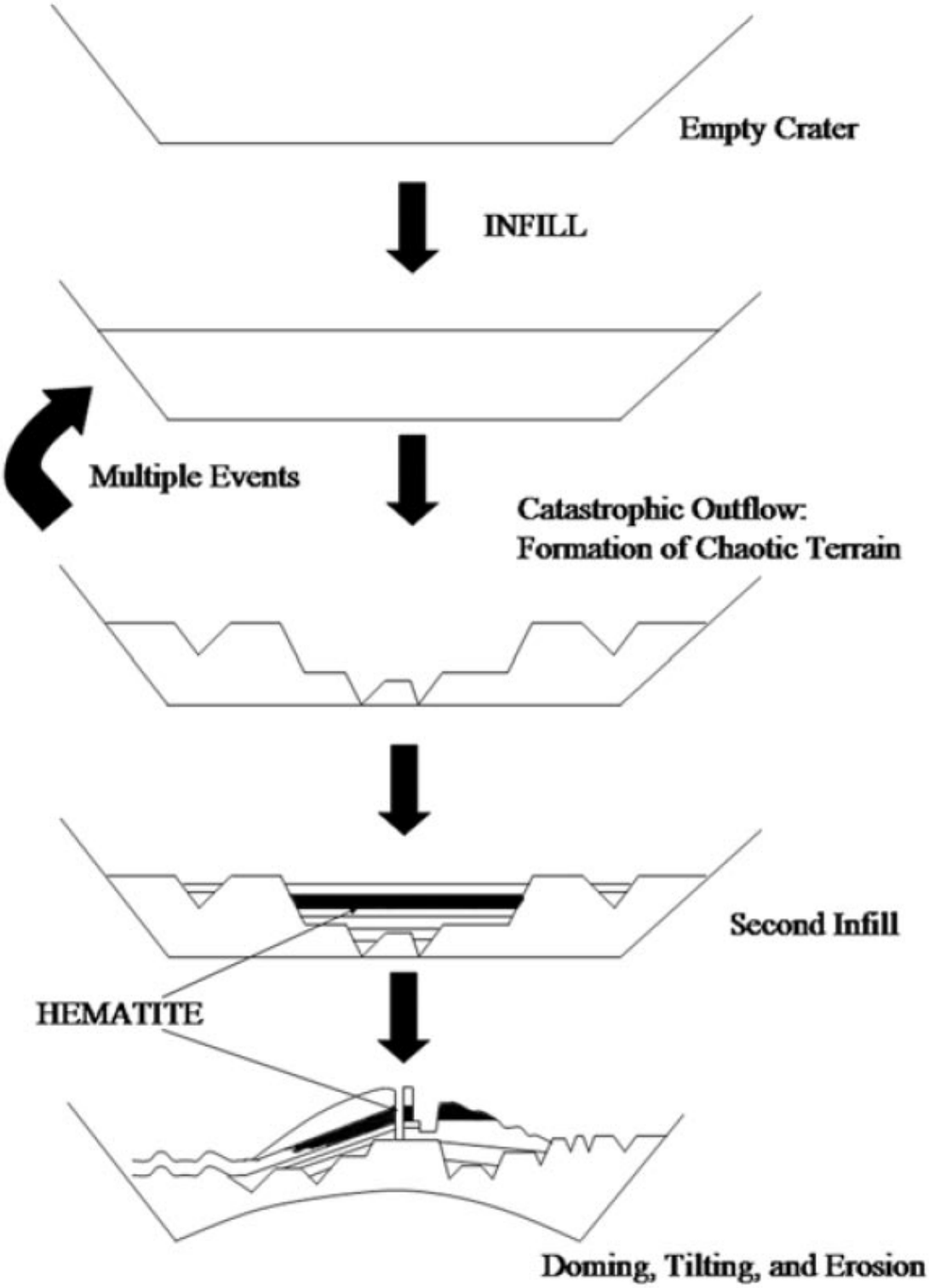

Figure 3.12. Possible stages of Aram Chaos development proposed by Glotch and Christensen (2005).

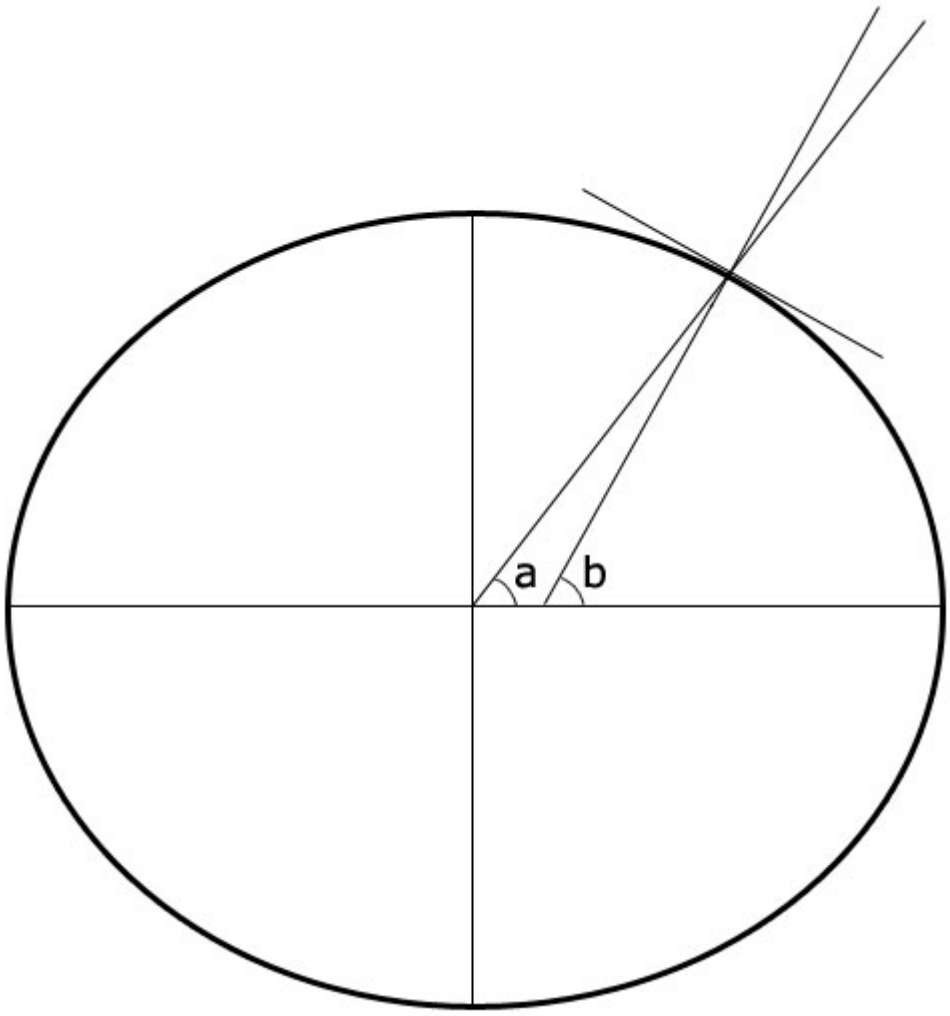

Figure 4.1. The planetocentric latitude (**a**) vs. the planetographic latitude (**b**).

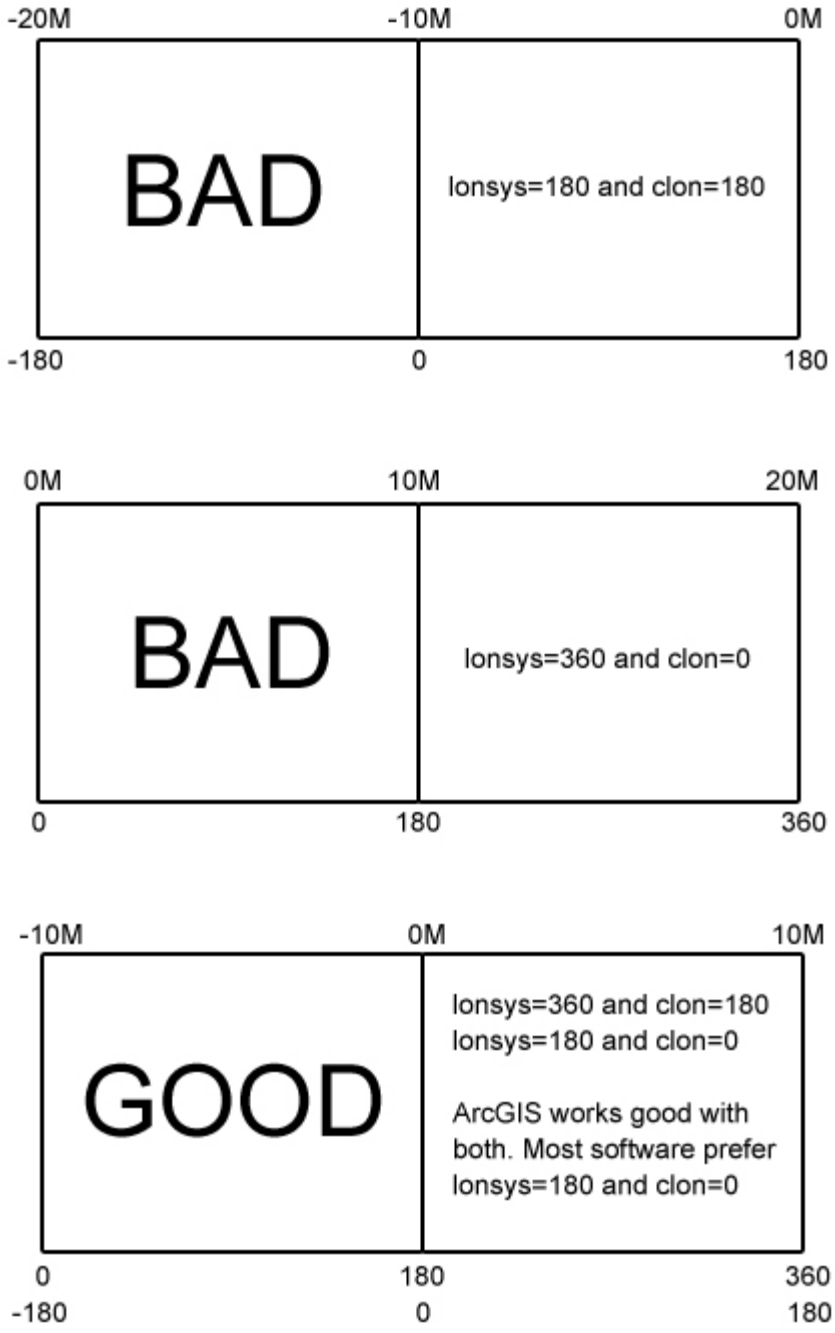

Figure 4.2. Different variations of the Longitude System (lonsys) and the Central Longitude (clon) combination. The Longitude System can either be between 0° and 360° (lonsys = 360) or between –180° and 180° (lonsys = 180). The Central Longitude can be 0° or 180°. Only lonsys = 360 and clon = 180 or lonsys = 180 and clon = 0 work with ArcGIS.

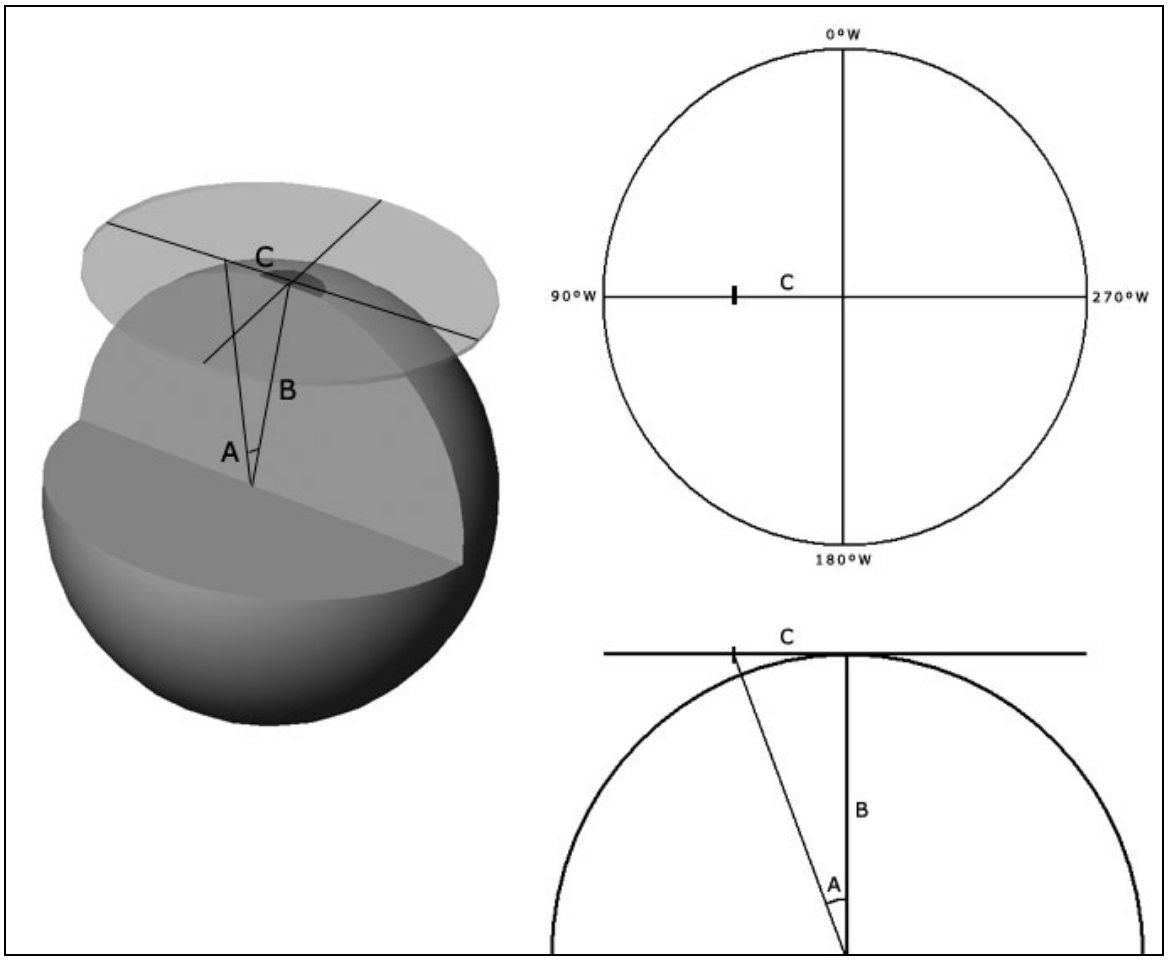

Figure 4.3. Polar Stereographic Projection.

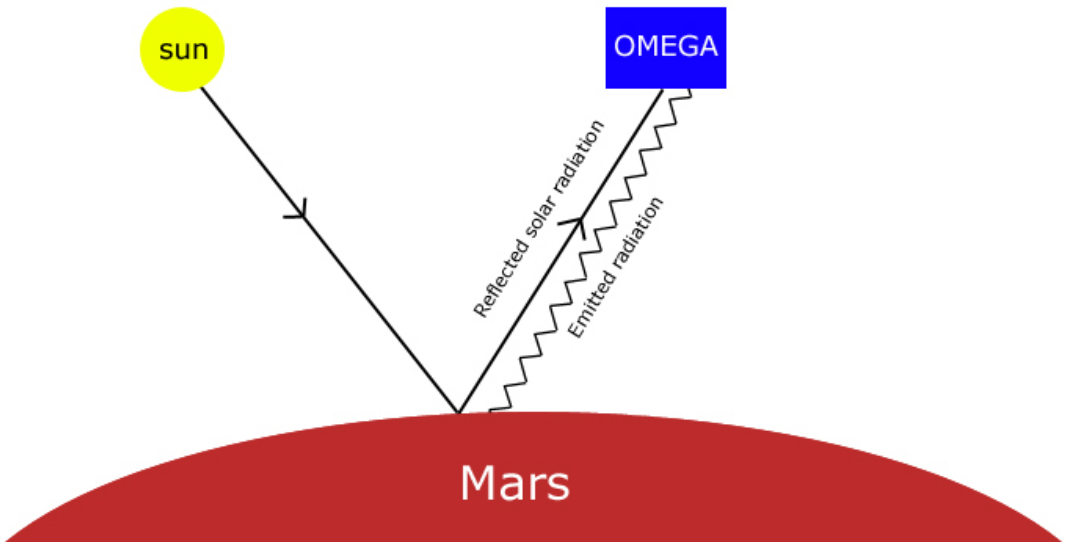

Figure 4.4. OMEGA orbiting Mars, sensoring reflected solar radiation and thermal emitted radiation. Redrawn after Van der Meer and De Jong (2004).

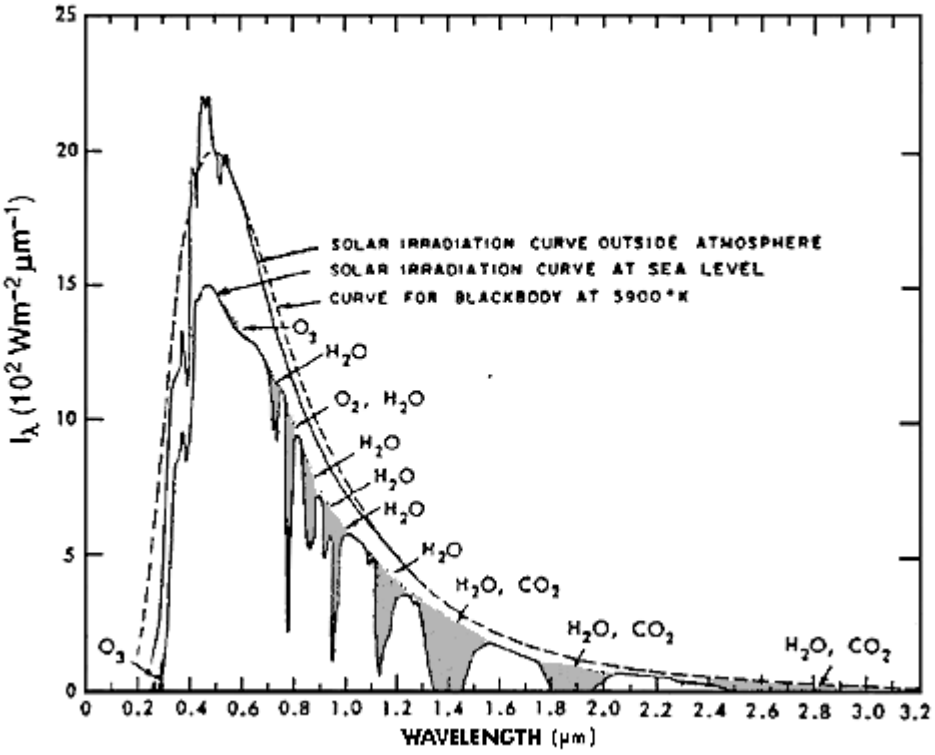

Figure 4.5. The solar irradiance curve for Earth (Source: http://ceos.cnes.fr:8100/cdrom-00b/ceos1/ science/dg/dg1.htm).

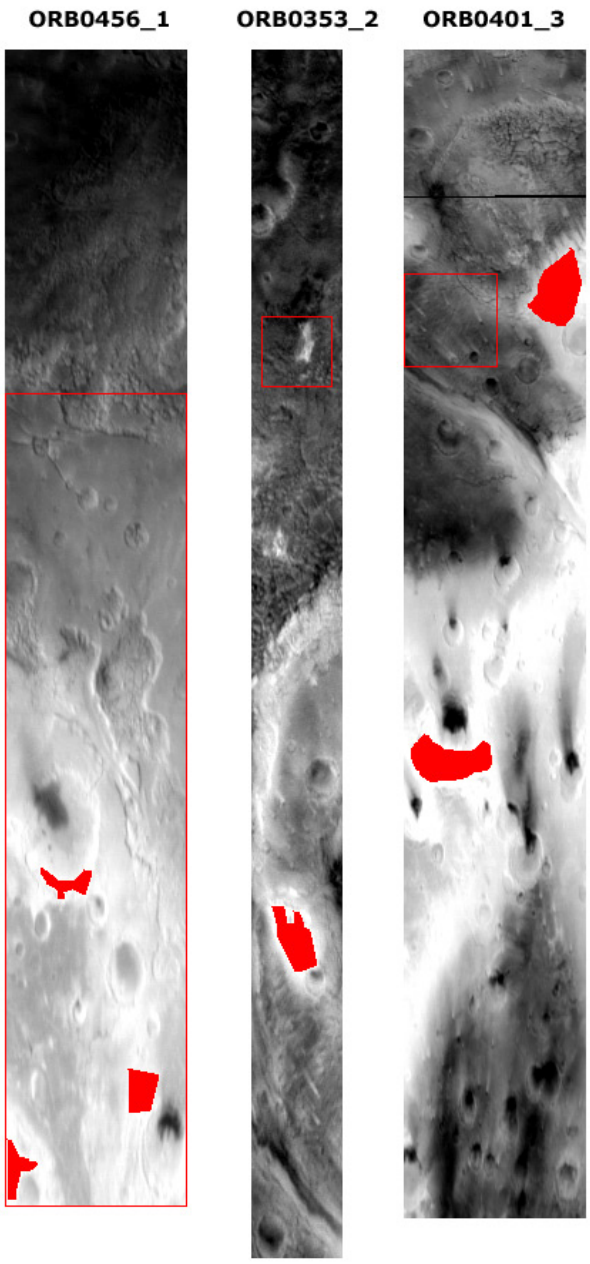

Figure 4.6. ROIs of bright albedo regions within the three OMEGA orbits.

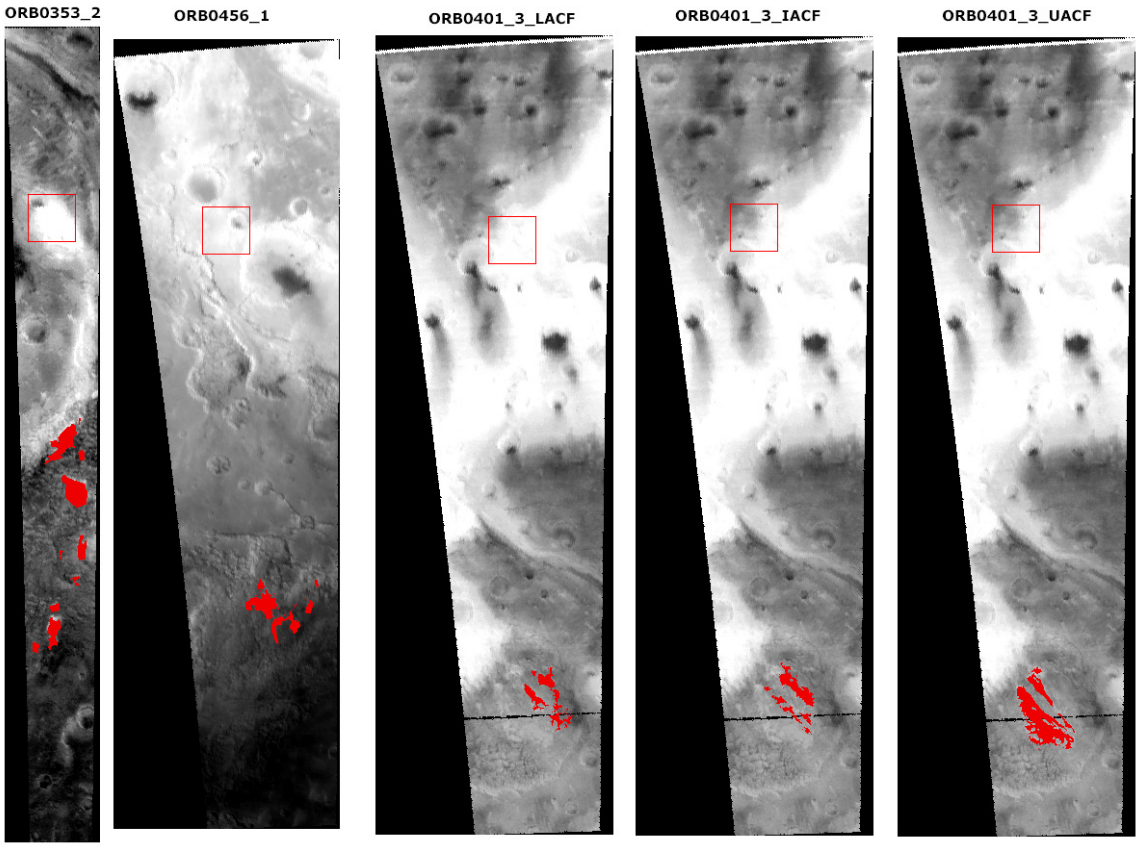

Figure 4.7. ROIs of the different deposits on top of the OMEGA orbits.

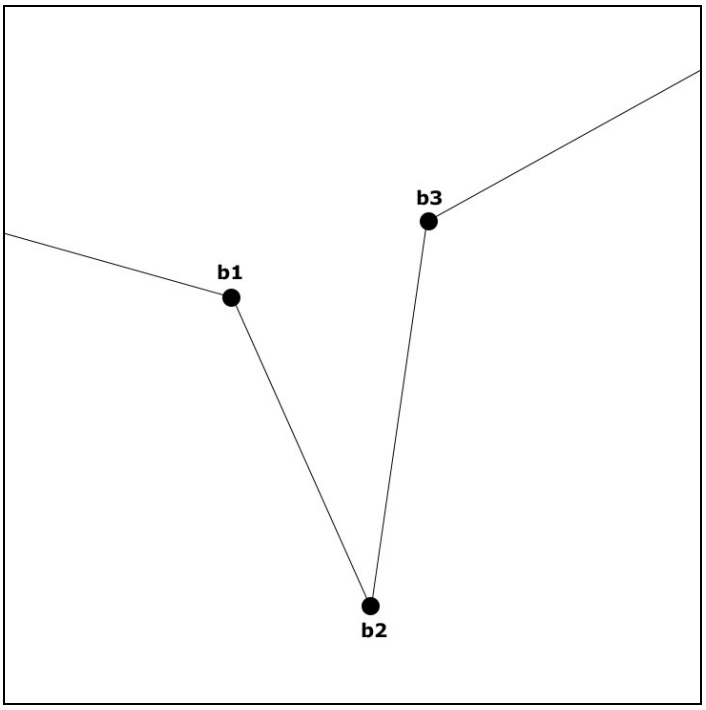

Figure 4.8 Calculating ratios ((b1+b3)/2*b2) between the shoulders (b1 and b3) and lowest point (b2) of absorption features in spectra.

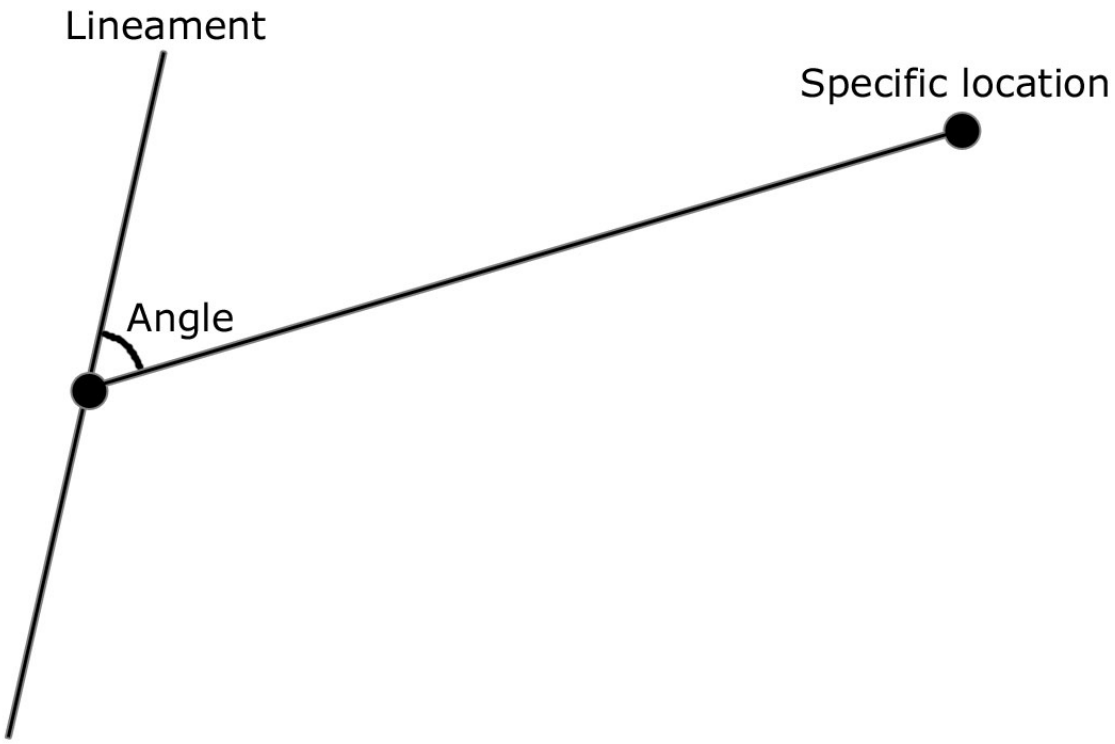

Figure 4.9. Explanation of Concentricity / Radiality.

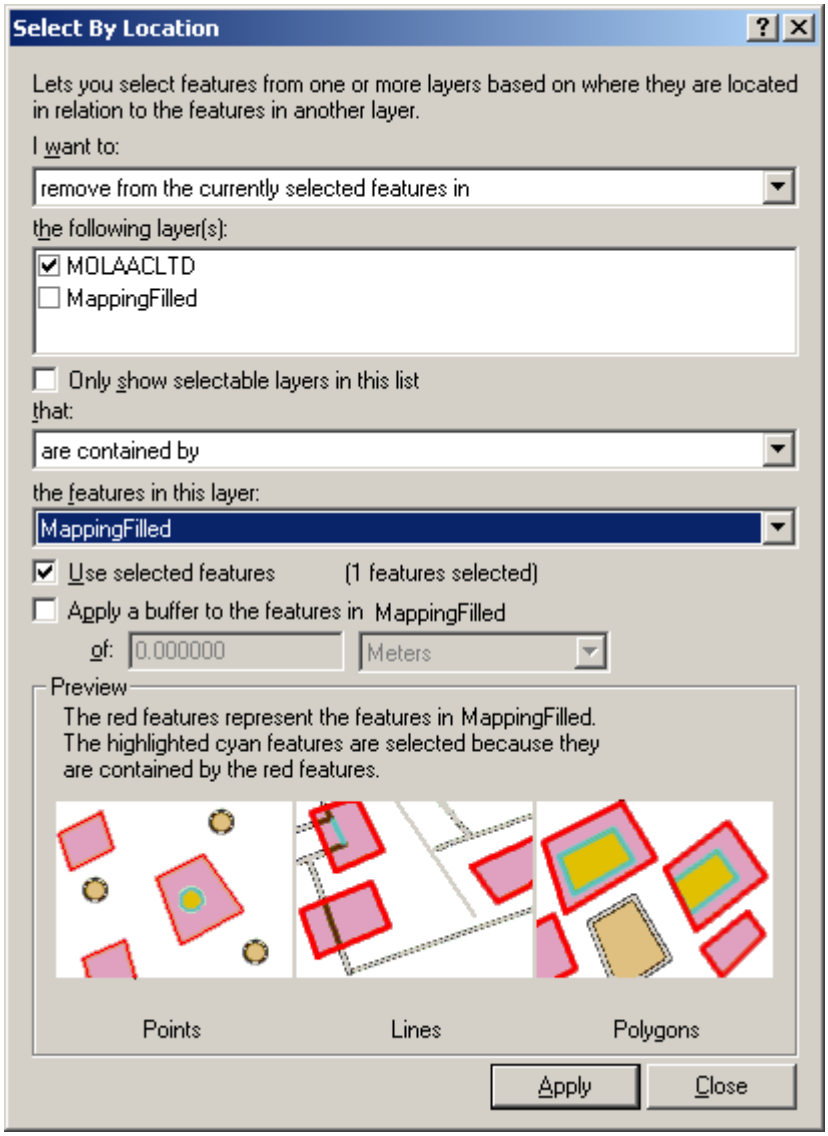

Figure 4.10. The Select By Location window.

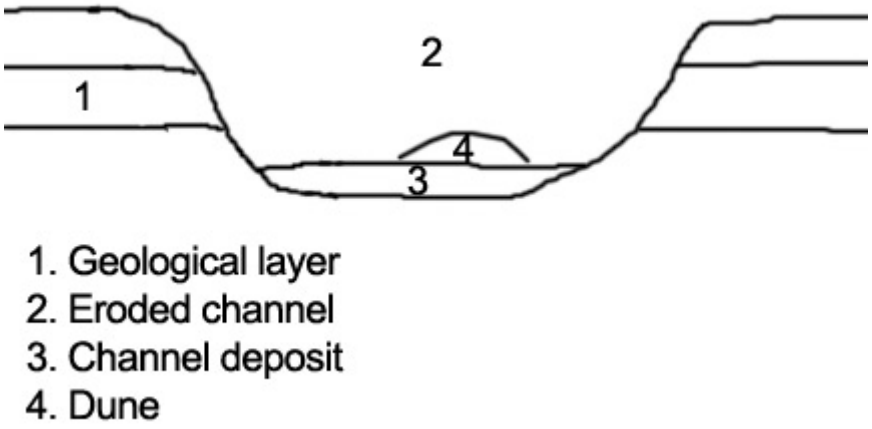

Figure 5.1.1. The difference between geology and geomorphology. The geological layer is considered geology. It however forms part of the topography, which is geomorphology. The eroded channel is considered geomorphology, but not geology (it defines a lack of geology, the layers have been eroded). The dune and the channel deposit are both geology and geomorphology.

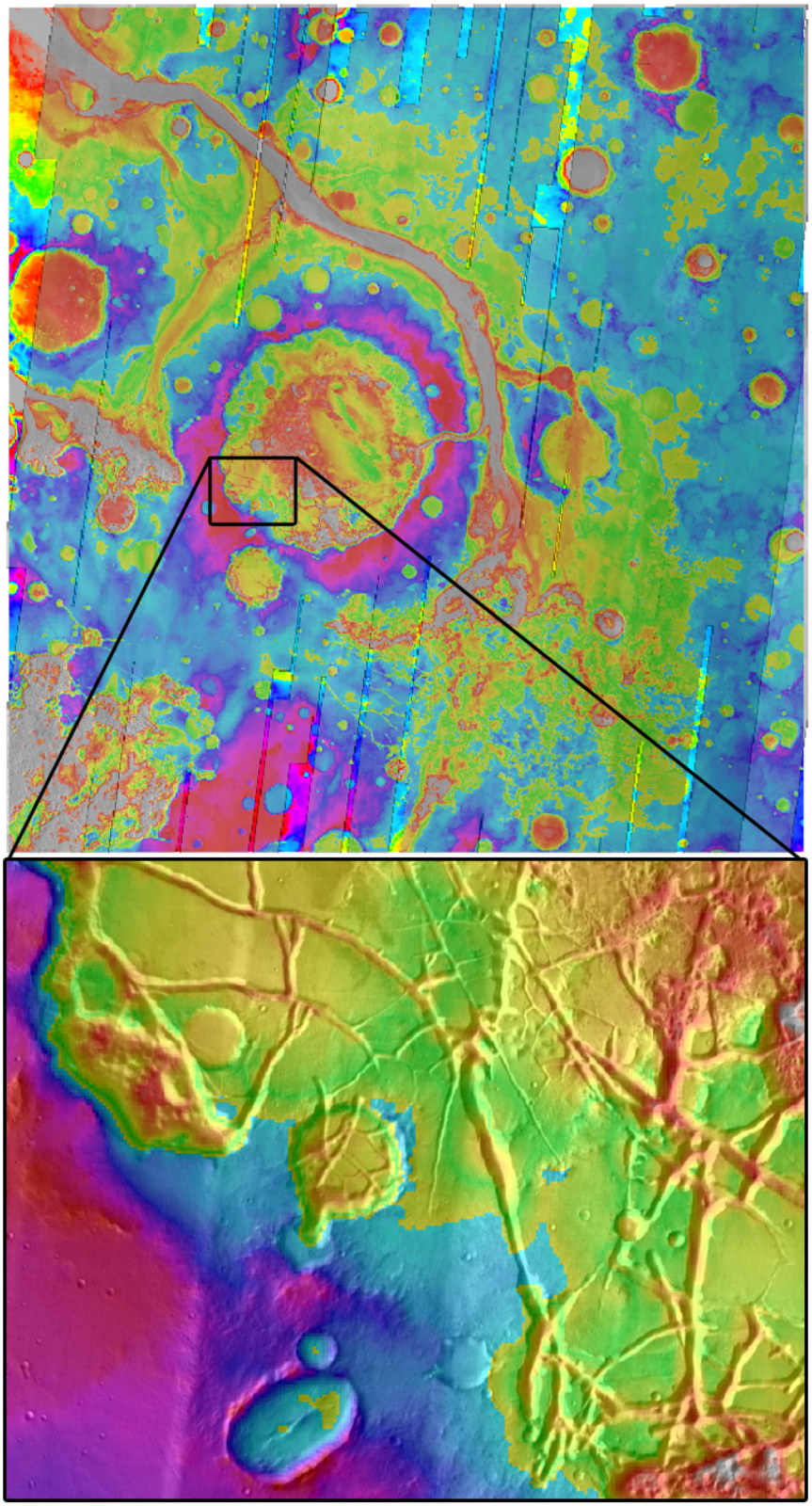

Figure 5.1.2. 50% transparent THEMIS IR day on top of color-coded MOLA elevation data in ArcGIS. This provides a sense of 3D, combining morphology and elevation.

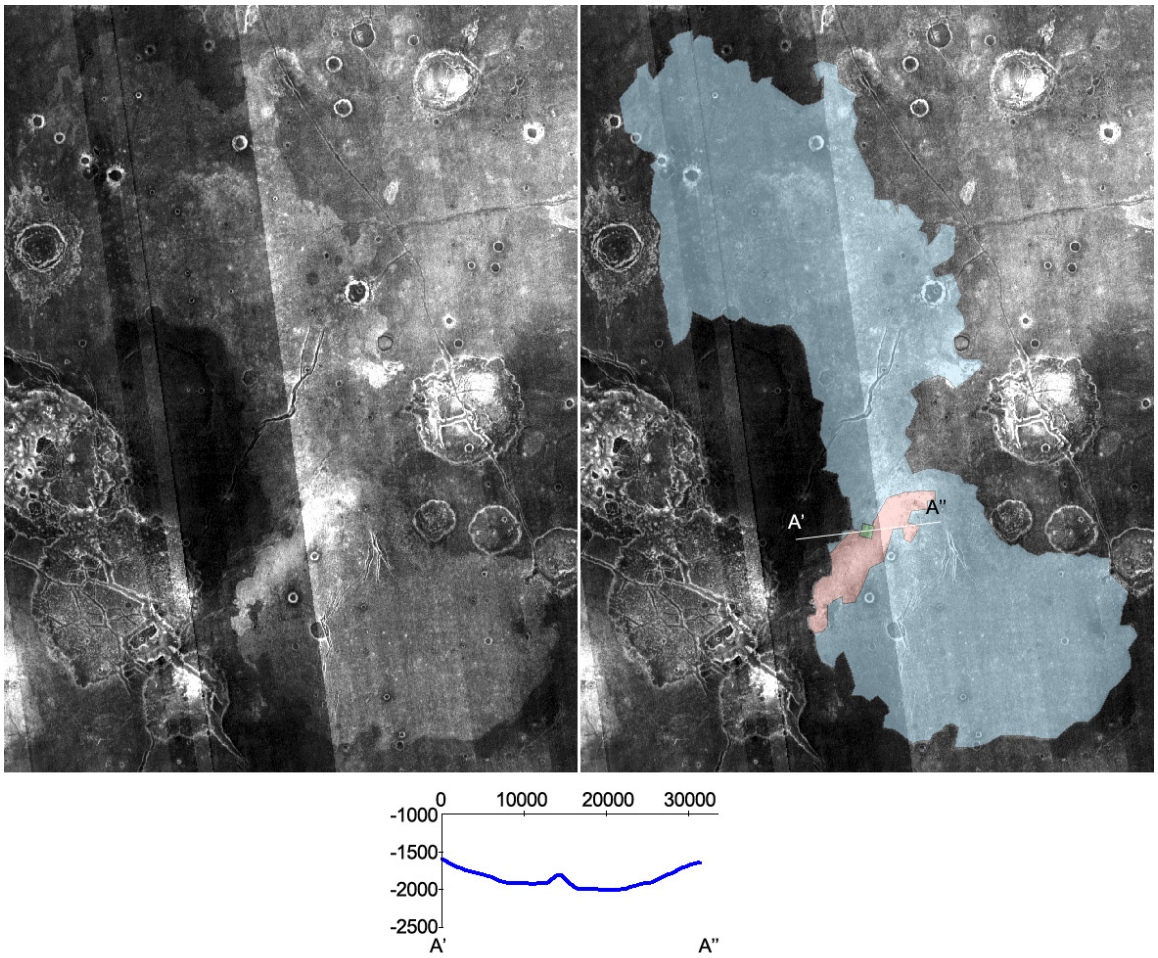

Figure 5.1.3. Possible volcanic deposits visible in THEMIS IR night (Thermal Inertia) data. The TI of the area (pink) around the ~3 km in diameter and 200 m high possible volcanic construct (green) is high compared to the TI of the area farther away (blue). No high resolution data (MOC, THEMIS VIS, HRSC) is currently available covering the possible volcanic construct. Crater counts have not been performed so no age estimate is known.

Geological Map of Aram Chaos and surrounding region, Mars

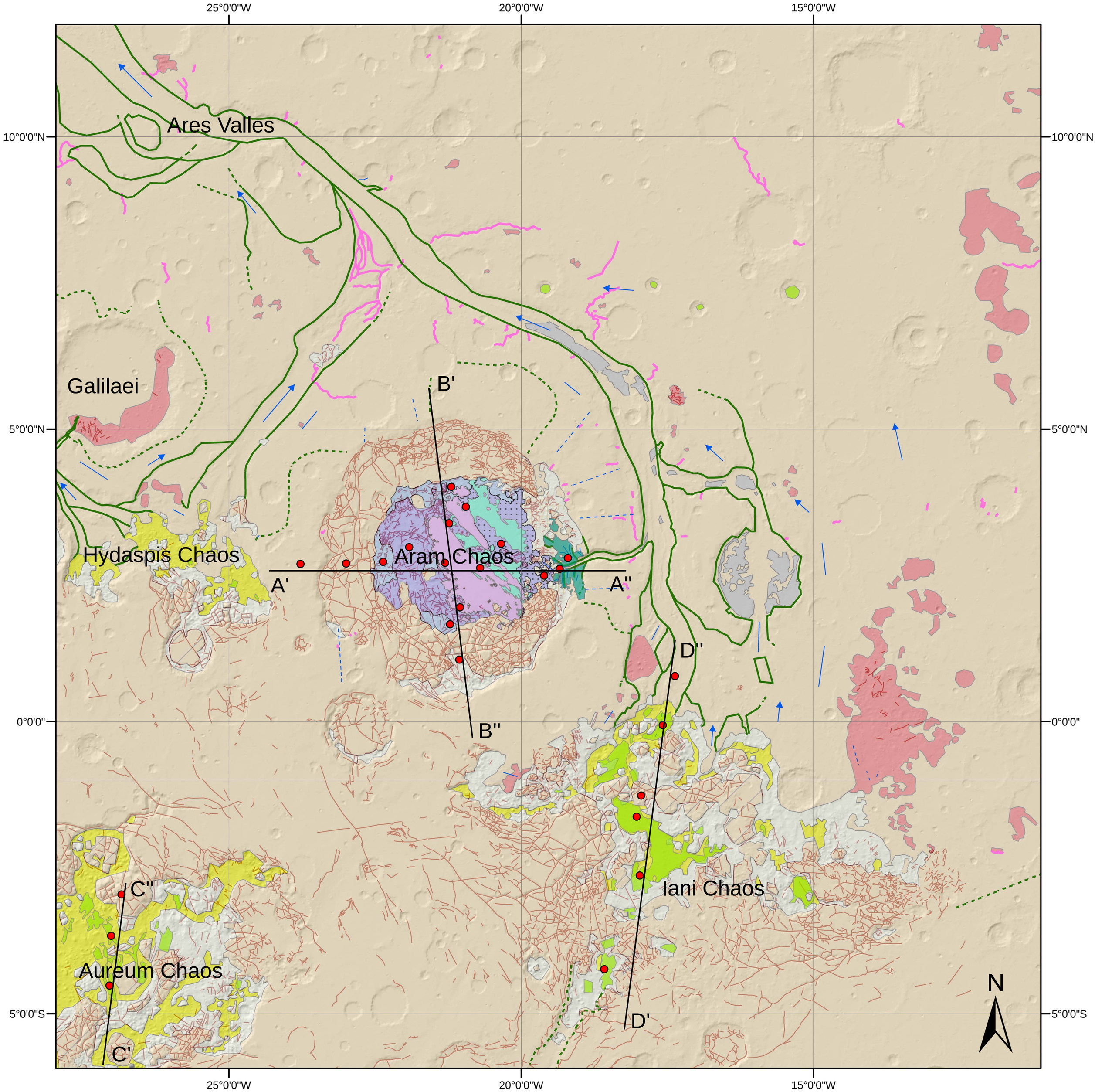

The basemap is a MOLA shaded relief map converted from the MOLA elevation using ArcGIS 9.1.
The projection used is Simple Cylindrical and a sphere radius of 3396190.0 m.
The zero degree longitude is defined as the center of the Airy-0 crater.
The datum used is the USGS MOLA 0 m datum which is the sphere radius of 3396190.0 m.

Legend

Aram Chaos

- Aram Ares Channel Deposits (AACD)
- Upper Aram Chaos Formation (UACF)
- Intermediate Aram Chaos Formation (IACF)
- Lower Aram Chaos Formation (LACF) (broken, fractured, smooth)

Regional

- Light Toned Channel Deposits (LTCD)
- Iani Chaos Deposits (ICD) type 5
- Iani Chaos Deposits (ICD) type 4
- Iani Chaos Deposits (ICD) type 3
- Iani Chaos Deposits (ICD) type 2
- Iani Chaos Deposits (ICD) type 1
- Aureum Chaos Deposits (ACD)
- Highland Terrain (HT) - HT mesas - Intermediate Chaotic Terrain (ICT) - Chaotic Terrain Floor (CTF) - Small-scale Fractured and Chaotic Terrain (SFCT)

Channel morphology

- Clear channel outline
- Unclear channel outline
- Clear direction of flow
- Unclear direction of flow
- Unclear flow morphology
- Small channels

Other

- Fractures
- Cross Sections
- Stratigraphical columns

Figure 5.1.4. The (Structural) Geological and Geomorphological map of Aram Chaos and surrounding region, Mars.

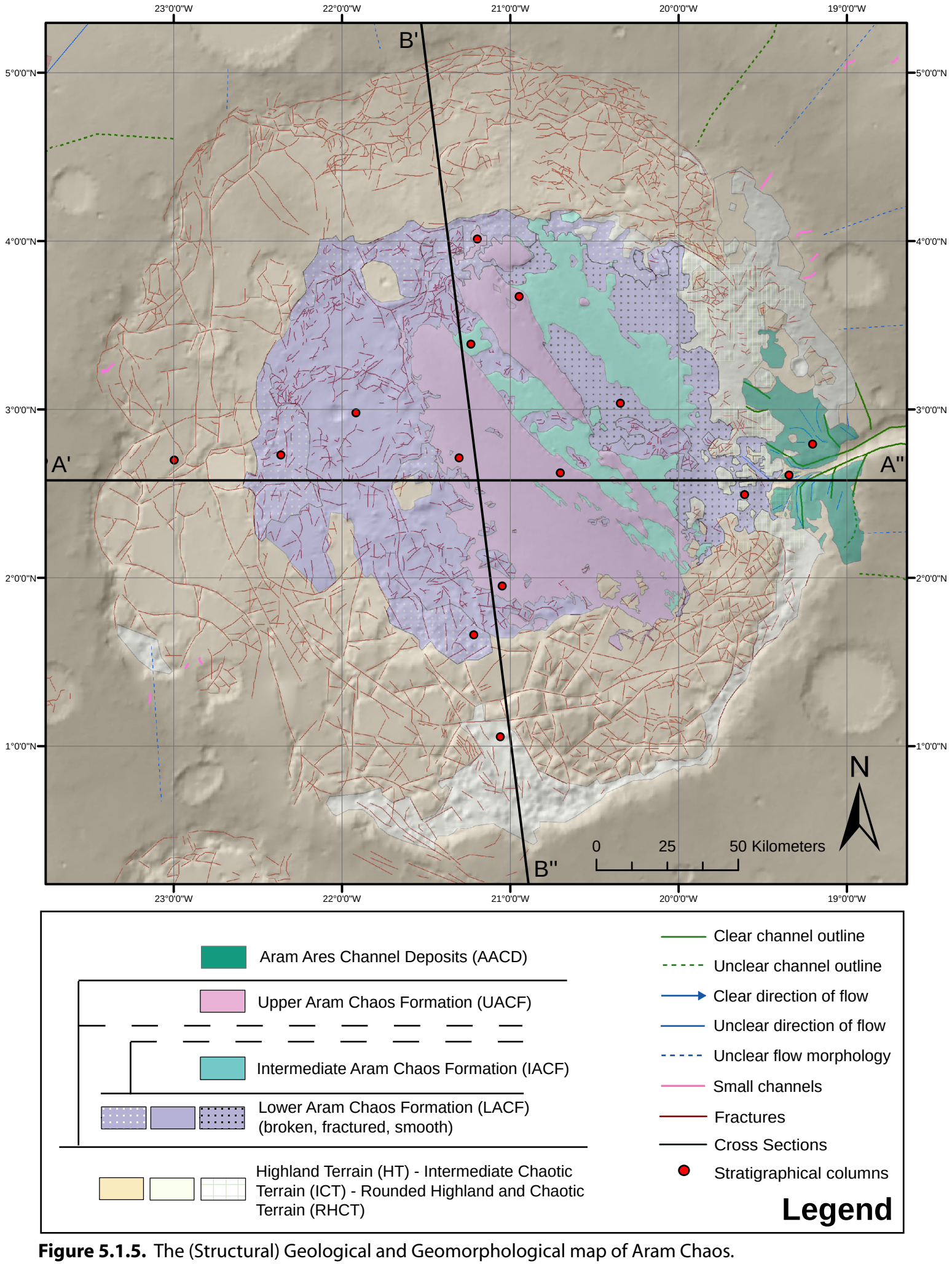

Figure 5.1.5. The (Structural) Geological and Geomorphological map of Aram Chaos.

Geological Mapping of the NE part of Aureum Chaos, Mars

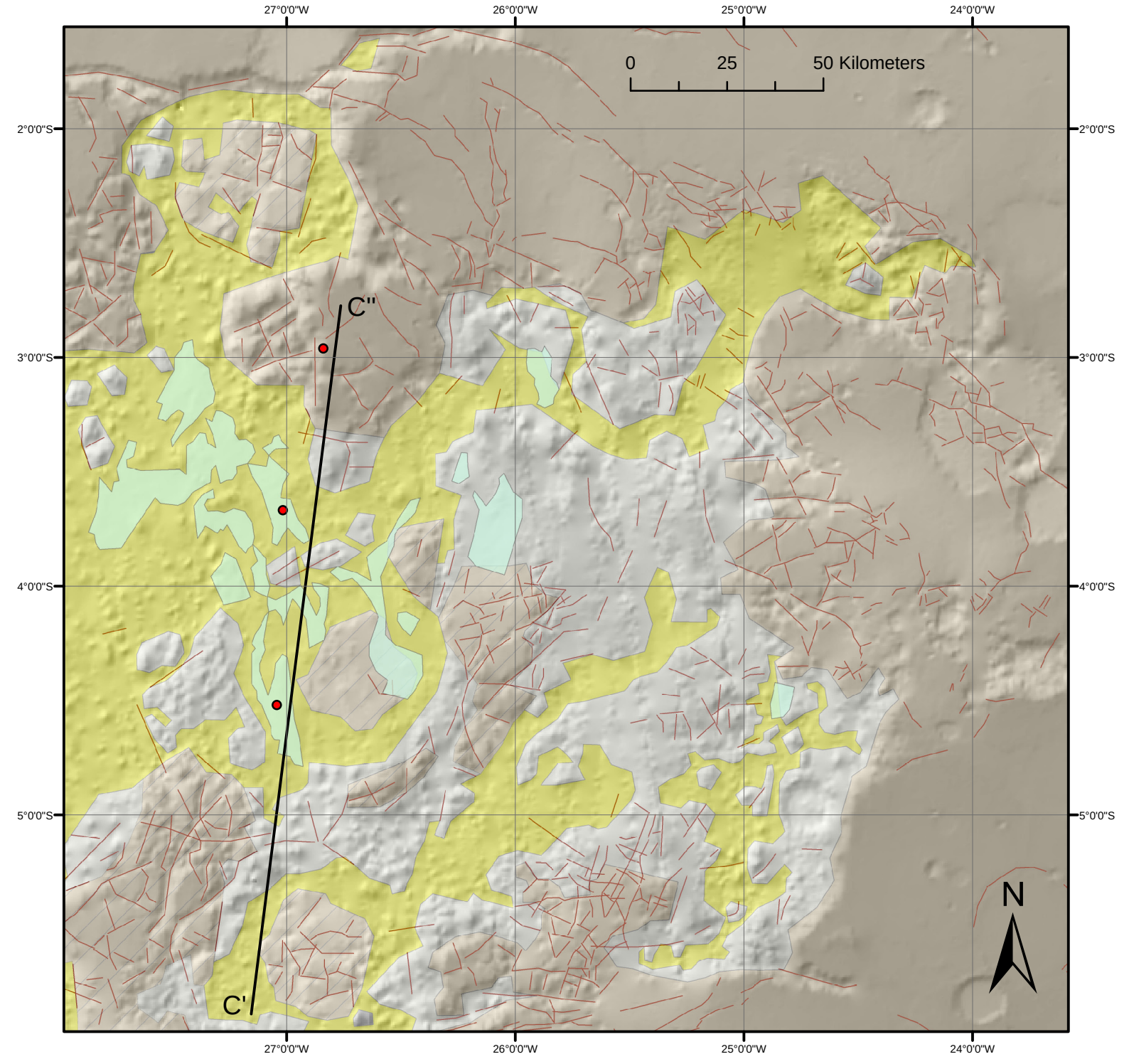

Legend

- Aureum Chaos Deposits (ACD)
- Highland Terrain (HT) - Highland Terrain mesas - Intermediate Chaotic Terrain (ICT) - Chaotic Terrain Floor (CTF)
- Fractures
- Cross Sections
- Stratigraphical columns

Figure 5.1.6. The (Structural) Geological and Geomorphological map of the NE part of Aurum Chaos.

Geological Mapping of Iani Chaos, Mars

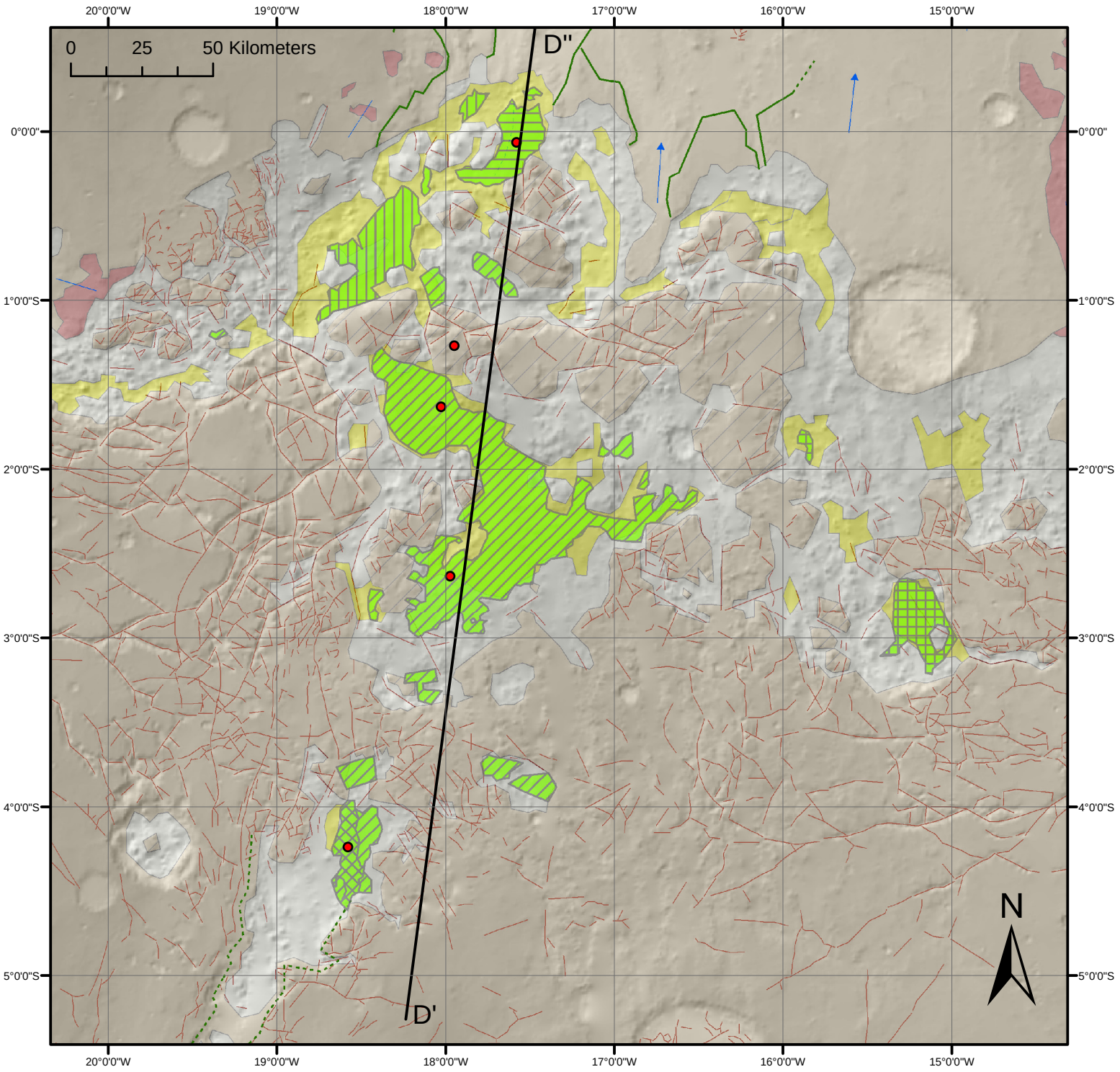

Iani Chaos Deposits (ICD) type 5

Iani Chaos Deposits (ICD) type 4

Iani Chaos Deposits (ICD) type 3

Iani Chaos Deposits (ICD) type 2

Iani Chaos Deposits (ICD) type 1

Highland Terrain (HT) - Highland Terrain mesas - Intermediate Chaotic Terrain (ICT) - Chaotic Terrain Floor (CTF) - Small-scale Fractured and Chaotic Terrain (SFCT)

Clear channel outline

Unclear channel outline

Clear direction of flow

Unclear direction of flow

Unclear flow morphology

Small channels

Fractures

Cross Sections

Stratigraphical columns

Legend

Figure 5.1.7. The (Structural) Geological and Geomorphological map of Iani Chaos.

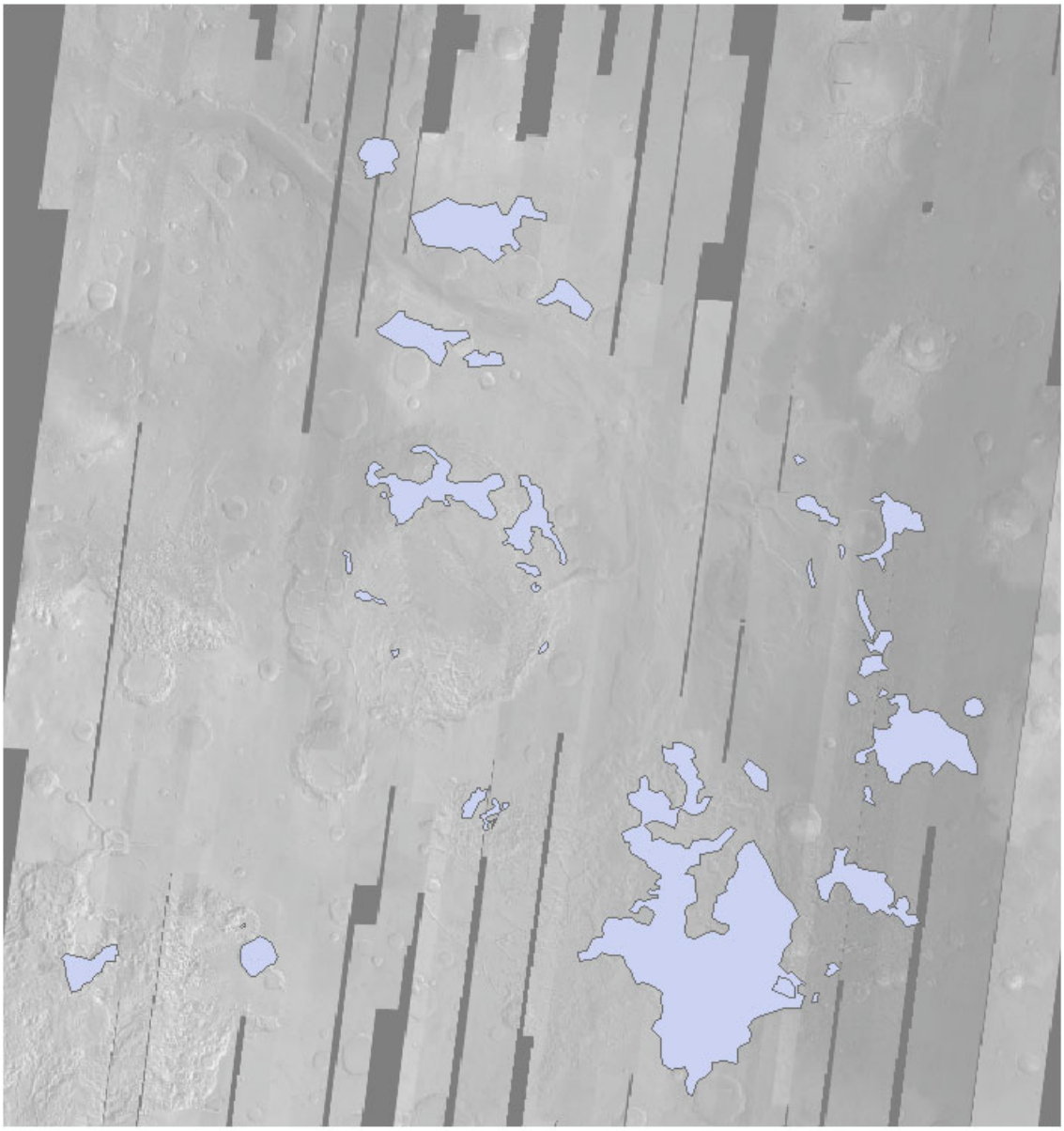

Figure 5.1.8. Mapped occurrences of Small-scale Hills Terrain.

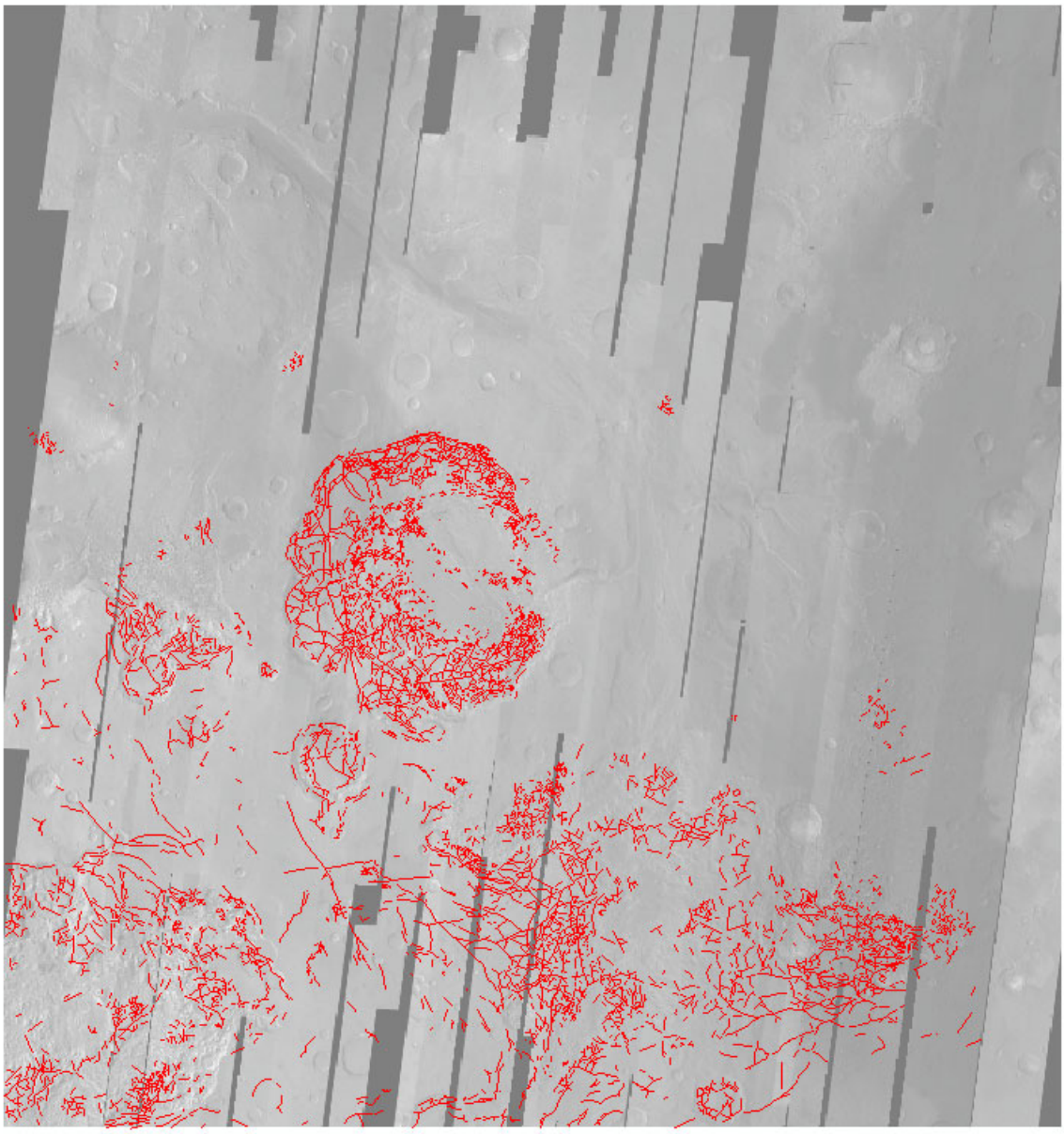

Figure 5.1.9. The mapped lineaments.

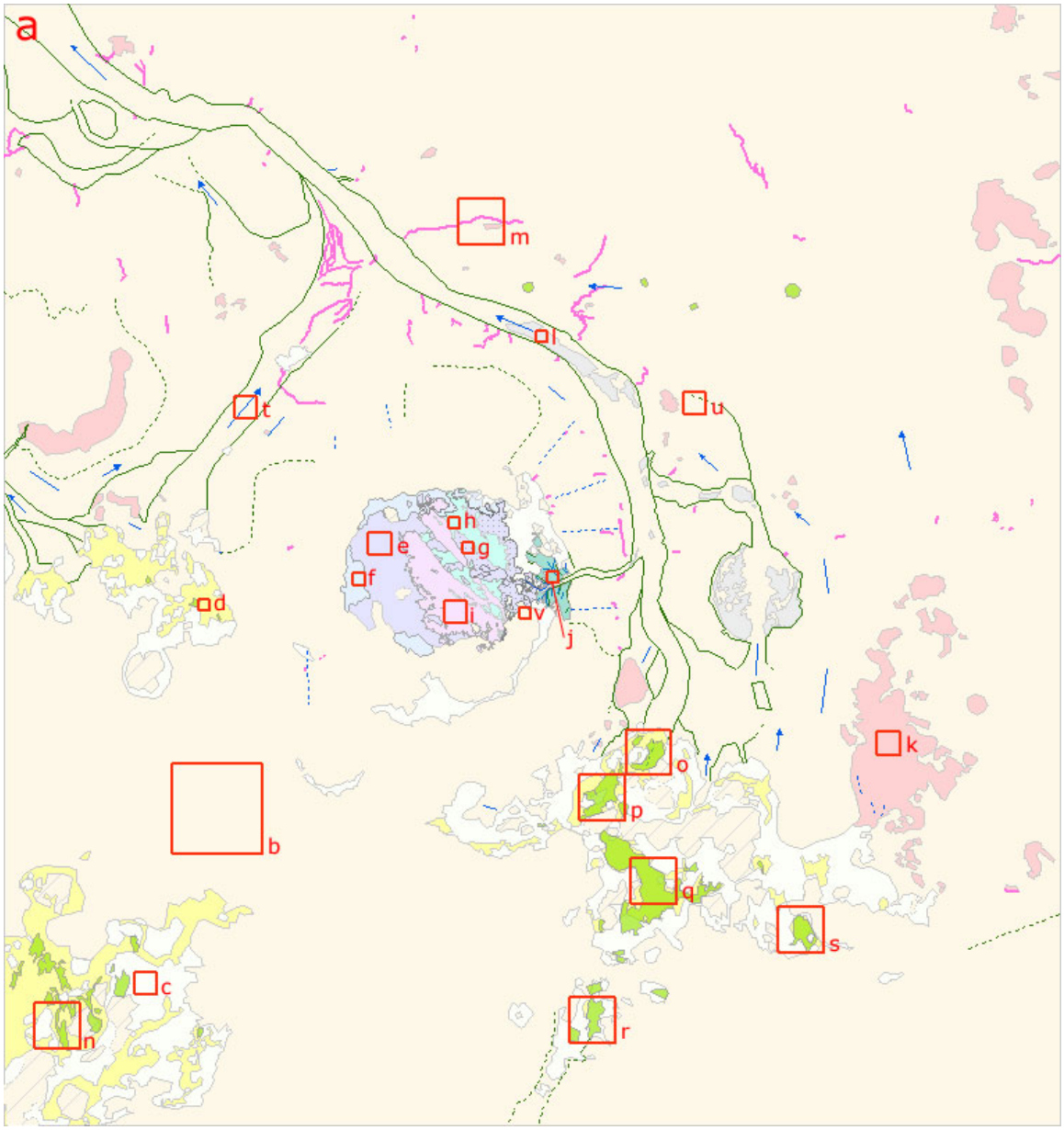

Figure 5.1.10. Mapped unit type locations. For explanation of the images see Table 5.1.

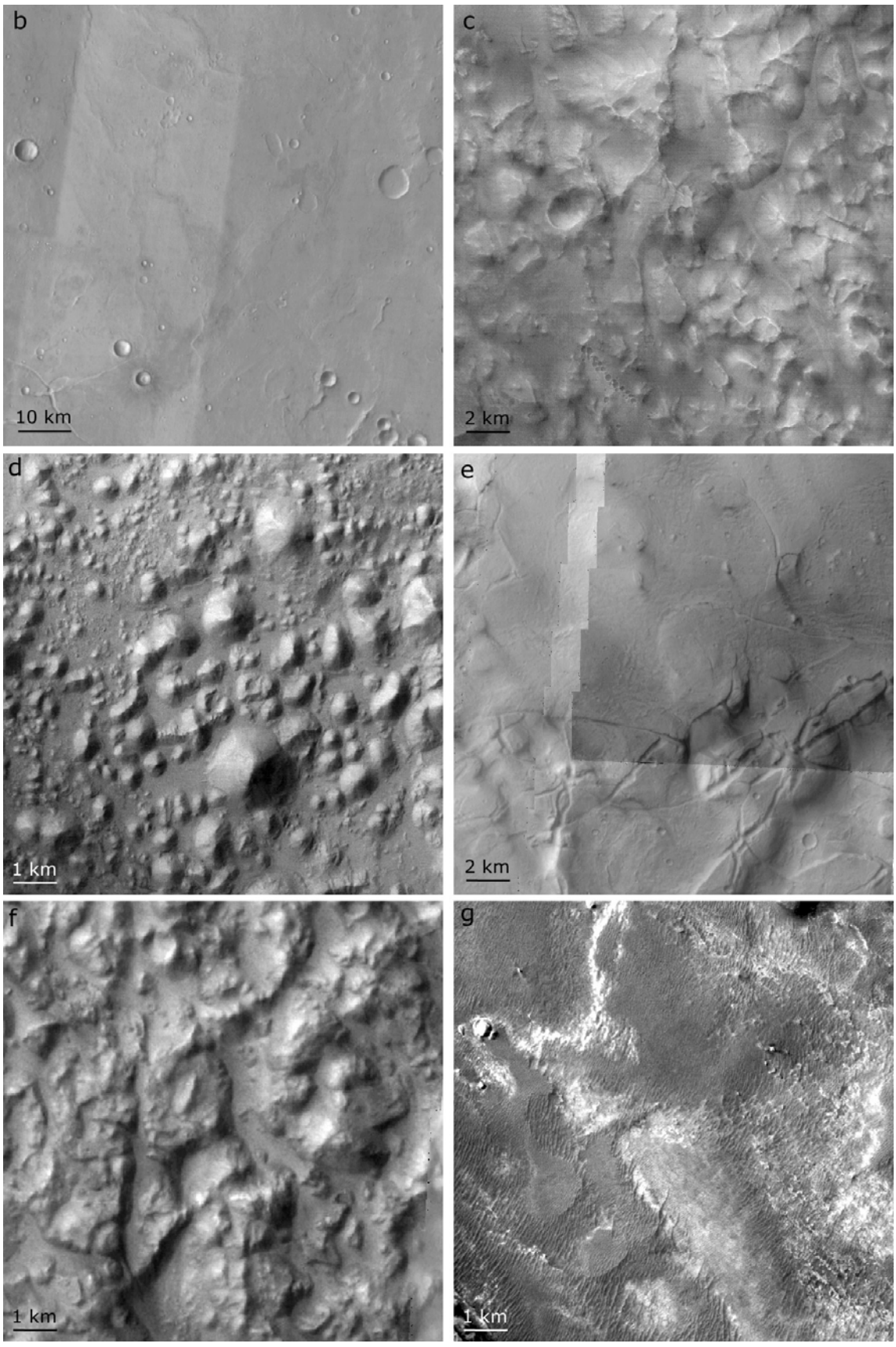
b
10 km
c
2 km
d
1 km
e
2 km
f
1 km
g
1 km

Figure 5.1.10 (continued). b. Highland Terrain (THEMIS IR day). **c.** Intermediate Chaotic Terrain (HRSC nadir). **d.** Chaotic Terrain Floor (HRSC nadir). **e.** Fractured Lower Aram Chaos Formation (THEMIS VIS). **f.** Broken Lower Aram Chaos Formation (THEMIS VIS). **g.** Smooth Lower Aram Chaos Formation (HRSC nadir).

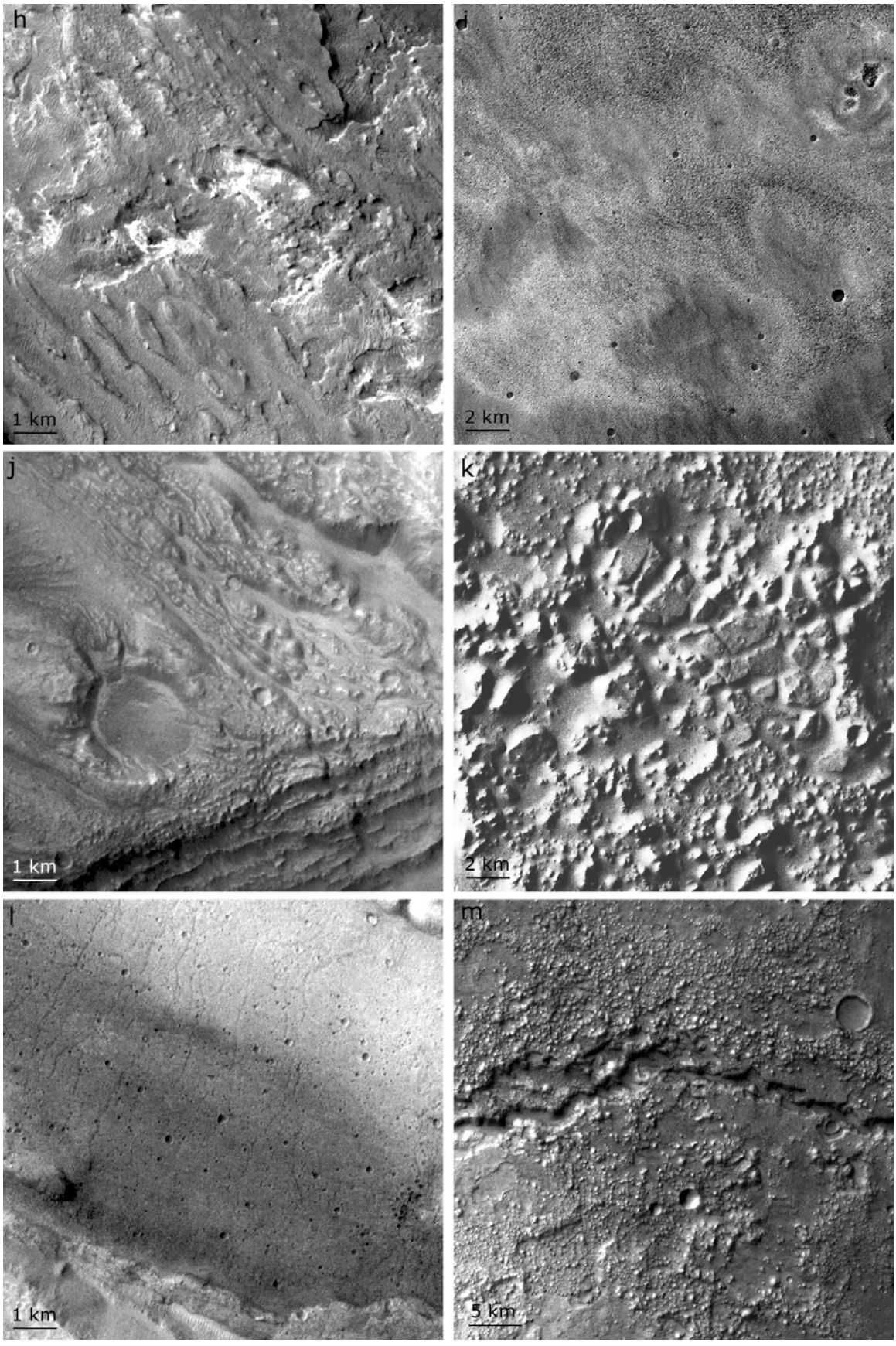
h
1 km
i
2 km
j
1 km
k
2 km
l
1 km
m
5 km

Figure 5.1.10 (continued). h. Intermediate Aram Chaos Formation (HRSC nadir). **i.** Upper Aram Chaos Formation (HRSC nadir). **j.** Aram Ares Channel Deposits (HRSC nadir). **k.** Small-scale Fractured and Chaotic Terrain (HRSC nadir). **l.** Light Toned Channel Deposits (HRSC nadir). **m.** Small-scale Hills Terrain (HRSC nadir).

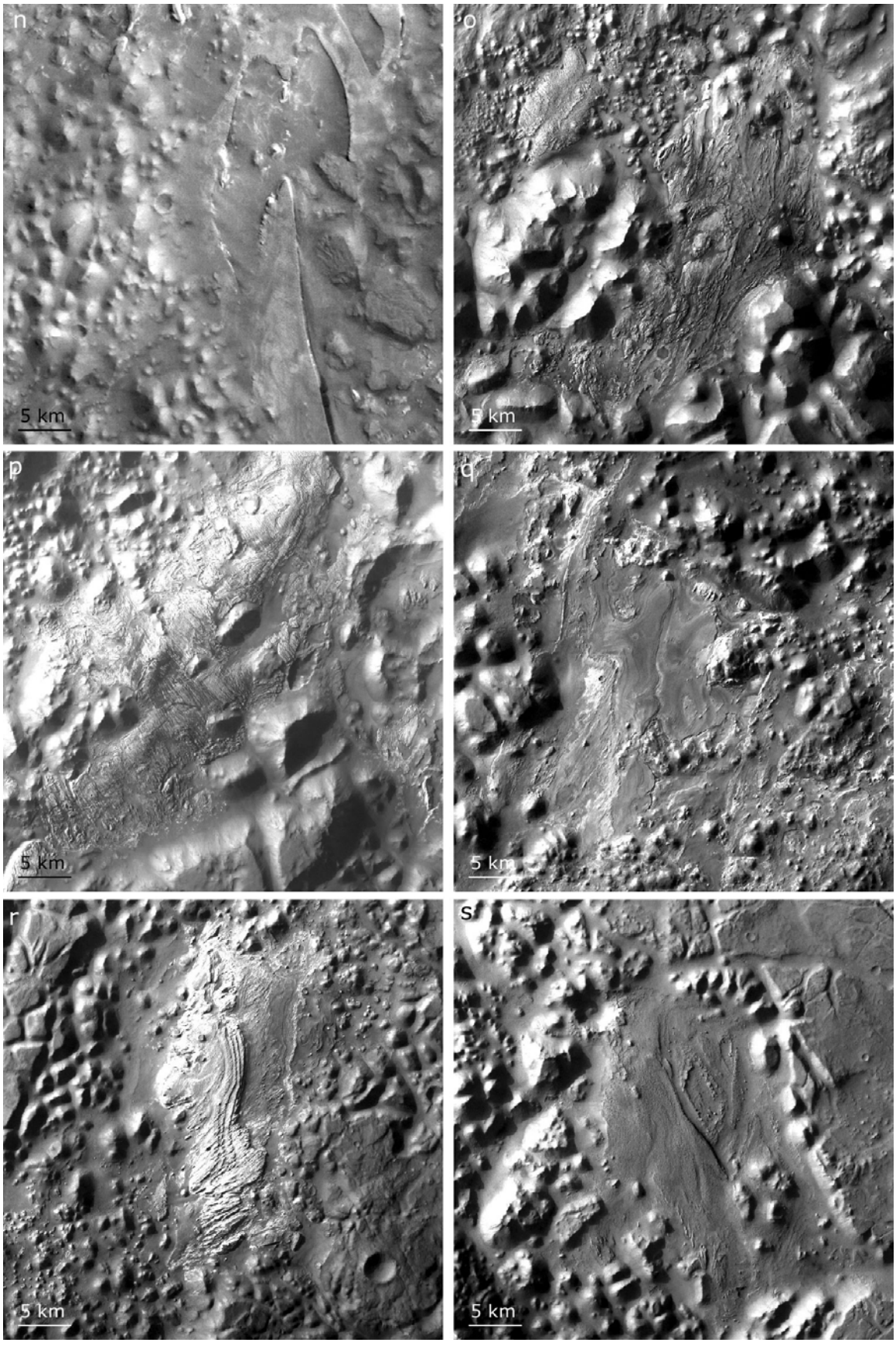
n
5 km
o
5 km
p
5 km
q
5 km
r
5 km
s
5 km

Figure 5.1.10 (continued). n. Aureum Chaos Deposits (THEMIS IR day). **o.** (HRSC nadir). **p.** (HRSC nadir). **q.** (HRSC nadir). **r.** (HRSC nadir). **s.** (HRSC nadir).

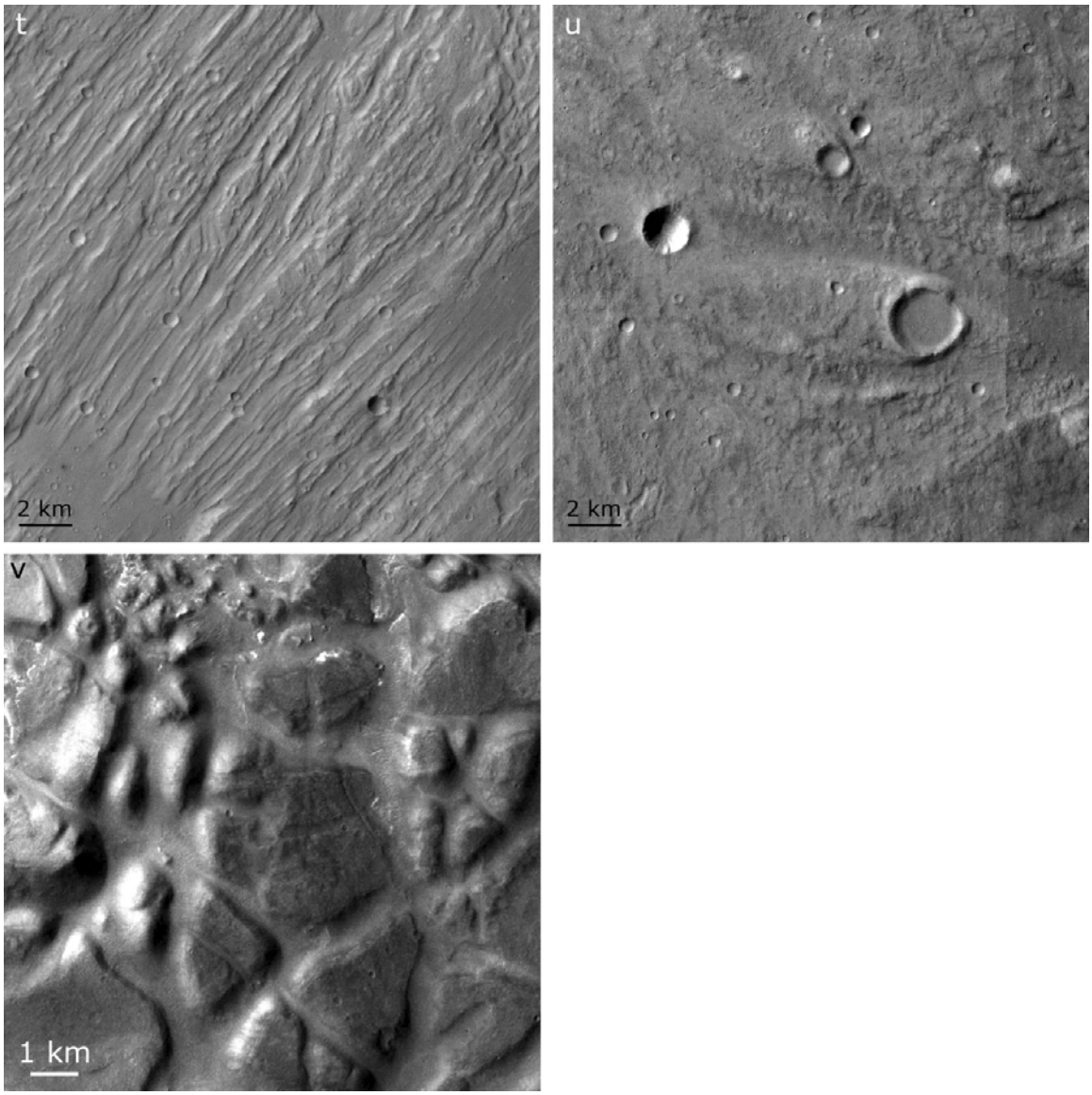

Figure 5.1.10 (continued). t. Outflow Channel Terrain (HRSC nadir). **u.** Flooded Highland Terrain (HRSC nadir). **v.** Rounded Chaotic and Highland Terrain (HRSC nadir).

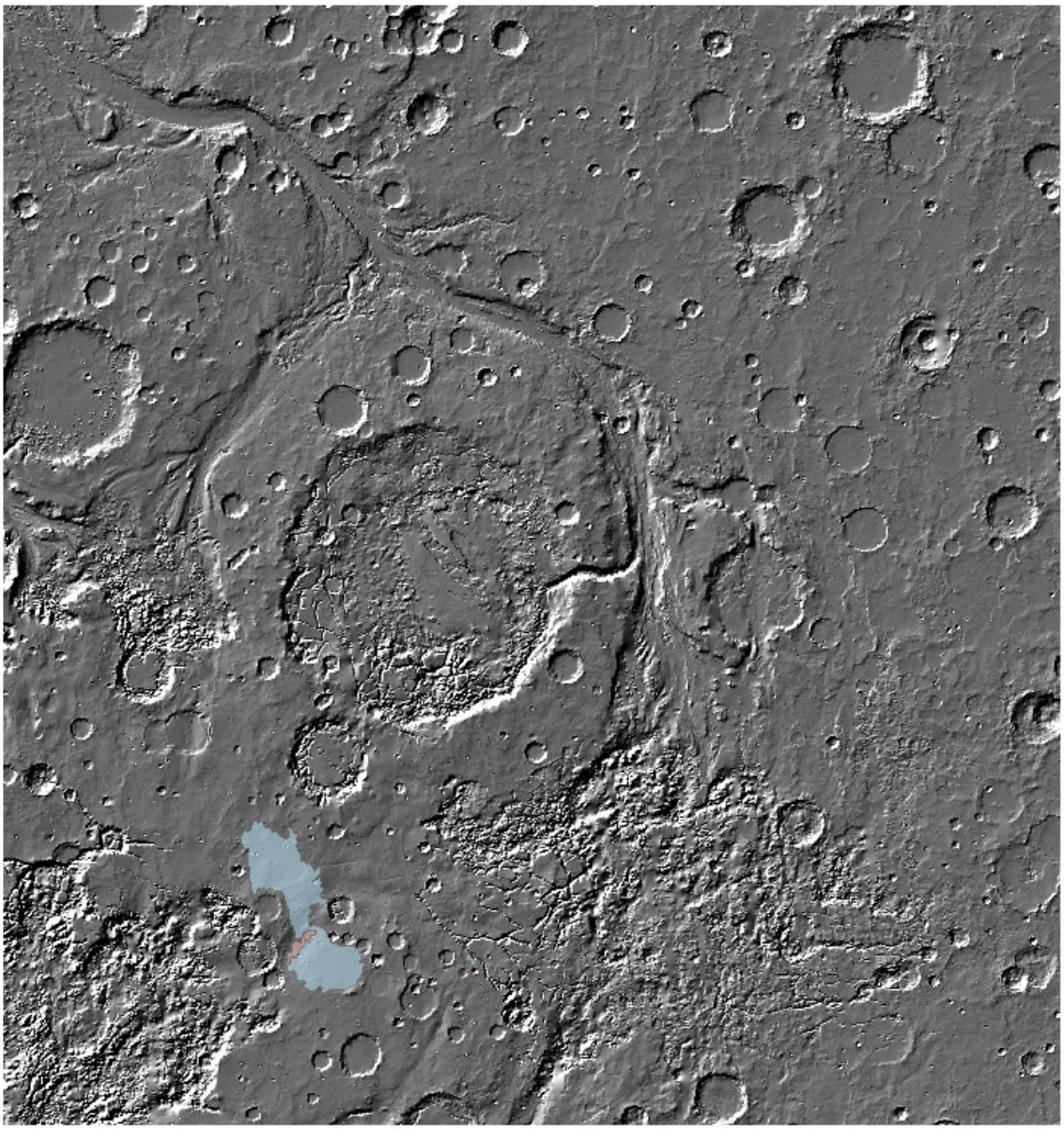

Figure 5.1.11. Possible volcanic deposits (Figure 5.1.3). The base map is a MOLA shaded relief map.

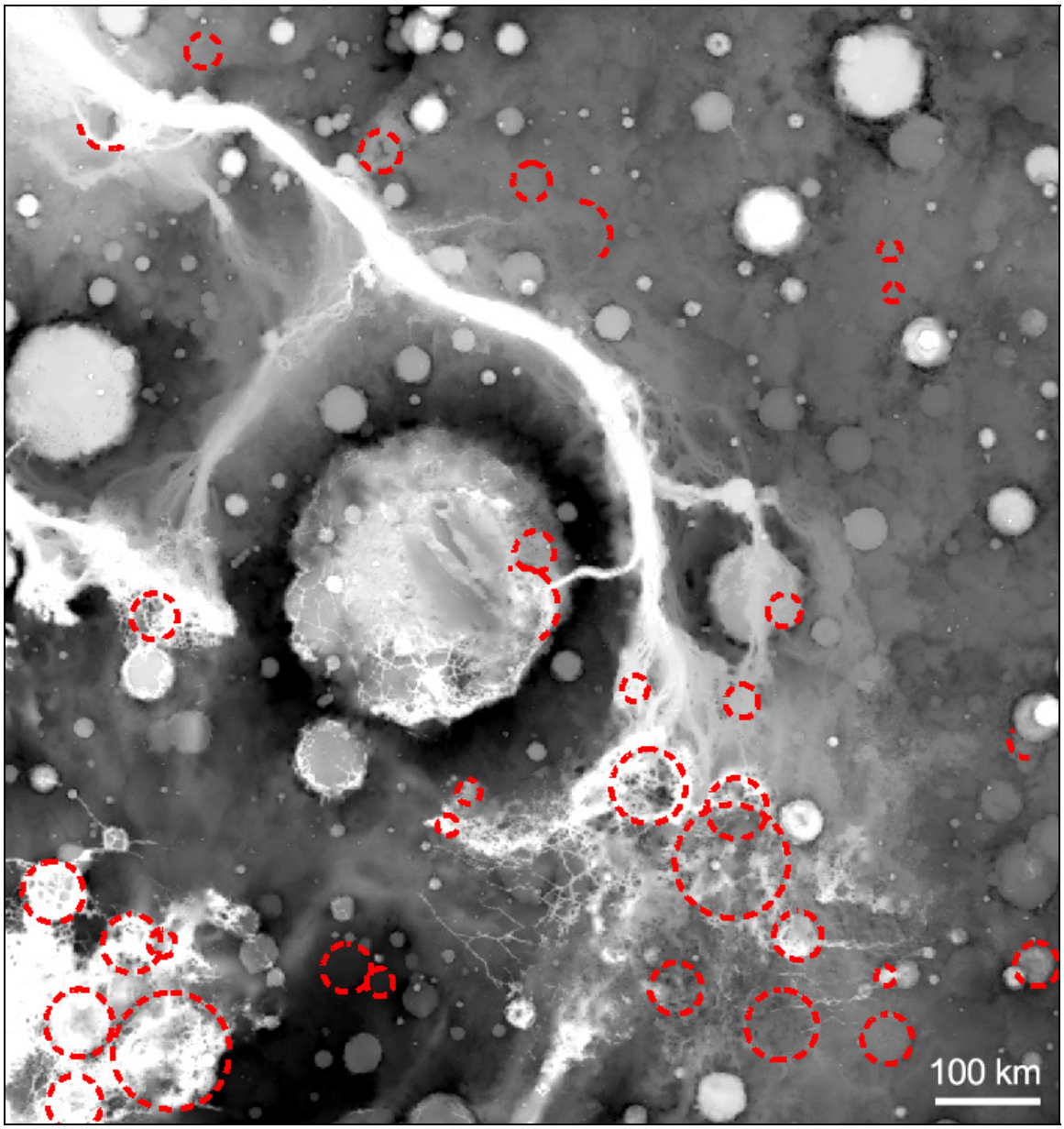

Figure 5.1.12. Mapped remnants of possible impact craters on top of MOLA elevation data (black is high, white is low).

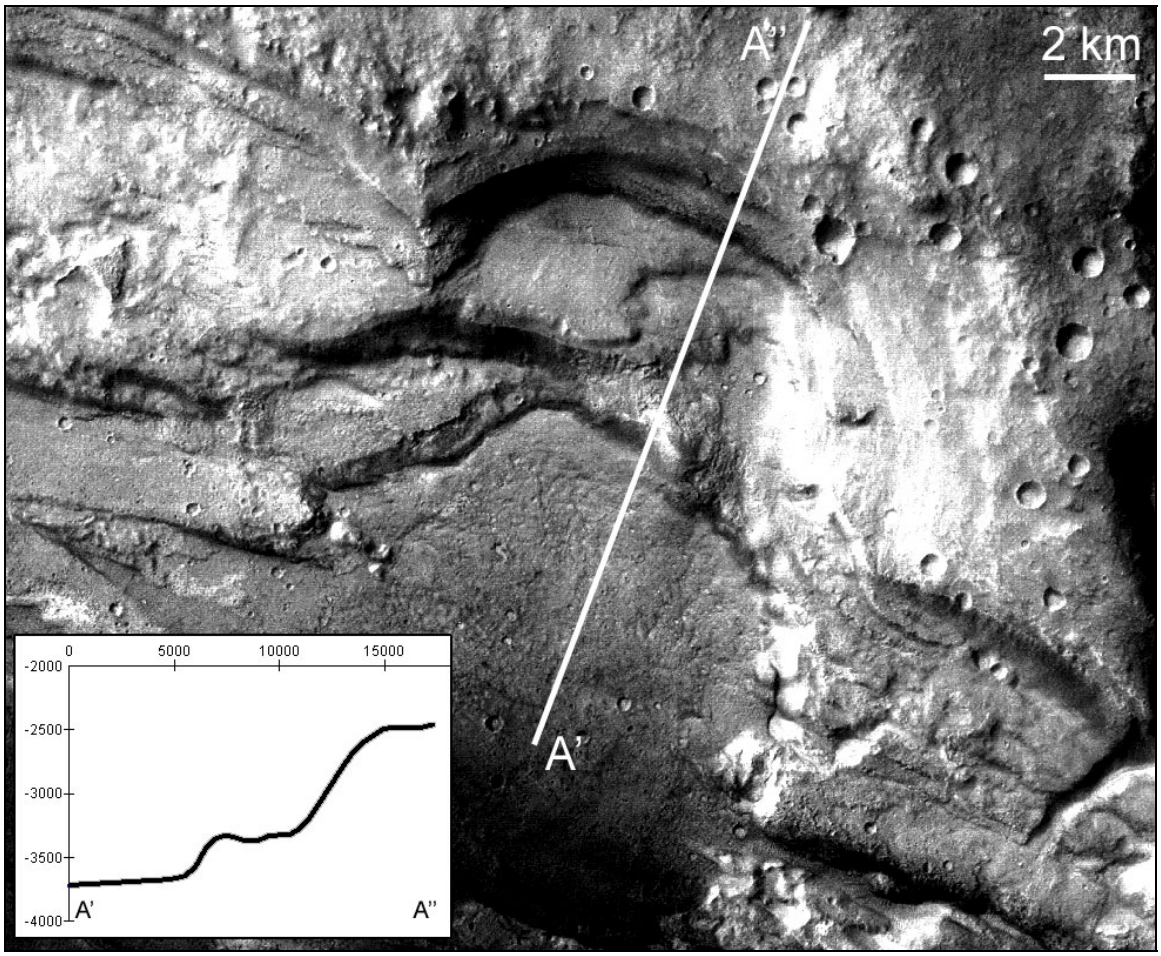

Figure 5.1.13. Approximately 100-200m scale layering of Highland Terrain, forming terraces, is visible in the ~1 km high main Ares Vallis channel wall. The circular shape of the terraced escarpment suggests the HT consists of buried impact craters.

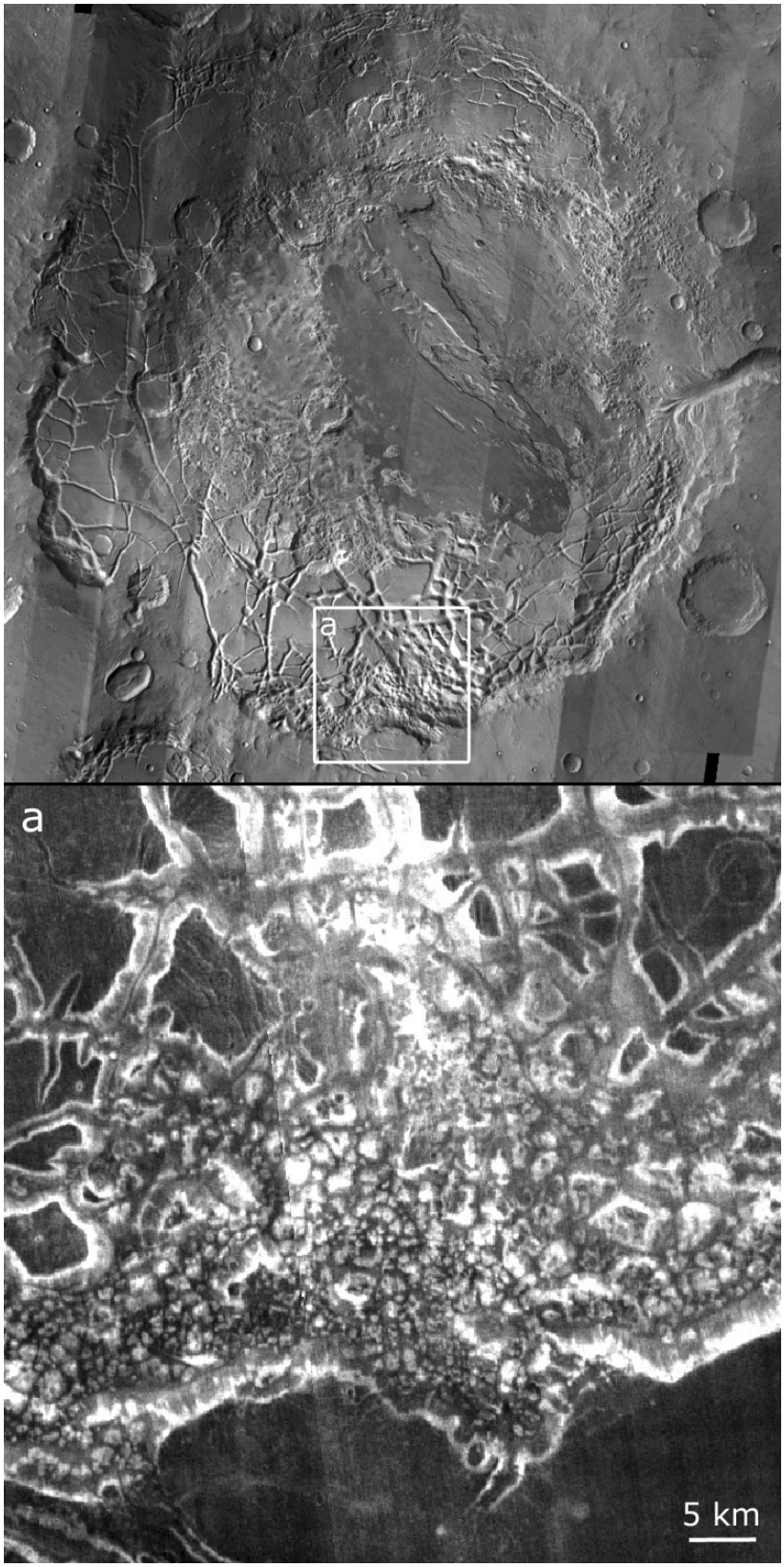

Figure 5.1.14. THEMIS IR night image showing numerous km scale hills within the southern Chaotic Terrain of Aram Chaos.

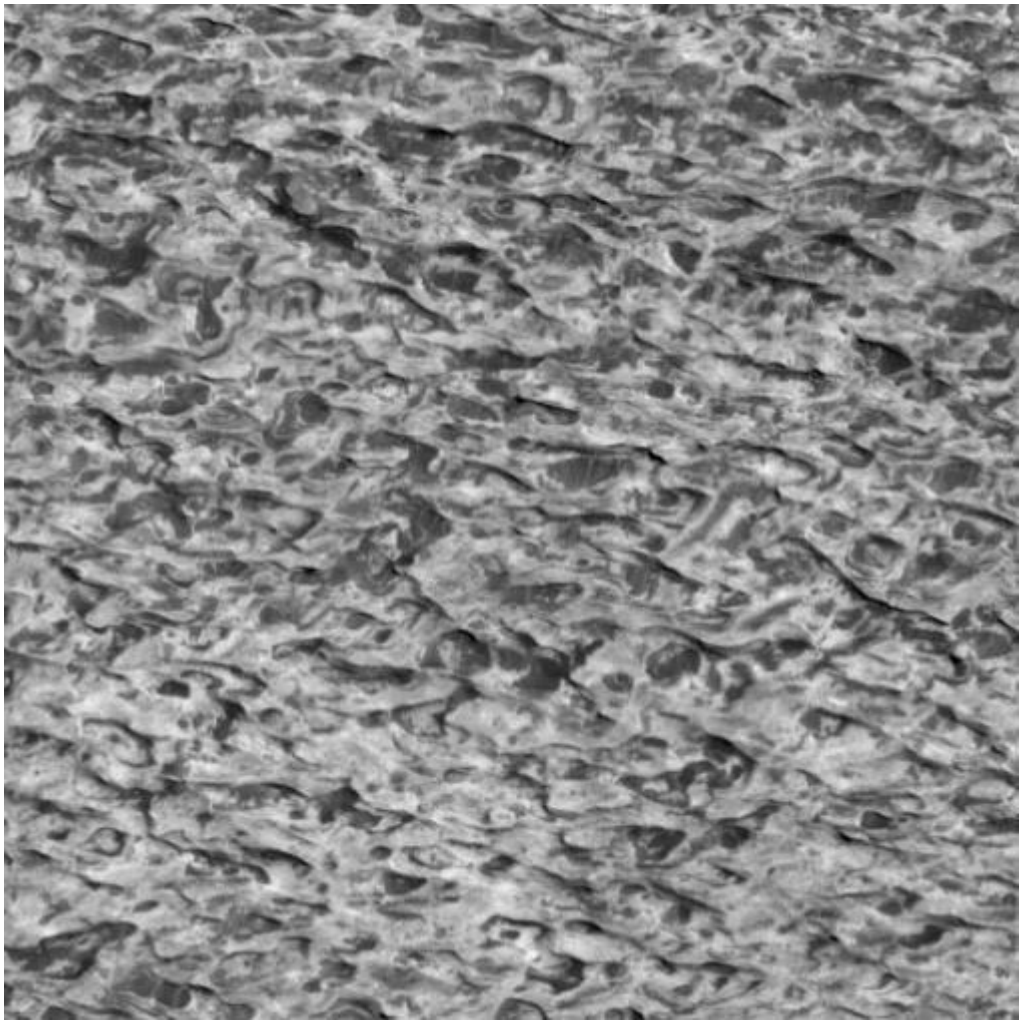

Figure 5.1.15. The surface morphology of the Upper Aram Chaos Formation (Part of MOC image M1201687, 2.93 m/pixel resolution).

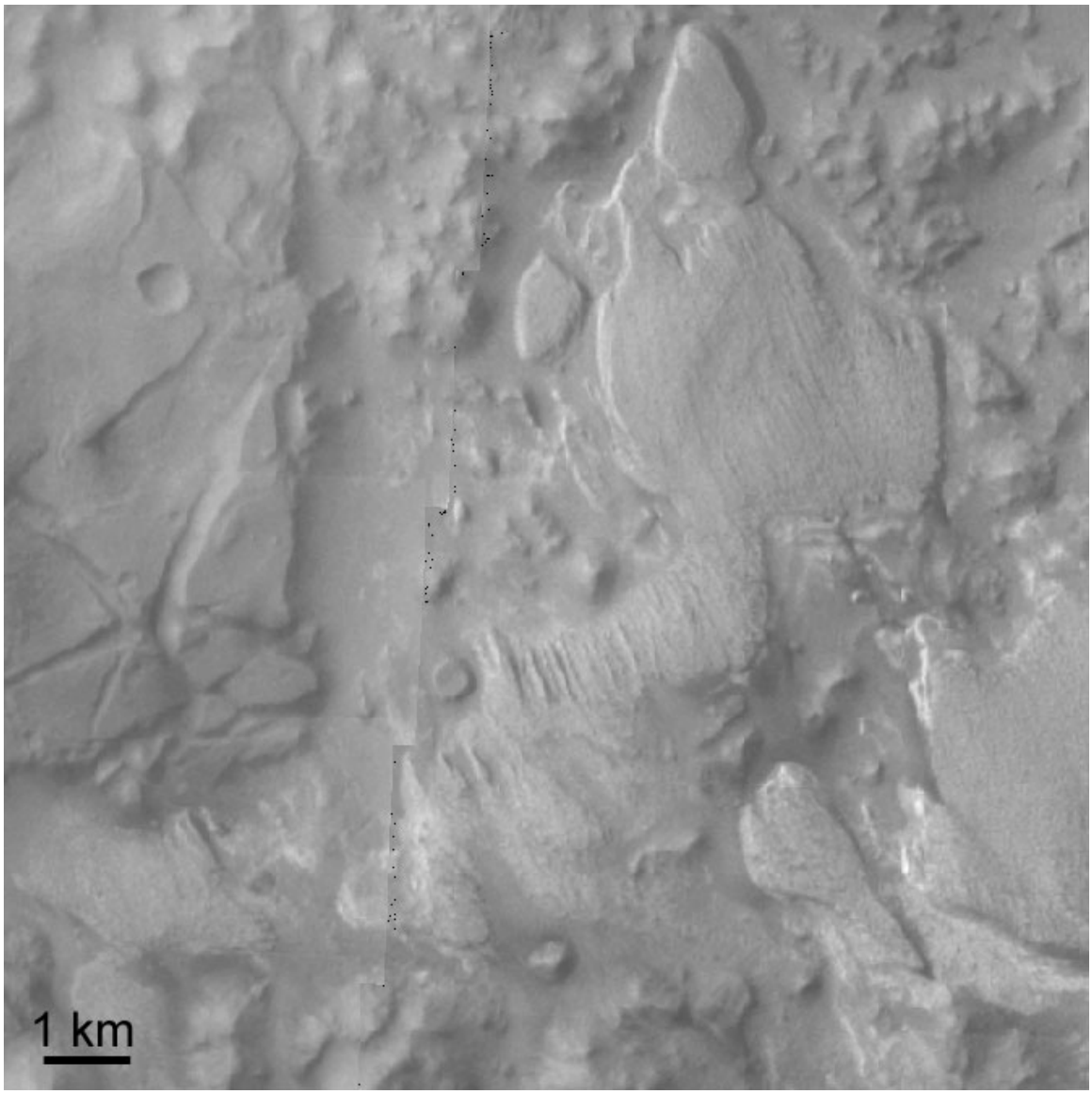

Figure 5.1.16. Wind eroded lineations in the Upper Aram Chaos Formation material (THEMIS VIS, image center 338.77°E, 3.99°N).

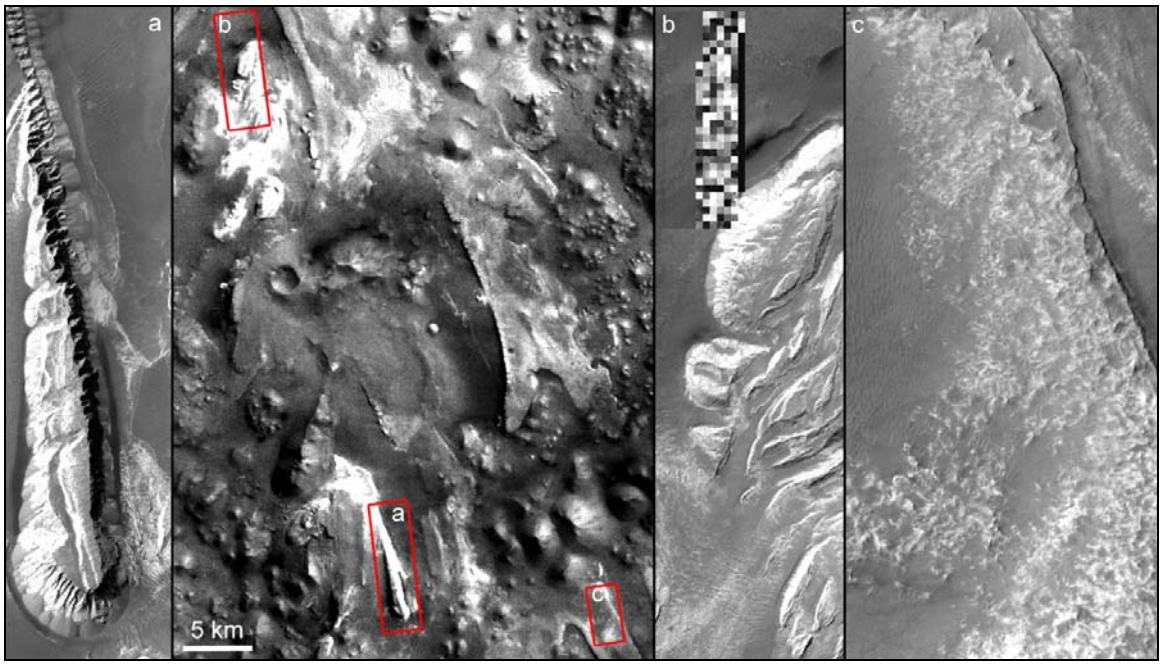

Figure 5.1.17. The Aureum Chaos Deposits. For explanation see text. Main image center 332.85°E, 3.69°S. **a.** Part of MOC image E0300828. **b.** Part of MOC image M1901566. **c.** Part of MOC image R1702066.

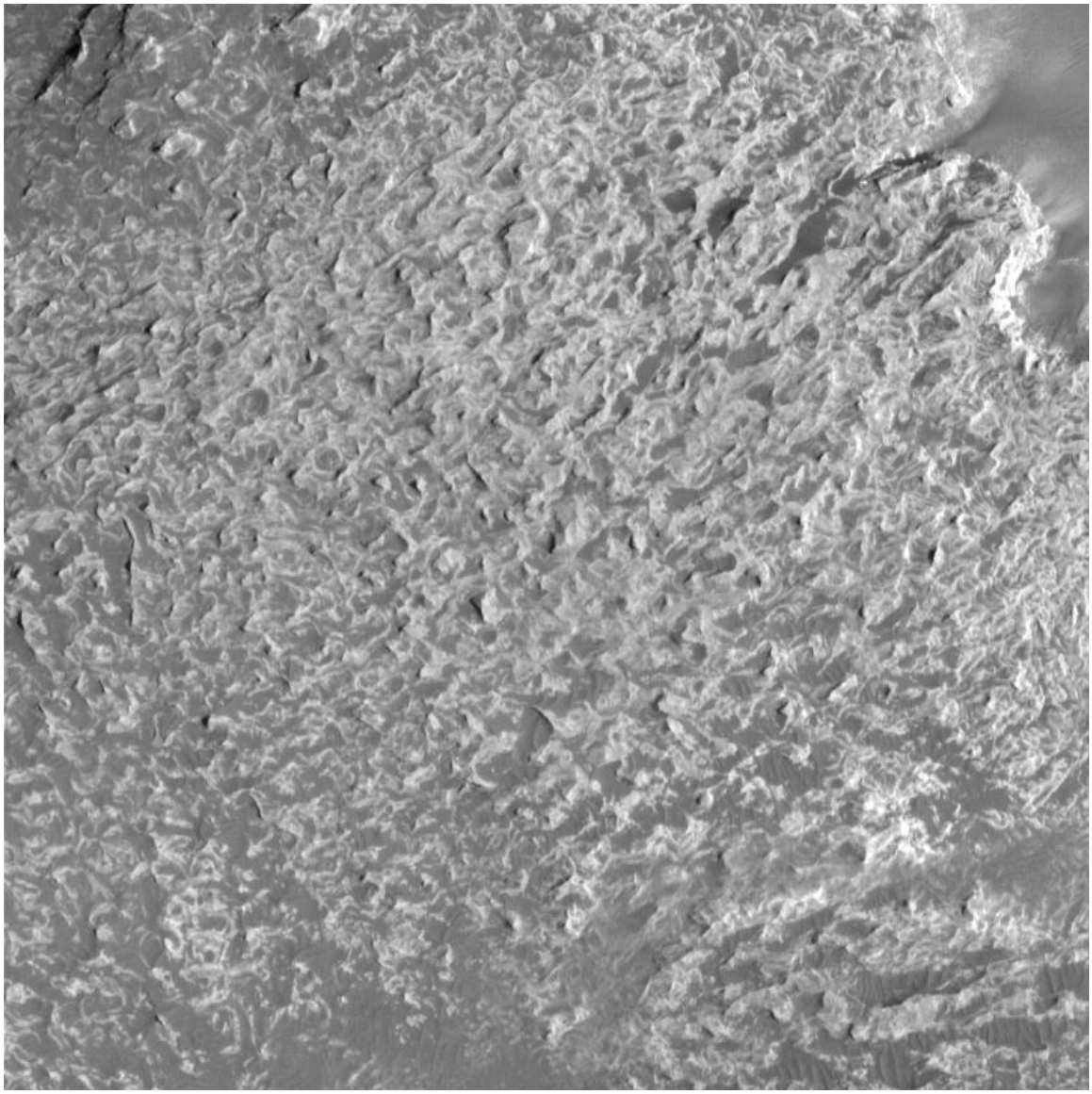

Figure 5.1.18. Part of the surface of the Aureum Chaos Deposits (Part of MOC image E0503434, 3.50 m/pixel resolution).

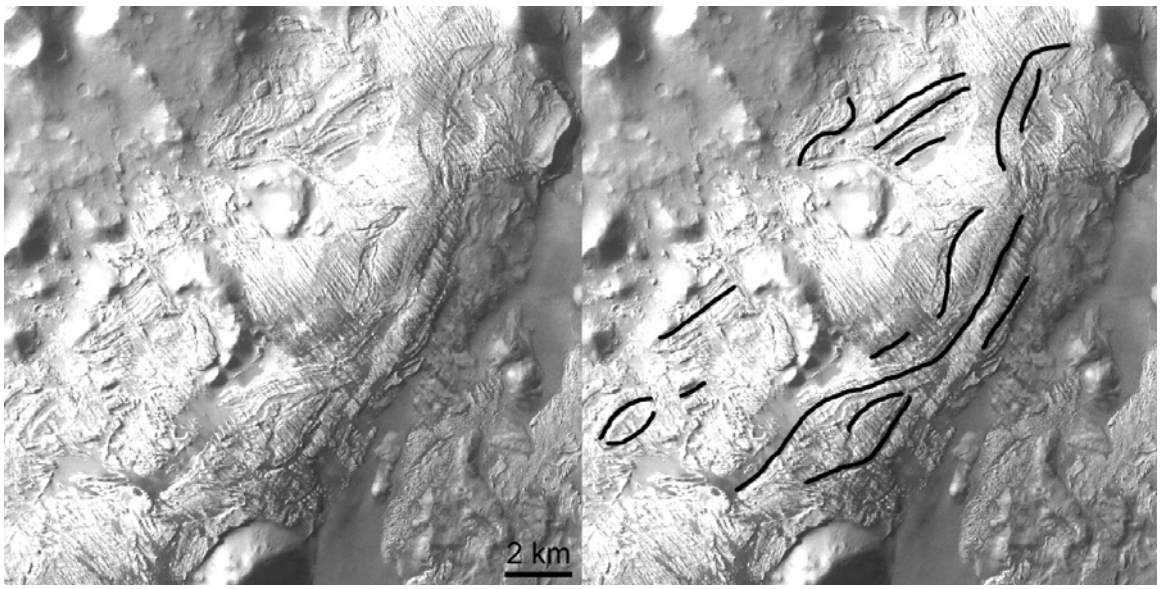

Figure 5.1.19. Flow morphology observable in the Iani Chaos Deposit type 2 (HRSC nadir).

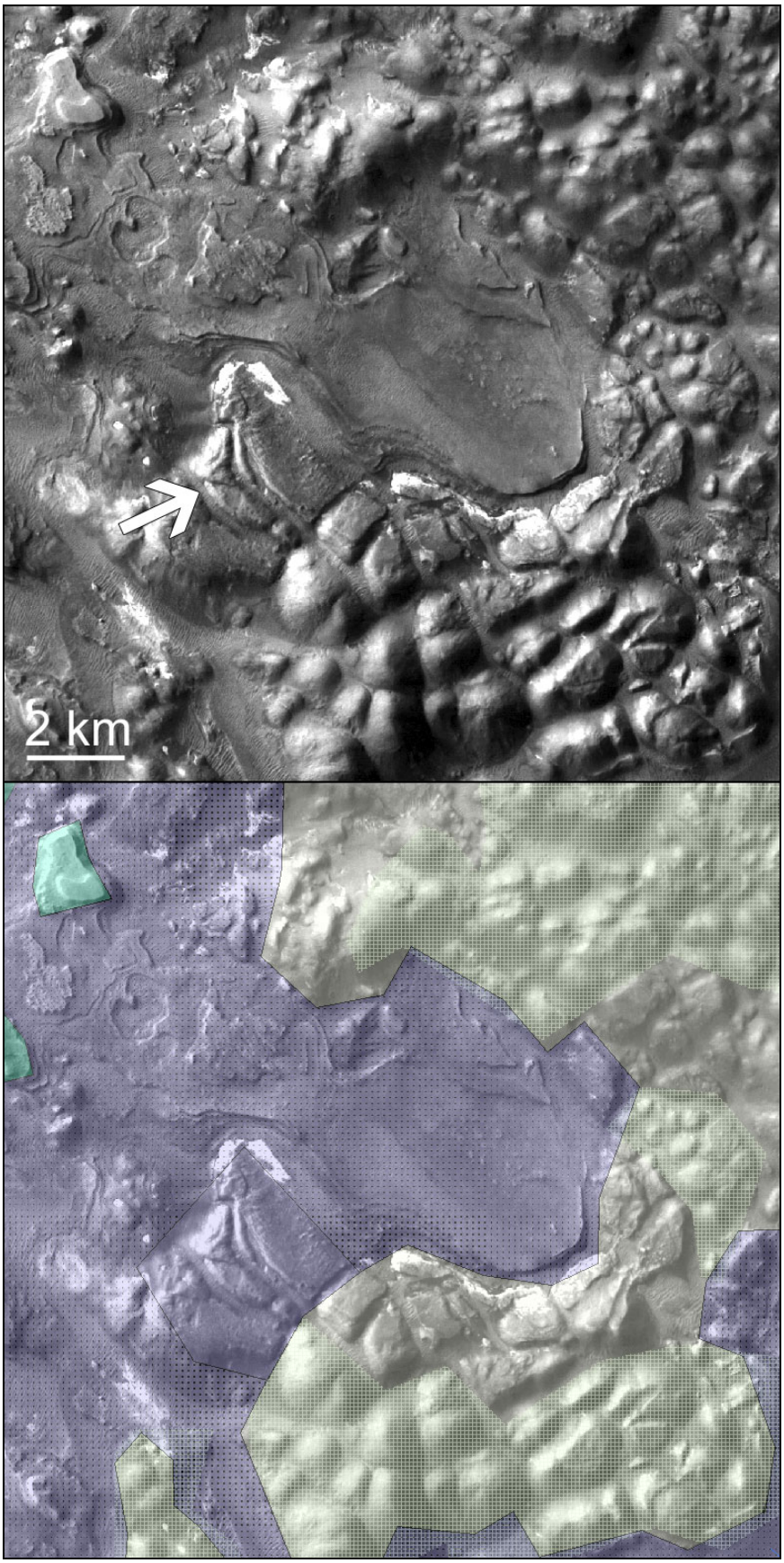
2 km

Figure 5.1.20. The boundary of the smooth Lower Aram Chaos Formation (dotted purple) with CT (grey) and Rounded Chaotic and Highland Terrain (RCHT) (yellow). The LACF is observed to have been locally fractured (arrow, mapped as fractured LACF). The fracturing pattern is observed to continue within the CT. This suggests the LACF formed after the formation of the Chaotic Terrain and its more rounded RCHT lateral unit. The fractured LACF could subsequently have formed after localized activity occurred (e.g. subsidence or water release) (HRSC nadir, image center 240.23°E, 2.88°N).

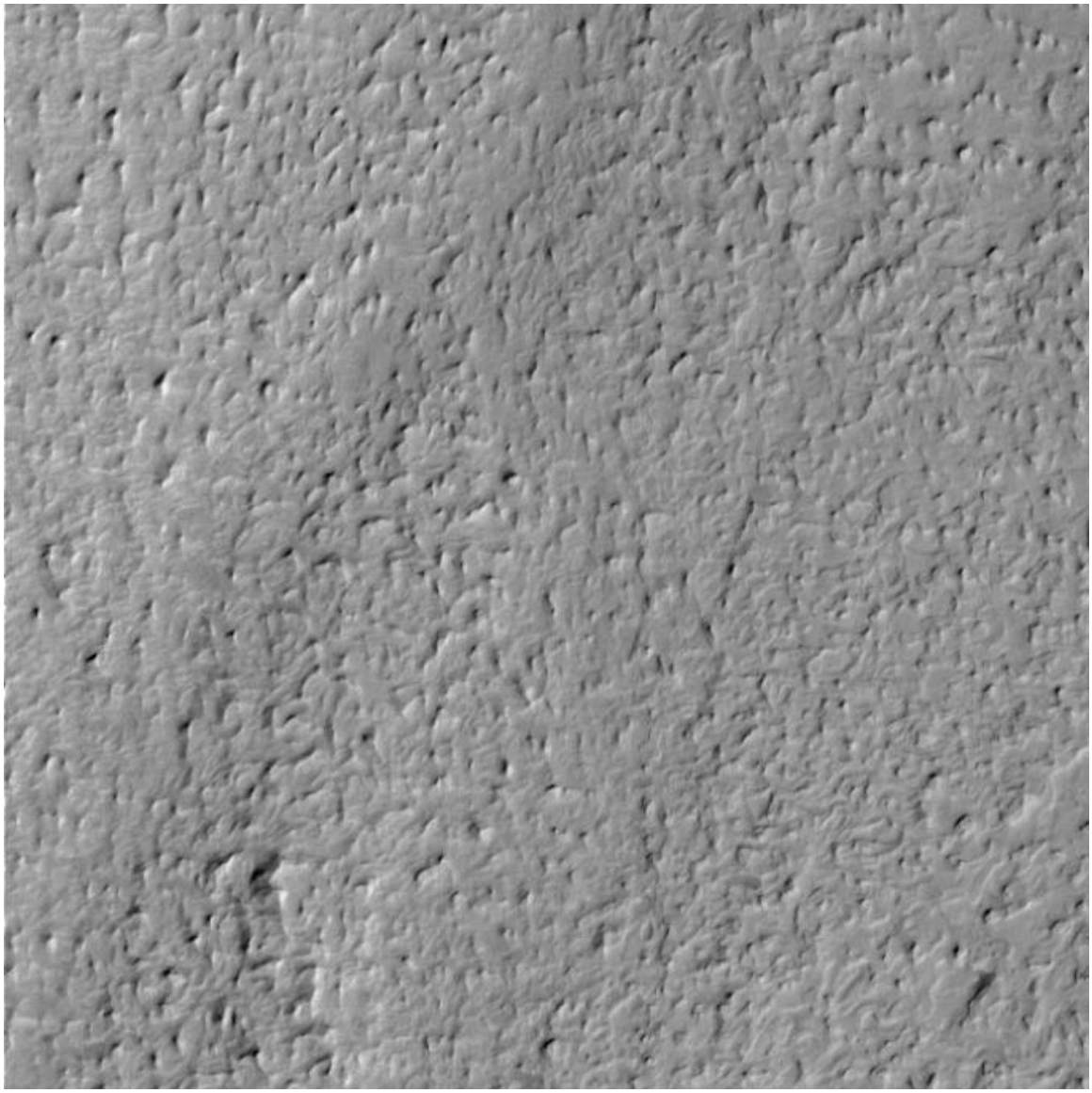

Figure 5.1.21. Morphology of the Iani Chaos Deposits type 5 (Part of MOC image E2000722, 4.47 m/pixel resolution).

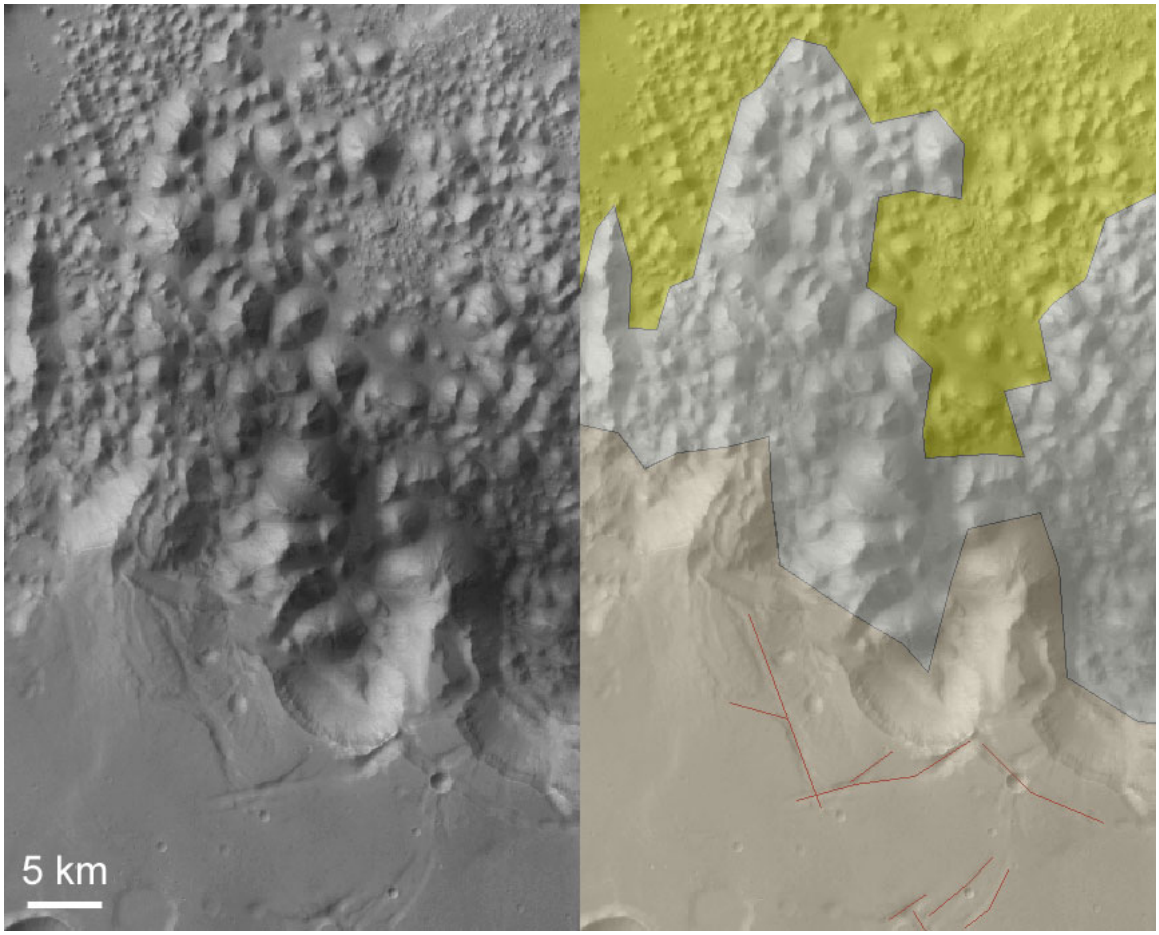

Figure 5.1.22. Grading of high elevated Highland Terrain (dark yellow) via Intermediate Chaotic Terrain (grey) to low elevated Chaotic Terrain Floor (yellow) (Hydaspis Chaos) (HRSC nadir, image center 332.65°E, 2.31°N).

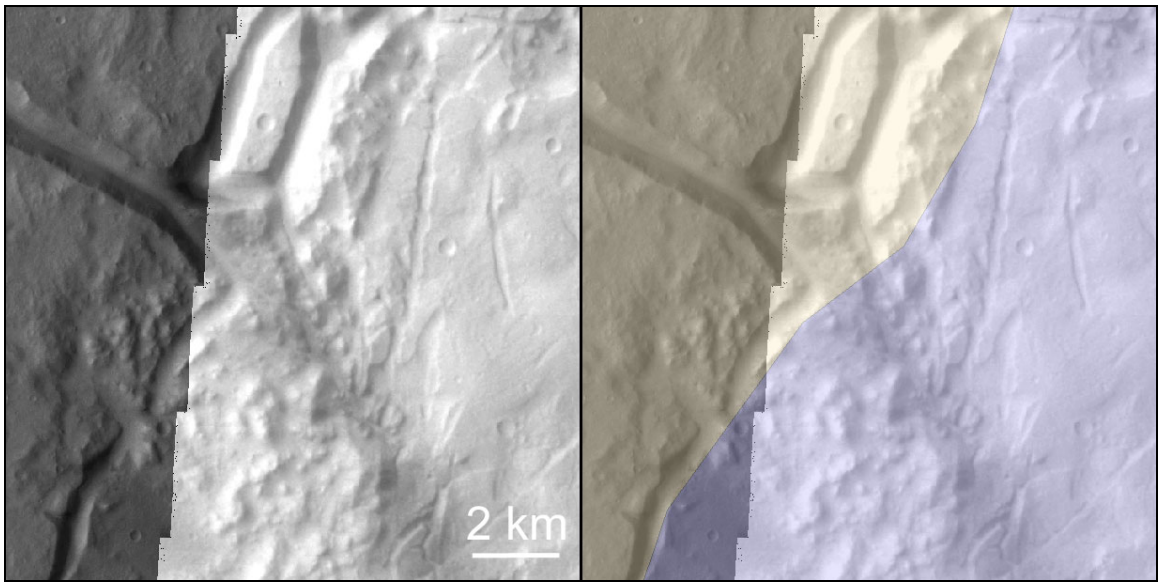

Figure 5.1.23. Boundary between fractured Highland Terrain (yellow) and fractured Lower Aram Chaos Formation (purple) (THEMIS VIS, image center 337.64°E, 3.41°N).

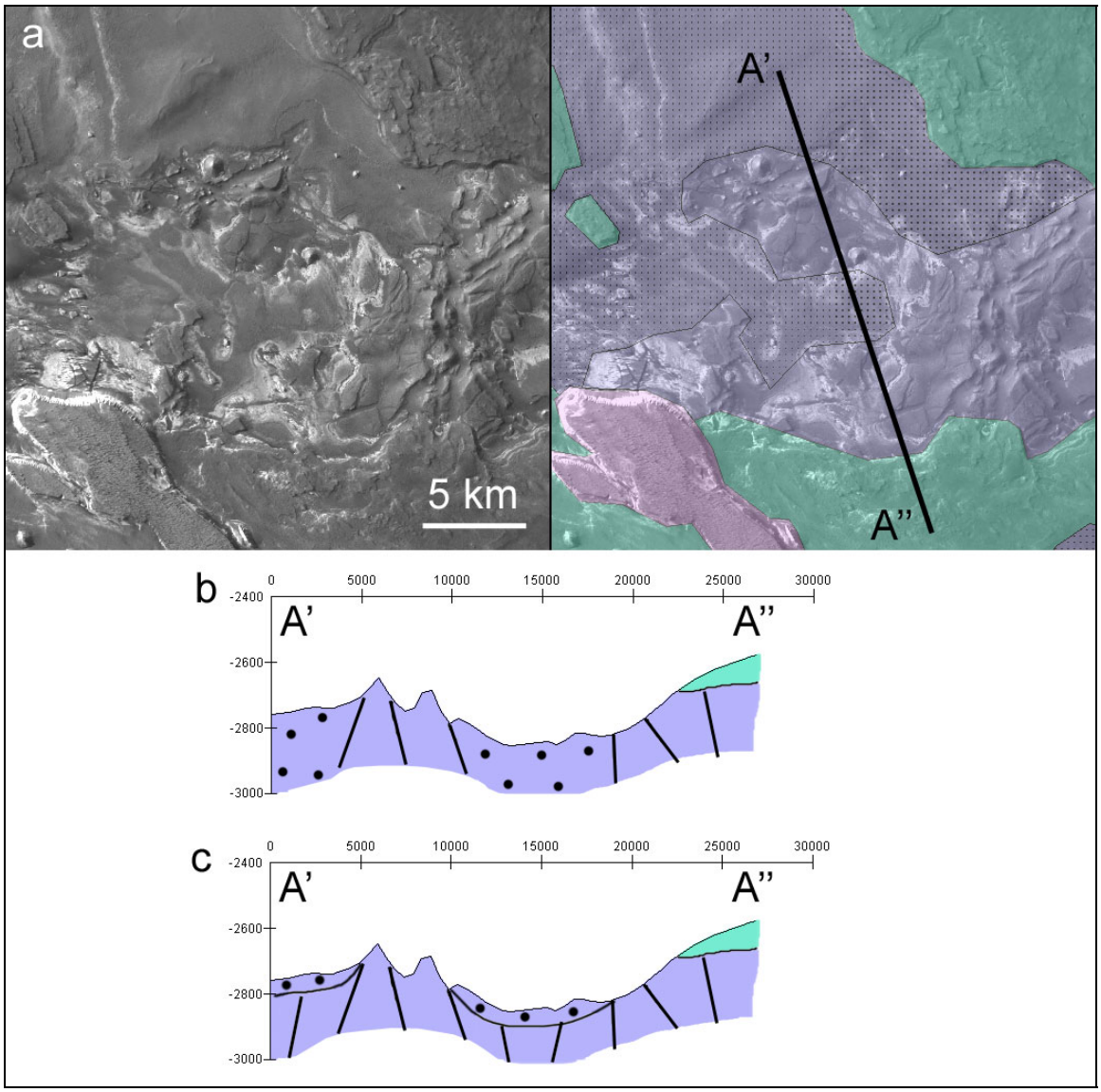

Figure 5.1.24. Smooth (dotted purple) versus fractured (purple) Lower Aram Chaos Formation. The smooth LACF could either be locally fractured (**b**) or it is a distinct deposit on top of the fractured LACF (**c**). Green is the Intermediate Aram Chaos Formation (HRSC nadir, image center 339.75°E, 2.84°N).

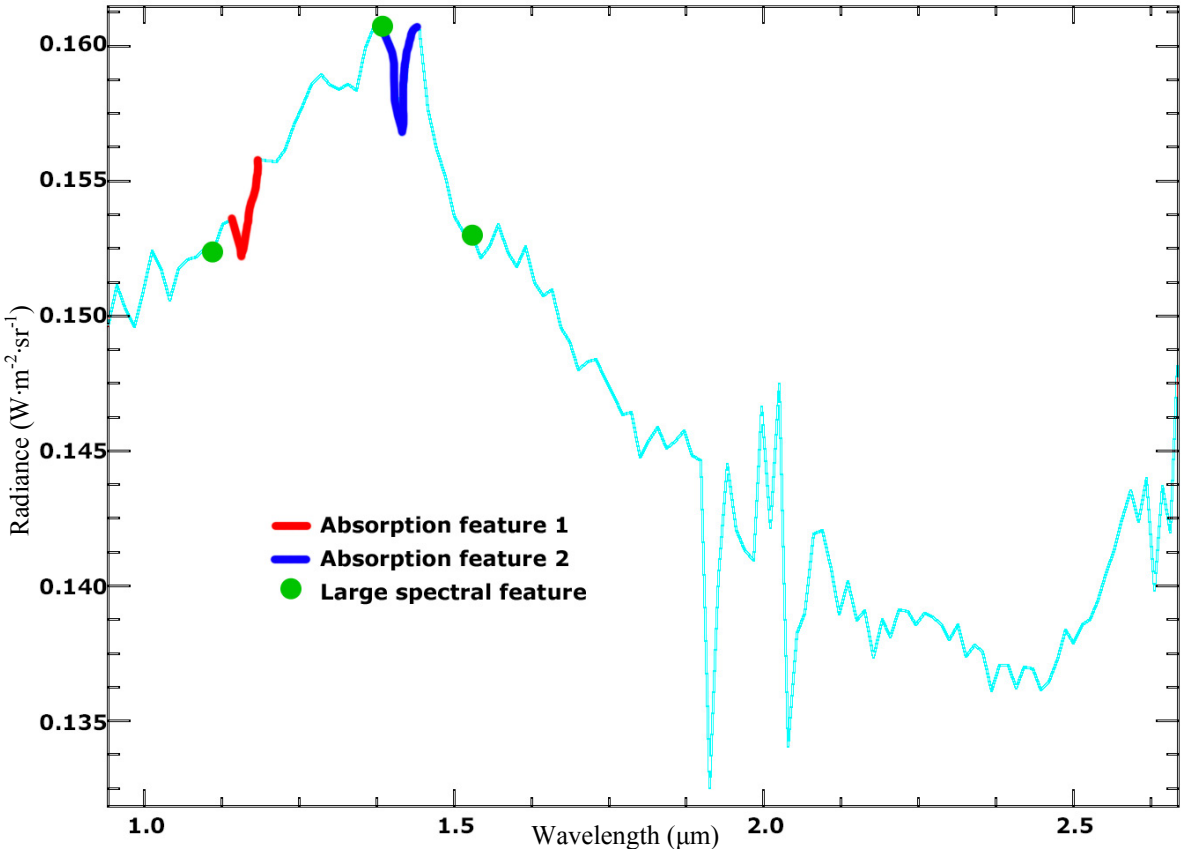

Figure 5.1.25. Mean spectra of the Aureum Chaos Deposits.

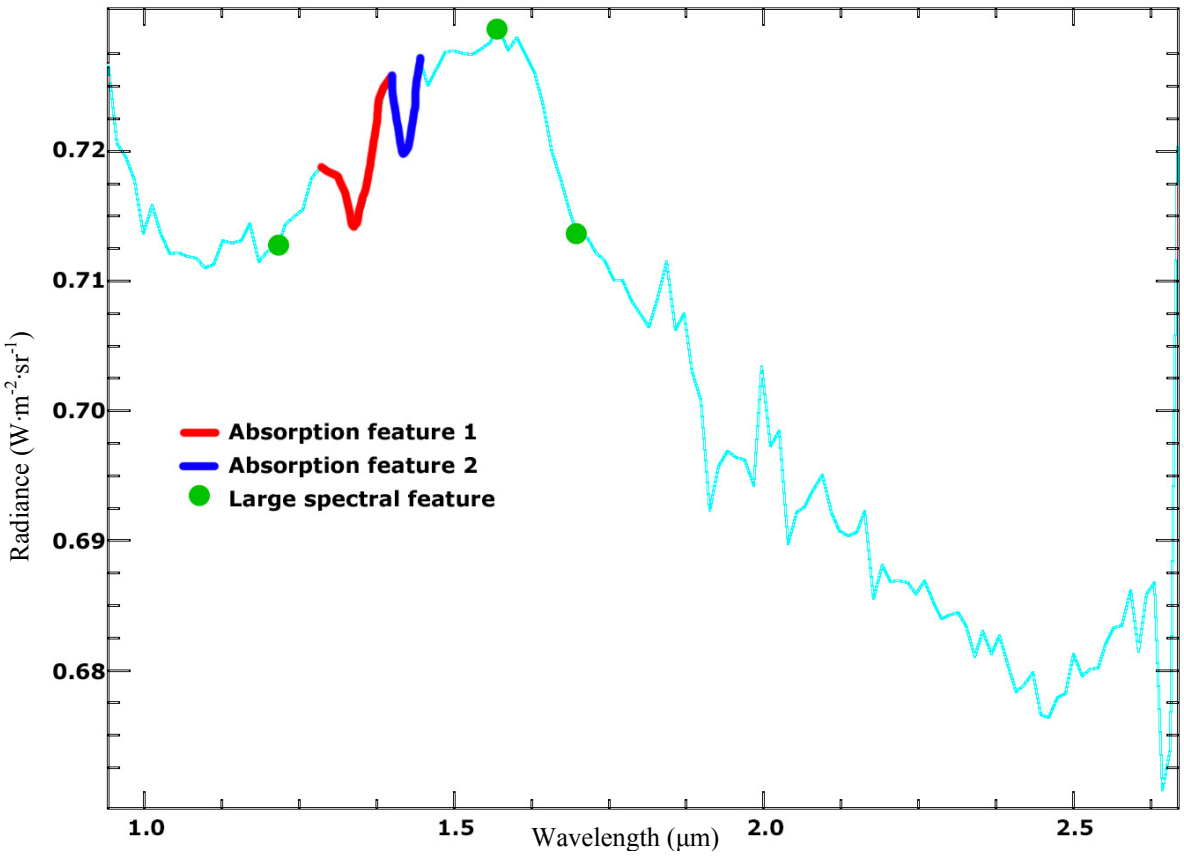

Figure 5.1.26. Mean spectra of the Iani Chaos Deposits.

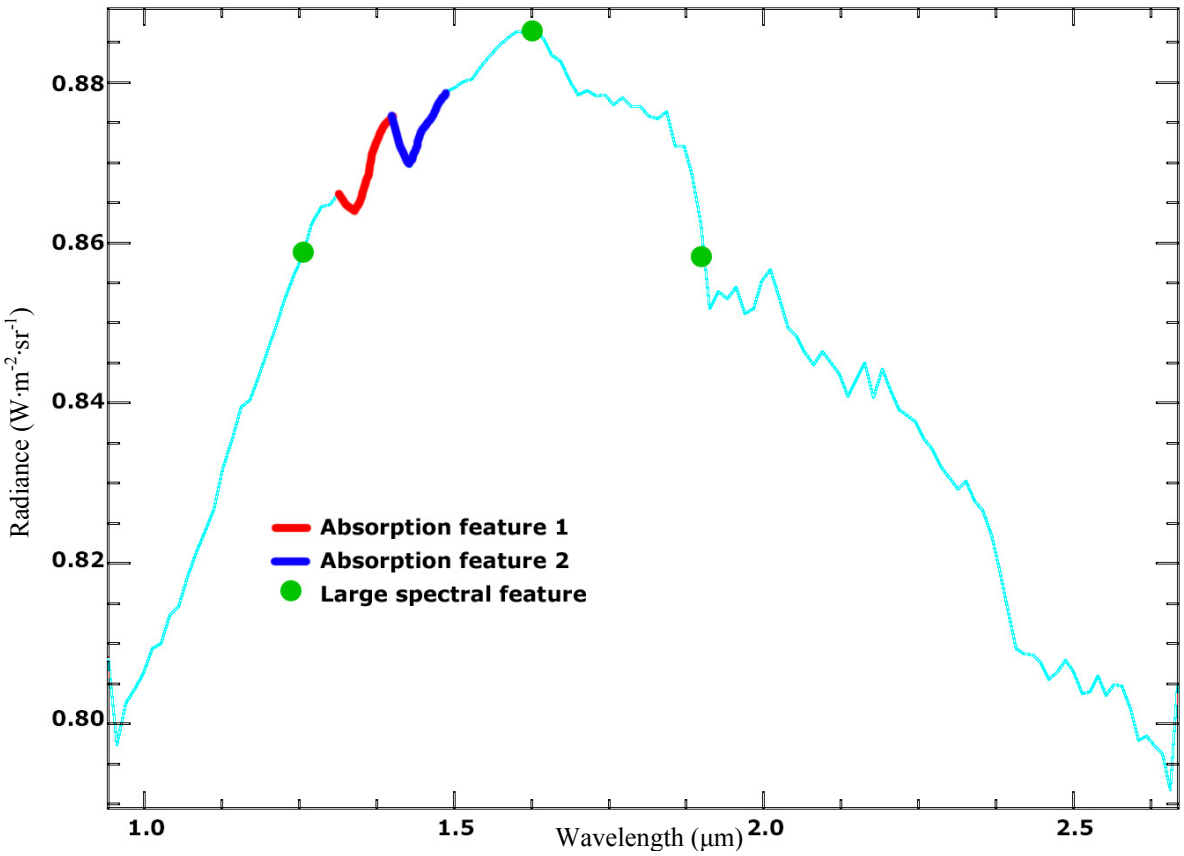

Figure 5.1.27. Mean spectra of the smooth Lower Aram Chaos Formation.

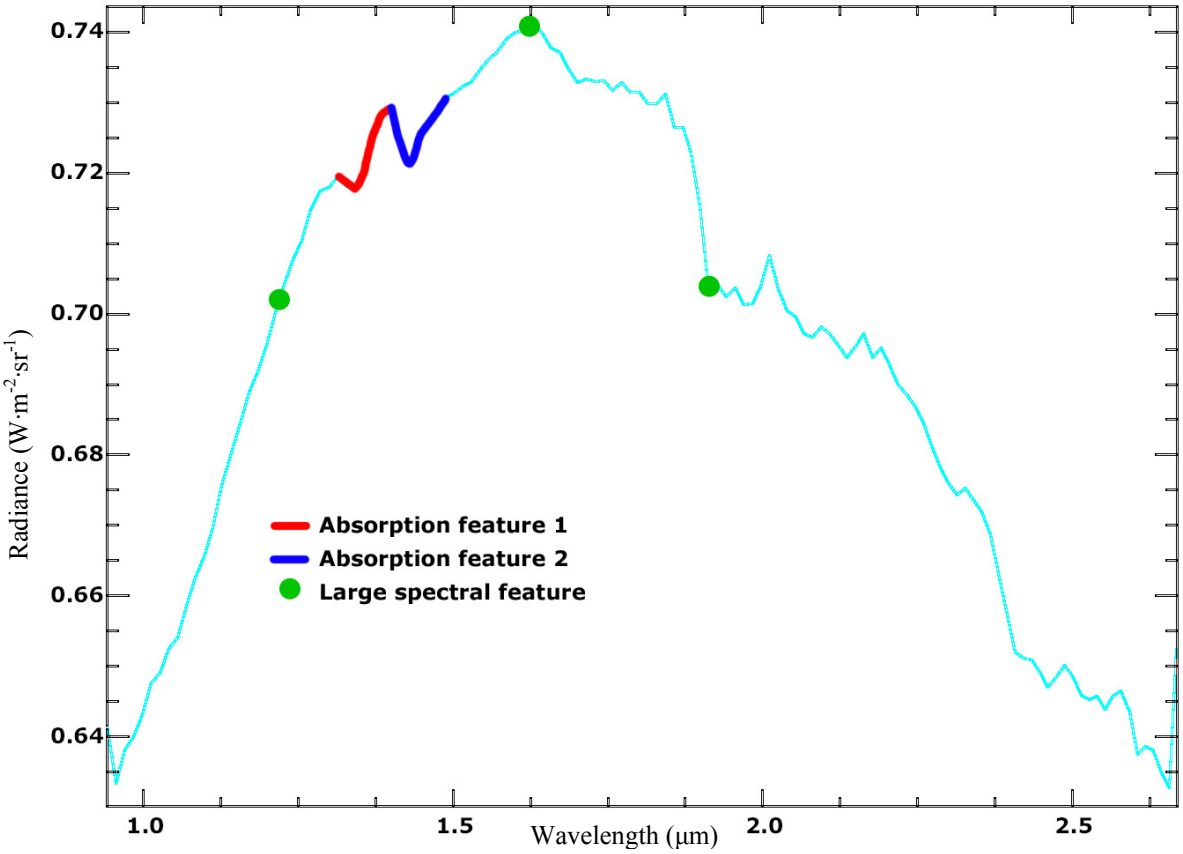

Figure 5.1.28. Mean spectra of the Intermediate Aram Chaos Formation.

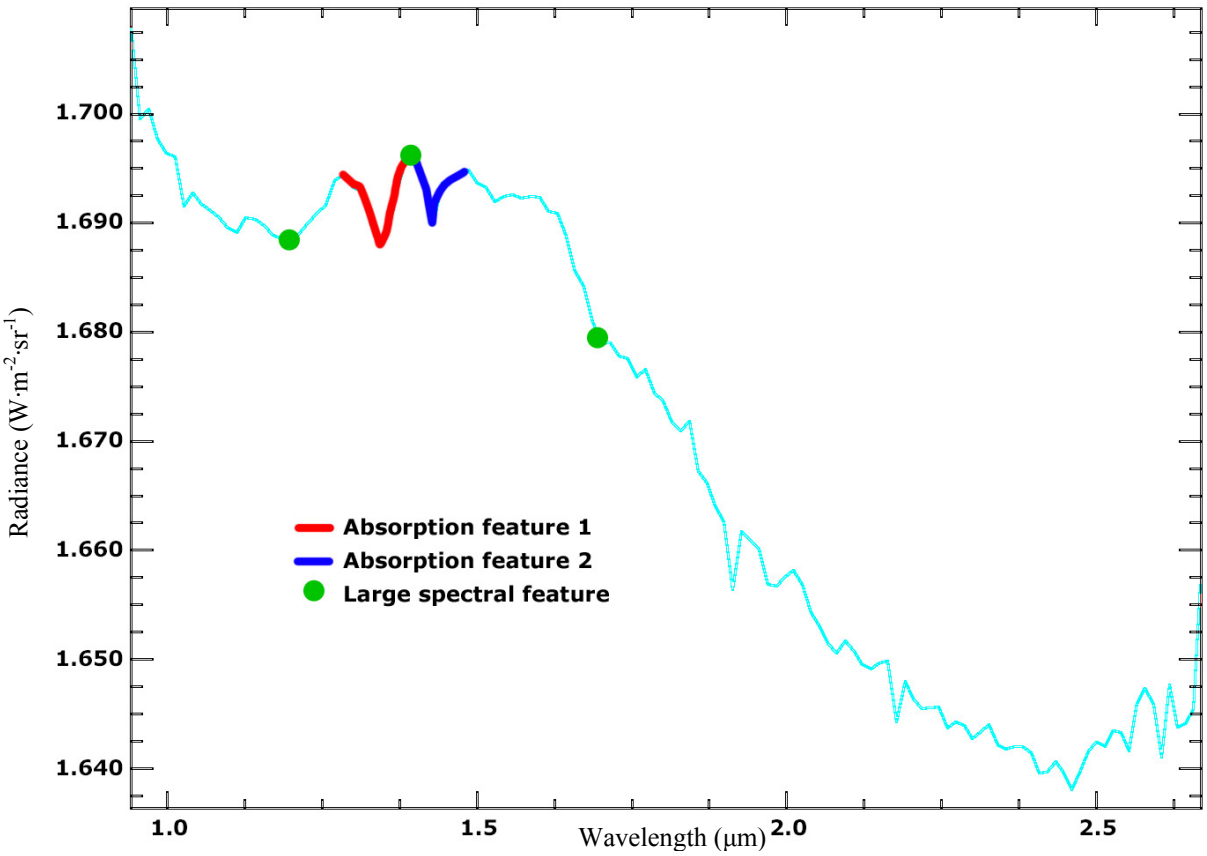

Figure 5.1.29. Mean spectra of the Upper Aram Chaos Formation.

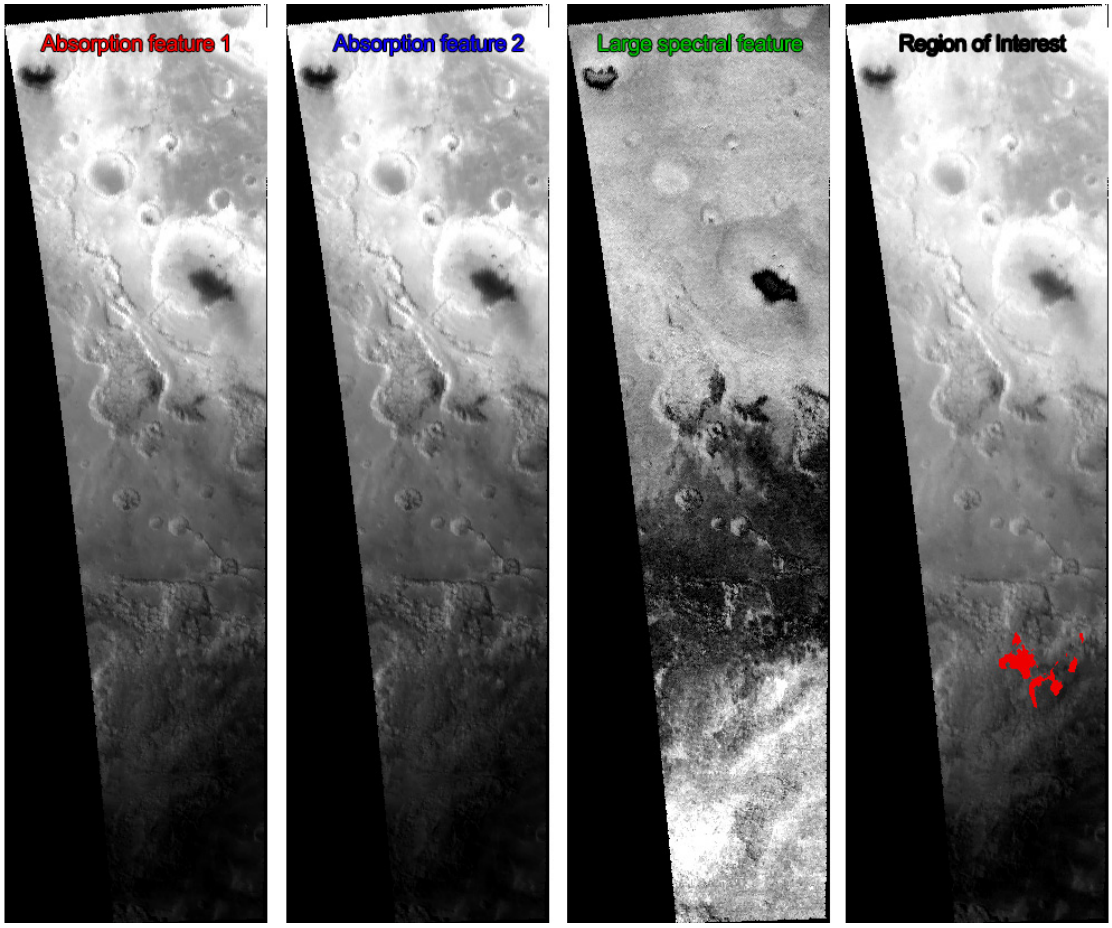

Figure 5.1.30. The band ratio maps for the Aureum Chaos Deposits belonging to the two absorption features and the large spectral feature. The Region of Interest is projected on one of the normal bands.

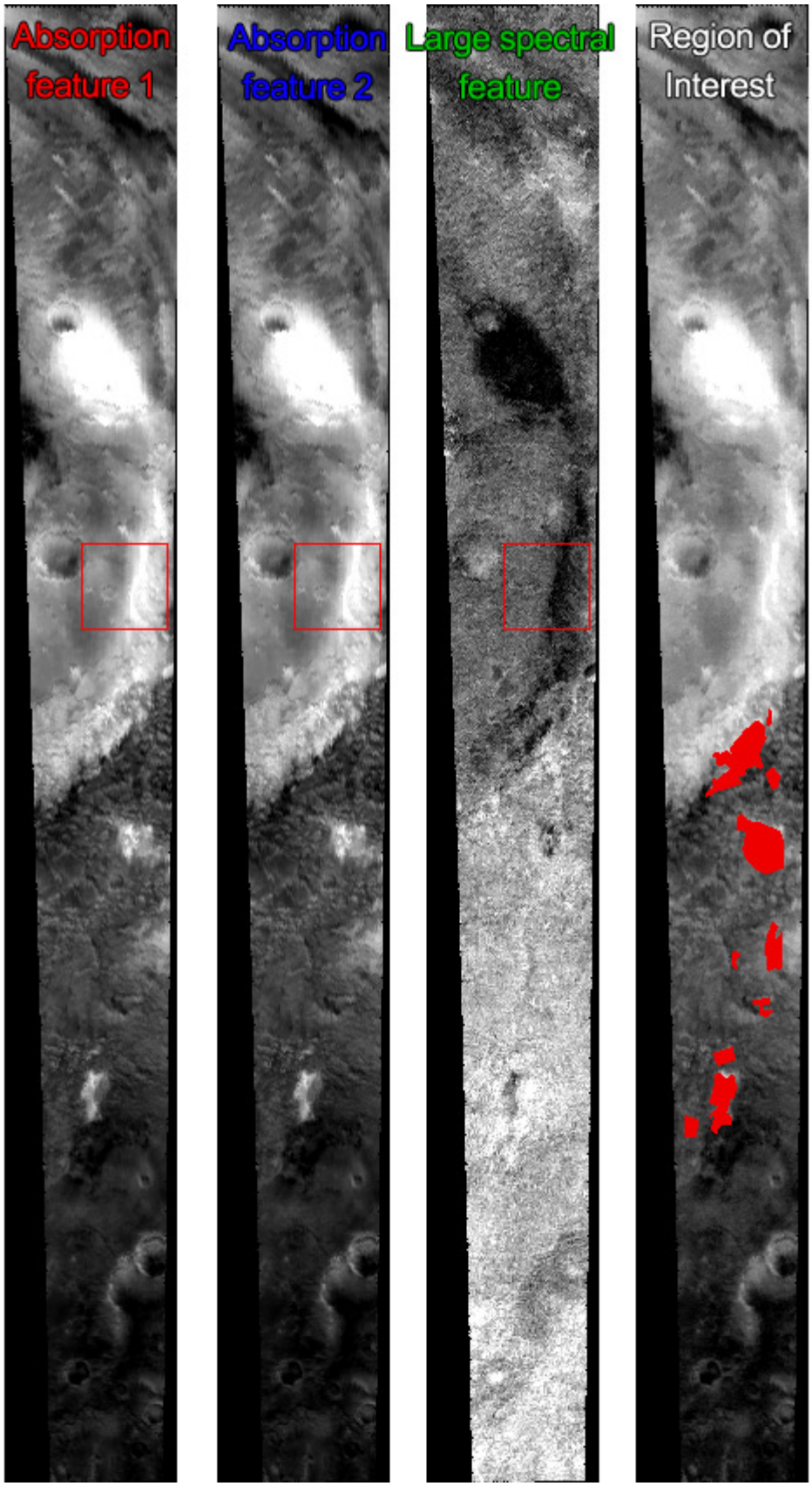
Absorption feature 1
Absorption feature 2
Large spectral feature
Region of Interest

Figure 5.1.31. The band ratio maps for the Iani Chaos Deposits belonging to the two absorption features and the large spectral feature. The Region of Interest is projected on one of the normal bands.

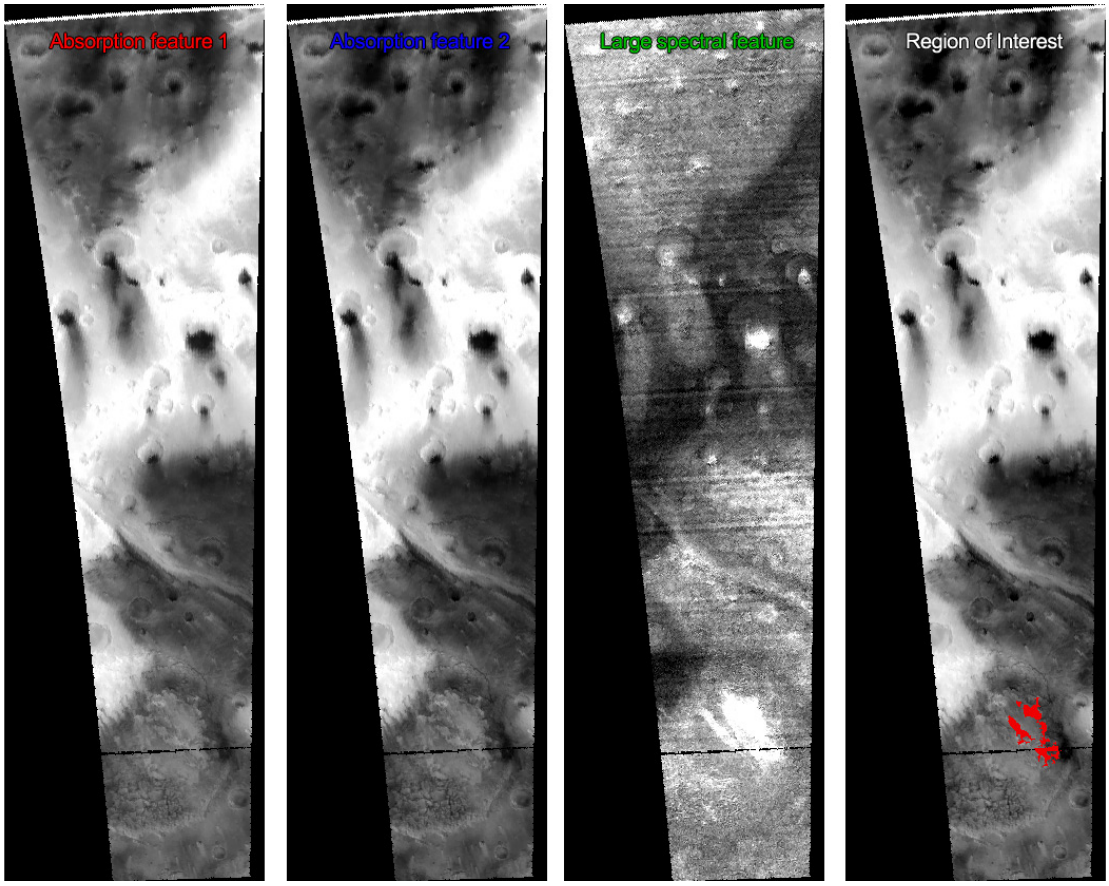

Figure 5.1.32. The band ratio maps for the smooth Lower Aram Chaos Formation belonging to the two absorption features and the large spectral feature. The Region of Interest is projected on one of the normal bands.

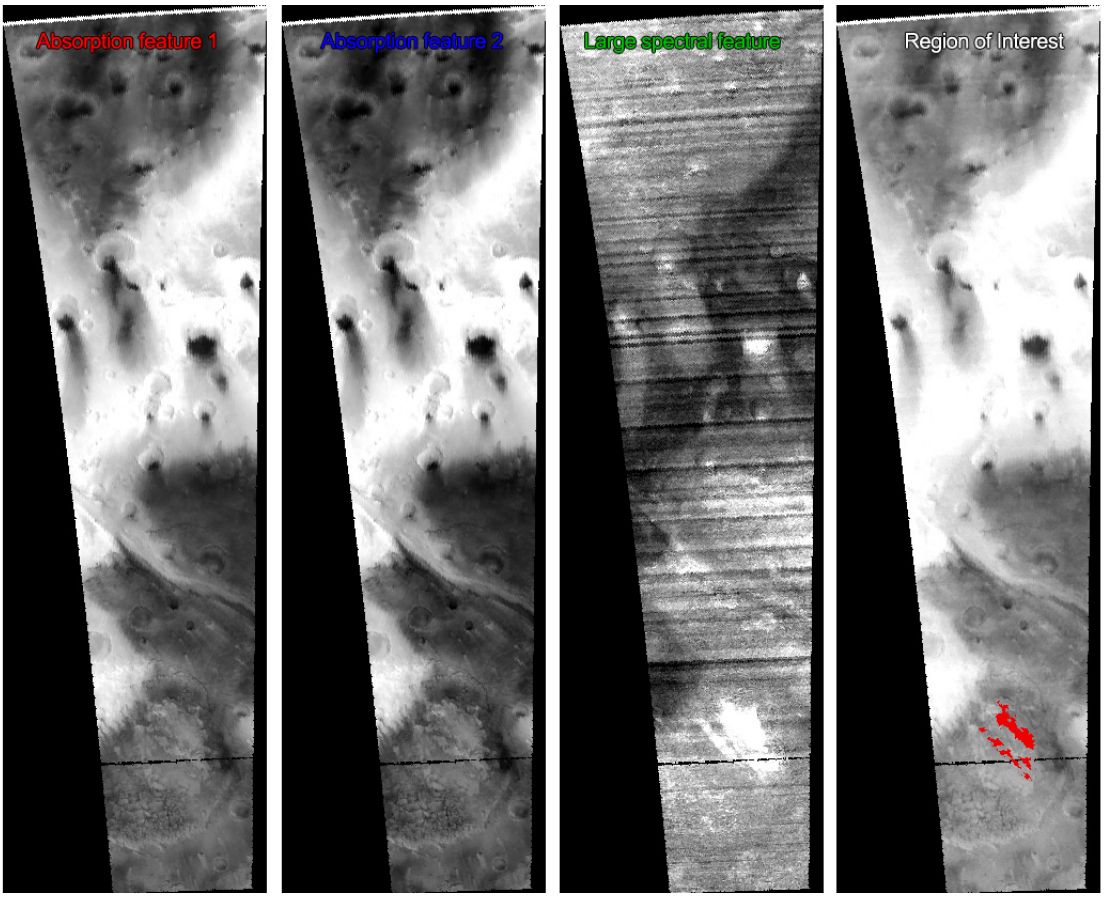

Figure 5.1.33. The band ratio maps for the Intermediate Aram Chaos Formation belonging to the two absorption features and the large spectral feature. The Region of Interest is projected on one of the normal bands.

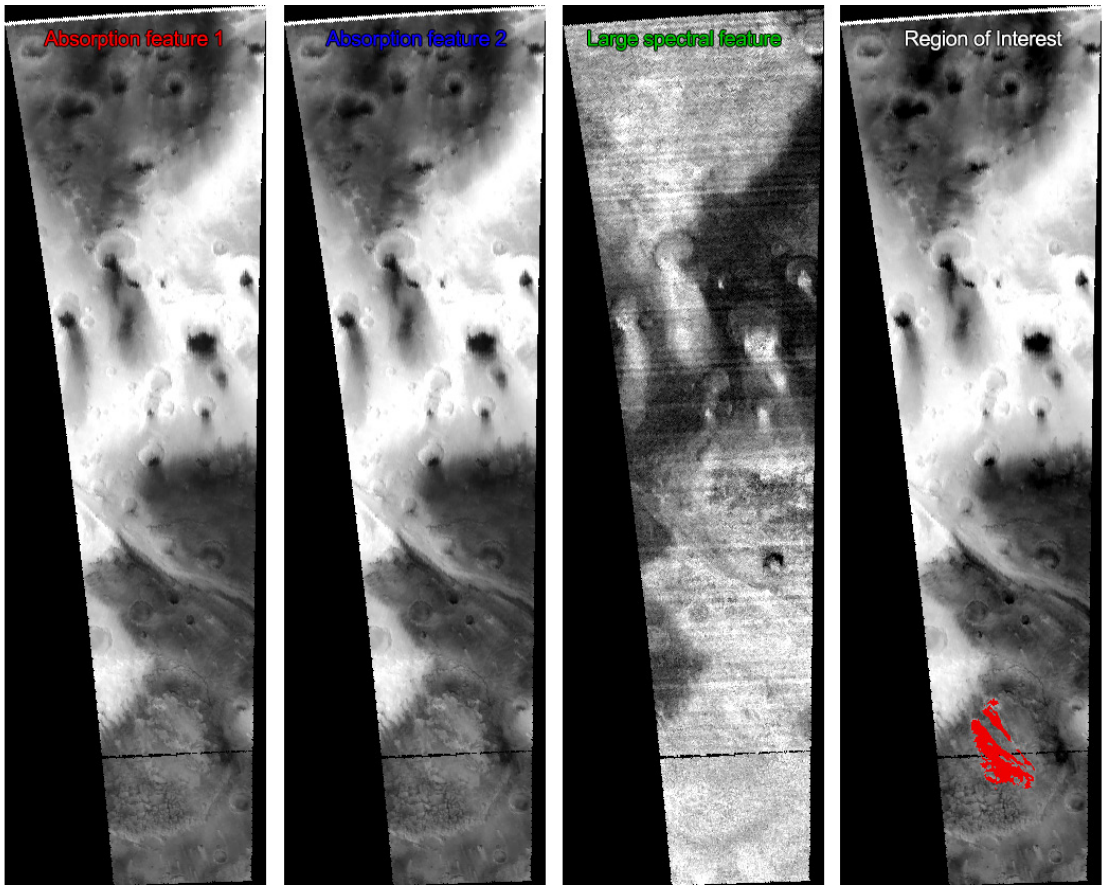

Figure 5.1.34. The band ratio maps for the Upper Aram Chaos Formation belonging to the two absorption features and the large spectral feature. The Region of Interest is projected on one of the normal bands.

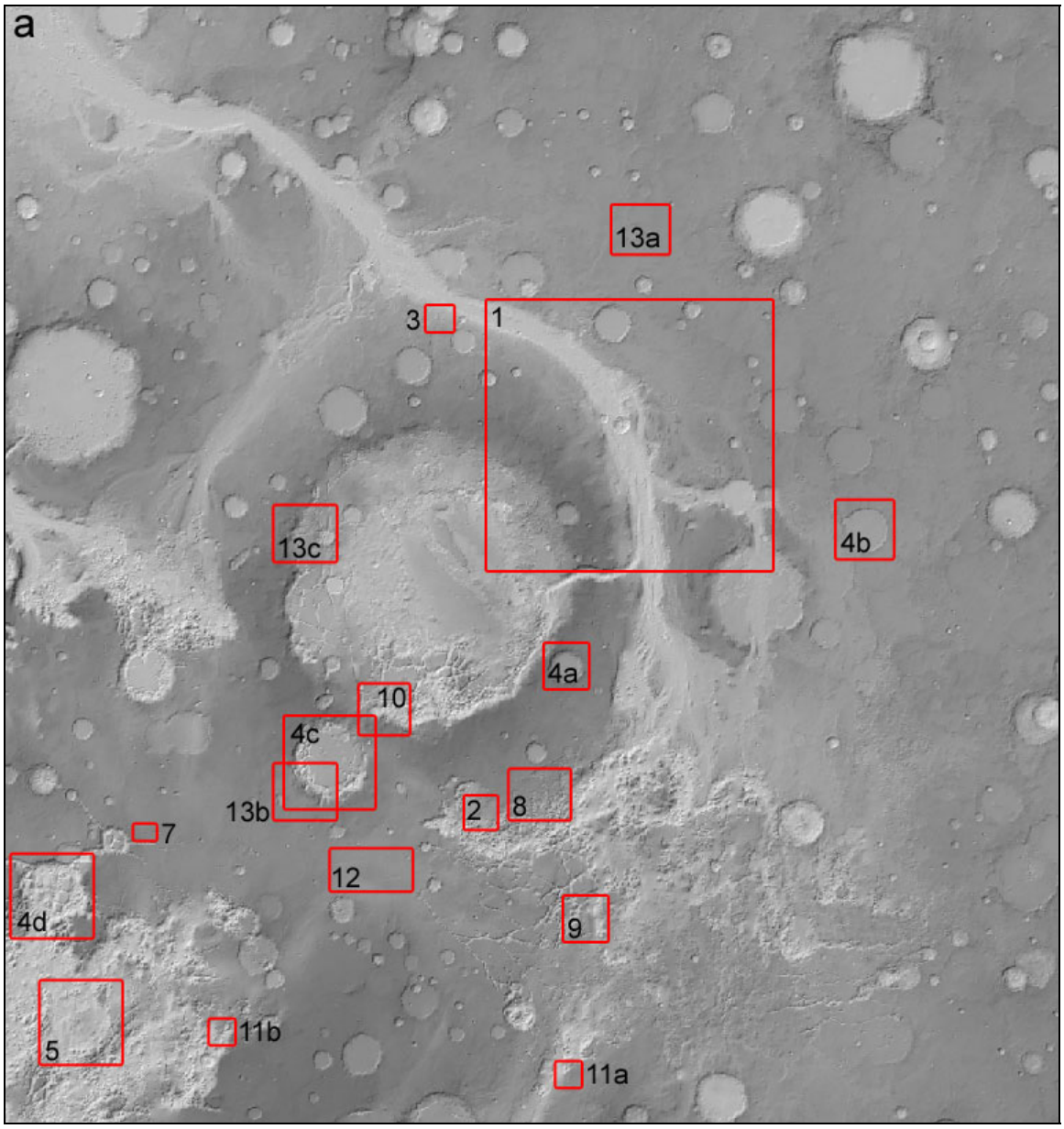

Figure 5.2.1. Overview of the different geological observations. The numbers refer to the observations numbers. **a.** Regional. **b.** Aram Chaos.

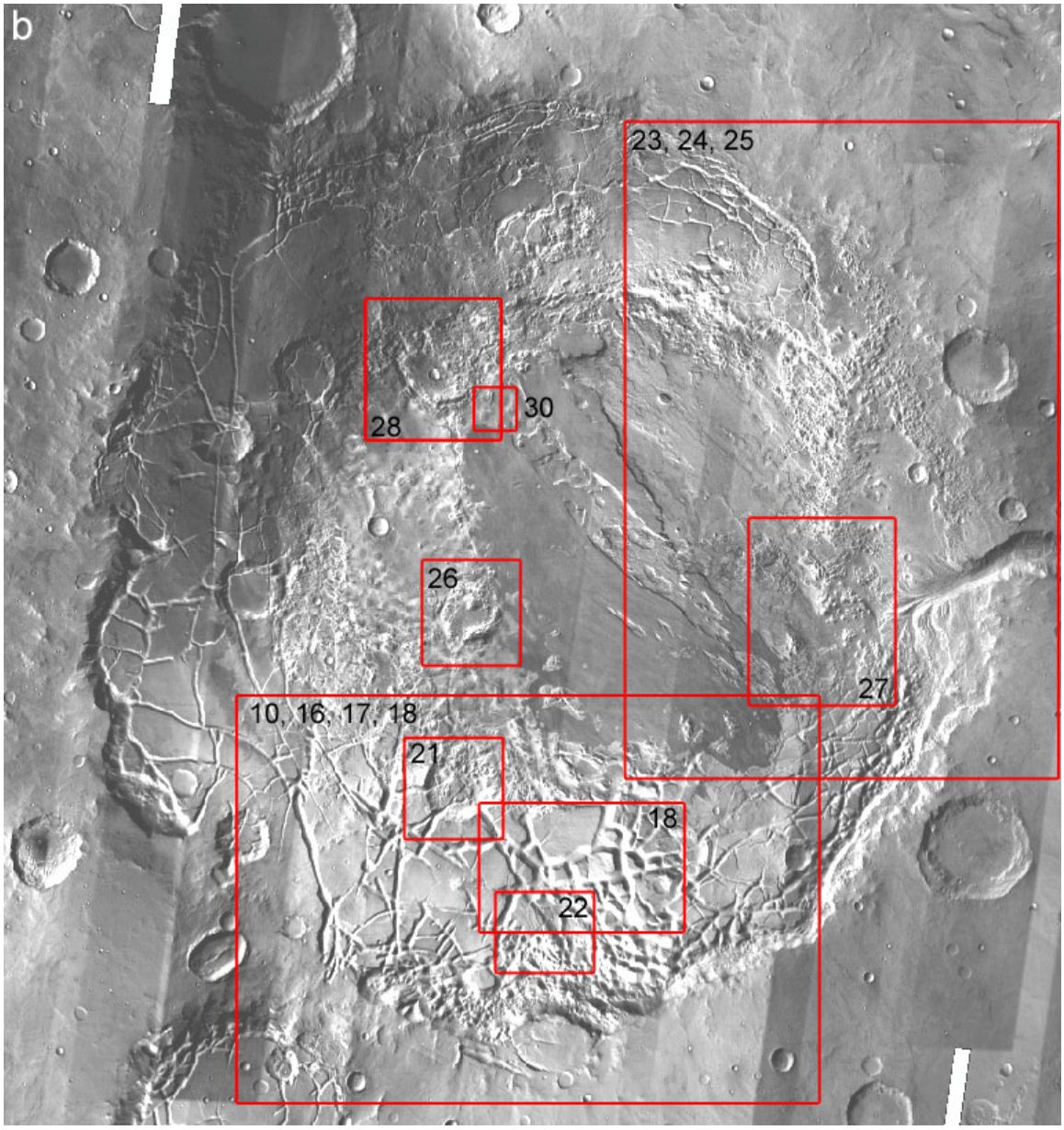

Figure 5.2.1 (continued).

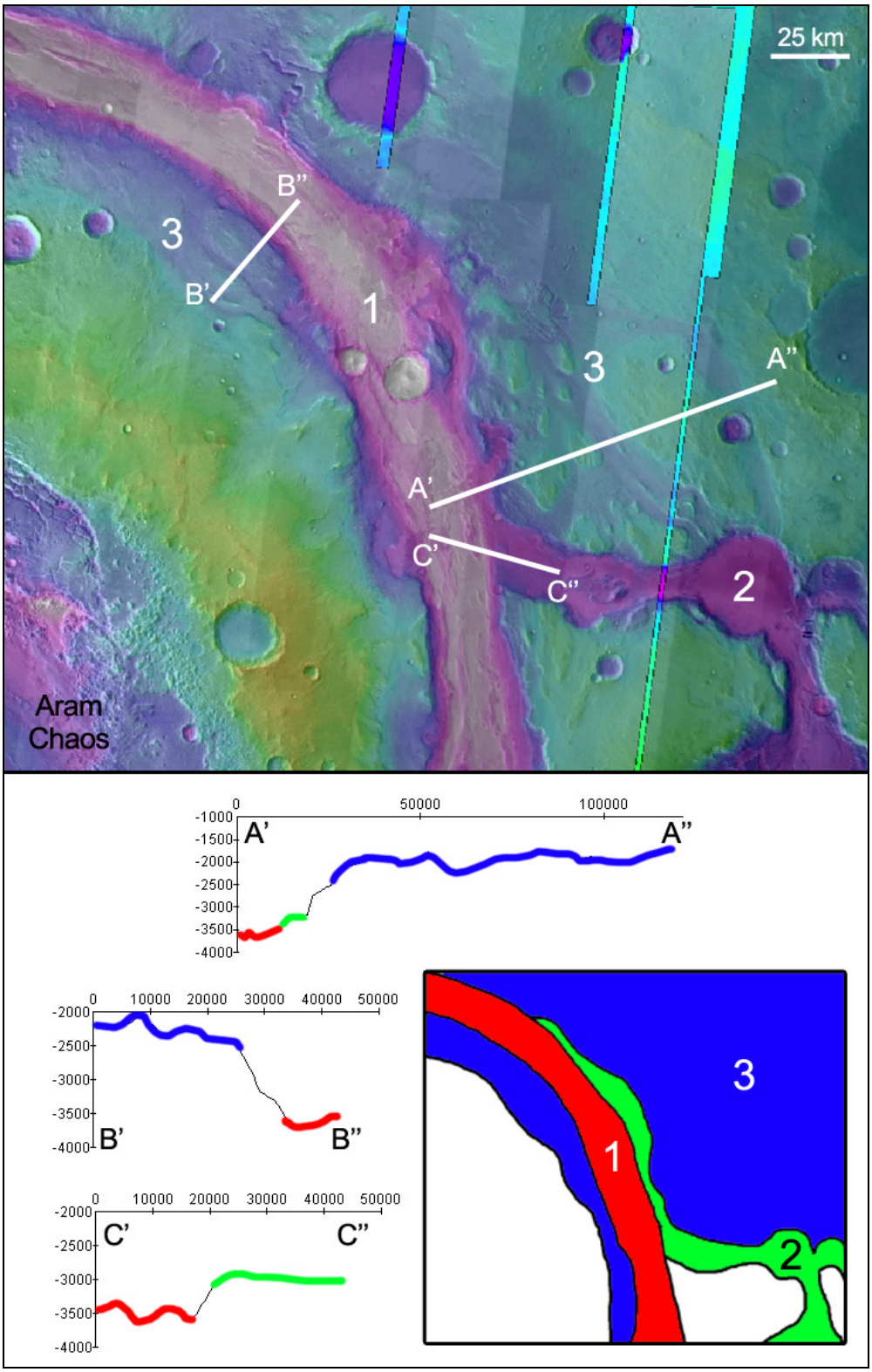

Figure 5.2.2. The Ares Vallis outflow channel system consists of multiple cross-cutting channels (1 in Figure 5.2.1a for overview). The youngest outflow event incised the main Ares Vallis outflow channel (1). It is observed to cross cut an older channel (2 and profile

C). Channels 1 and 2 incised into an higher elevated outflow terrace (3 and profiles A and B) (THEMIS IR day and color coded MOLA elevation).

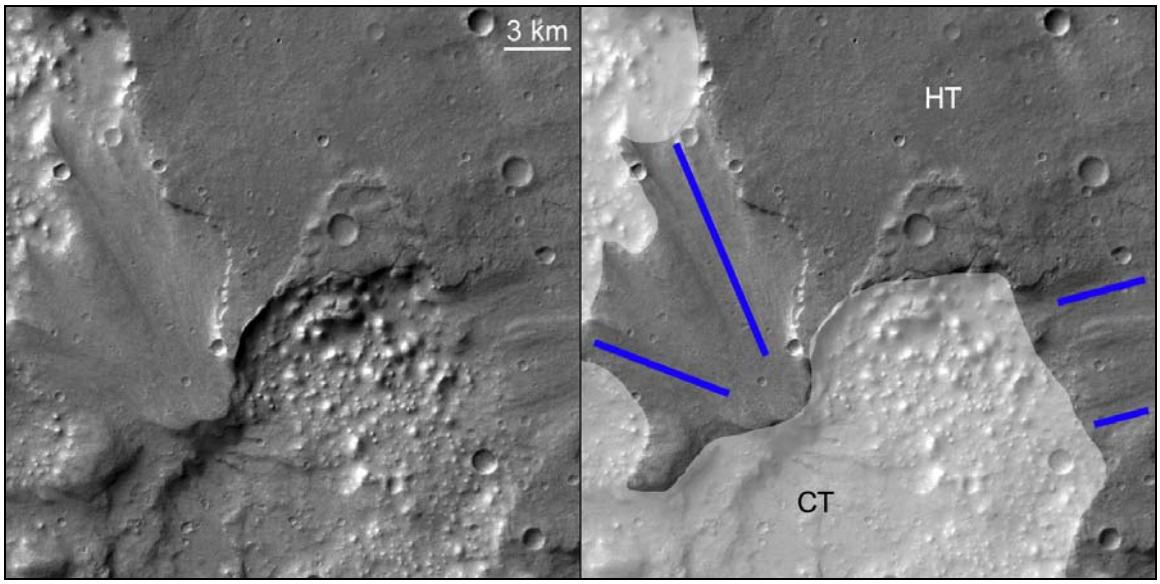

Figure 5.2.3. Outflow channels in HT (flow lineations in blue) have been cross cut by chaotization in CT (2 in Figure 5.2.1a) (HRSC nadir, image center 339.86°N, 0.74°S).

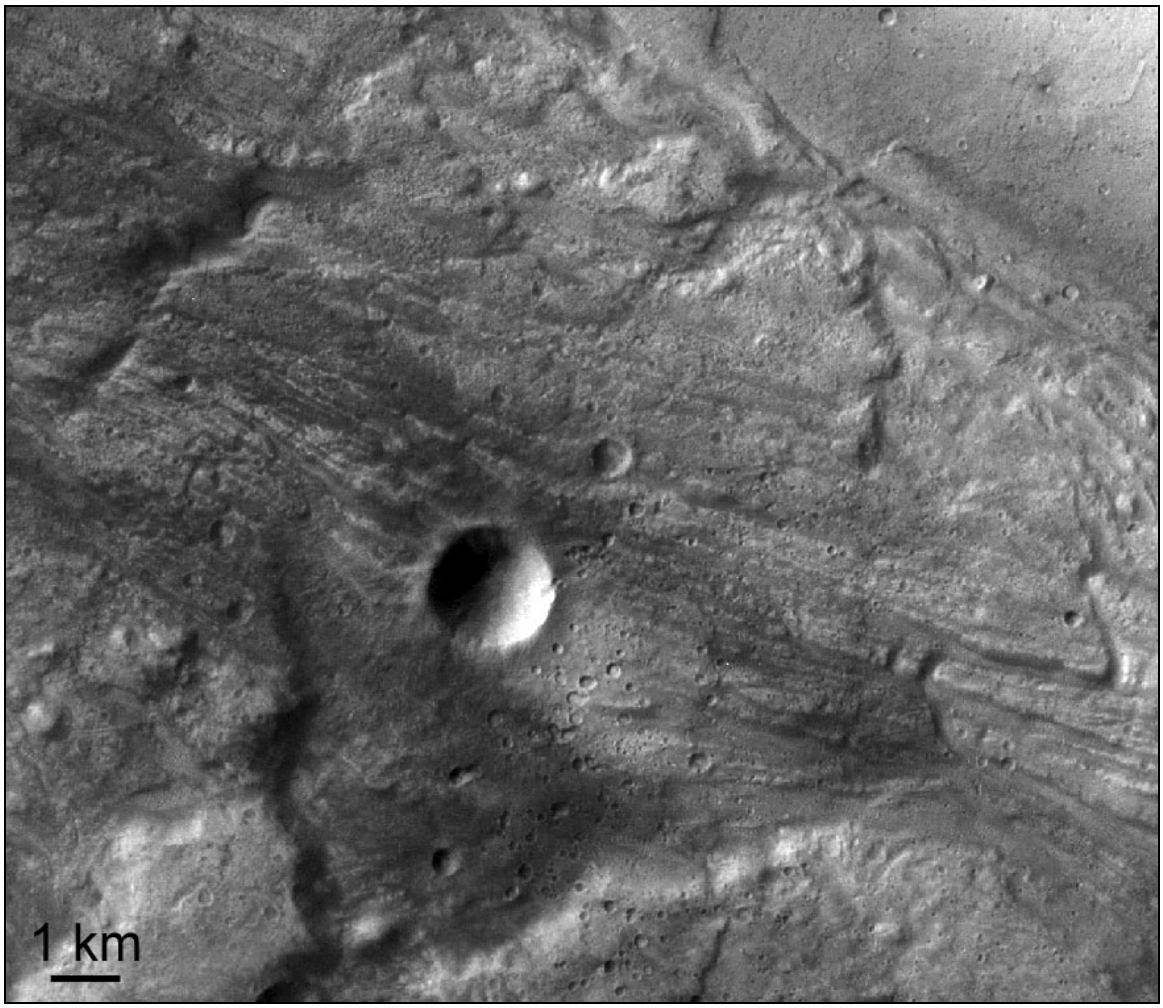

Figure 5.2.4. Surface morphology similar to the AACD (compare with Figure 5.1.10j) located on a terrace of Ares Vallis, North of Aram Chaos (3 in Figure 5.2.1a for overview).

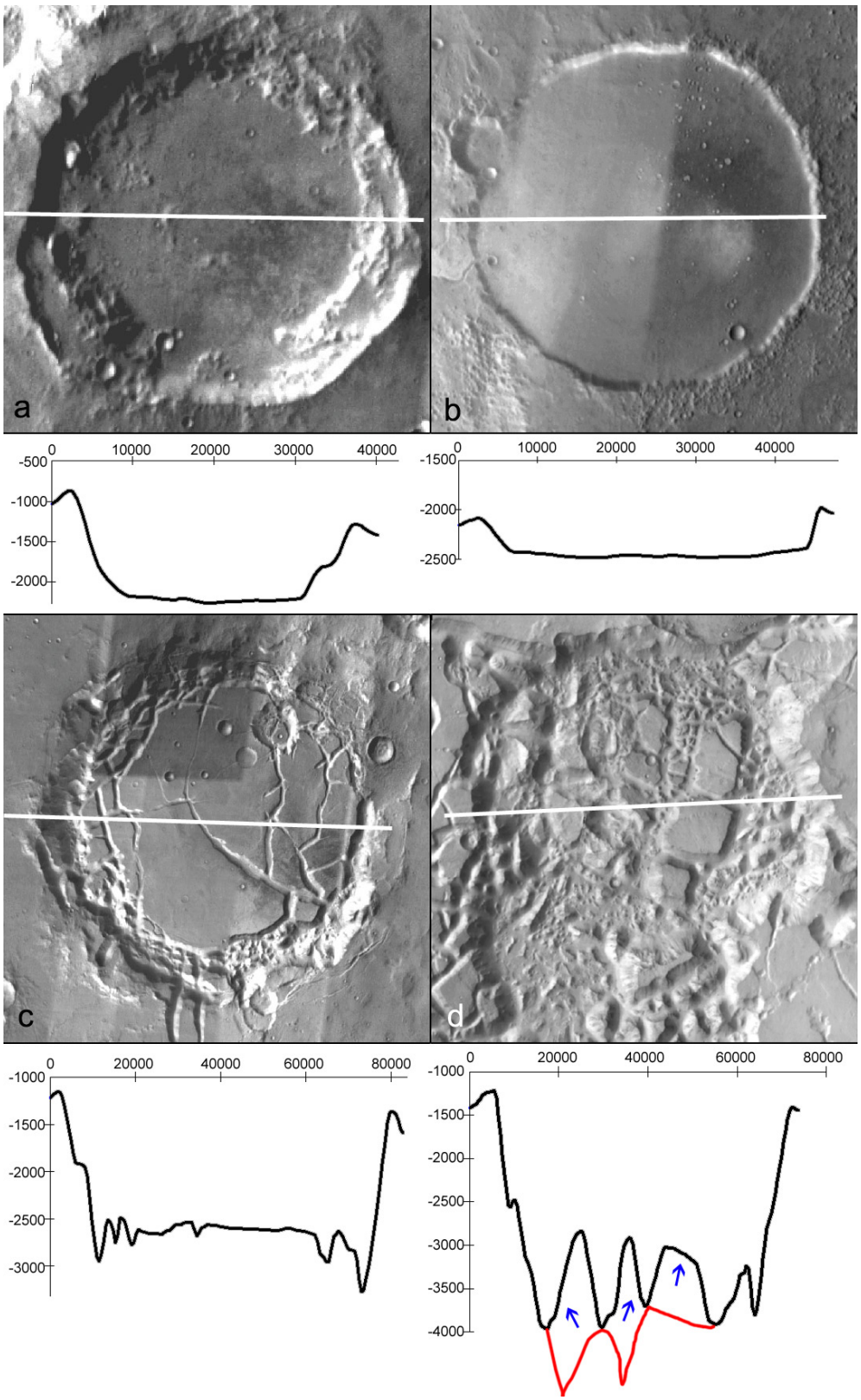

Figure 5.2.5. Different types of craters (THEMIS IR day). The profile axes are in meters. **a.** unfractured crater, 32 km in diameter, within the unflooded HT (4a in Figure 5.2.1a). **b.** unfractured crater, 40 km in diameter, within the flooded HT (4b in Figure 5.2.1a). **c.**

fractured crater, 75 km in diameter within the HT (4c in Figure 5.2.1a). **d.** Fractured crater remnant, 60 km in diameter, within the Chaotic Terrain (4d in Figure 5.2.1a). The red lines are interpretations of the collapsed blocks. The blue arrows point to the block surface top.

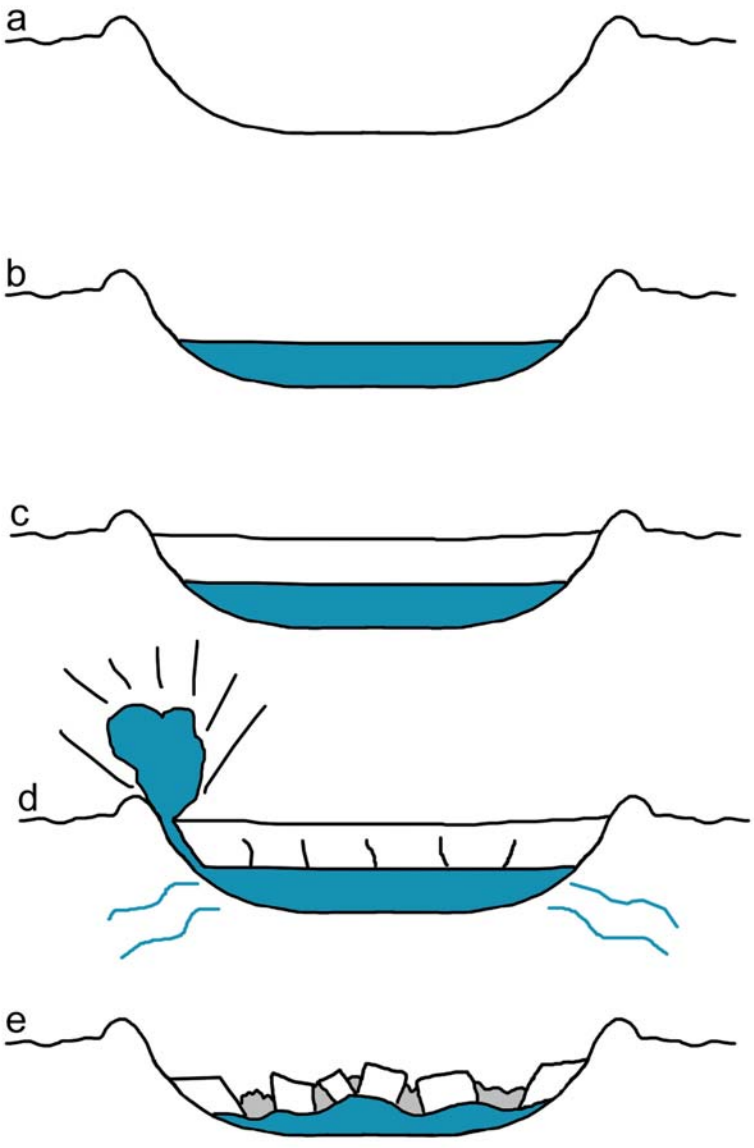

Figure 5.2.6. Proposed scenario of fractured craters and crater remnants formation. **a.** Crater formation. **b.** Deposition of material within the crater with a high water content. **c.** Deposition of a cap deposit within the crater. **d-e.** Fracturing, collapse of the cap material and the (explosive) release of water. The grey material located between the collapsed blocks consists of relatively small hills and could be brecciated cap material (see also Observation 10). I interpret the collapse to be caused by subsurface topography of material underneath (possibly the water rich material). For complex craters or larger the subsurface topography could perhaps also be explained by a central uplift or a peak ring.

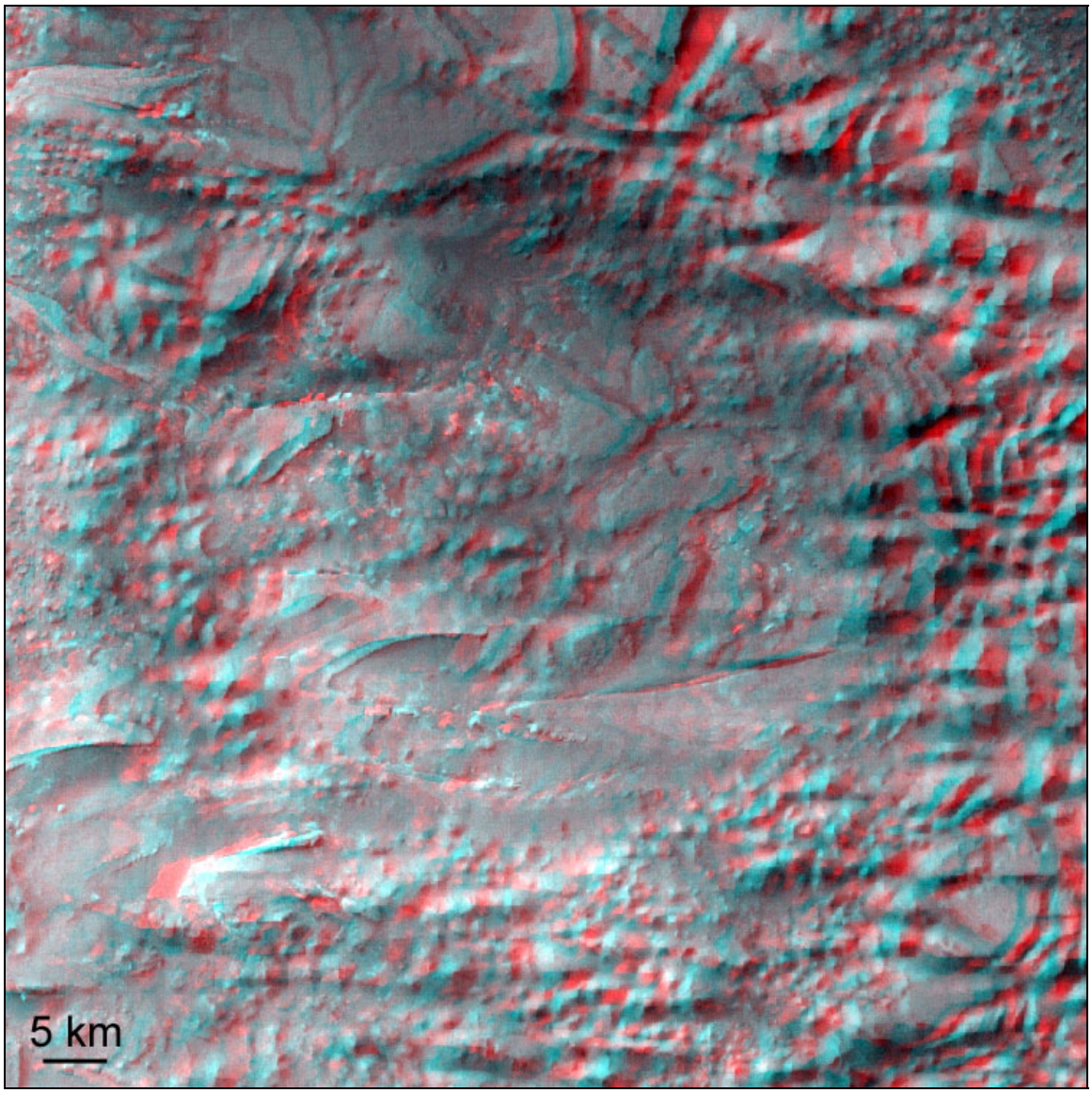

Figure 5.2.7. An impact remnant within Aureum Chaos (5 in Figure 5.2.1a). The sharp-edged deposits are Aureum Chaos Deposits (HRSC anaglyph, east is upward).

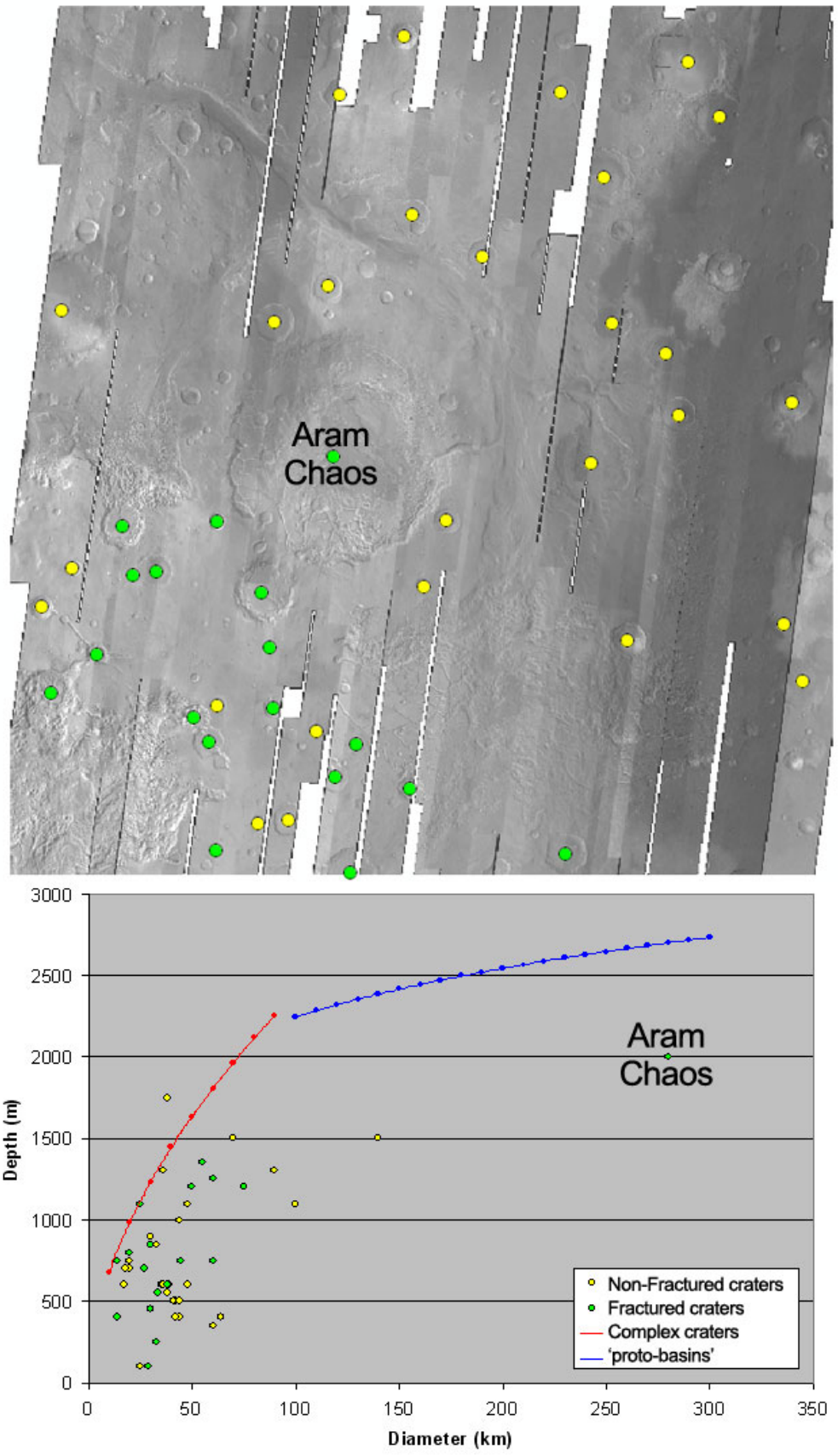
Aram
Chaos
Aram
Chaos
Depth (m)
Diameter (km)
0
500
1000
1500
2000
2500
3000
0
50
100
150
200
250
300
350
Non-Fractured craters
Fractured craters
Complex craters
'proto-basins'

Figure 5.2.8. Crater diameter vs. crater depth, measured for 18 fractured (including Aram Chaos) and 27 non-fractured craters in my research area. The crater depth was determined by estimating, using MOLA profiles, the difference between the mean elevation of the surface surrounding the crater and the mean crater floor elevation. The red and blue lines show the diameter-depth relation for complex craters ($d = 0.19 \times D^{0.55}$) and 'proto-basins', craters larger then 90 km in diameter ($d = 0.98 \times D^{0.18}$), respectively. The relations were derived by Garvin et al. (1999, 2000) using MOLA profiles of over 1300 craters. Complex craters are defined as craters which exhibit a central uplift. They occur in the diameter range between 6-7 km (the transition from simple to complex craters) and 90 km (the complex-to-proto-basin transition). Proto-basin craters can have a ring uplift (peak ring) and/or have multiple rings (such as Aram Chaos).

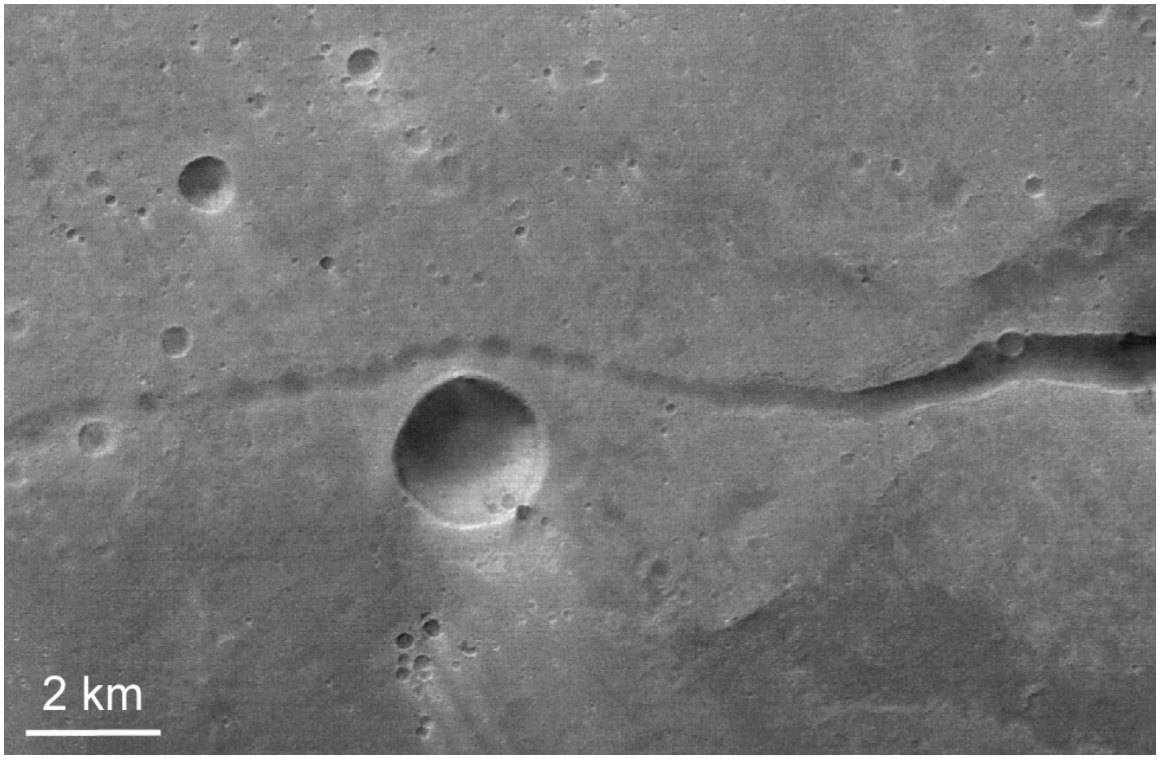

Figure 5.2.9. The occurrence of crater pits along a fault trace (7 in Figure 5.2.1a) (HRSC nadir, image center 334.33°E, 1.32°S).

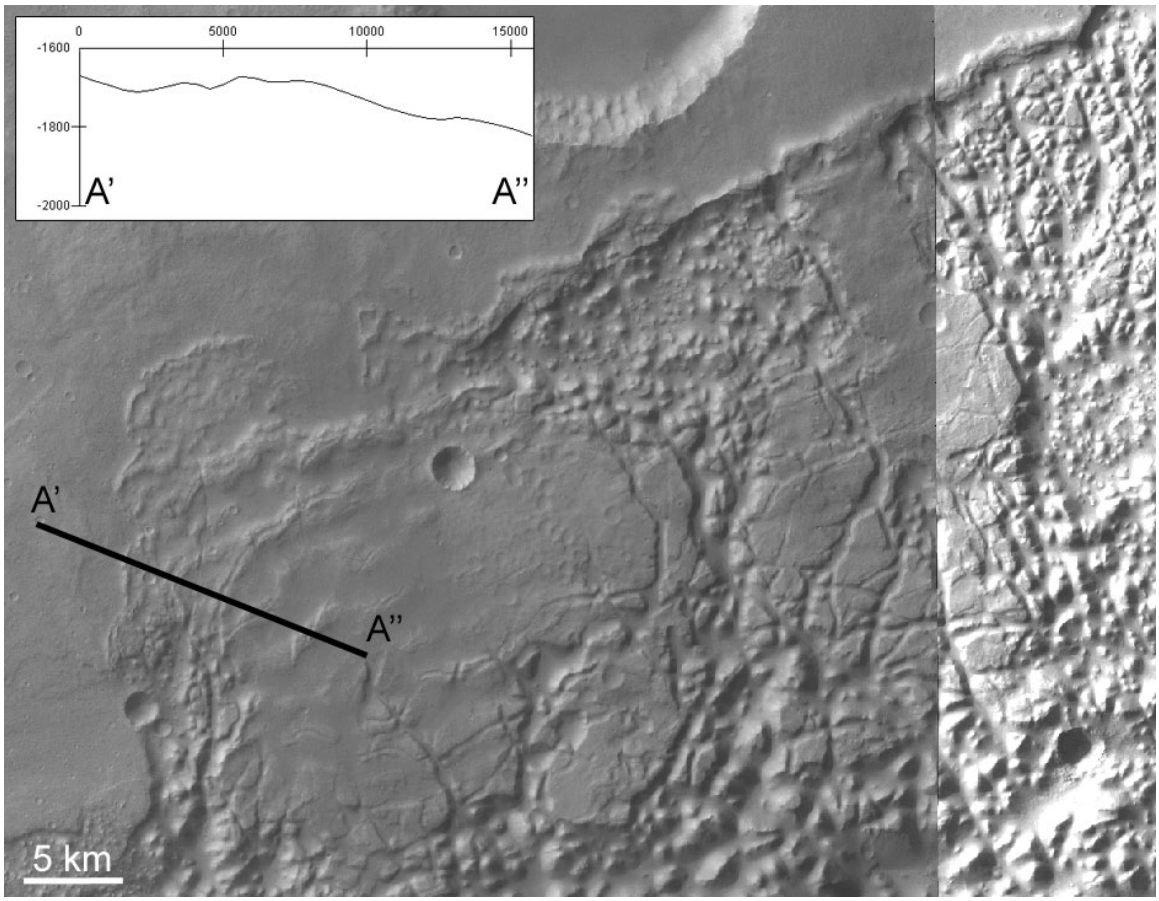

Figure 5.2.10. Possible compression ridges at the edges of Northern Iani Chaos (8 in Figure 5.2.1a) (HRSC nadir, image center 340.59°E, 0.51°S).

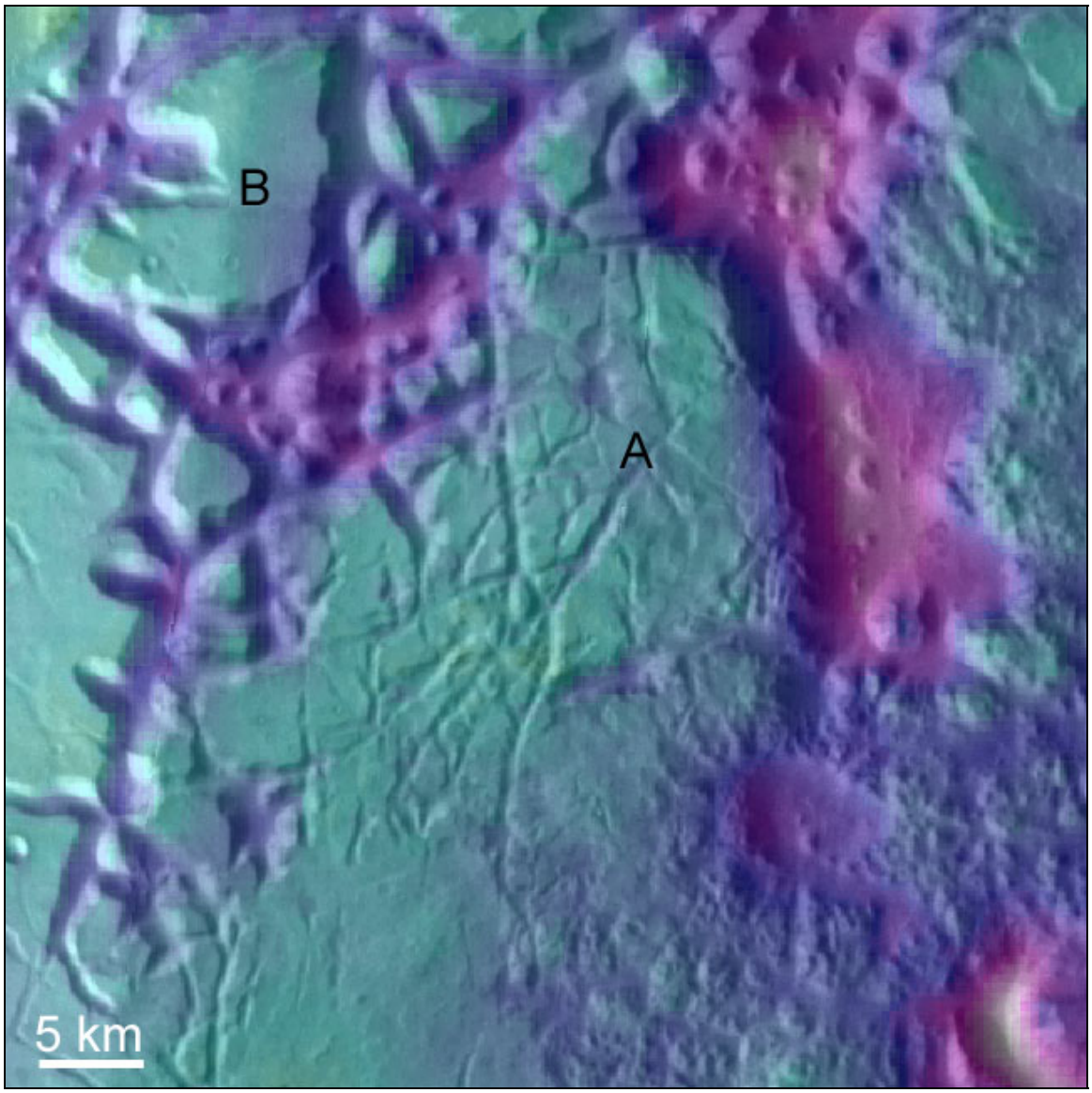

Figure 5.2.11. Fractured HT in Iani Chaos with some mesas having a small-scale fracture pattern on its surface (compare mesa A with mesa B) (9 in Figure 5.2.1a) (THEMIS IR day combined with color-coded MOLA elevation (green is high, purple is low elevation)).

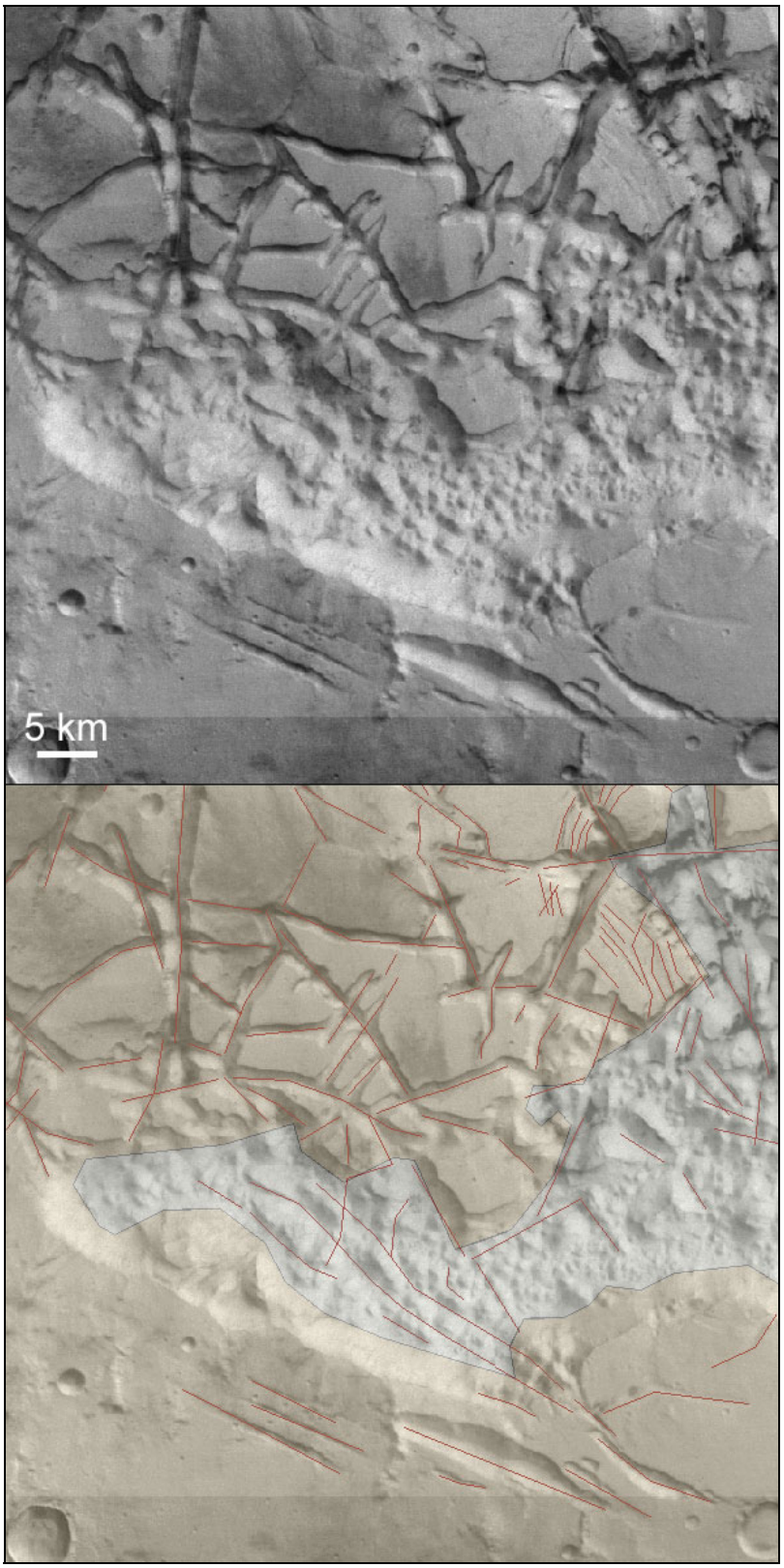

Figure 5.2.12. Example of Highland Terrain (yellow) fractures (red) continuing in the Chaotic Terrain (grey) in Aram Chaos (10 in Figure 5.2.1a) (HRSC nadir).

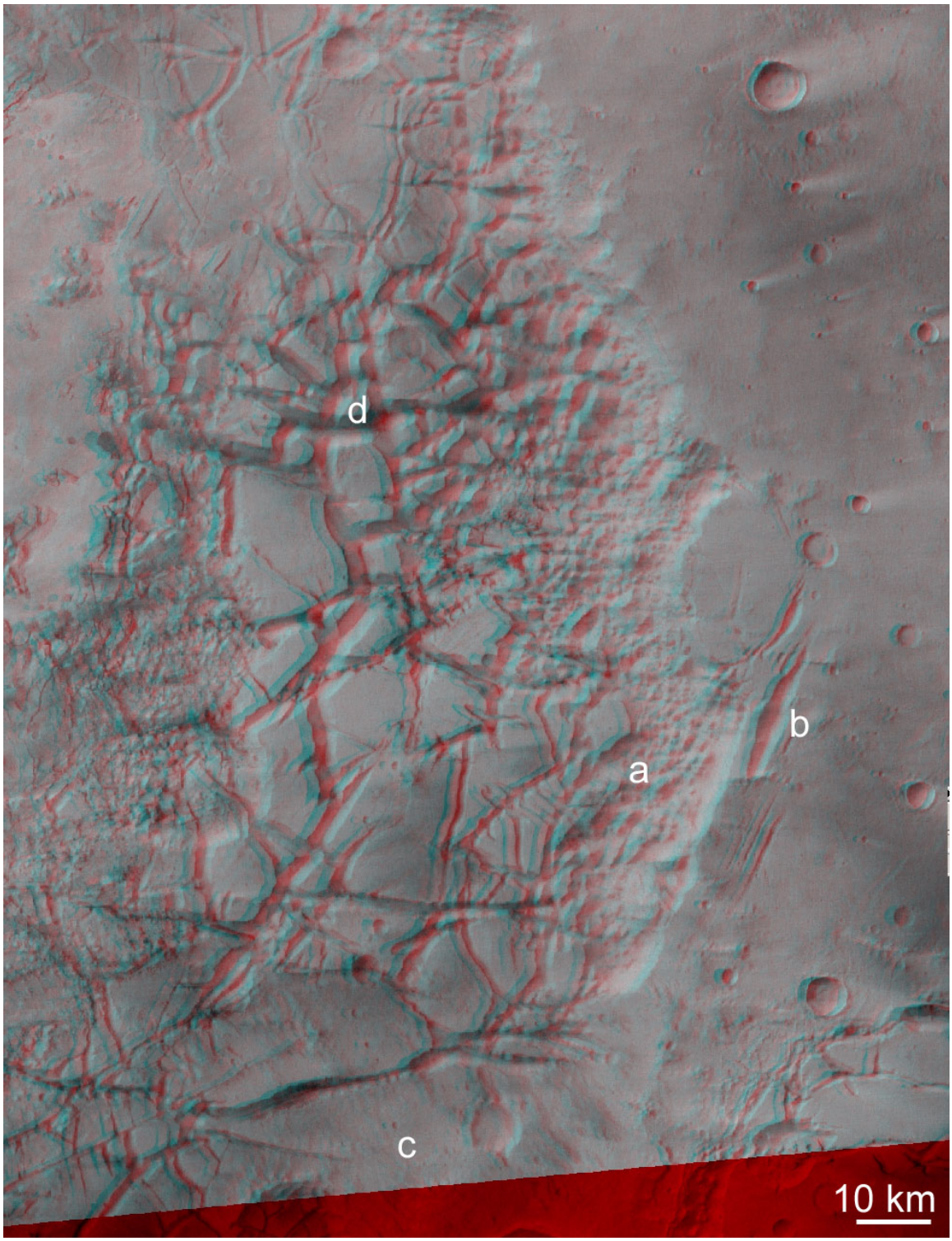

Figure 5.2.13. HRSC anaglyph (East is up, for location see Figure 5.2.1b). **a.** Fractures within the Aram Chaos Chaotic Terrain (Observation 10, see also Figure 5.2.12). **b.** Tearing of the HT (Observation 16) **c.** The fractured Highland Terrain continues into Aram Chaos (Observation 17) **d.** A ~30 km in diameter circular elevated area consisting of HT blocks (Observation 18, see also Figure 5.2.20).

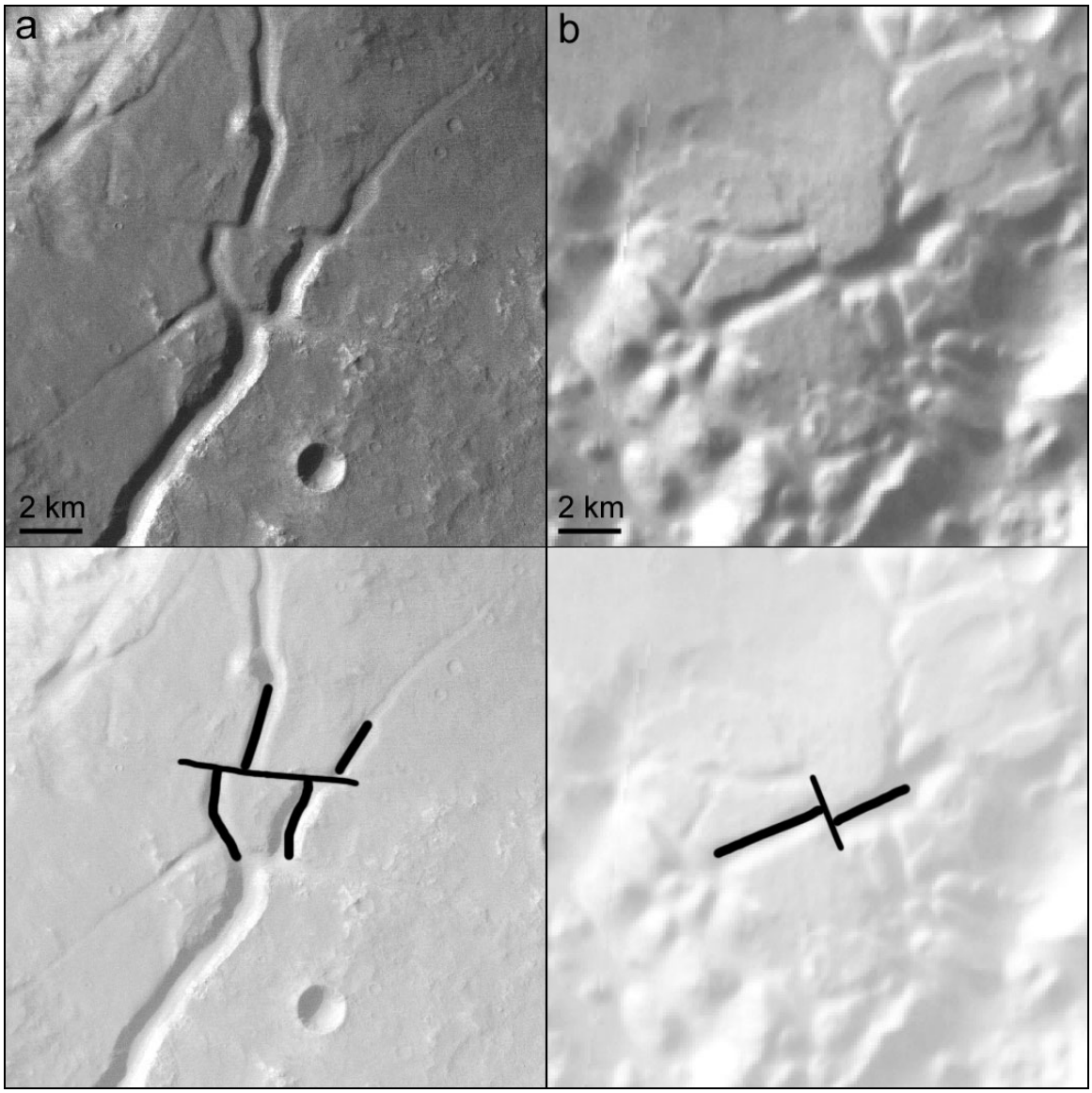

Figure 5.2.14. Possible fracture offsets. **a.** At the southern border of Iani Chaos (11a in Figure 5.2.1a) (HRSC nadir). **b.** Within Aureum Chaos (11b in Figure 5.2.1a) (THEMIS IR day).

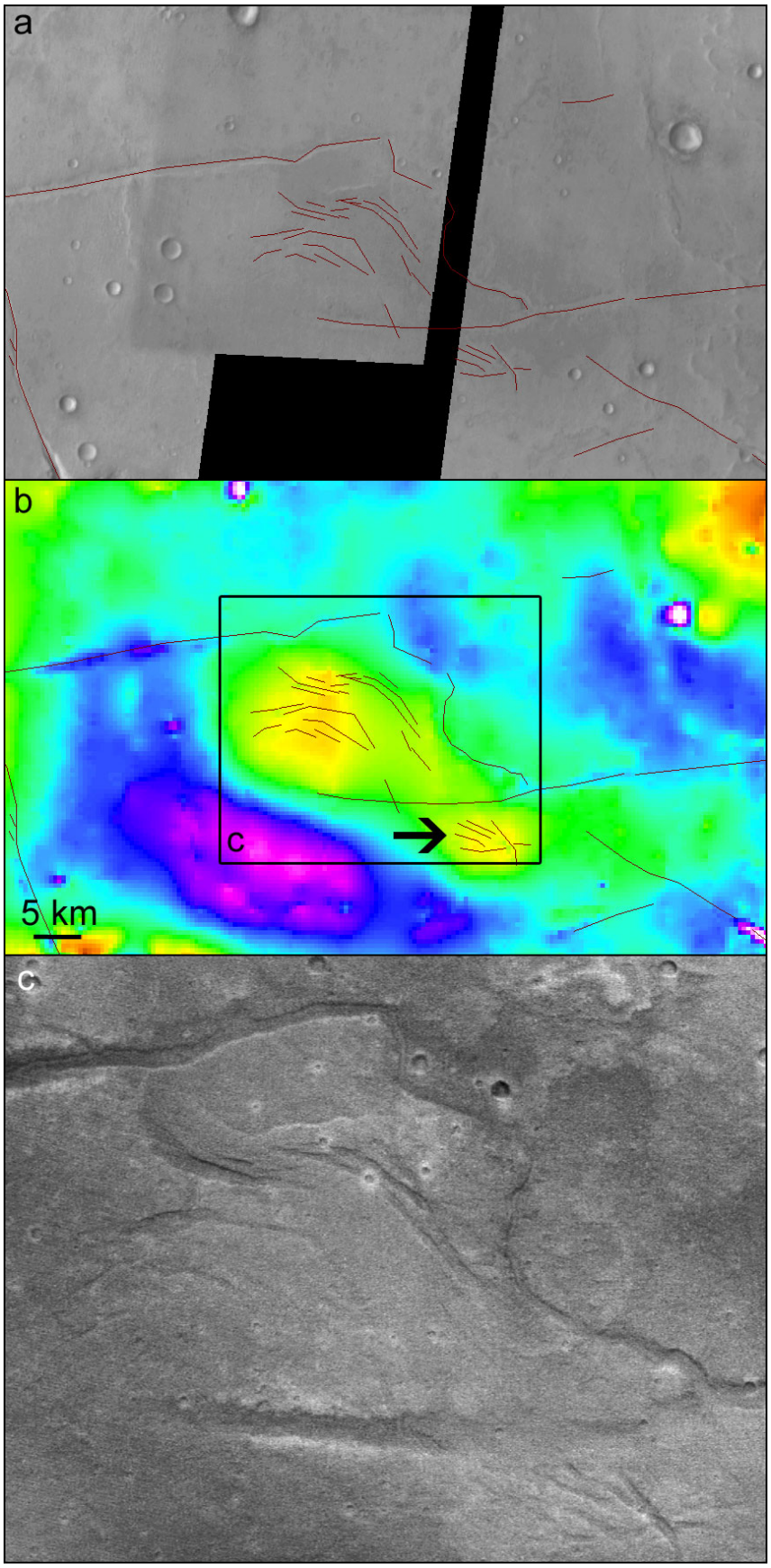
a
b
c
5 km
c

Figure 5.2.15. A possible contractional duplex system (12 in Figure 5.2.1a). **a.** THEMIS IR day image with fractures and interpreted sinistral movement. **b.** Color-coded MOLA elevation (orange is high, pink is low elevation) with fractures. **c.** Zoom of possible contractional duplex system fractures (HRSC nadir).

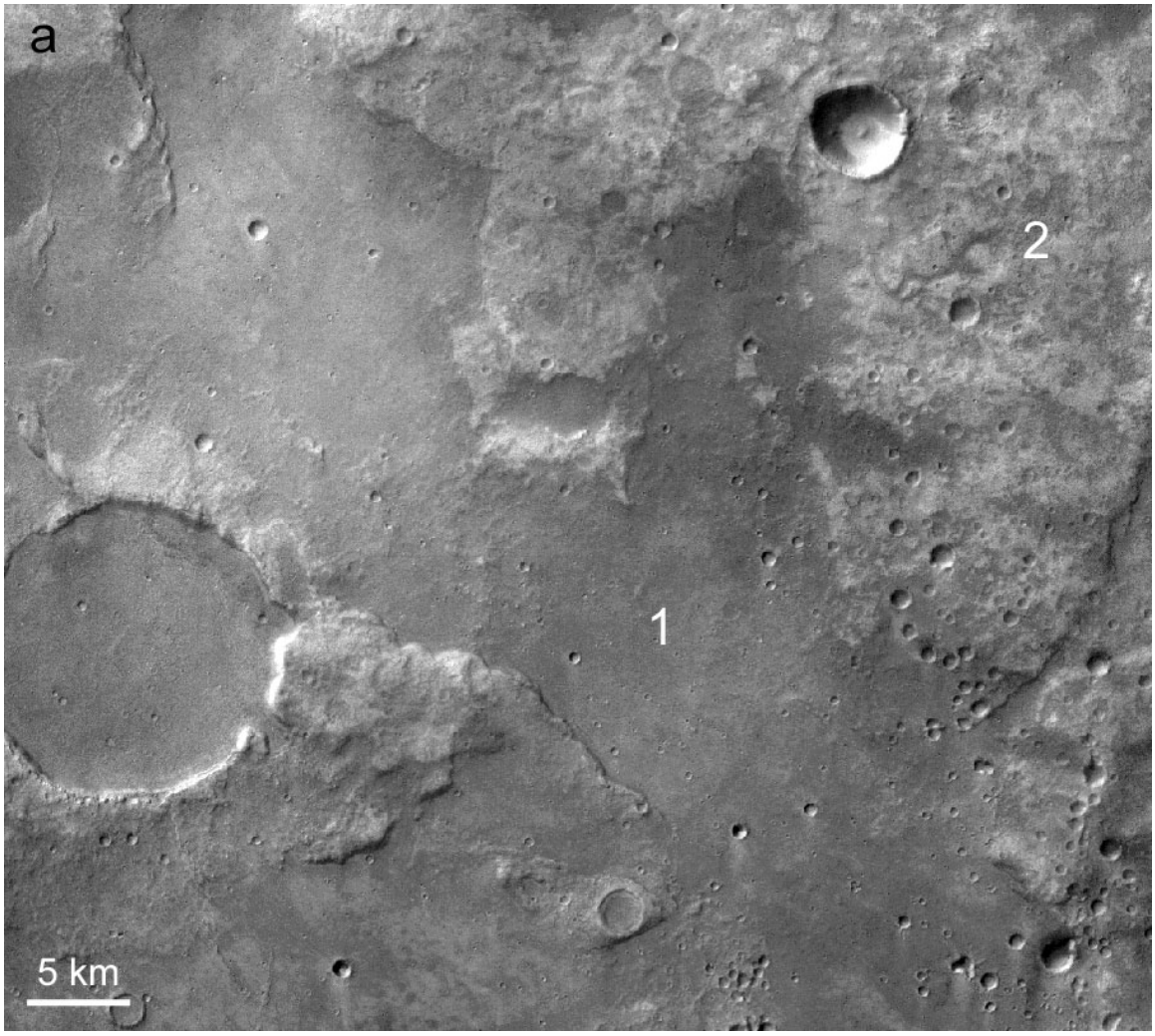

Figure 5.2.16. Variability of Highland Terrain surface morphology. **a.** Flooded Highland Terrain (13a in Figure 5.2.1a). Two different morphologies can be distinguished (1 and 2) (HRSC nadir). **b.** Highland Terrain South of Aram Chaos (13b in Figure 5.2.1a) A smooth morphology occurs outside and within a fractured crater (3 and 4). A more rugged and cratered surface morphology occurs to the North (5). **c.** Rugged morphology is observed outside (6) and within (7) the Aram Chaos crater (13c in Figure 5.2.1a).

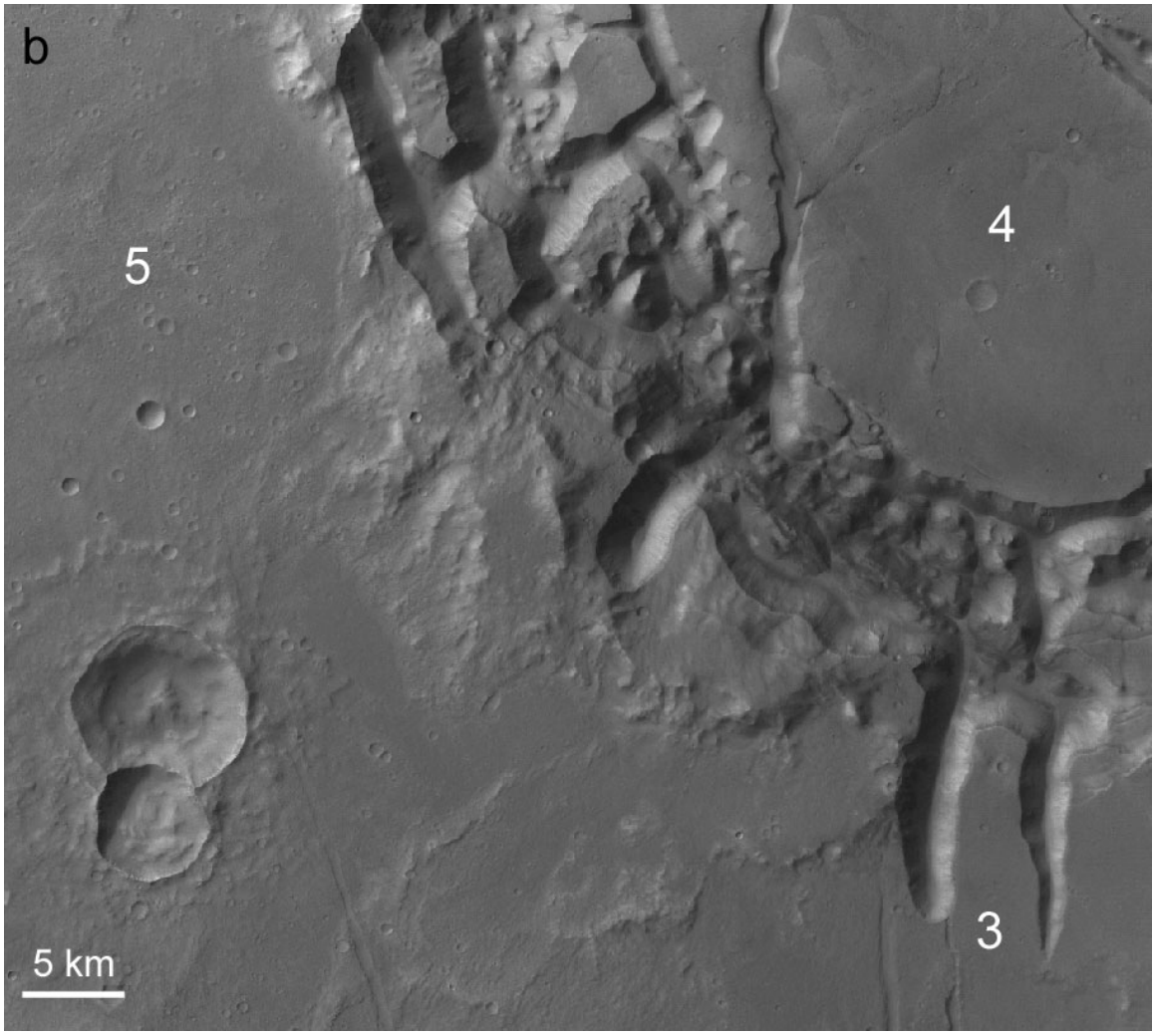

Figure 5.2.16 (continued).

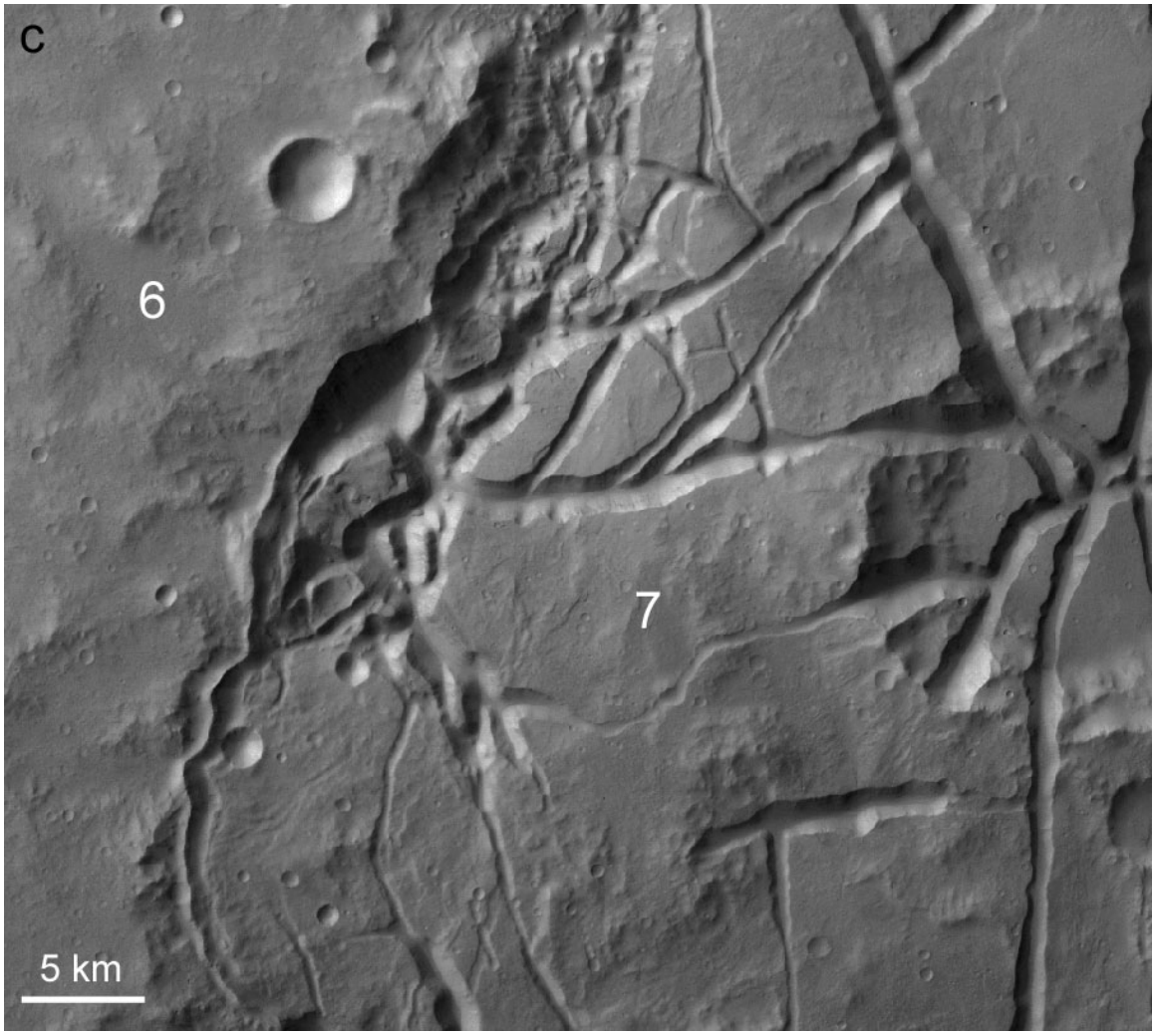

Figure 5.2.16 (continued).

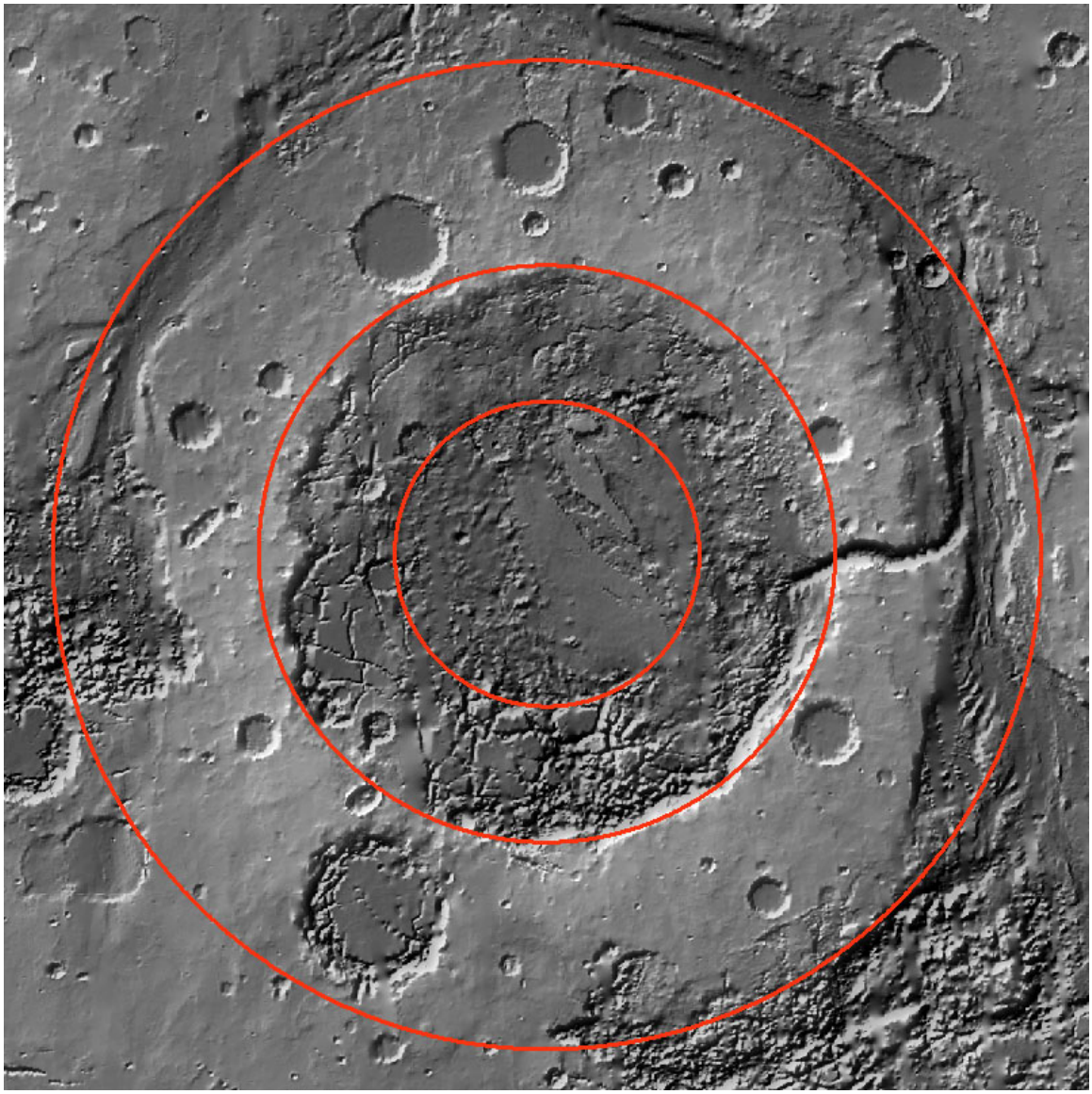

Figure 5.2.17. The rings of the Aram Chaos multiring crater.

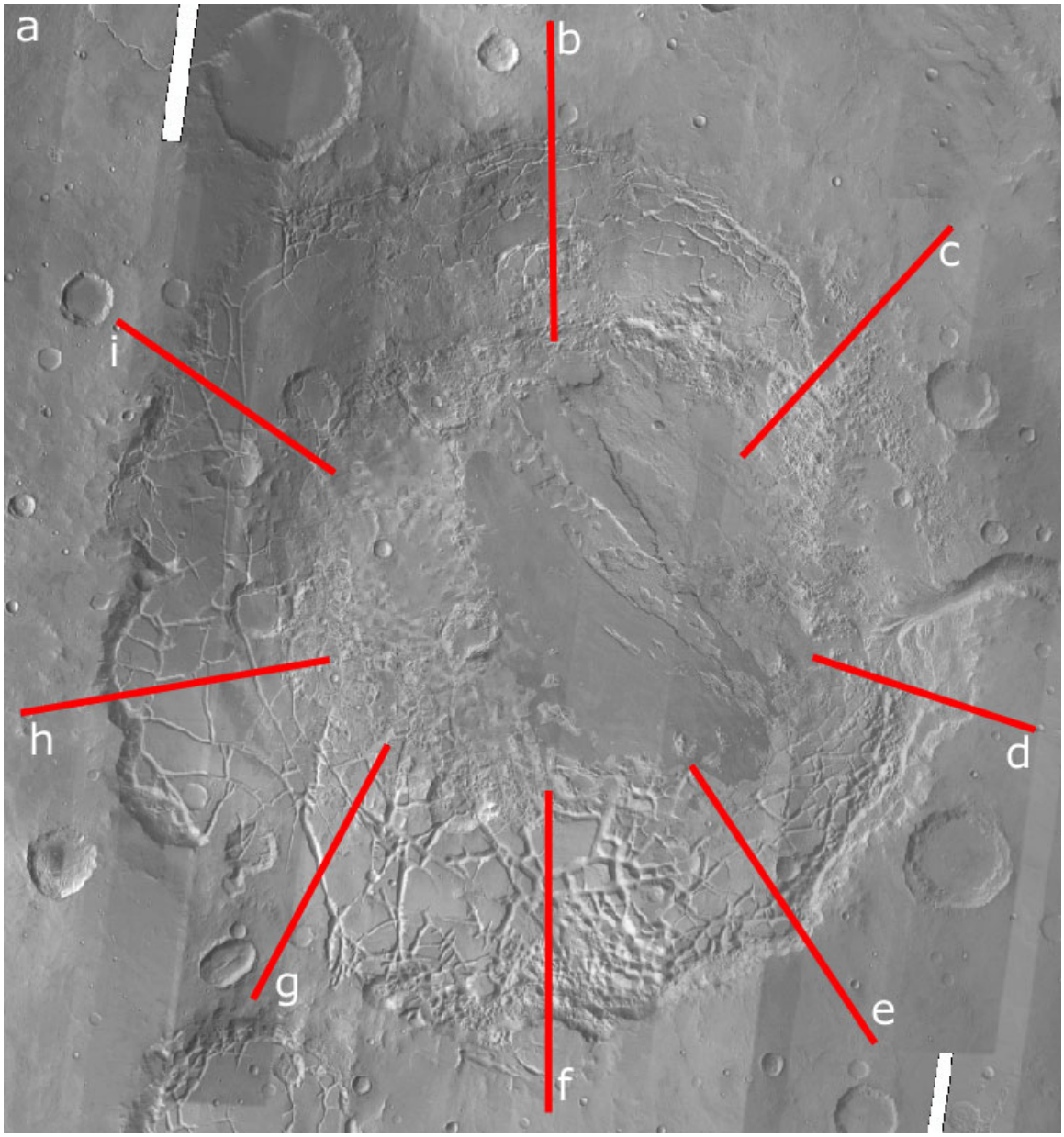

Figure 5.2.18. Estimation of a pre-subsidence Aram Chaos HT elevation. **a.** The profile outlines on top of THEMIS IR day. **b-i.** The different MOLA profiles and an estimate of the pre-subsidence Aram Chaos HT elevation (red line) for each profile. This line was drawn at the location of the main crater rim, where a sudden change in elevation occurs. Most lines lie between –1500 and –2000.

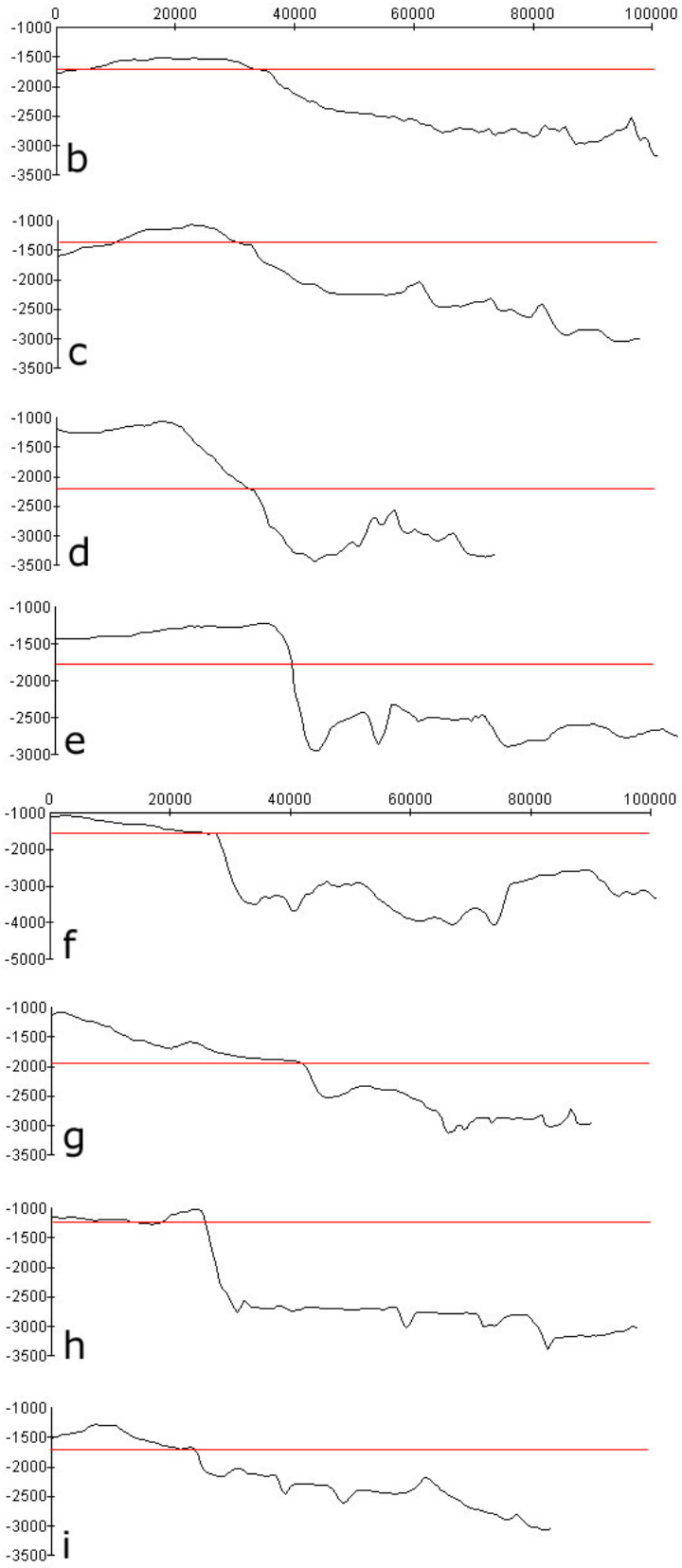

Figure 5.2.18 (continued).

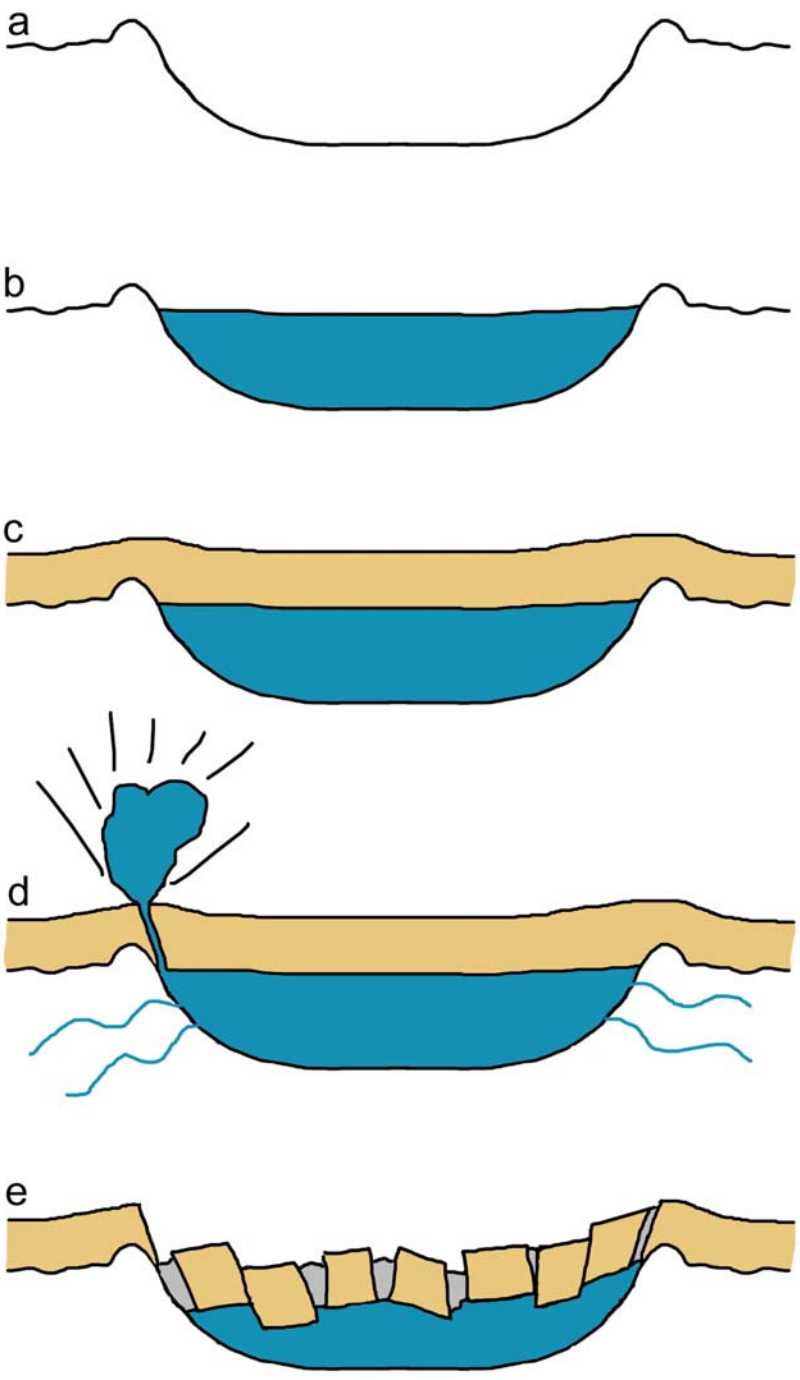

Figure 5.2.19. Cartoon of possible events leading to current Aram Chaos HT geometry (the cartoon doesn't depict a true cross section through Aram Chaos). **a.** Aram Chaos crater formation. **b.** Deposition of material within the crater with a high water content. **c.** Deposition of the HT material. **d-e.** Withdrawal of the water rich material, via crater fractures or to the surface in an explosive manner. This resulted in fracturing and brecciation (grey areas, see Observation 10) of the HT which subsequently collapsed.

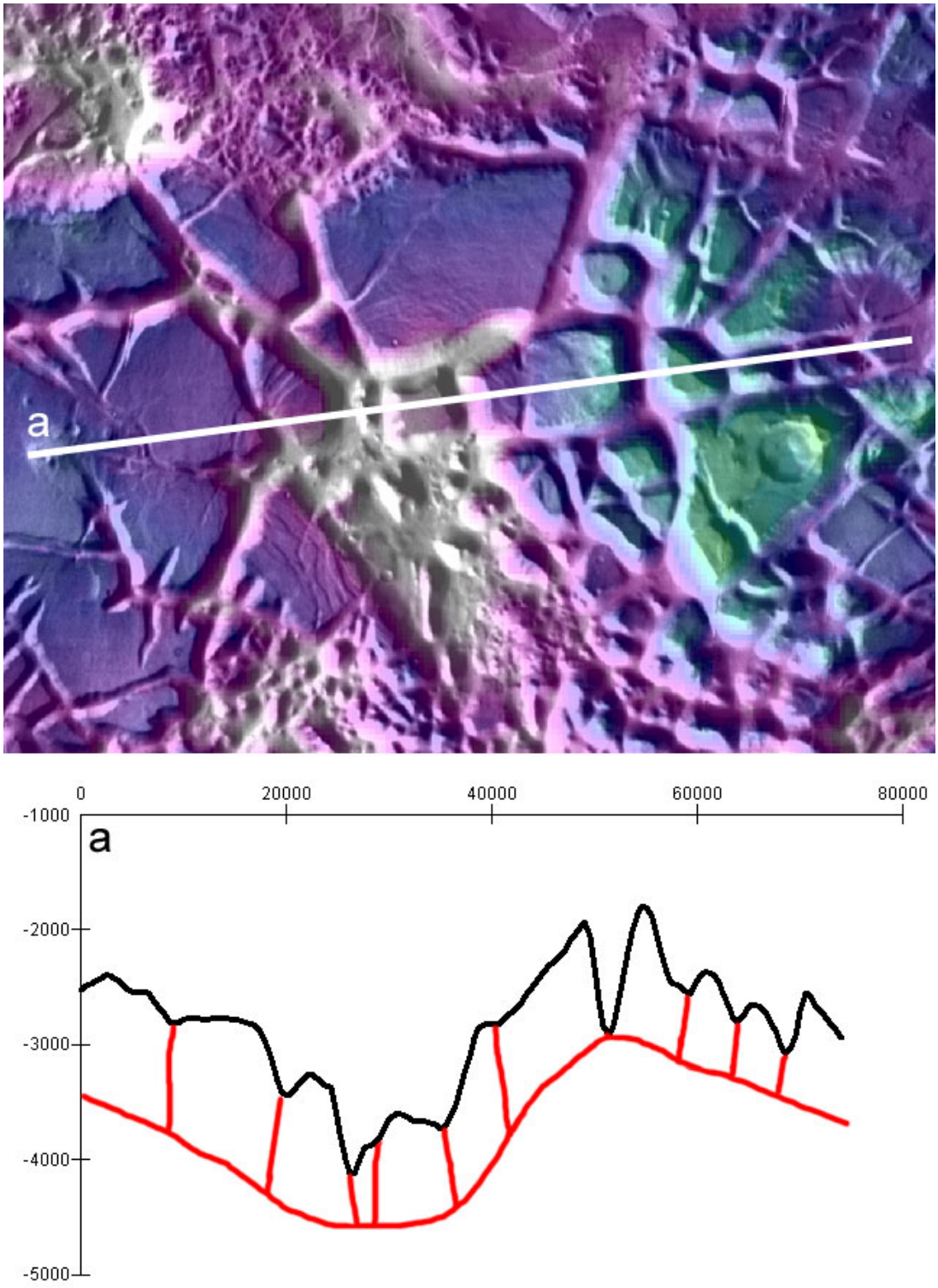

Figure 5.2.20. Image showing Aram Chaos HT collapse to be varying (THEMIS IR day and color-coded MOLA elevation (green is high, grey is low elevation). For the location see 18 in Figure 5.2.1b. **a.** MOLA derived profile (black) and interpreted HT fault bounded blocks (red) The HT blocks are interpreted to be draped over subsurface topography. The profile is ~10 times exaggerated.

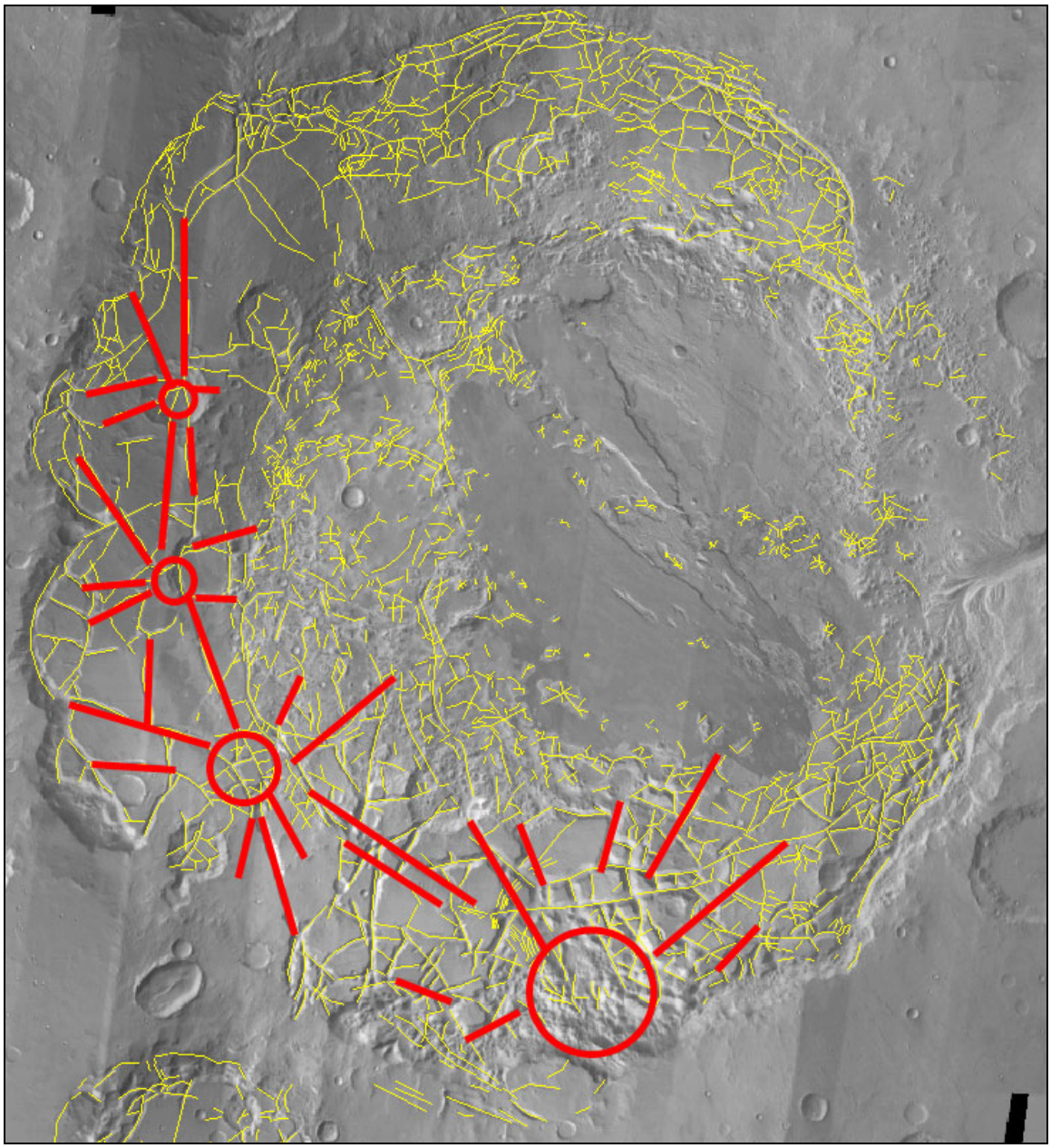

Figure 5.2.21. Fractures radial (red lines) to 4 localities (red circles) within Aram Chaos. The upper locality consists of an impact crater.

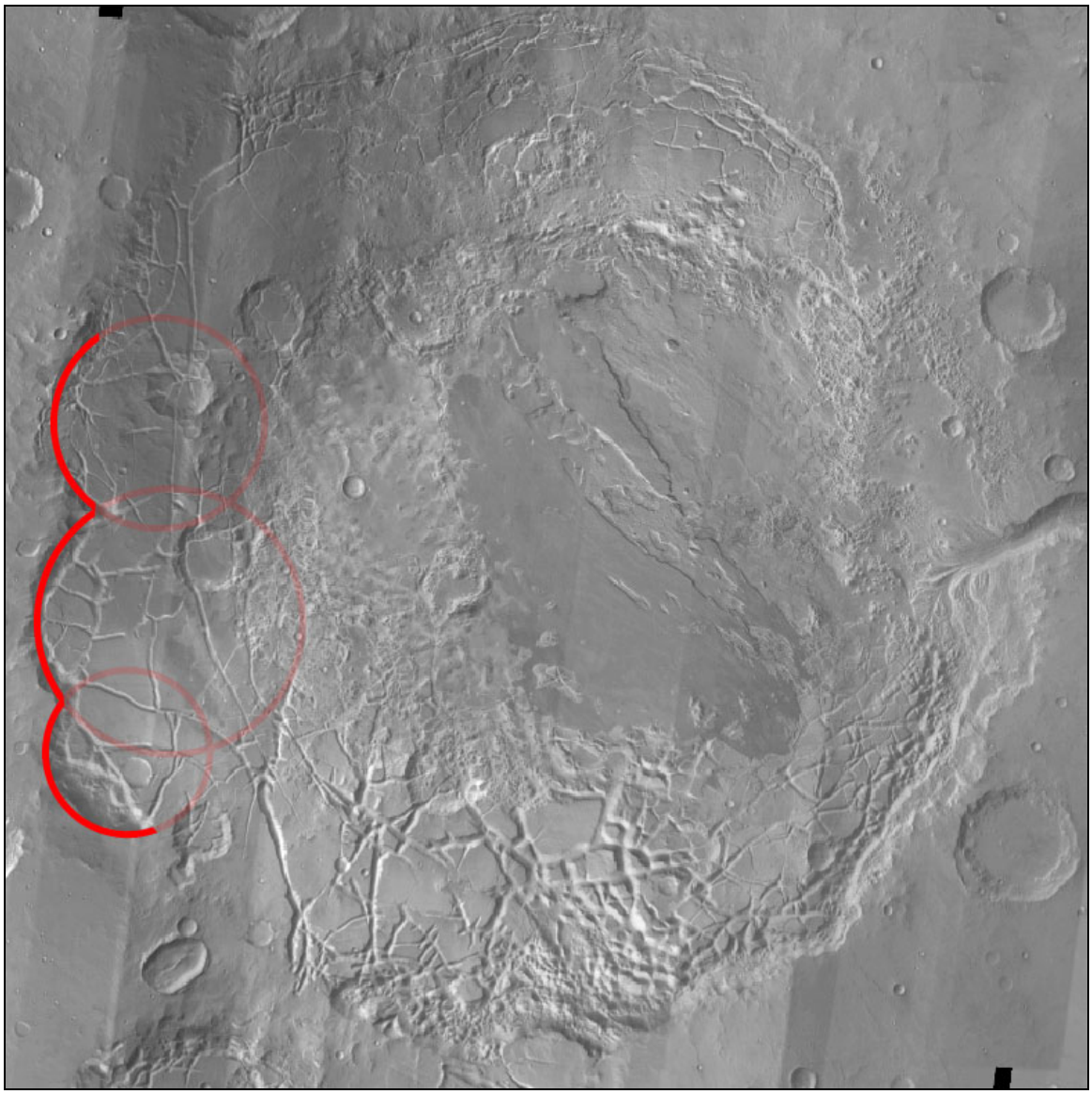

Figure 5.2.22. Small arcs can be observed in the Western Aram Chaos rim.

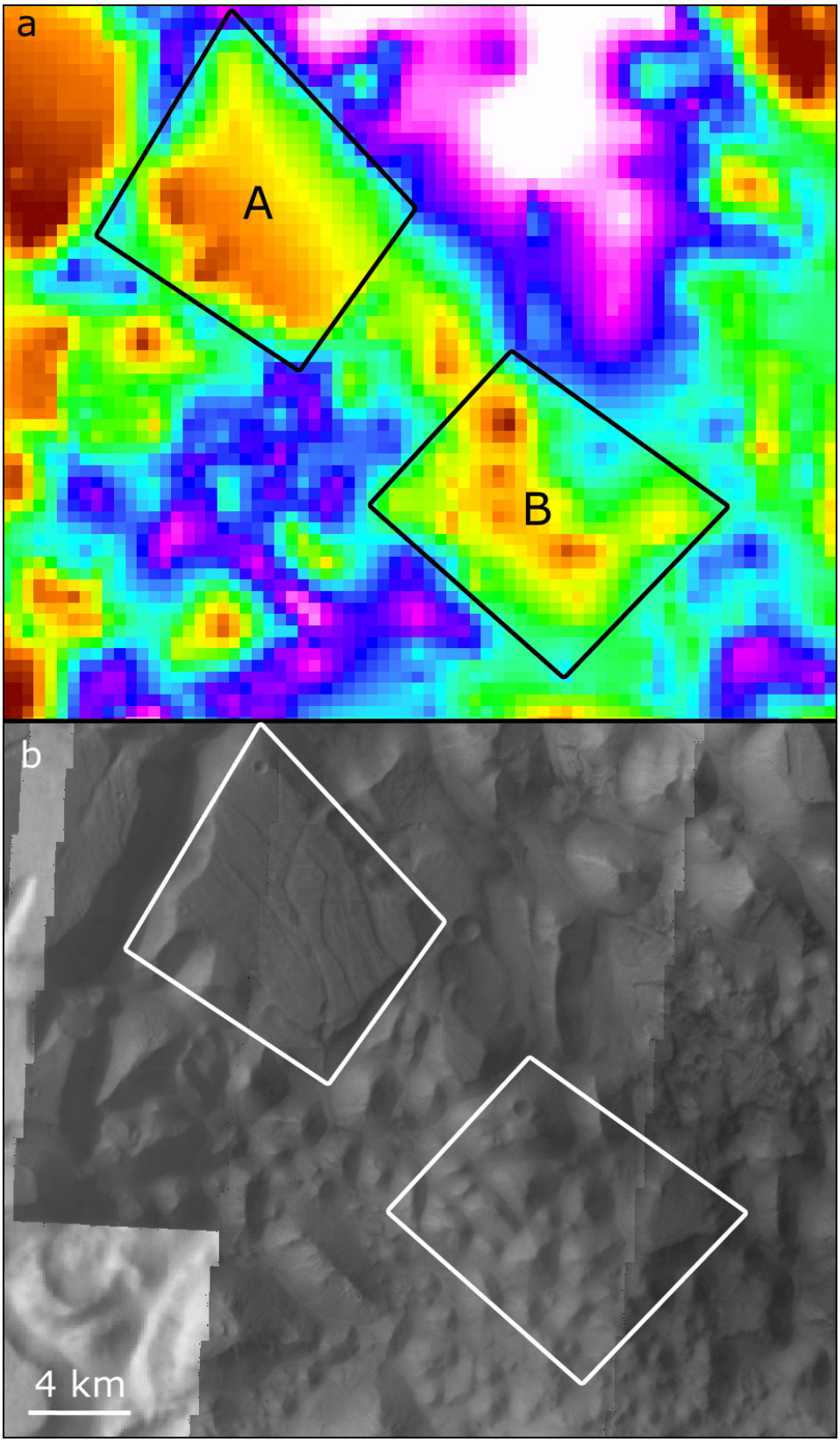

Figure 5.2.23. A mesa is observed at the edge of the southern Chaotic Terrain (CT) of Aram Chaos (A) (for overview see 21 in Figure 5.2.1b). This mesa is observed to be

fractured. MOLA data (**a**) shows a similar sized area within the CT (B). This is interpreted to be a fractured mesa which underwent erosion. **a.** Color-coded MOLA data (white is low, orange is high elevation). **b.** Mosaic of THEMIS VIS and THEMIS IR day images.

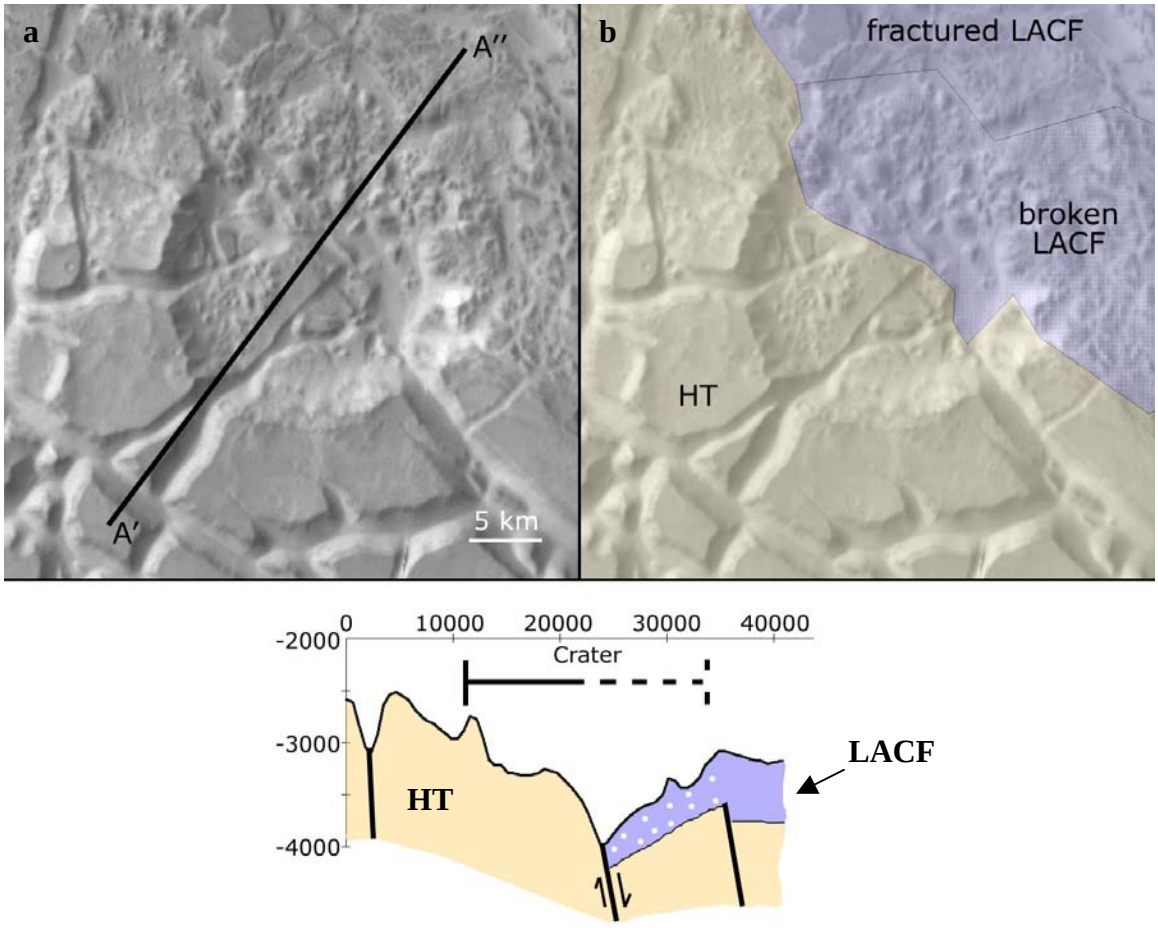

Figure 5.2.24. A half crater occurs within Aram Chaos at the boundary between the fractured HT and the Lower Aram Chaos Formation (LACF) (for overview see 22 in Figure 5.2.1b). **a.** THEMIS IR day image. **b.** THEMIS IR day image and mapping.

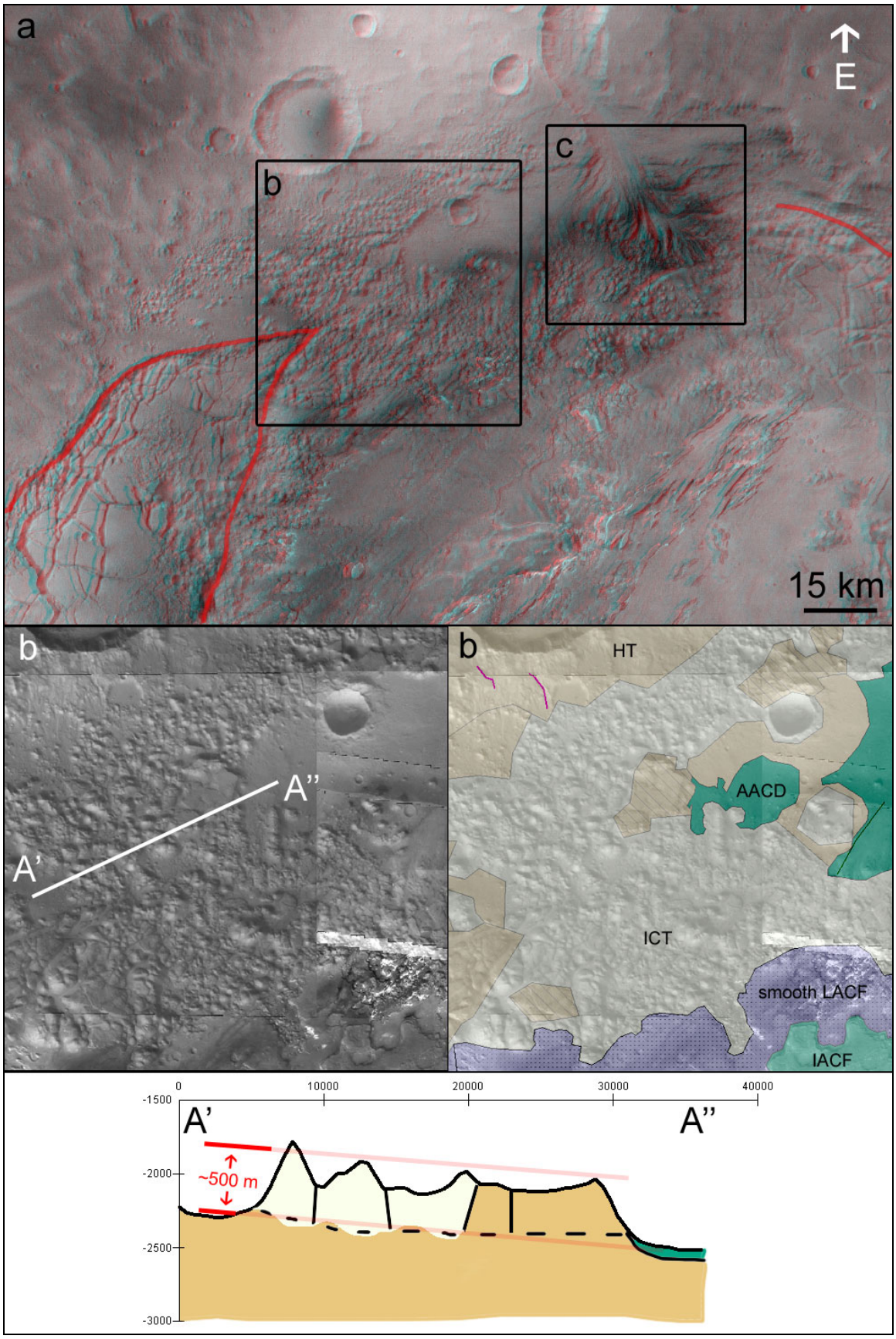
a
E
b
c
15 km
b
A'
A''
b
HT
AACD
ICT
smooth LACF
IACF
0
10000
20000
30000
40000
-1500
-2000
-2500
-3000
A'
A''
~500 m

Figure 5.2.25. The East part of Aram Chaos. **a.** Concentric rim fractures (red lines) did not develop in the East of Aram Chaos (HRSC anaglyph, East is up, for location see 19 in Figure 5.2.1b). **b.** Small-scale chaotization forming mesas ~500 m high (see Profile A). **c.** Multiple AACD (green) terraces have been formed by the Aram Chaos channel outflow. The AACD is observed to form a delta-shaped feature (HRSC anaglyph, West is up). **d.** Layering of AACD in the Aram Chaos channel wall (HRSC nadir). **e.** The AACD is observed to grade into smooth LACF. The observation could however also be explained by the gradual thinning of the smooth LACF. This would make the smooth LACF younger then the AACD.

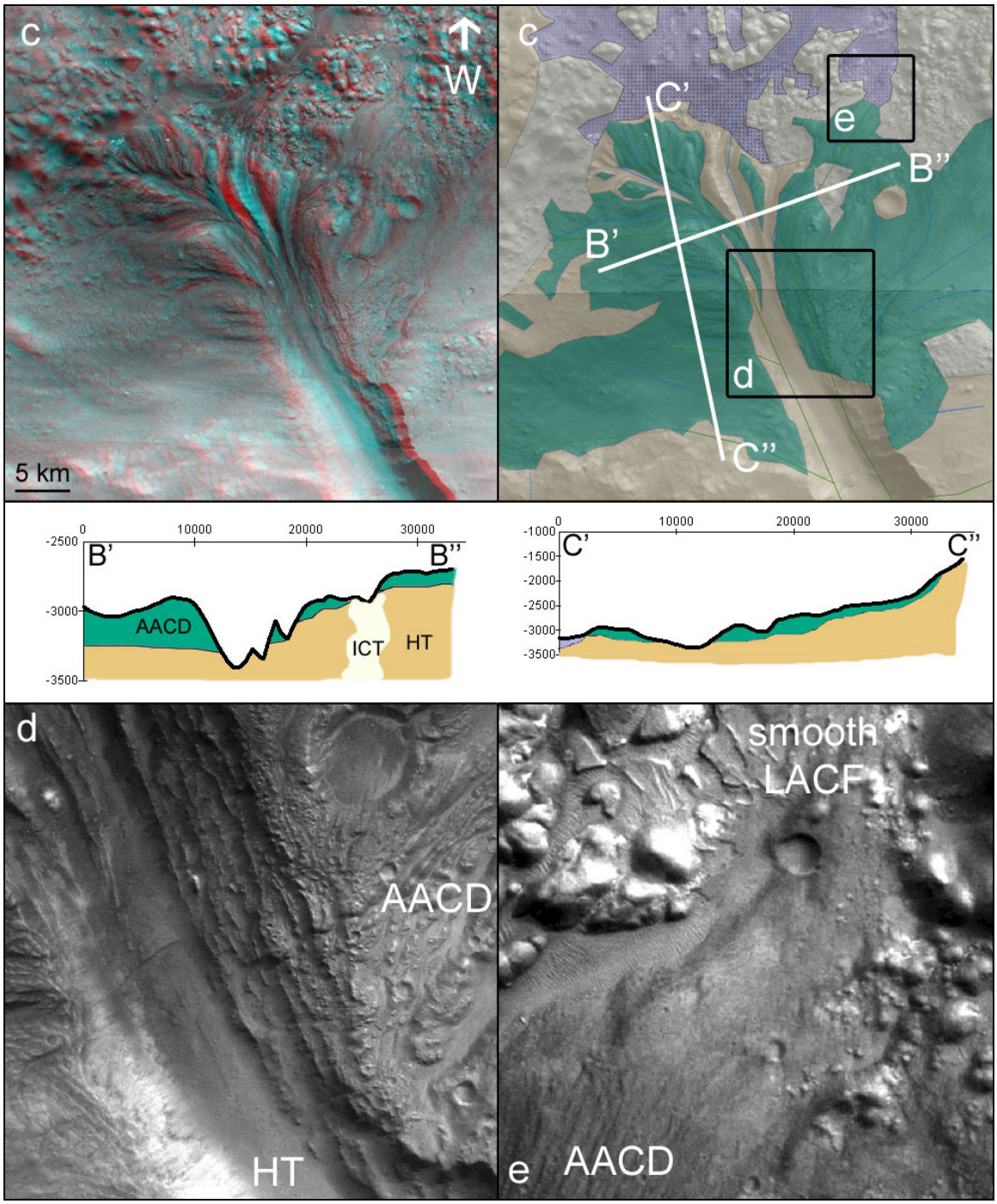

Figure 5.2.25 (continued).

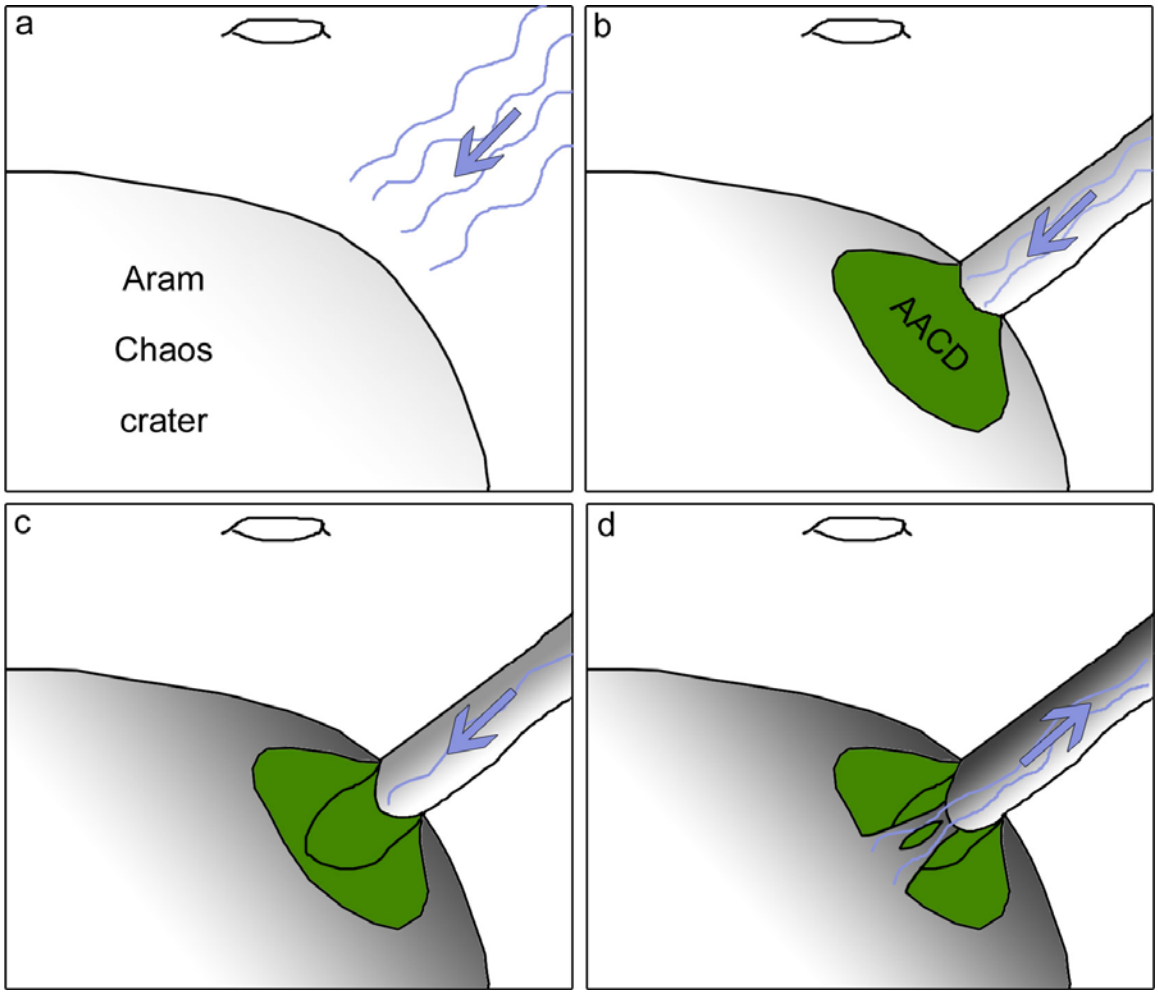

Figure 5.2.26. Cartoon showing possible events in the formation of the Aram Chaos channel and the AACD. **a.** Overflow of Aram Chaos, forming the Aram Chaos channel (see also Observation 3), **b-c.** Deposition of the AACD and continued incision of the Aram Chaos channel (also cutting through AACD) due to Aram Chaos subsidence **d.** Incision of the Aram Chaos channel by crater outward flow forming the streamlined HT mesas and eroding AACD.

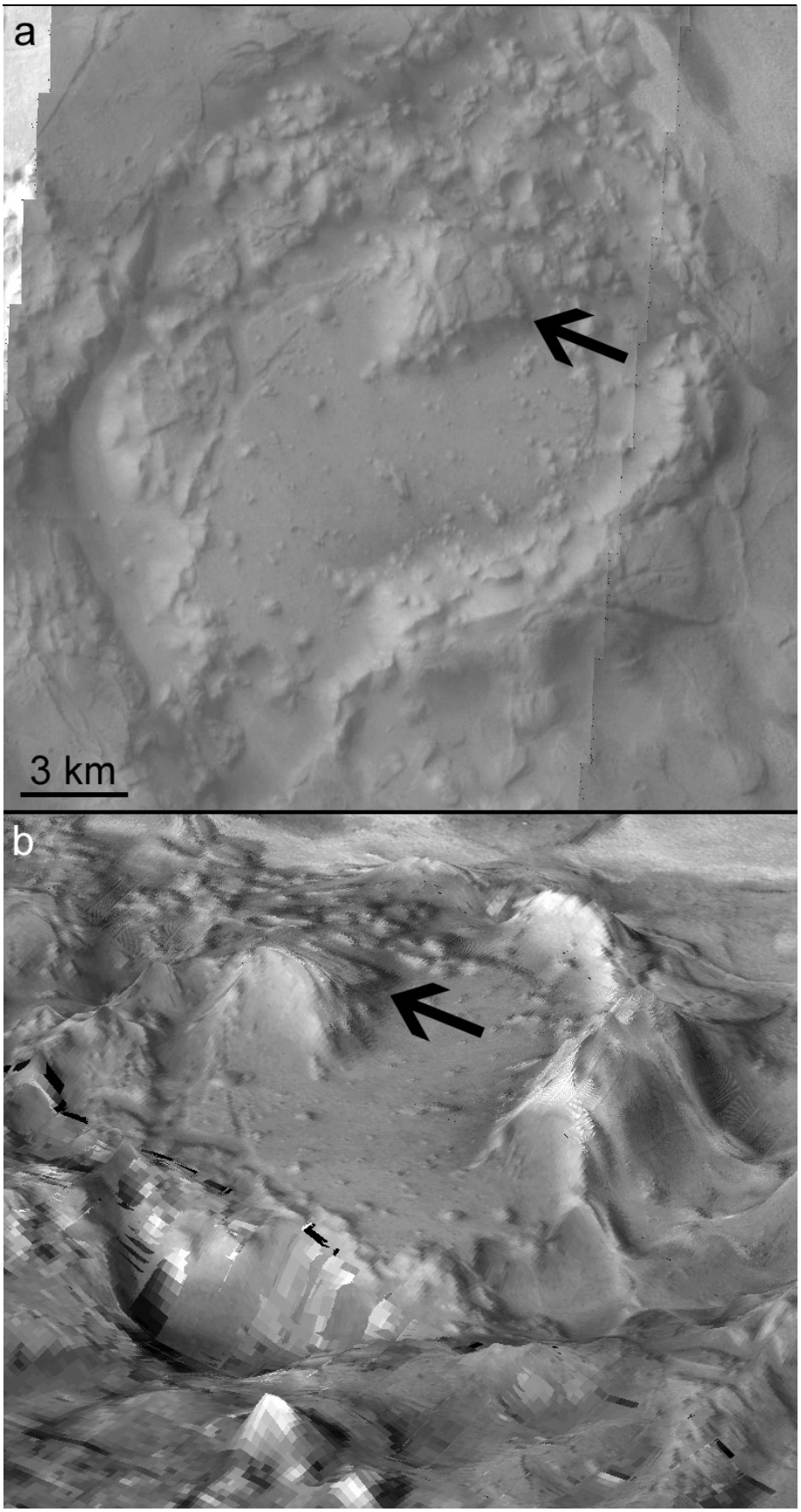
a
3 km
b

Figure 5.2.27. A fractured Lower Aram Chaos Formation mesa (arrow) stratigraphically on top of a Highland Terrain window. **a.** THEMIS VIS image (22 in Figure 5.2.1b). **b.** Birds eye view of THEMIS VIS draped over MOLA elevation (5x vertical exaggeration) showing the LACF mesa. **c.** Birds eye view with mapping overlay (purple = fractured LACF, purple with dots = broken LACF, yellow = HT, pink = UACF).

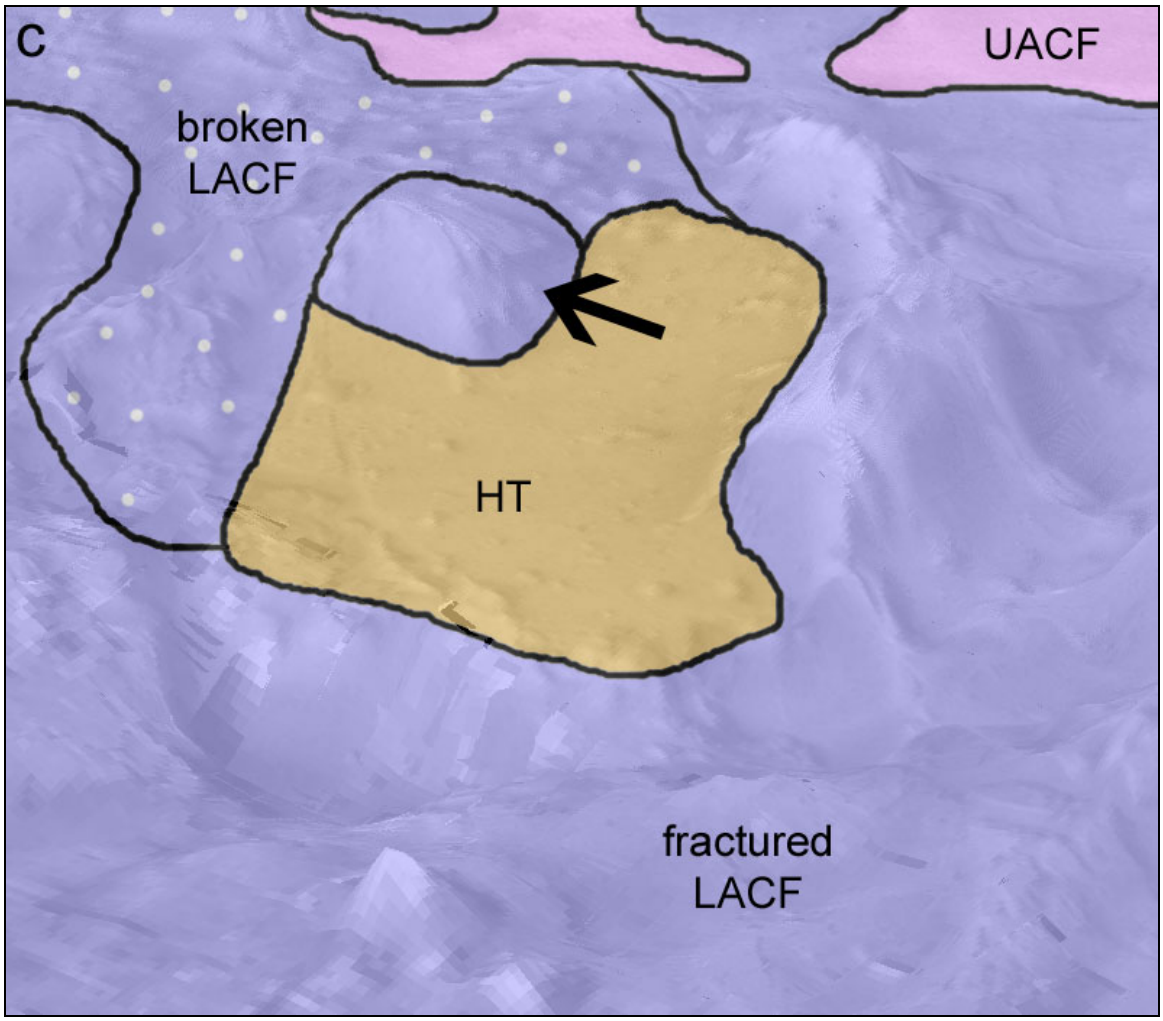

Figure 5.2.27 (continued).

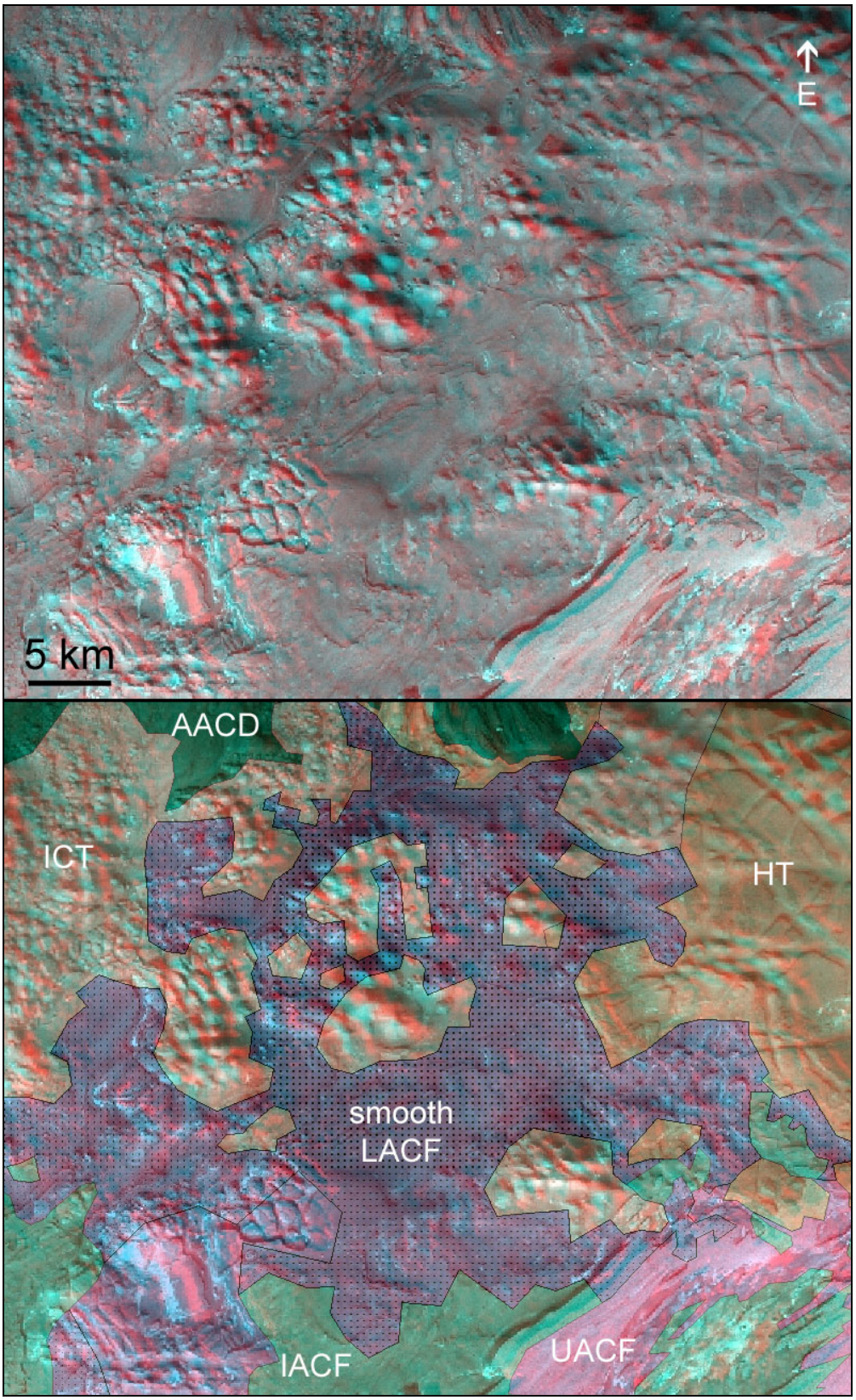

Figure 5.2.28. Draping of the smooth LACF (dotted purple) (HRSC anaglyph, East is up, for location see 23 in Figure 5.2.1b).

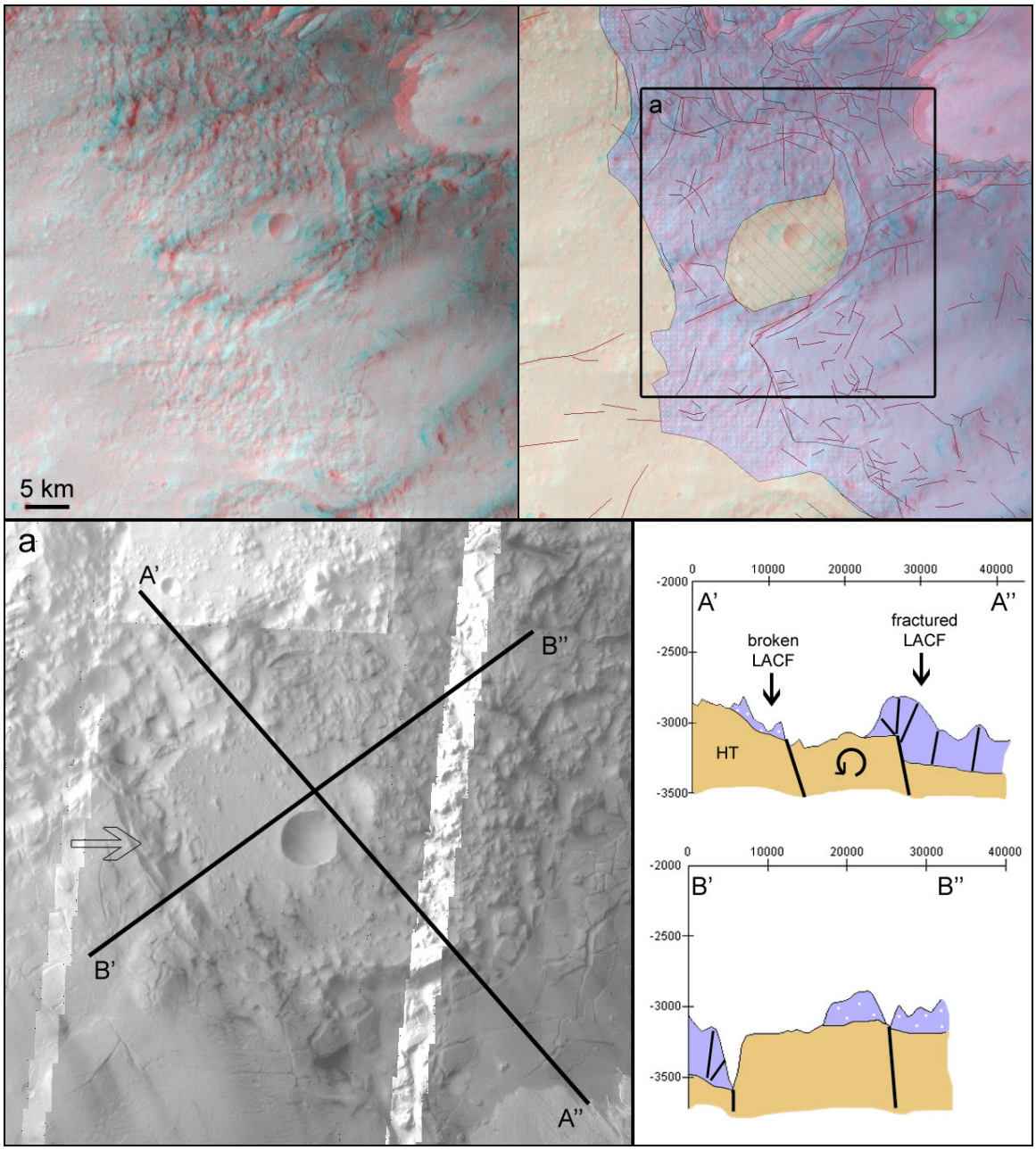

Figure 5.2.29. A Highland Terrain (yellow) window inside broken and fractured Lower Aram Chaos Formation terrain (purple). The HT window is interpreted to be a fracture bounded mesa which has been rotated due to collapse (HRSC anaglyph, East is up, for location see 24 in Figure 5.2.1b). **a.** THEMIS VIS mosaic (North is up) and profile lines A and B. Profile line A shows an elevated rim of broken LACF material along the southern edge of the HT mesa. Profile line B shows a valley along the western edge of the HT mesa where LACF material has collapsed (arrow).

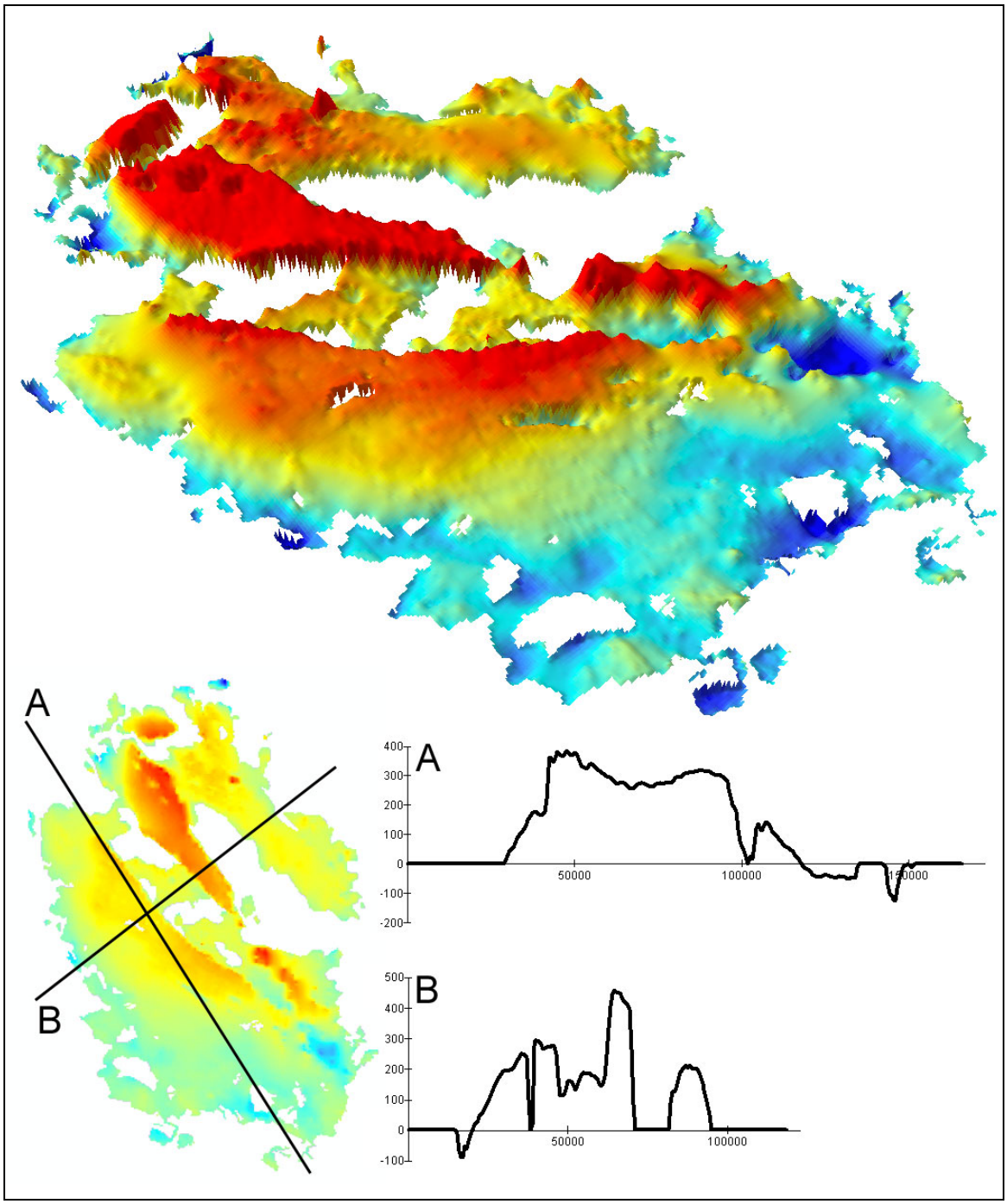

Figure 5.2.30. Derived thickness of the Intermediate and Upper Aram Chaos Formation (see *4.7.1. Deriving the thickness of the Intermediate and Upper Aram Chaos Formation* for method used). The thickness is calculated by subtracting the Nearest Neighbor interpolation from the MOLA elevation. A negative thickness value means that the Nearest Neighbor interpolation resulted in a higher elevation then the actual MOLA elevation and is subsequently not representative.

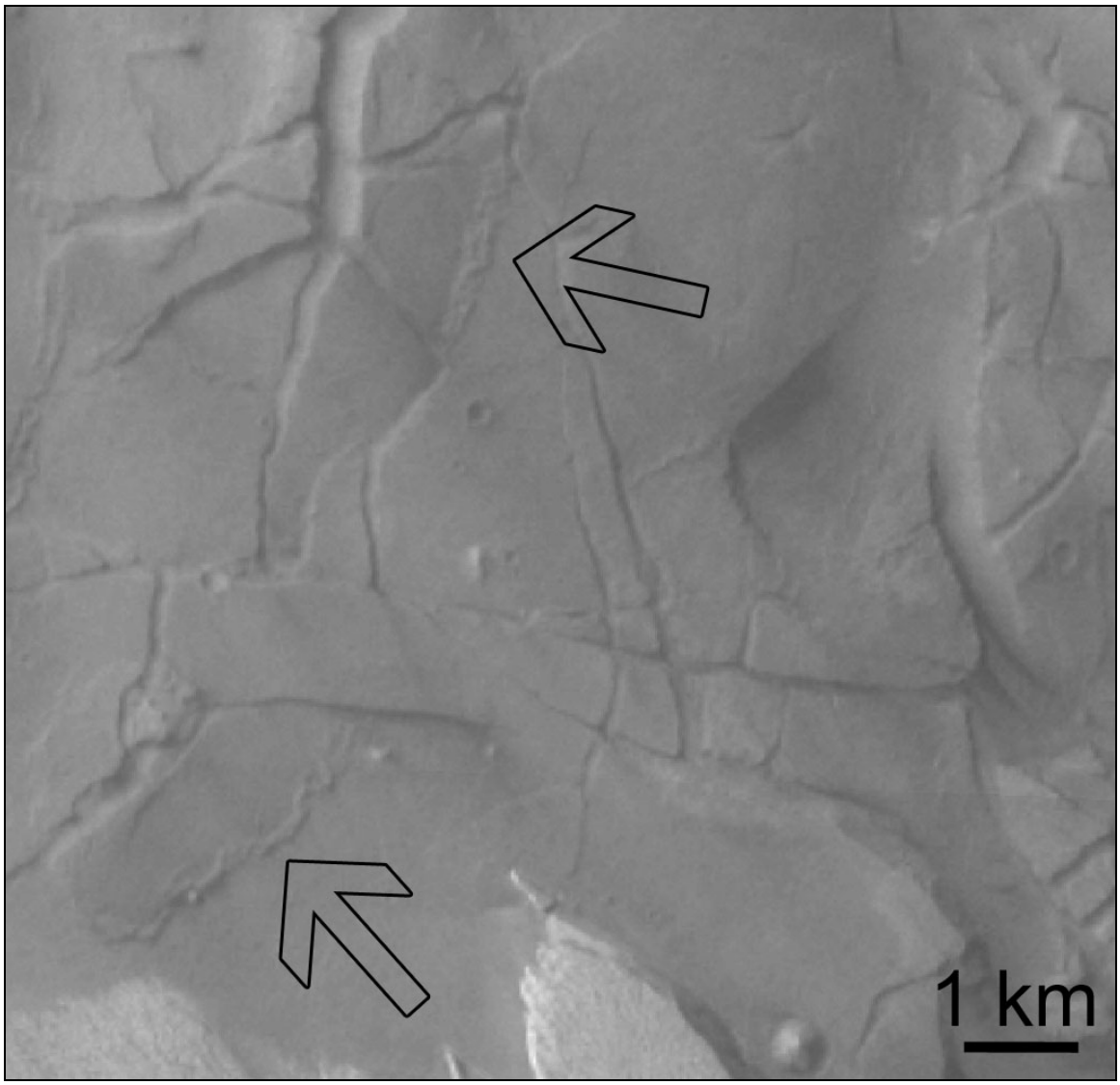

Figure 5.2.31. Thrusting normal to fractures in fractured Lower Aram Chaos Formation (image: THEMIS VIS).

Cross Section III through Aureum Chaos (S > N)

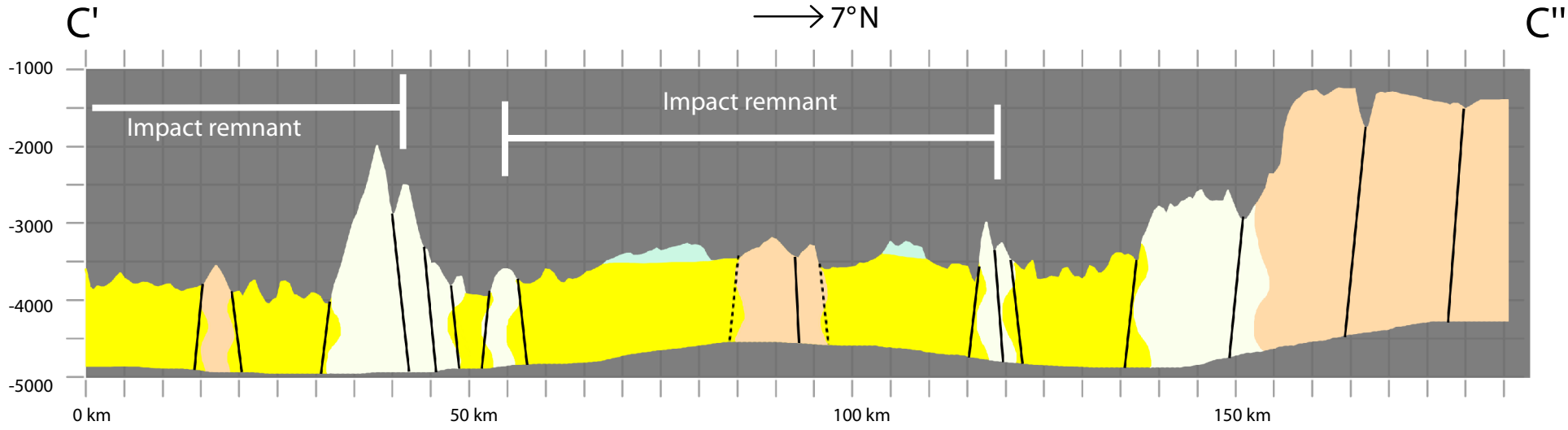

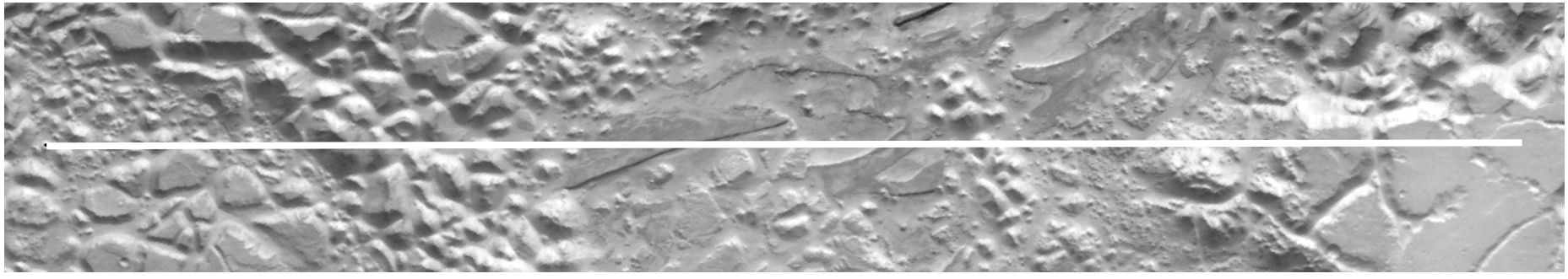

Figure 5.3.2. Cross Section III through Aureum Chaos.

Cross Section IV through Iani Chaos (S > N)

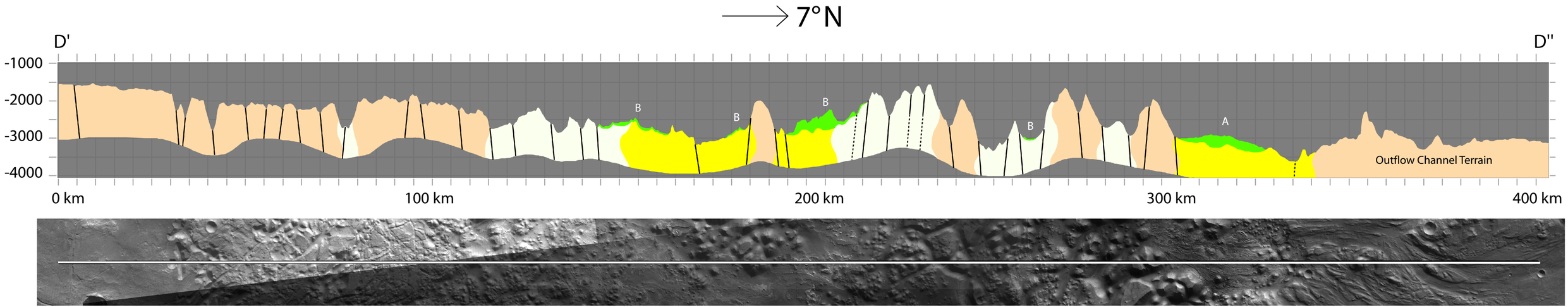

Figure 5.3.3. Cross Section IV through Iani Chaos. **A.** Iani Chaos Deposits Type I, **B.** Iani Chaos Deposits Type II.

Aram Chaos Stratigraphy

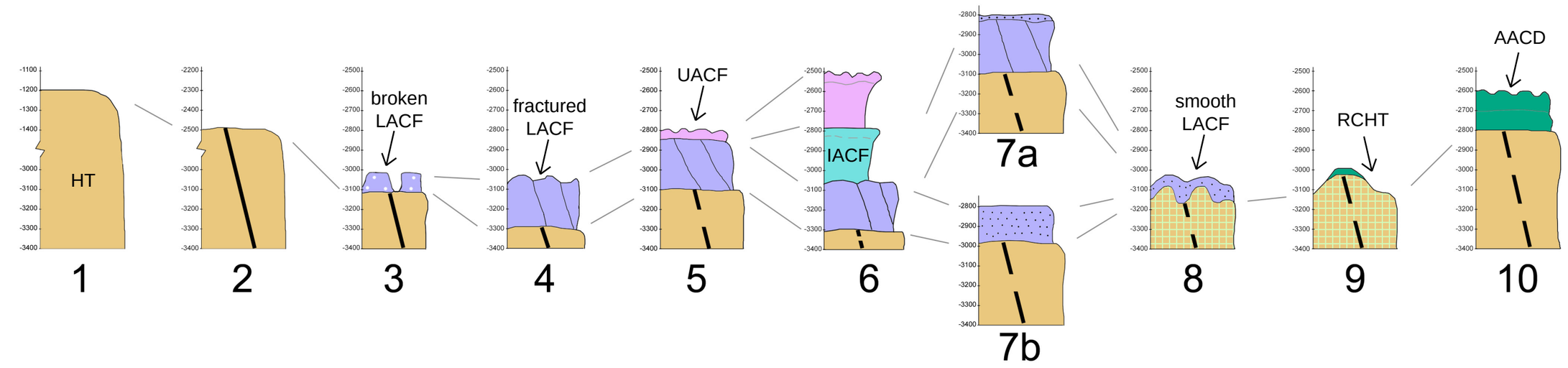

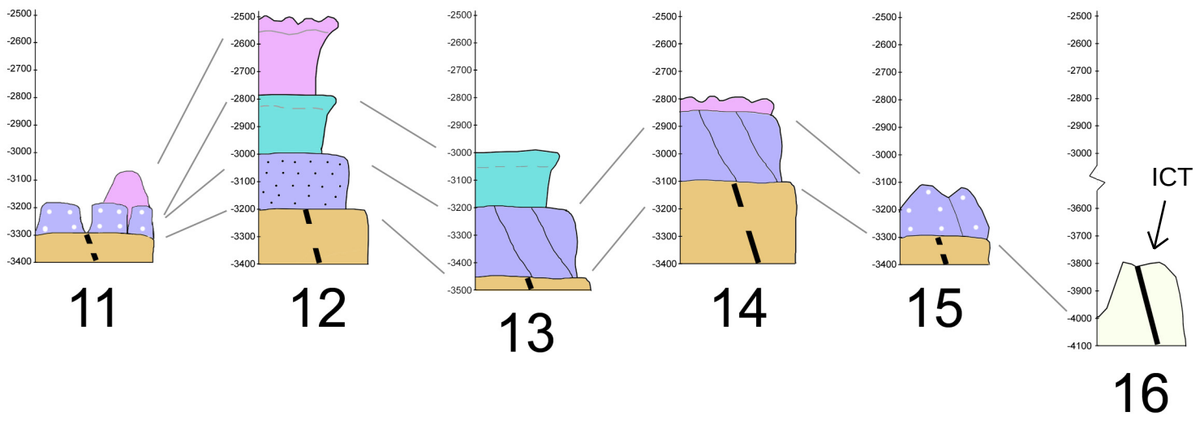

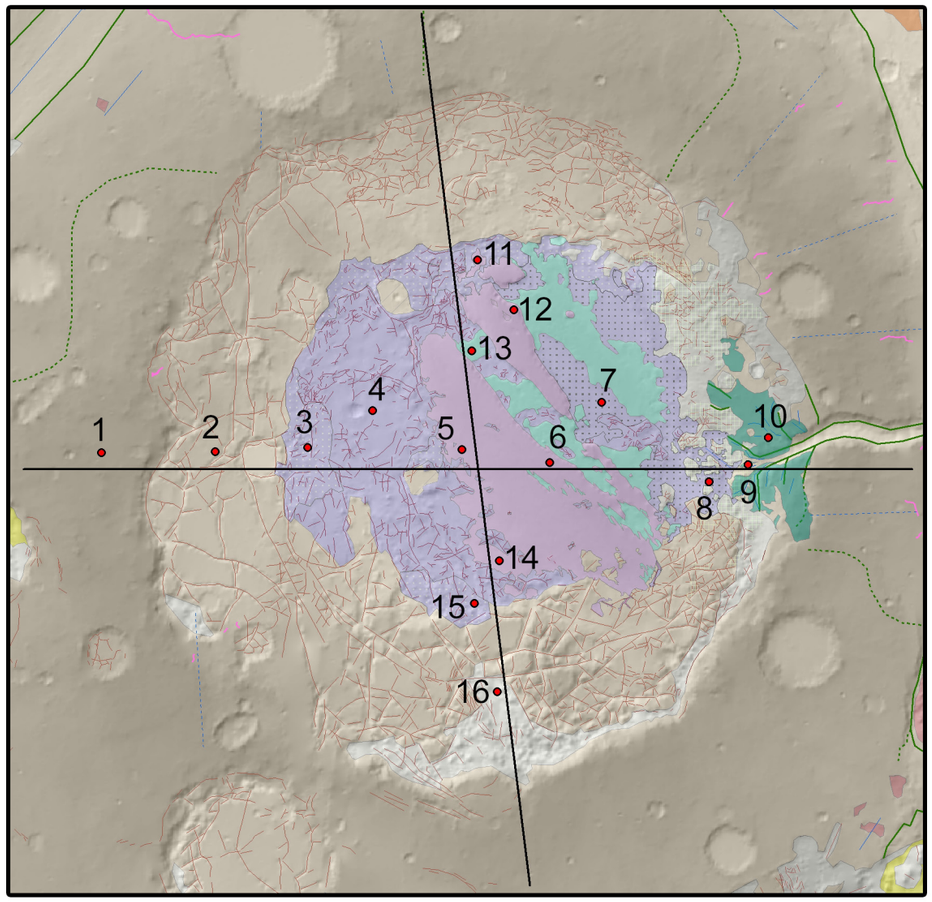

Figure 5.4.1. Aram Chaos Stratigraphy.

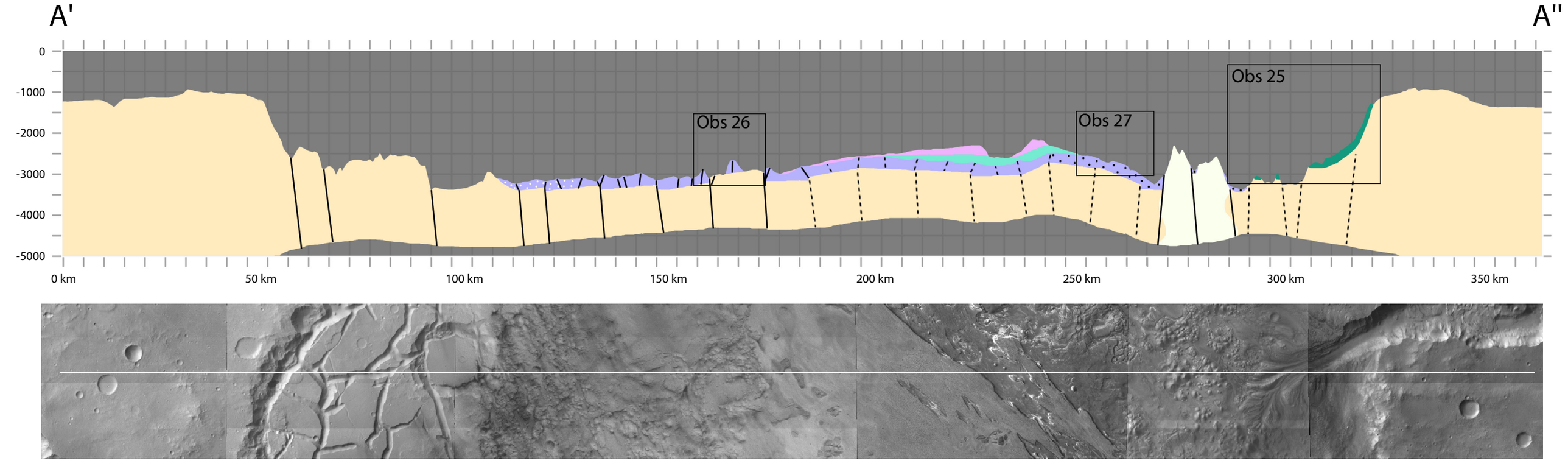

Figure 5.3.1. Cross Sections I & II through Aram Chaos.

Aureum and Iani Chaos Stratigraphy

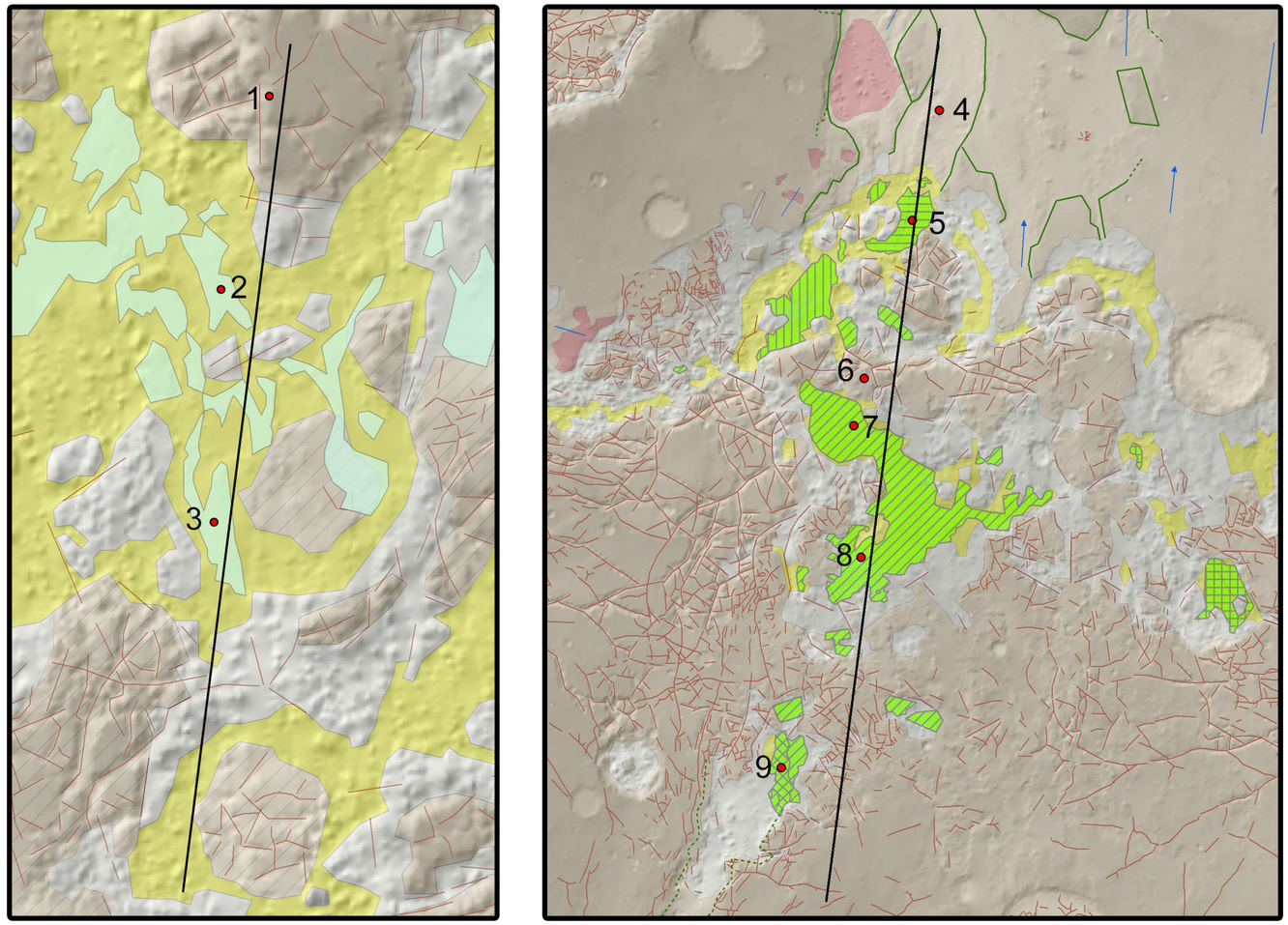

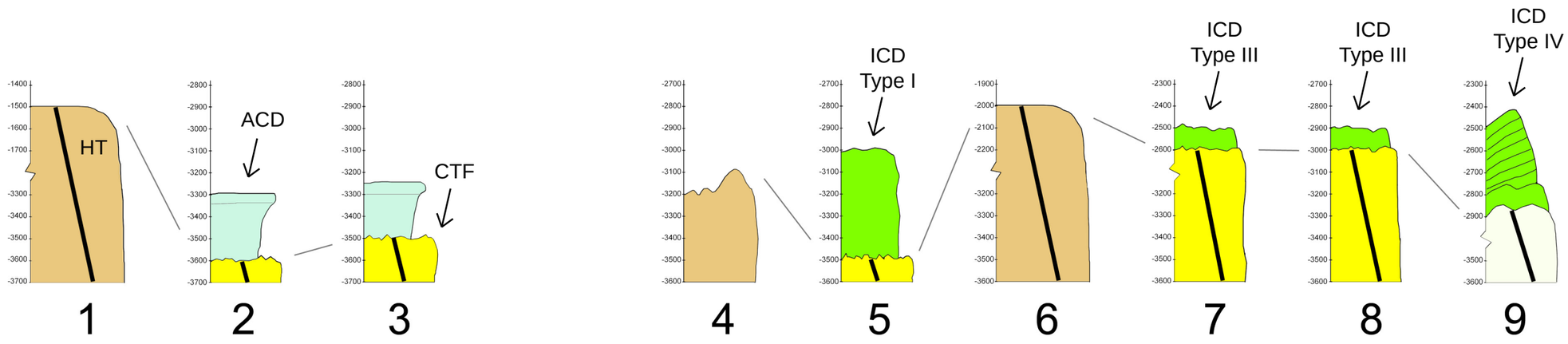

Figure 5.4.2. Aureum (1-3) and Iani Chaos Stratigraphy (4-9).

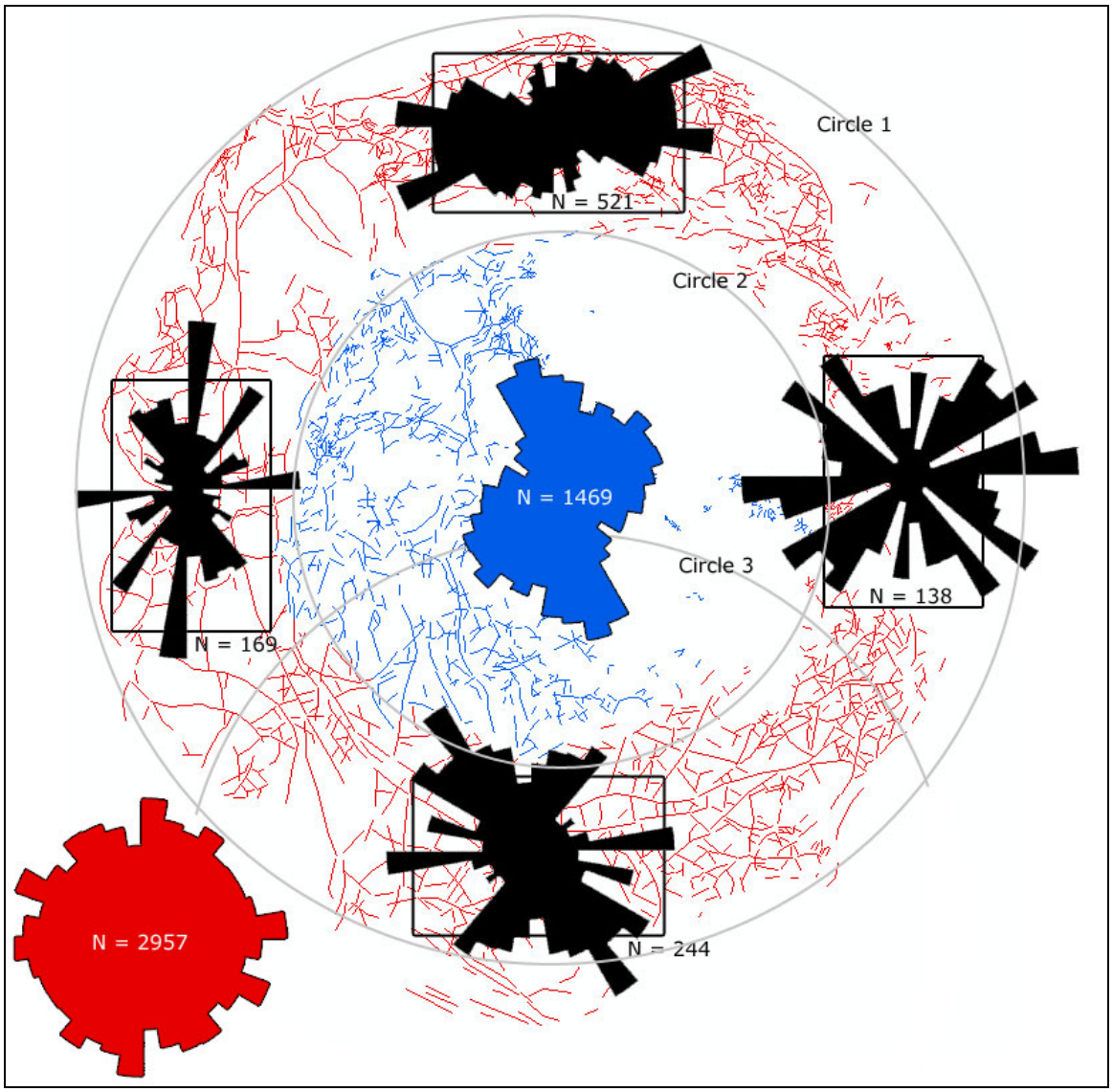

Figure 5.5.1. Aram Chaos Rose Diagrams. For explanation see text.

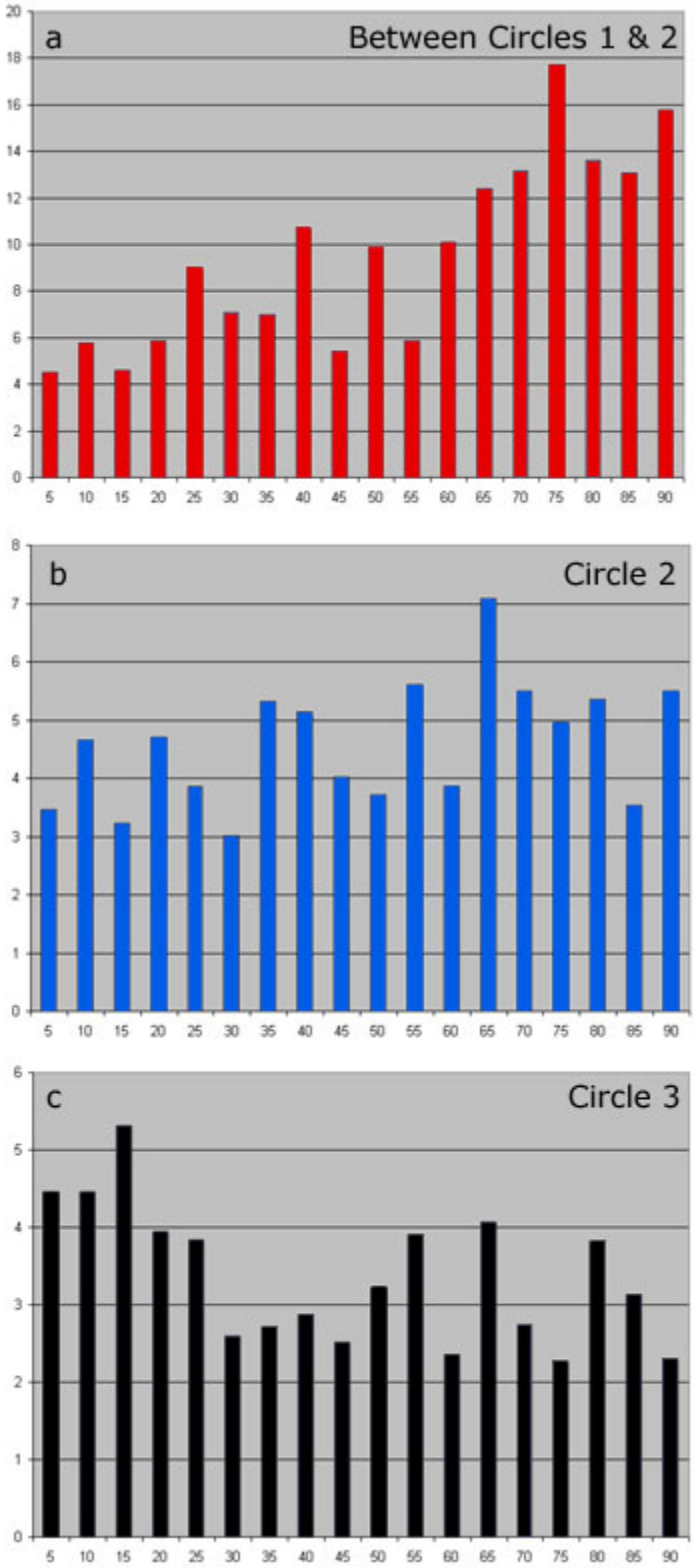

Figure 5.5.2. Length-weighted Concentricity of Aram Chaos and its major units. The vertical values are a multiplication of the amount of lineaments and the length fraction of

these lineaments (summed length per total length) (see *4.6.3. Concentricity / Radiality*). The columns represent bins of 5 degrees. **a.** Aram Chaos Highland and Chaotic Terrain lineaments (red lineaments of Figure 5.5.1). **b.** Aram Chaos inner ring lineaments (blue lineaments of Figure 5.5.1). **c.** Length-weighted Concentricity of lineaments within 120 km around the highest chaotisized area of Aram Chaos.

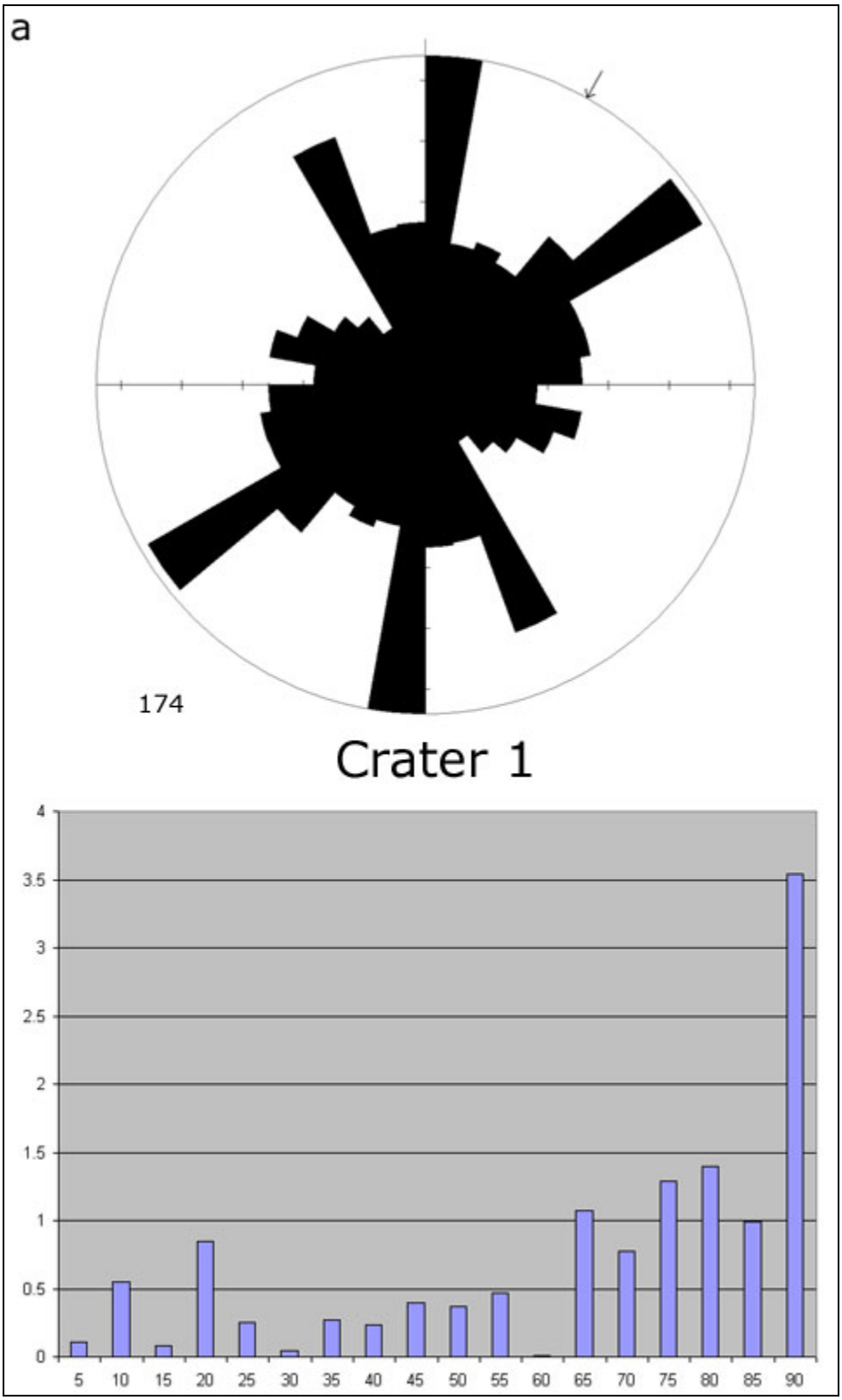

Figure 5.5.3. Rose Diagrams and length-weighted concentricity of Crater 1 (a) and Crater 2 (b) (see Figure PQ).

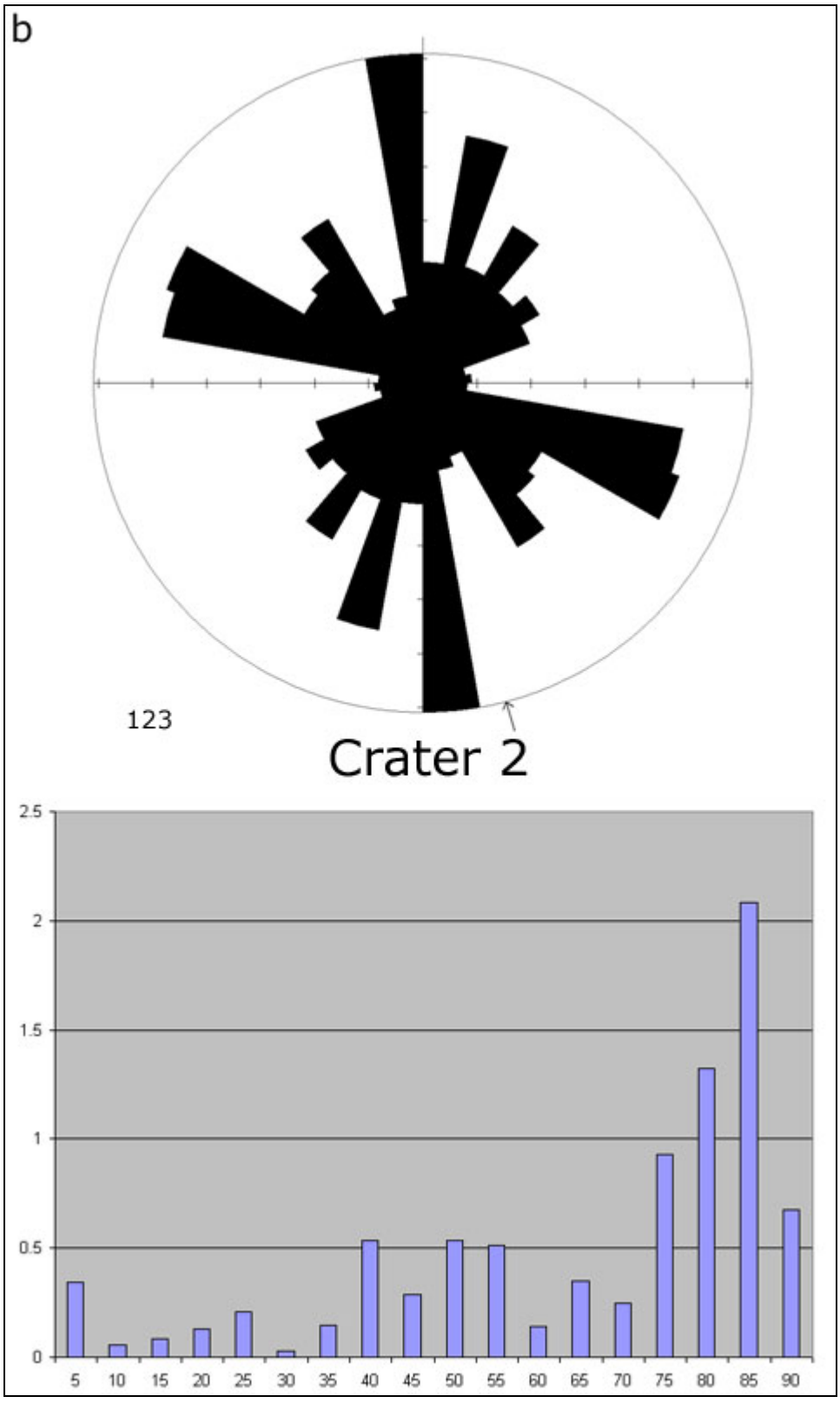

Figure 5.5.3 (continued).

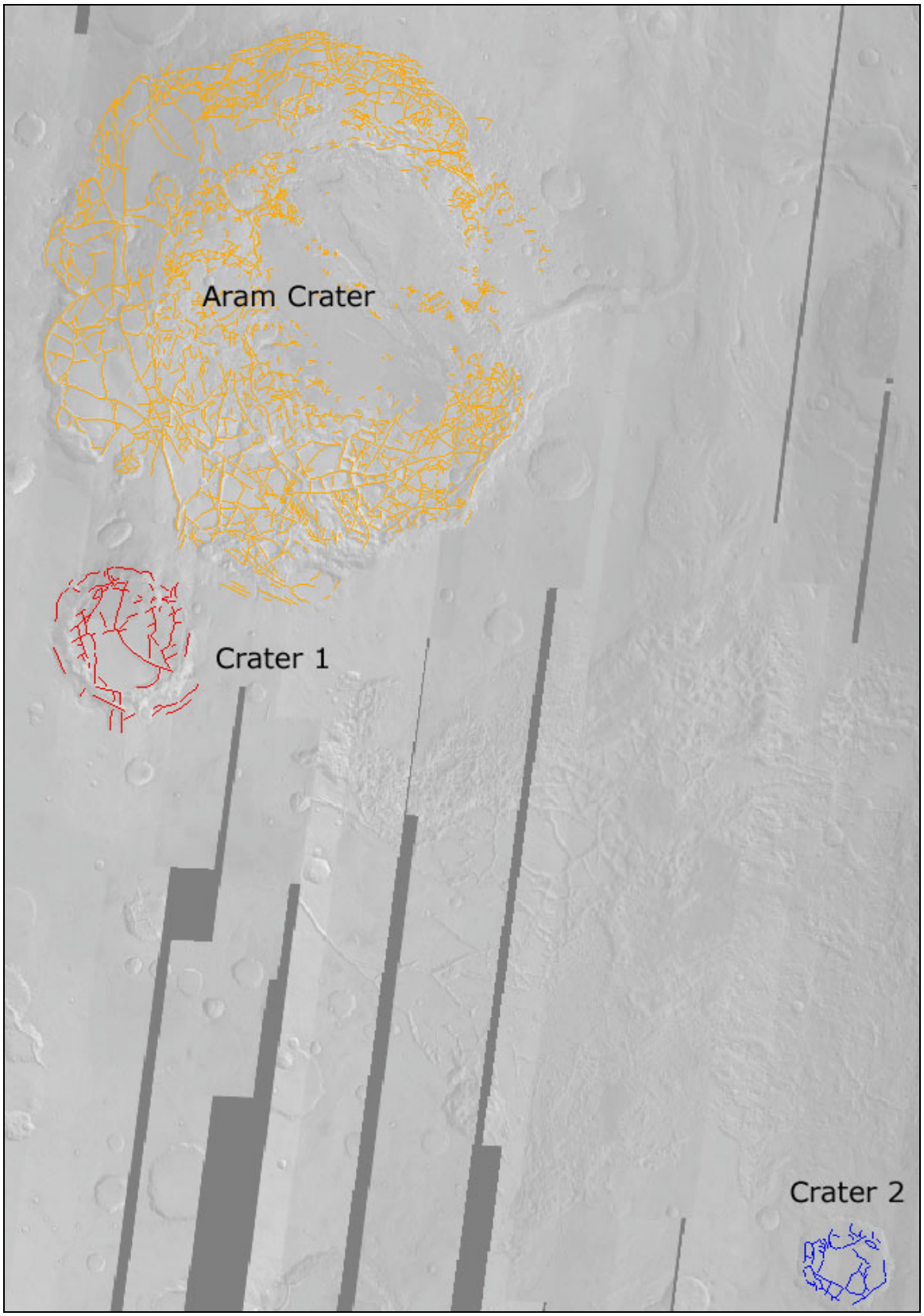

Figure 5.5.4. Overview of the largest fractured craters in my research area.

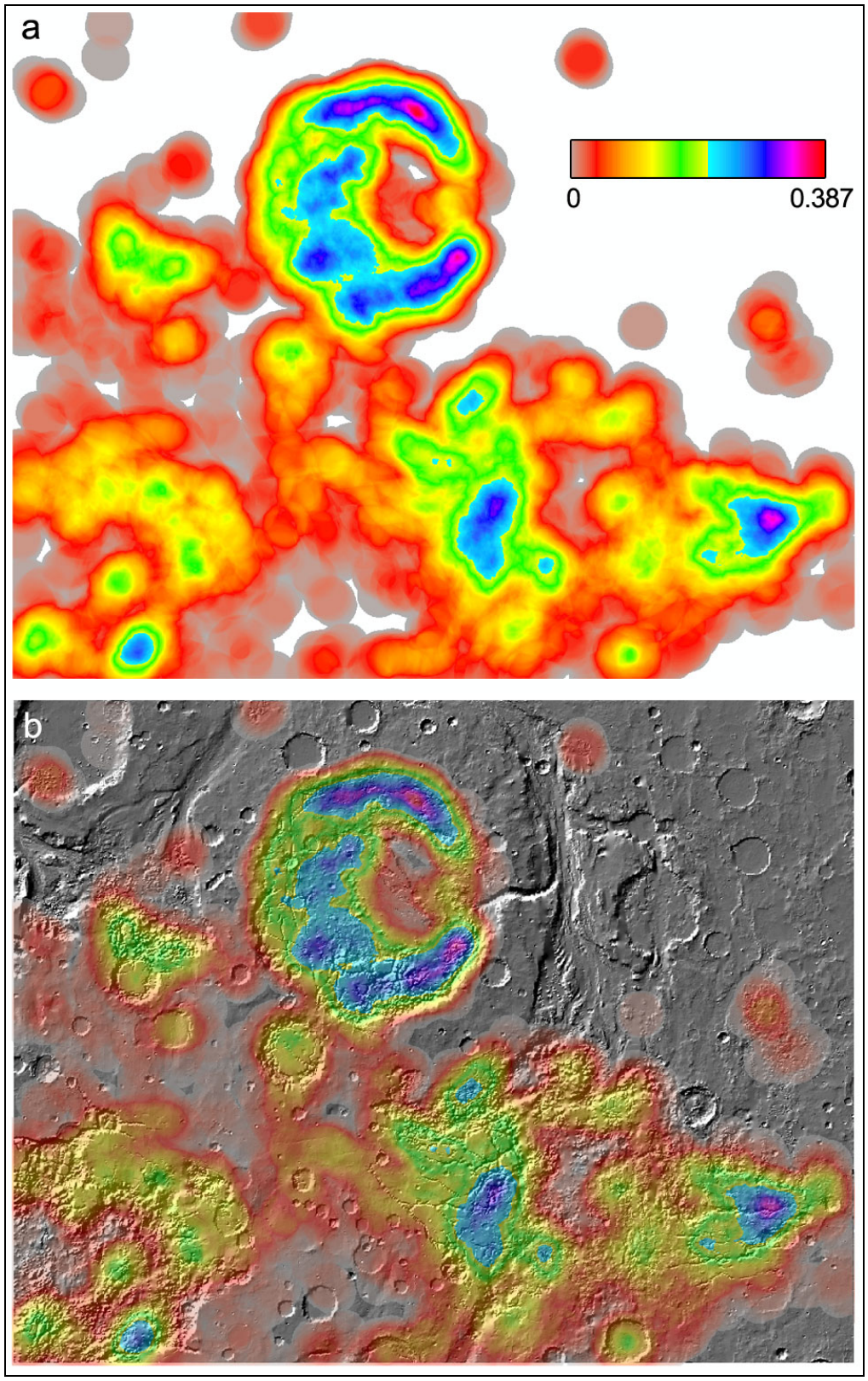

Figure 5.5.5. a. The lineament density map (See *5.6.5. Fracture Density*). The lineament density is defined as the lineament length per square kilometer (km^{-1}). **b.** The lineament density map on top of a MOLA shaded relief map.

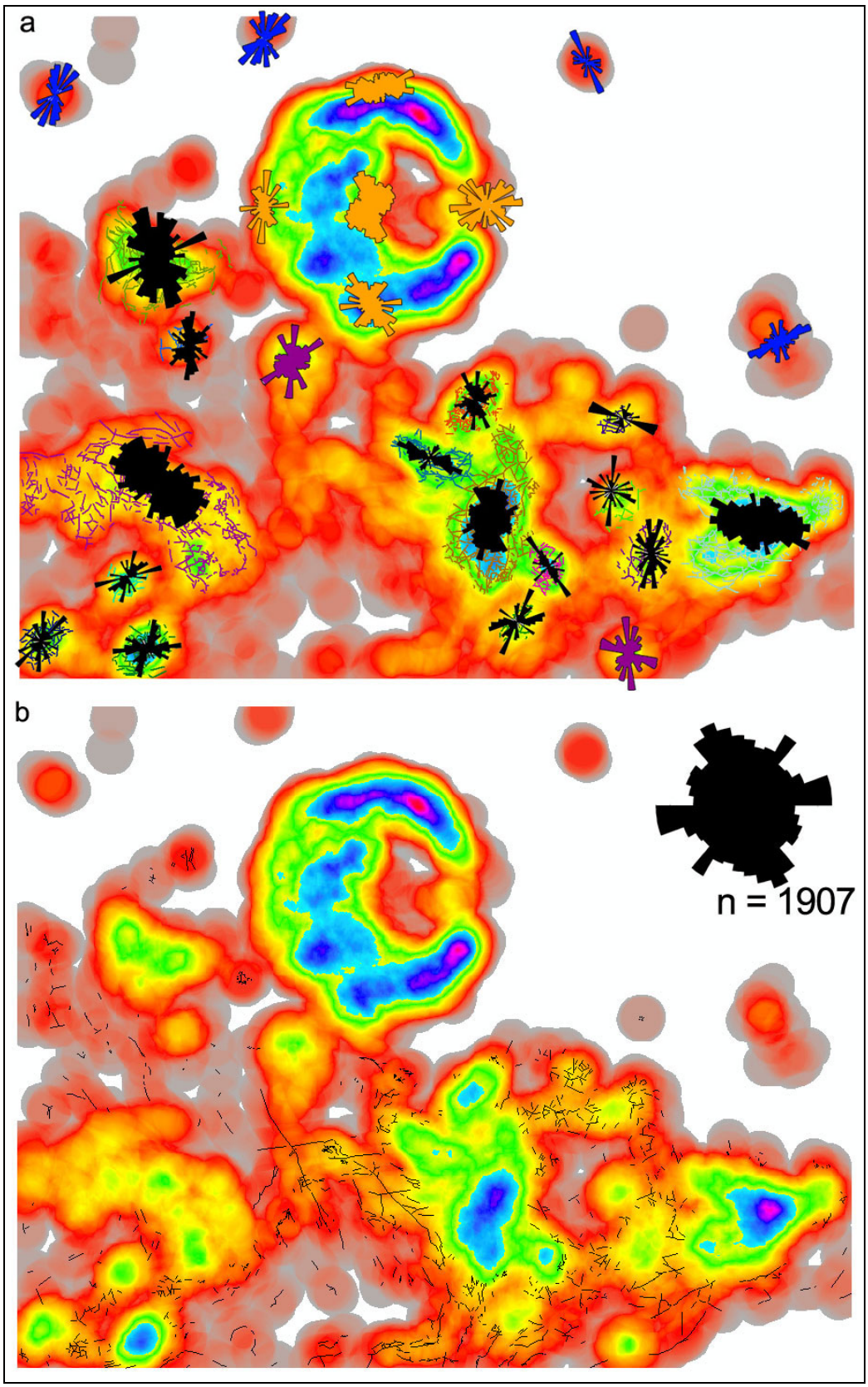
a
b
n = 1907

Figure 5.5.6. a. For each high fracture density area length-weighted Rose Diagrams were created (black). The blue RD's are from outcrops of Small-scale Fractured and Chaotic Terrain (SFCT) fractures. The purple RD's are from Crater 1 (left) and Crater 2 (right) (see Figures 5.5.3 and 5.5.4). The orange RD's are the Aram Chaos RD's (see Figure 5.5.1). **b.** All the lineaments in the non-flooded Highland Terrain and the low-fracture density Chaotic Terrain and the resulting RD.

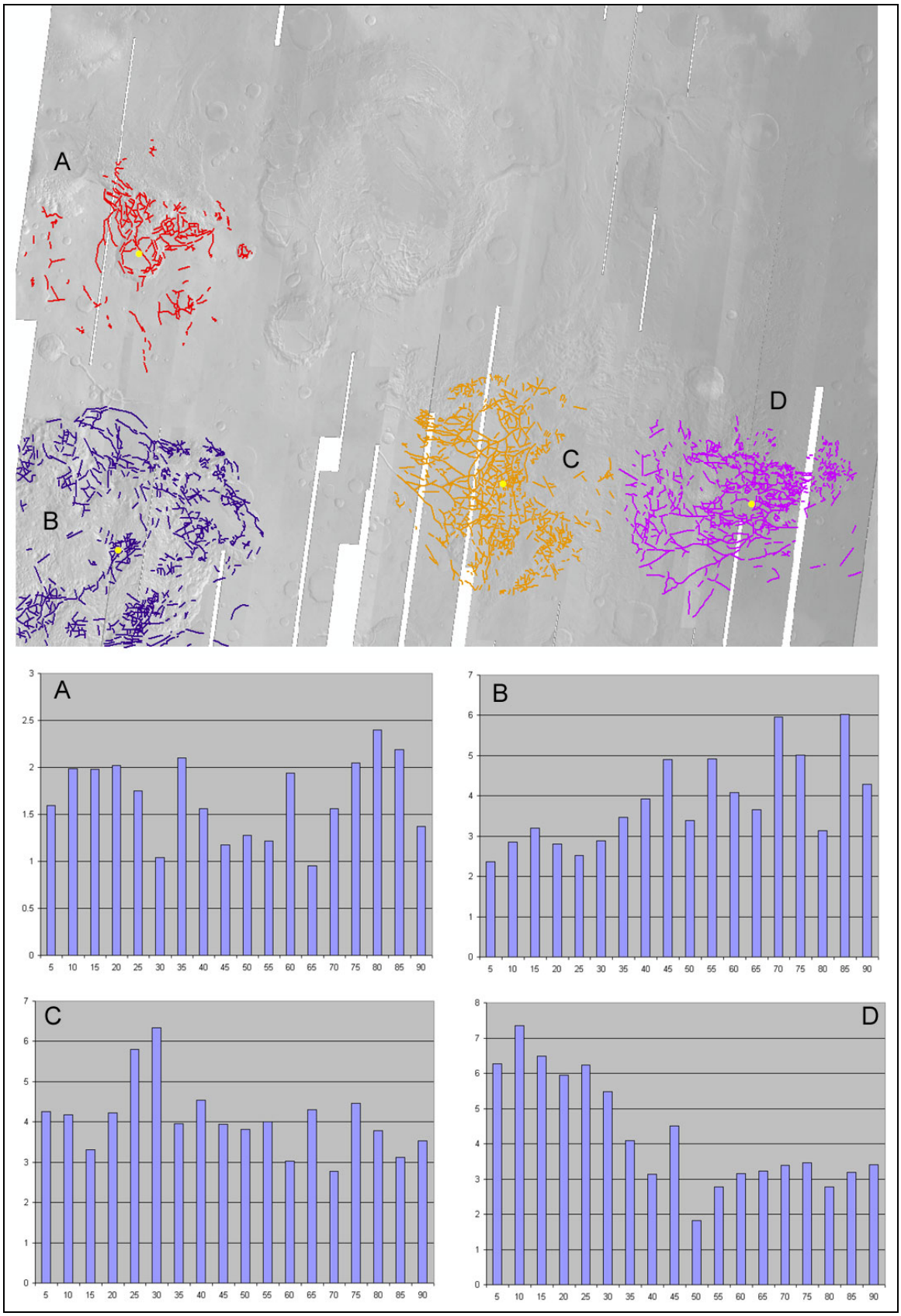
A
B
C
D
A
B
C
D

Figure 5.5.7. Length-weighted concentricity. The extent of the concentricity was arbitrarily chosen. Area B (Aureum Chaos) is not completely circular because it borders my researched area.

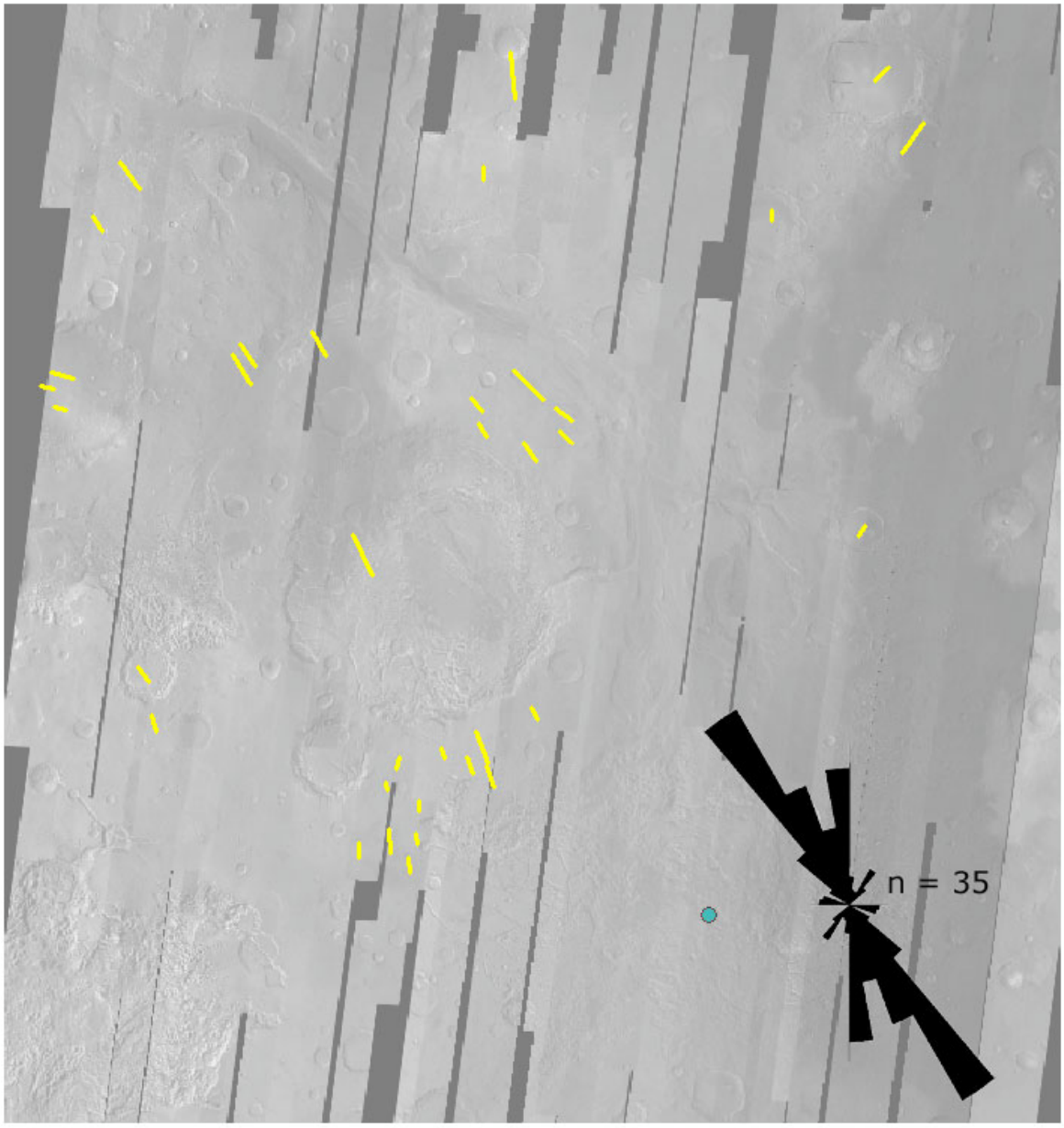

Figure 5.5.8. The wind directions derived from mapping wind streaks (see Figure 5.5.9) and a length-weighted Rose Diagram.

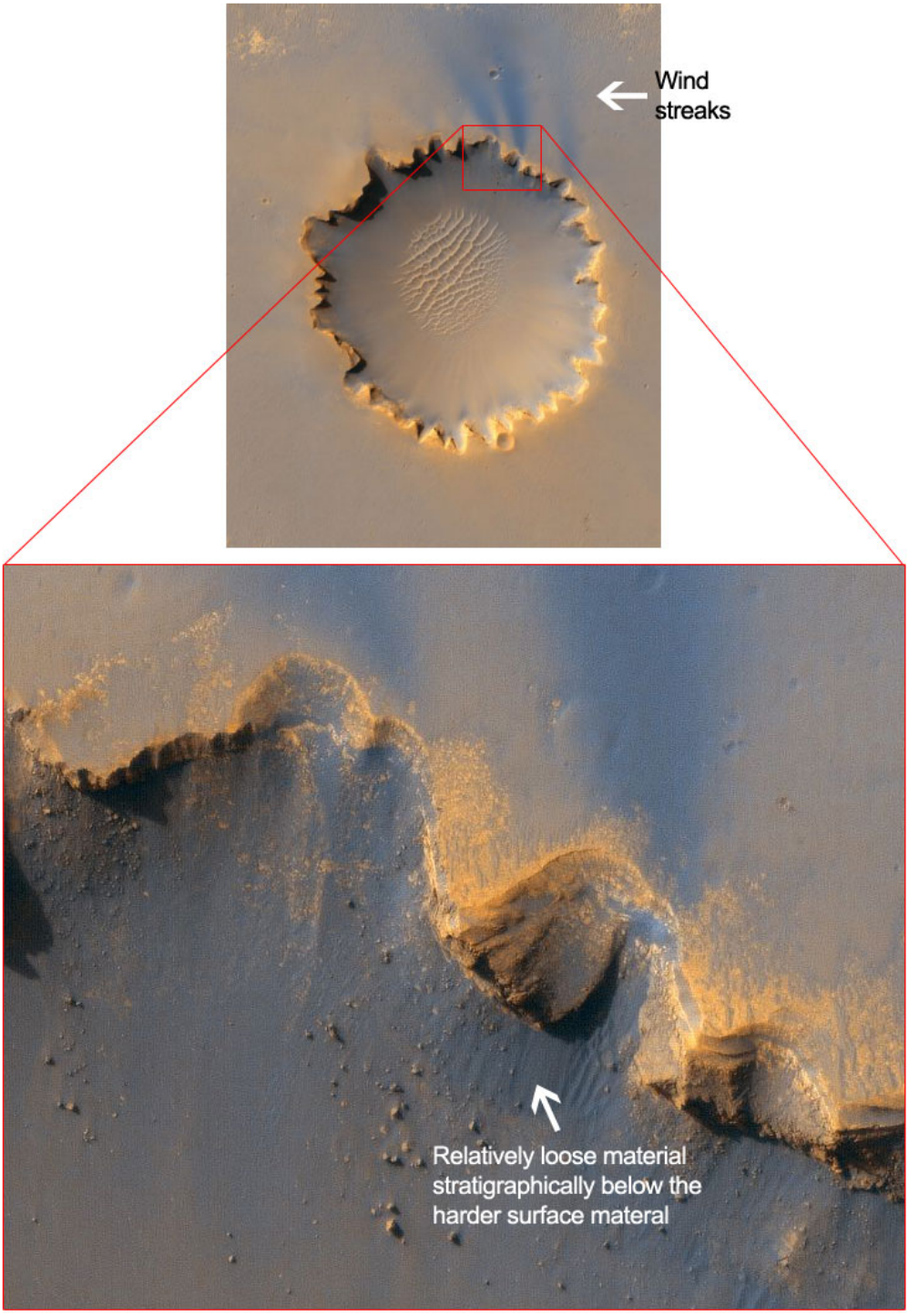

Figure 5.5.9. Color image from the HiRISE camera on board the Mars Reconnaissance Orbiter (MRO). The image shows 'Victoria crater', the final destination of the Opportunity MER Rover. The crater is ~800 m in diameter and the image is centered at -2.1 degrees latitude, 354.5 degrees East longitude. The wind streaks are relatively loose material below the harder surface material which in time get blown out of the crater forming wind streaks (image redrawn after http://hiroc.lpl.arizona.edu/images/TRA/TRA_000873_1780).

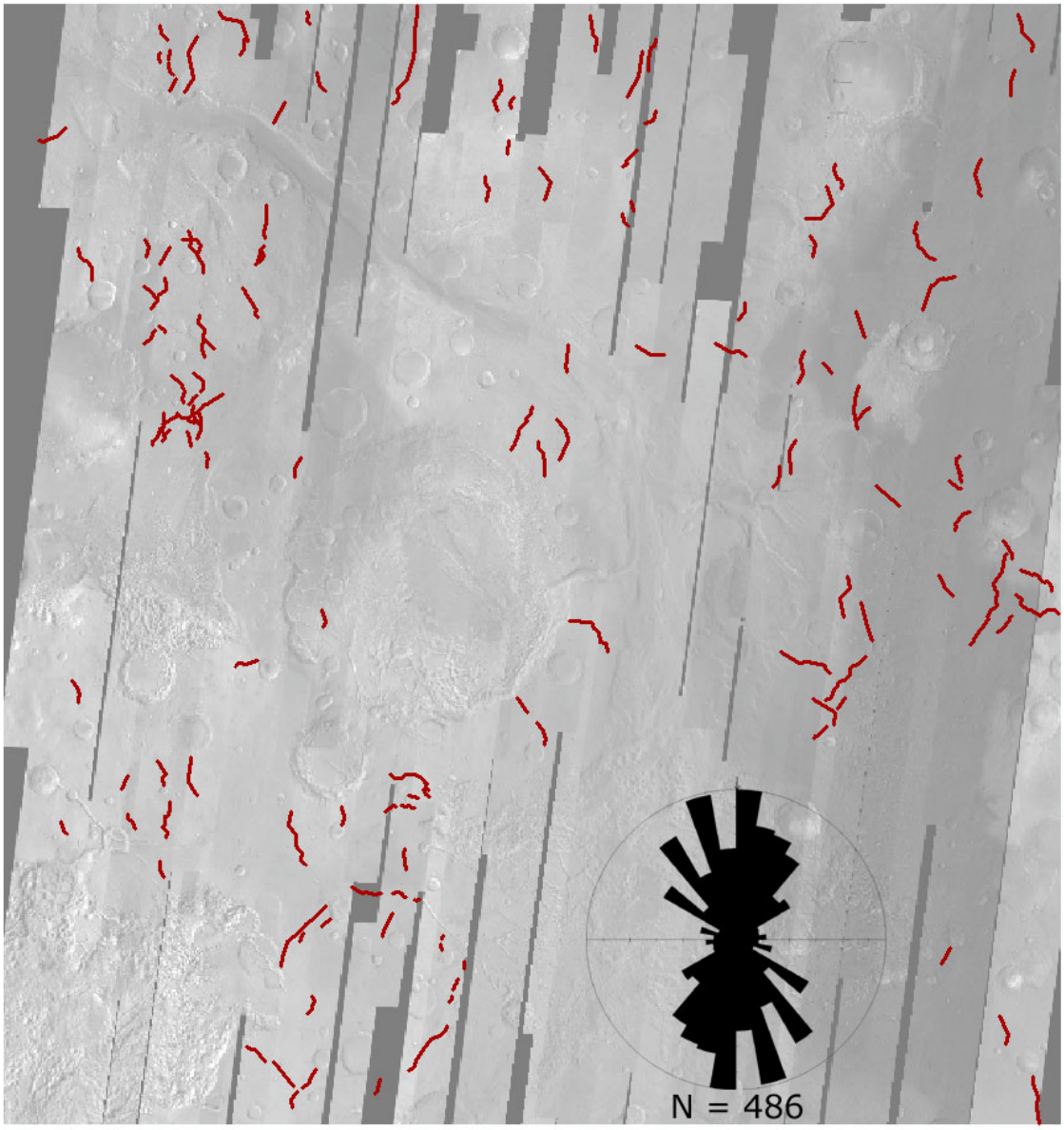

Figure 5.5.10. Mapped wrinkle ridges and Rose Diagram.

Time

Deformation

Stratigraphy

Water activity

AMAZONIAN <-> HESPERIAN

Erosion / Deflation?

UACF — Hematite?

IACF — Hydrous minerals

smooth LACF — Kieserite

HT fracturing, subsidence and collapse

LACF fracturing

? AACD (draping)

Eastern quadrant chaotization

Broken and fractured LACF

Forming of inner ring

Southern CT brecciation

? Channel incision

HT and CT water release

NOACHIAN

Tharsis related regional deformation

Highland Terrain deposition

? AACD (layering)

Formation of Aram Chaos crater

Water rich crater fill

Figure 6.1. Space-Time diagram of the sequence of event of the evolution of Aram Chaos. The Hesperian to Amazonian boundary is unclear and therefore both Periods are combined. Crater counting of the Aram Chaos Formation needs to be performed to distinguish between Hesperian and Amazonian units/erosion events.

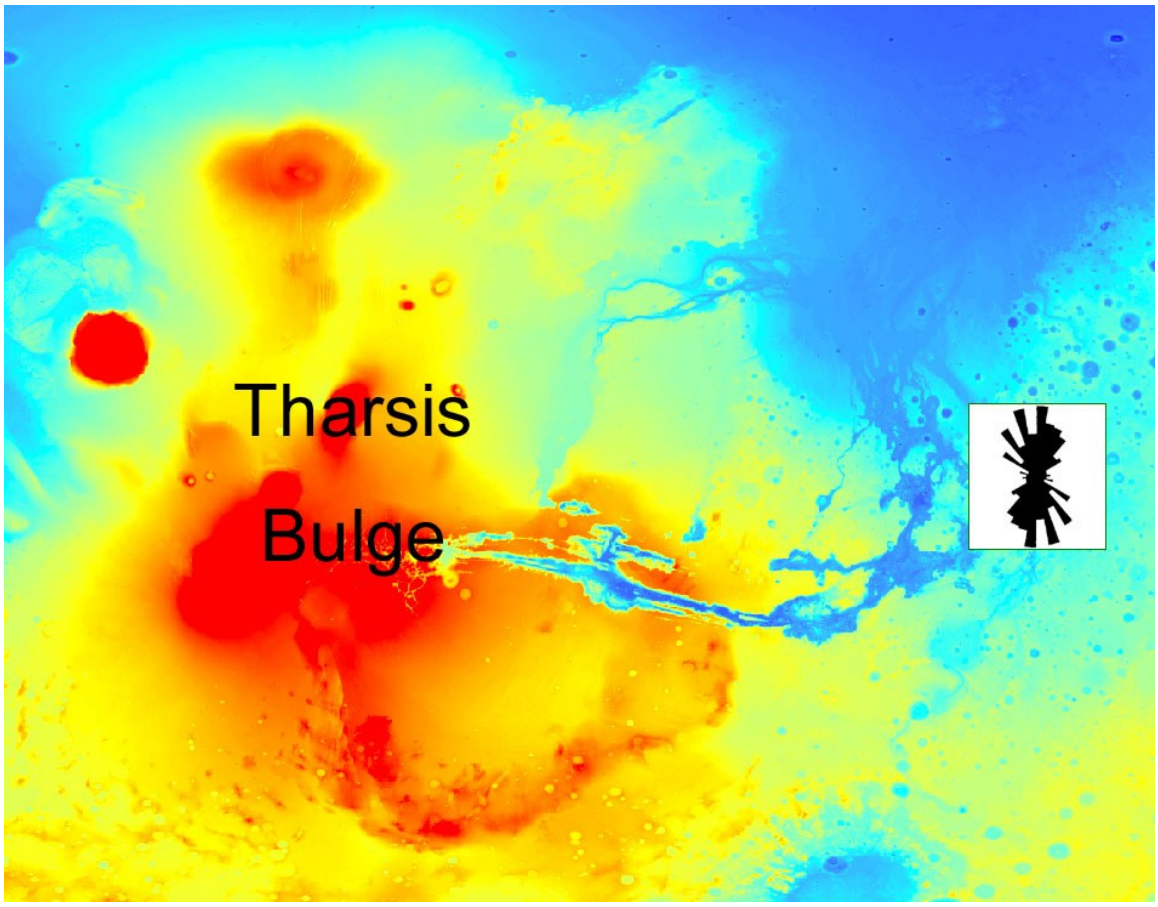

Figure 6.2. The mean wrinkle ridge orientation in my research area (white box) is concentric to Tharsis.

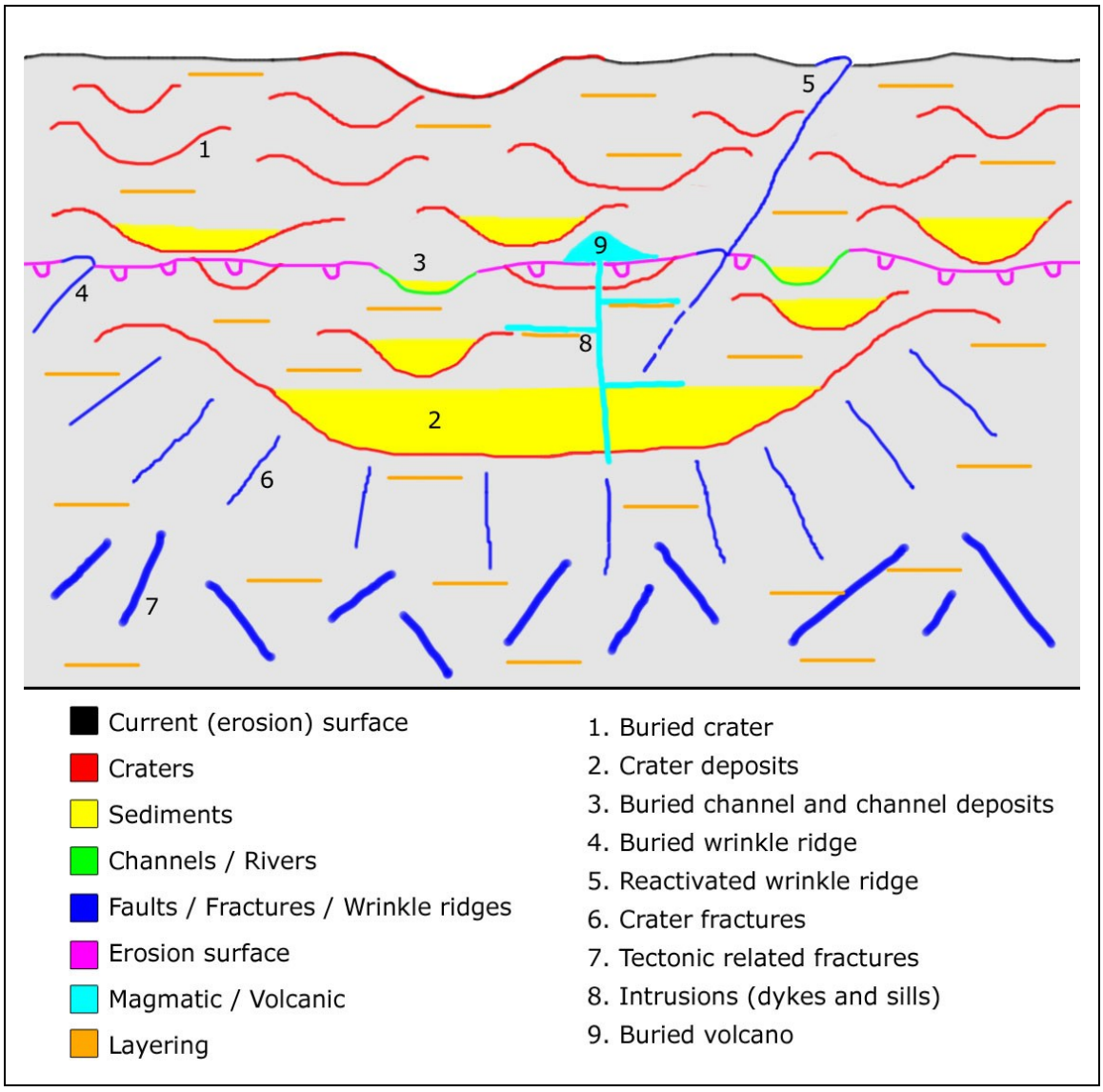

Figure 6.3. Schematized representation of the HT composition and structure. The HT thickness is at least 1-2 km thick.

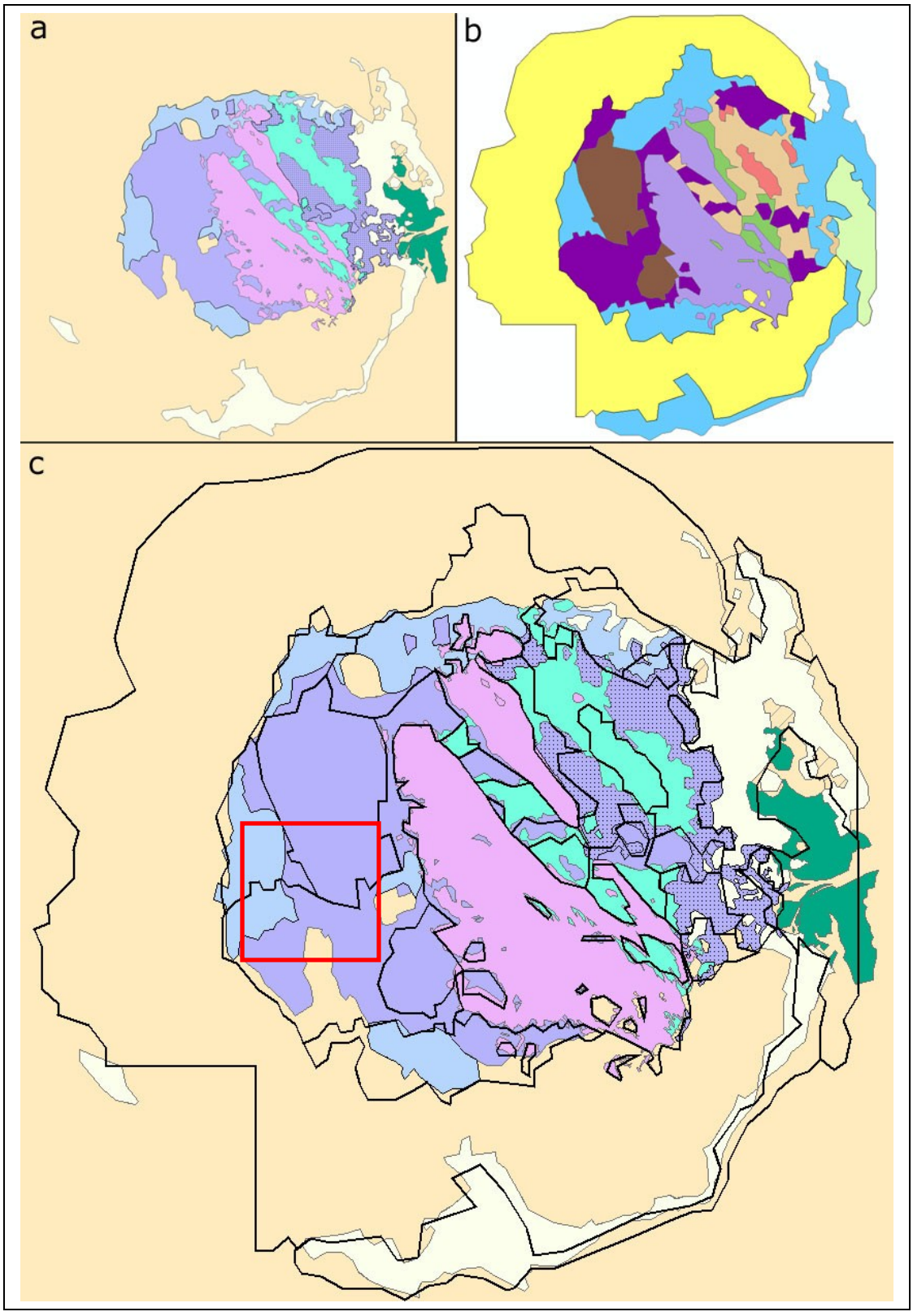

Figure 6.4. Comparison (**c**) between the mapping of this study (**a**) and the mapping by Glotch and Christensen (2005) (**b**). The red inlay is Figure 6.6.

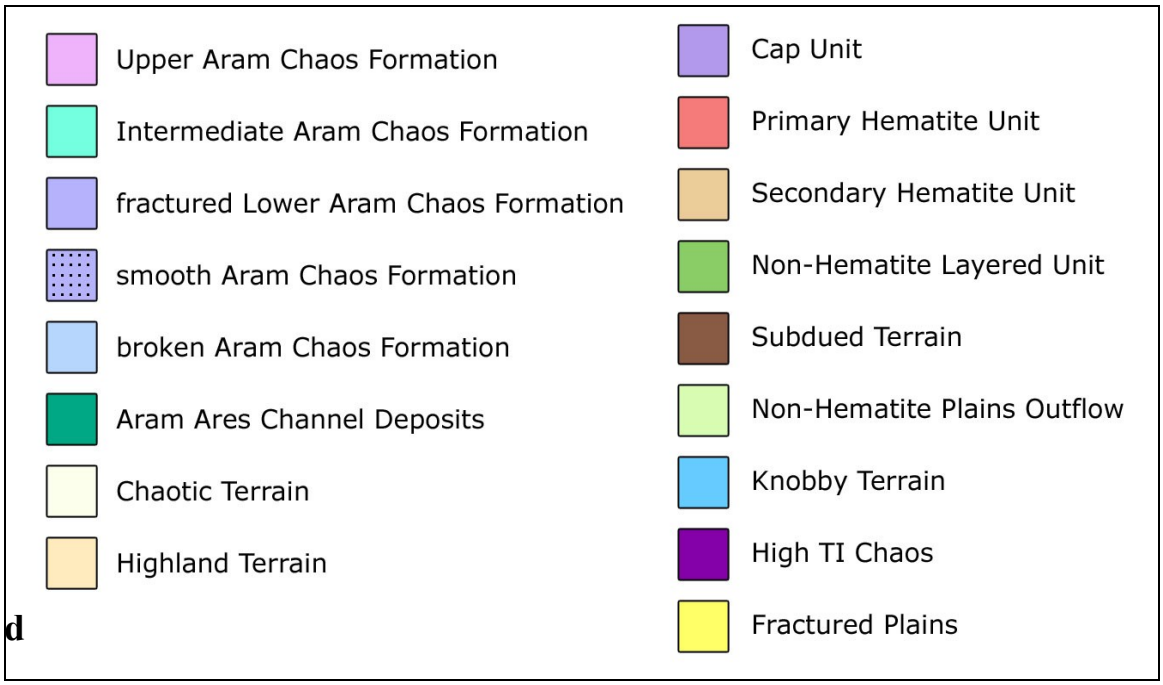

d

Figure 6.4 (continued). d. Left is the legend for the mapping of this study, right is the legend for the mapping by Glotch and Christensen (2005).

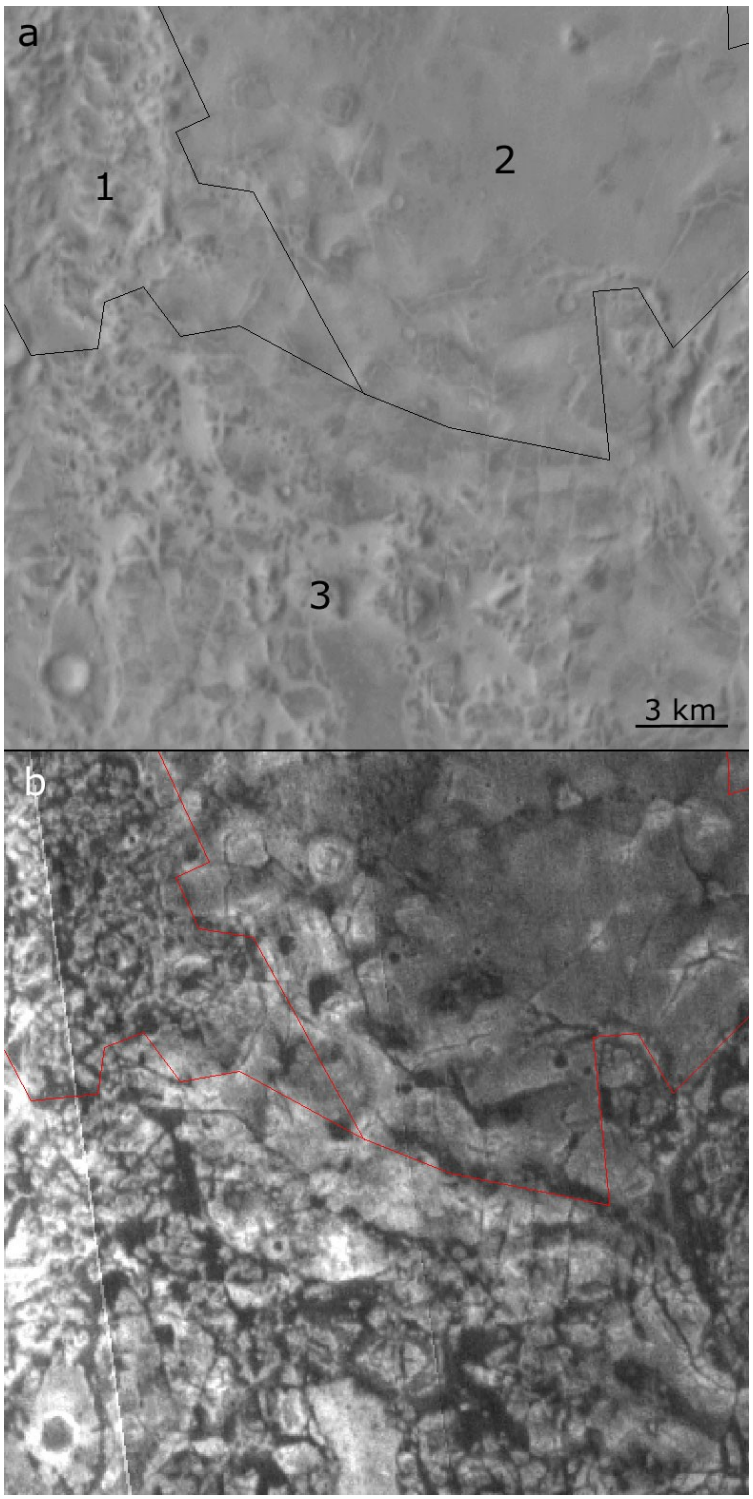

Figure 6.5. Comparison between the High TI Chaos (3) and the Subdued Terrain (2), mapped by Glotch and Christensen (2005) (1 is Knobby Terrain). For overview see red inlay in Figure 6.4. The difference in thermal inertia (**b**) between the High TI Chaos and Subdued Terrain is interpreted to be caused by the higher fracturing and chaotization in the High TI Chaos. In the mapping of this study both units are mapped as the fractured Lower Aram Chaos Formation. **a.** THEMIS IR day. **b.** THEMIS IR night.

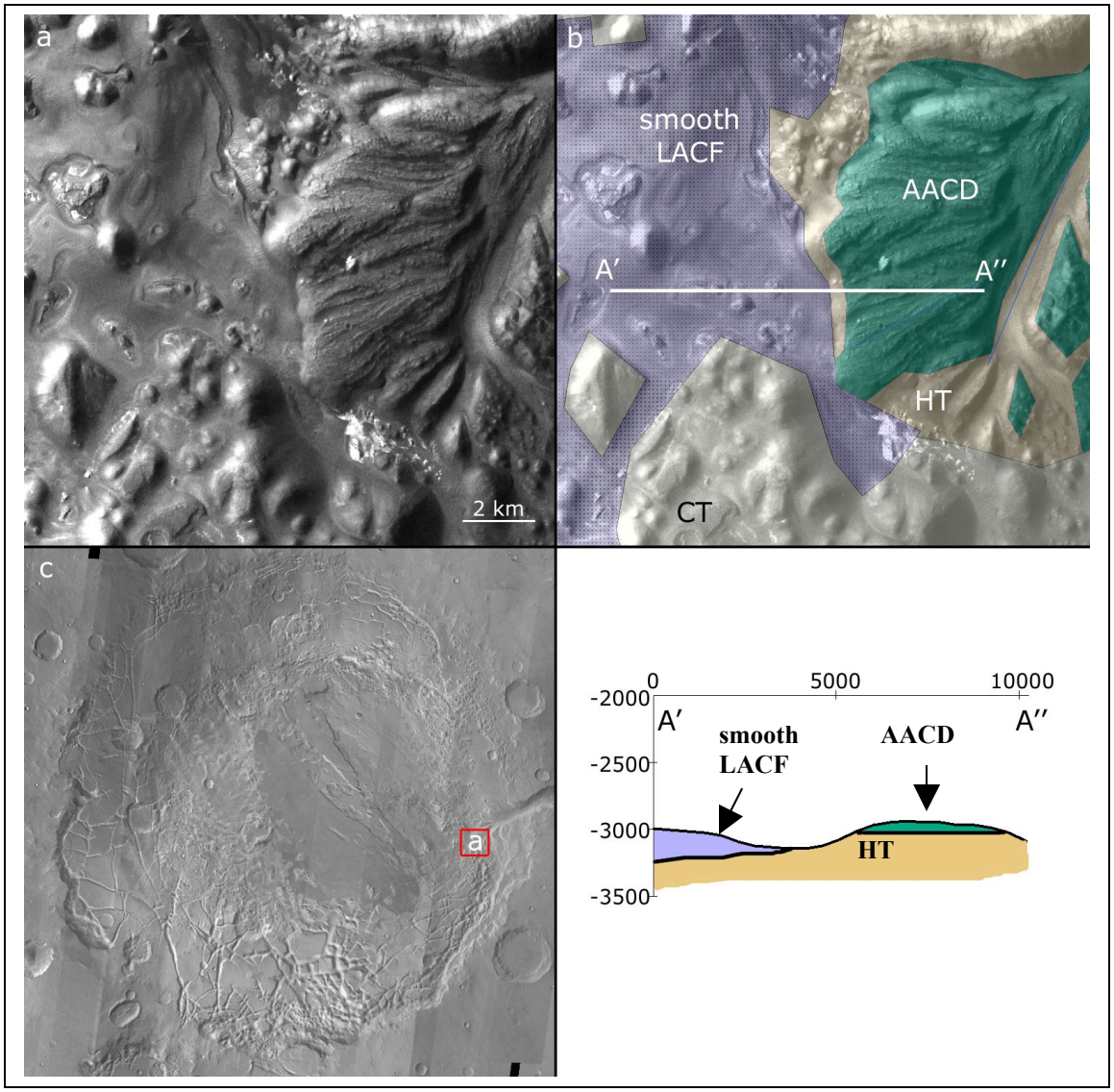

Figure 6.6. Streamlined HT mesas are observed to be capped by the AACD and embayed by smooth LACF. The streamlined HT mesas are interpreted to be formed by water flow. This makes the deposition of the AACD older then the water flow. The water flow most likely would have eroded the smooth LACF which suggests the smooth LACF is younger then the outflow and subsequently younger then the AACD. **a.** HRSC nadir image. **b.** Mapping with HRSC nadir image as background. **c.** Overview (THEMIS IR day as background).

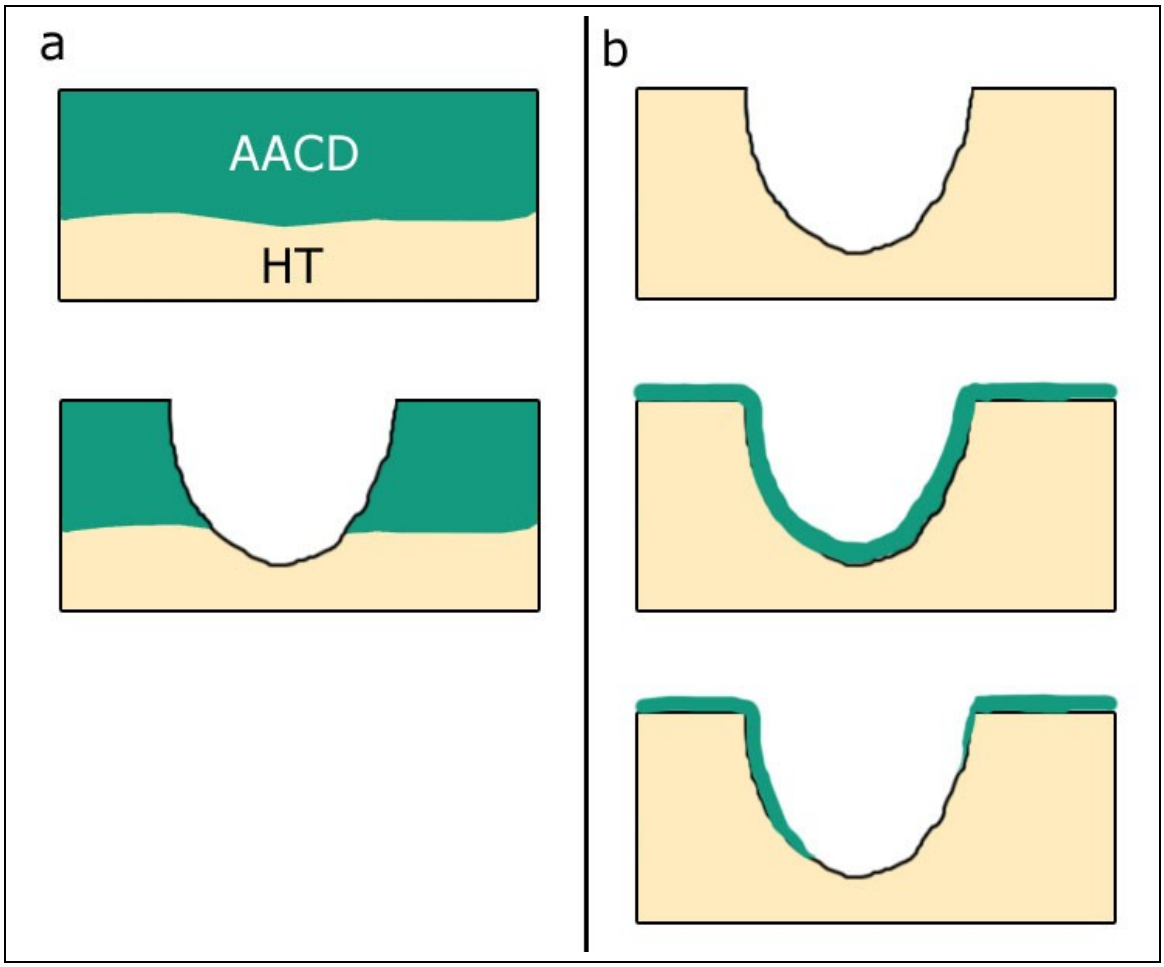

Figure 6.7. Two proposed scenarios to explain the observation of AACD in the wall of the Aram Chaos channel. For explanation see *6.2.2.4. Water activity in Aram Chaos*.

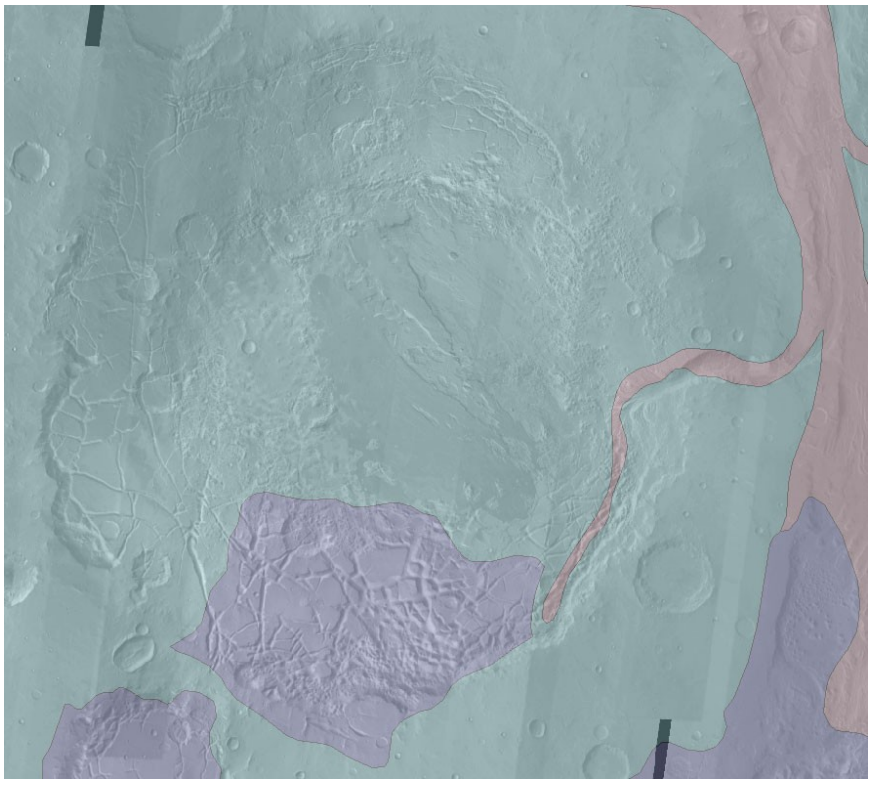

Figure 6.8. Mapping of Aram Chaos done by Rotto and Tanaka (1995) using Viking images (Background image: THEMIS IR day). The purple areas are chaotic terrain, the pink areas are outflow channels and the green areas are cratered terrain.

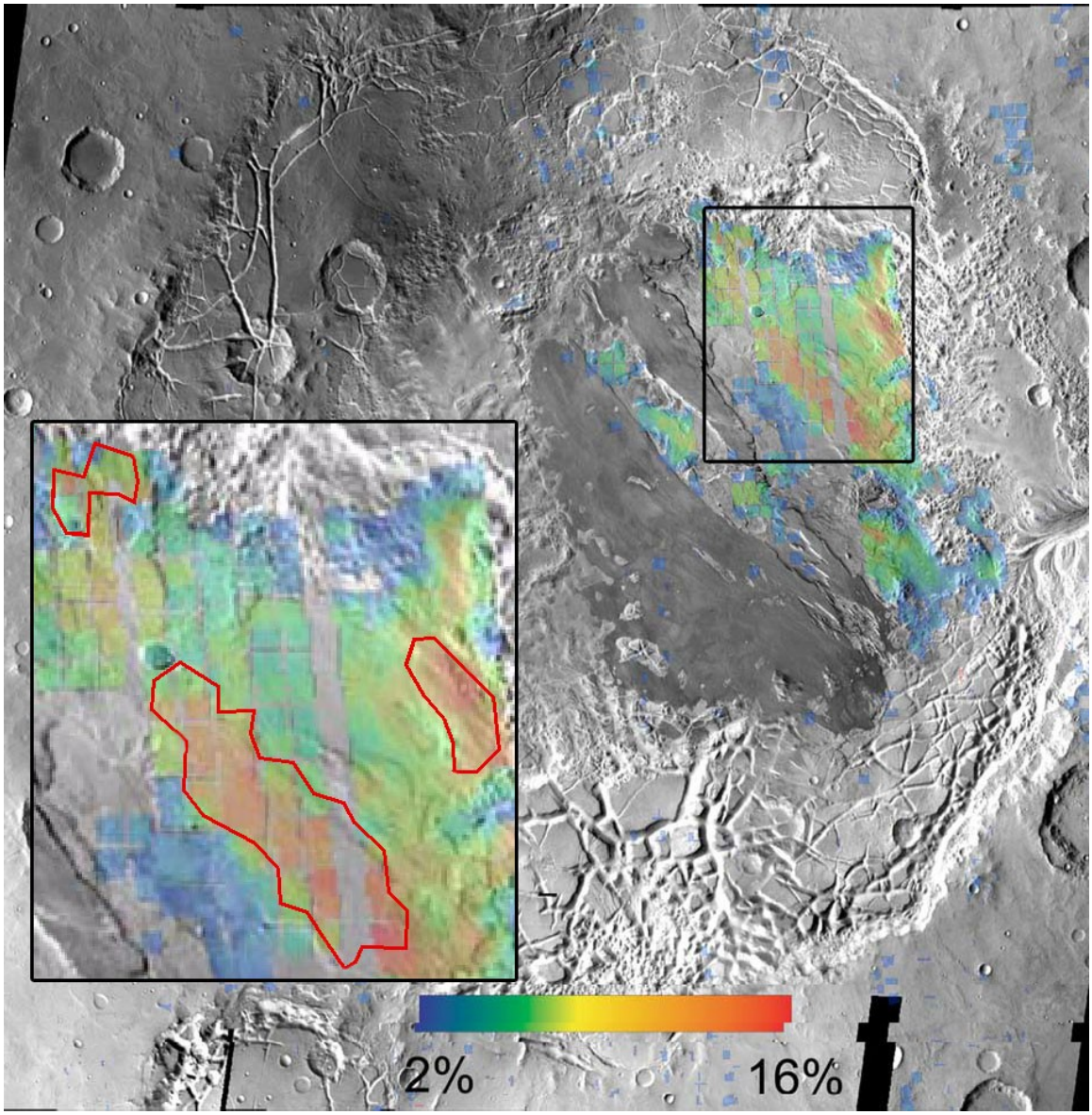

Figure 6.9. Map of hematite abundances within Aram Chaos, after Glotch and Christensen (2005). The inlay shows the Primary Hematite Unit extent, mapped by Glotch and Christensen (2005). See also Figure 6.10.

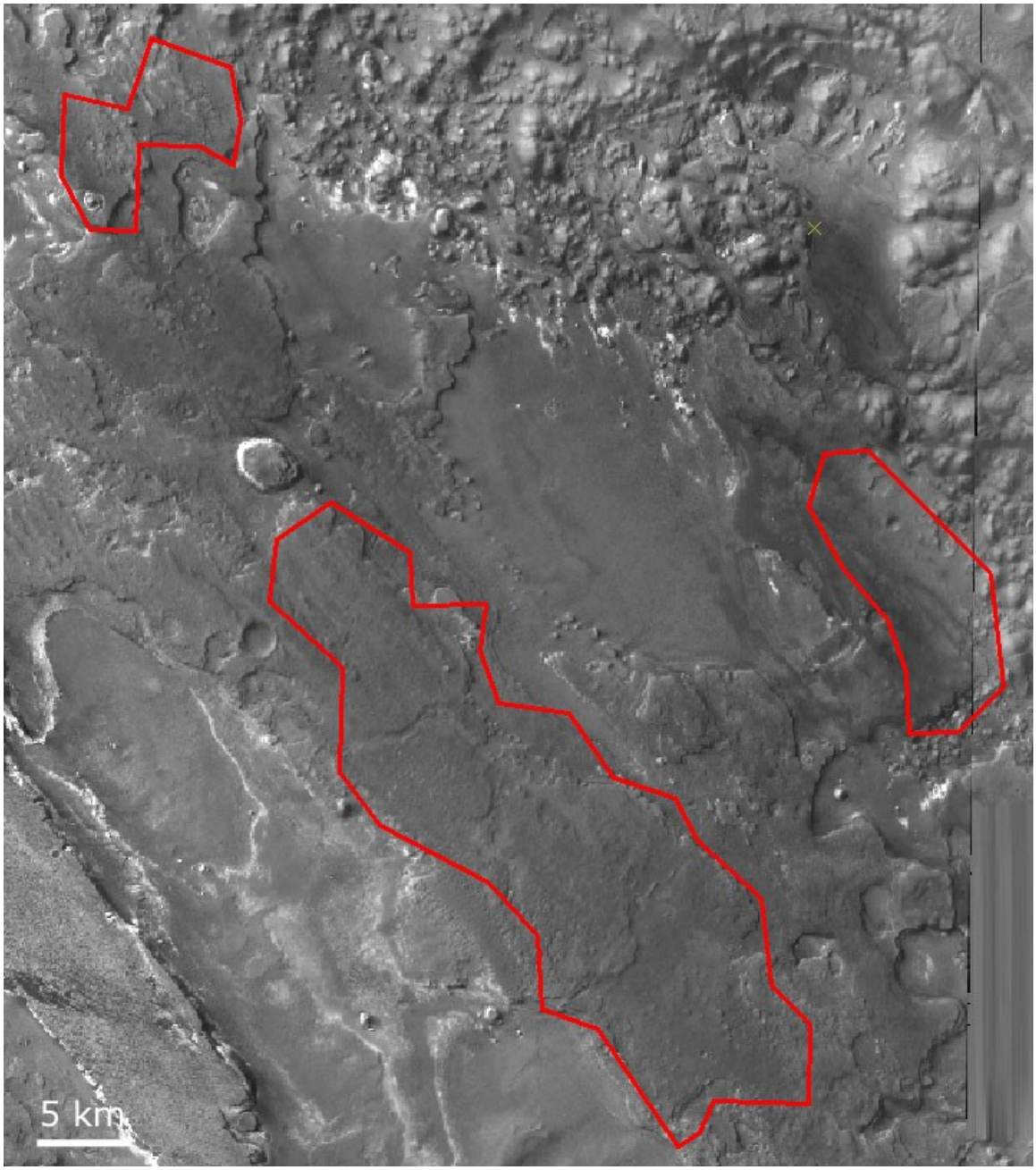

Figure 6.10. The extent of the Primary Hematite Unit, mapped by Glotch and Christensen, on top of high resolution HRSC data. The right patch is located in the smooth LACF, the other patches occur in the rougher IACF.

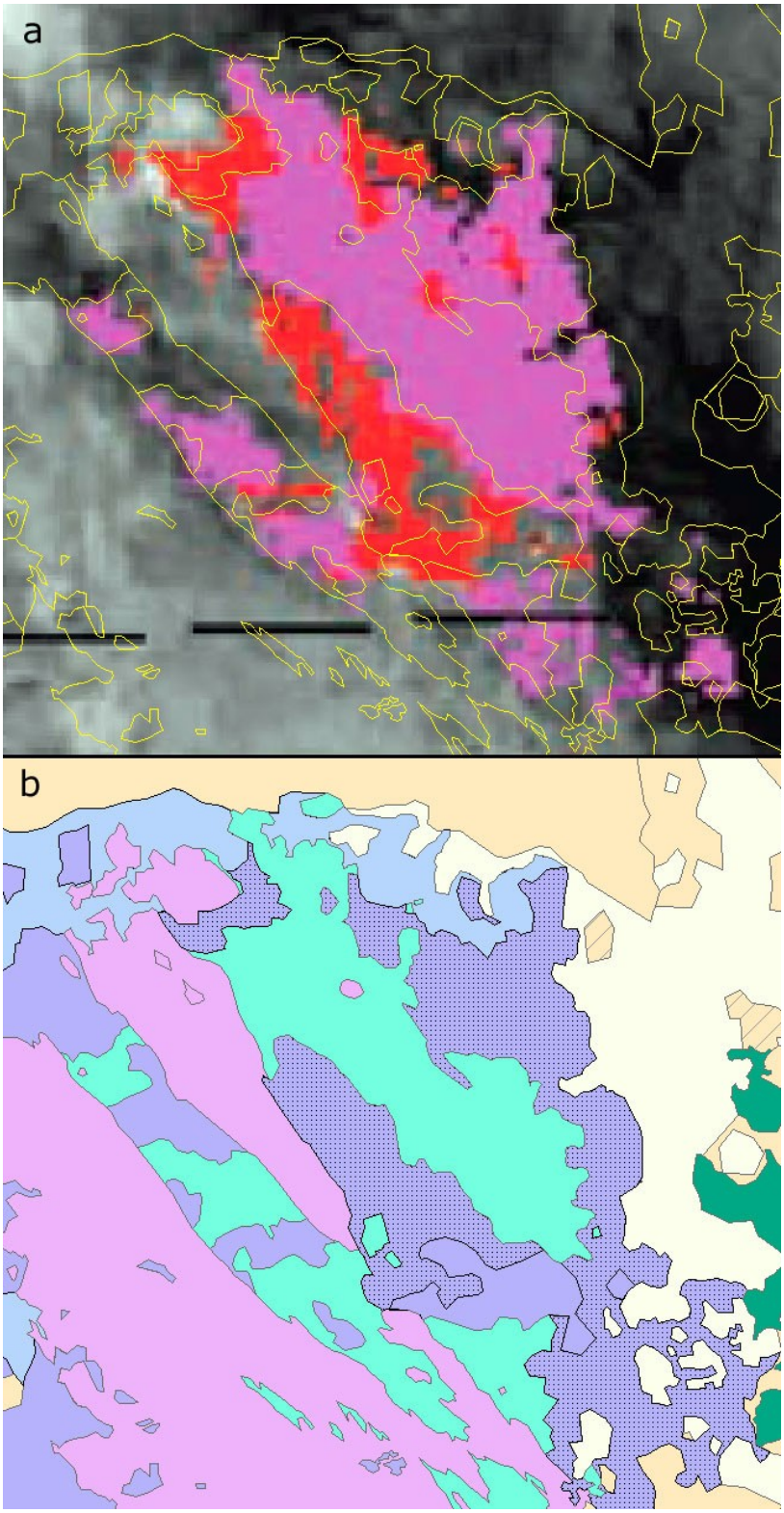

Figure 6.11. Comparison between (**a**) OMEGA detection of the suphate kieserite (red) and other hydrated minerals (pink) by Gendrin et al. (2005) and the (**b**) mapping of this study. **a.** Map redrawn from Gendrin et al. (2005) with yellow outlines of the mapping of this study. **b.** Mapping of this study. See Figure E for the legend.

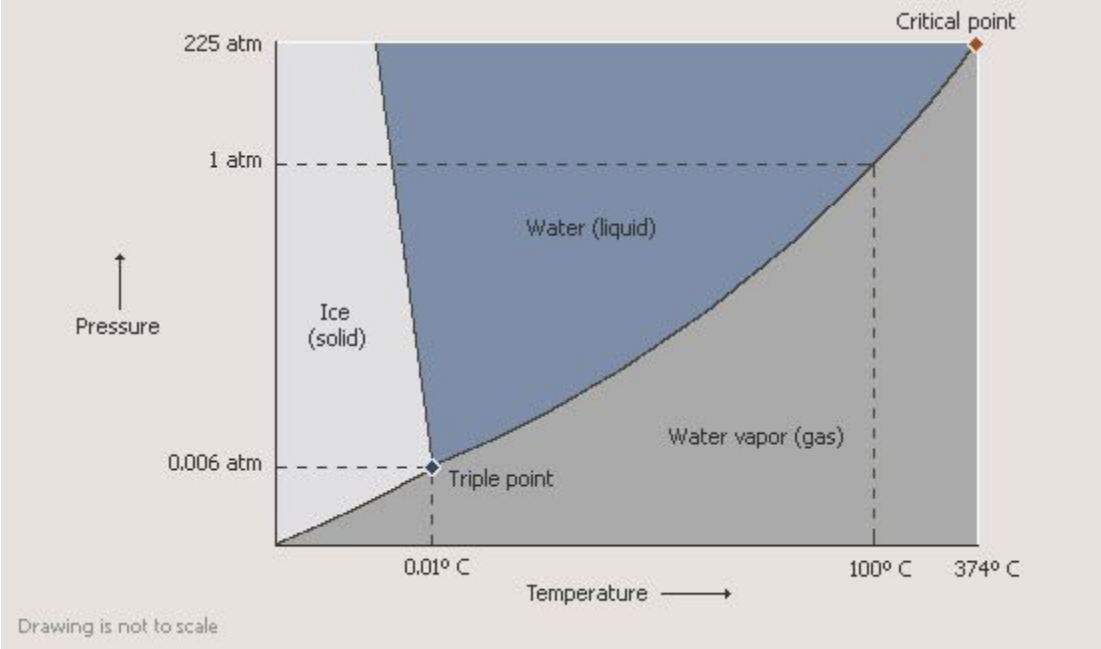

Figure 6.12. Pressure-Temperature (PT) diagram of water ice, liquid and vapour (image origin: http://www.aerospaceweb.org/question/astronomy/mars/water-phase.jpg)

Appendix A – Scripts

A.1. thmimgprev.pl
Create image preview download list from image number list.
Unix/DOS usage: perl thmimgprev.pl fromlist tolist

```
#!/usr/bin/perl –s

$from = $ARGV[0];
$to = $ARGV[1];
open(HTMLFILE,'<'.$from);
open(THEMISDOWN,'>'.$to);
while($thmnr = <HTMLFILE>)
   {
   chomp($thmnr);
   $url1 = "http://themis-data.asu.edu/img/browse/";
   $url = "$url1$thmnr\n";
   print THEMISDOWN $url;
   print $url;
   }
close HTMLFILE;
close THEMISDOWN;
```

A.2. download.pl
Downloads files using a download list using wget.
Unix/DOS usage: perl download.pl list

```
#!/usr/bin/perl –s

$ifile = $ARGV[0];
open(LST,"<$ifile");
while ($input=<LST>)
   {
   chomp($input);
   $return = system("wget --passive-ftp -nc $input");
   }
close(LST);
```

A.3. thmurl.pl
Create .QUB file download list from image number list.
Unix/DOS usage: perl thmurl.pl fromlist tolist

```
#!/usr/bin/perl –s

$from = $ARGV[0];
$to = $ARGV[1];
open(HTMLFILE,'<'.$from);
open(THEMISDOWN,'>'.$to);
while($thmnr = <HTMLFILE>)
   {
   chomp($thmnr);
   $url1 = "http://themis-data.asu.edu/pds/data/odt";
```

```
    $url2 = lc(substr($thmnr, 0, 1));
    $url3 = "r0_xxxx/";
    $url4 = $url2;
    $url5 = substr($thmnr, 1, 3);
    $url6 = "xxrdr/";
    $url7 = $thmnr;
    $url8 = "RDR.QUB";
    $url = "$url1$url2$url3$url4$url5$url6$url7$url8\n";
    print THEMISDOWN $url;
    print $url;
    }
close HTMLFILE;
close THEMISDOWN;
```

A.4. thmlev2.sh

Unix shell script adapted from scripts made by David Shean (http://webgis.wr.usgs.gov/docs/thmirmos.txt and http://webgis.wr.usgs.gov/docs/thmvismos.txt).

Unix usage: tcsh thmlev2.sh

```
# tcsh

set mappars = "SIMP:0,OCENTRIC"

foreach i (*RDR.QUB)
$ISISEXE/thm2isis.pl $i $i.l1 -- -- $ISISM01DATA/thm_kernels_both.def.8 -- 180 -- --

# Choose between IR day, IR night or VIS:
# dsk2dsk from=$i.l1 to=$i.l1.1b sfrom="'::2'"
# dsk2dsk from=$i.l1 to=$i.l1.1b sfrom="'::3'"
dsk2dsk from=$i.l1 to=$i.l1.1b sfrom="'::9'"

rm --force $i.l1

# Choose between using IR or VIS:
# $ISISEXE/thmirmc.pl $i.l1.1b -- -- -- $mappars -- -- -- -- 0.1
$ISISEXE/thmvismc.pl $i.1b -- -- -- $mappars -- -- -- -- -- -- -- -- -- -- -- -- 0.019

rm --force $i.l1.1b
end

foreach i (*irmc.cub)
dform.pl -t -gis=yes $i
end
```

A.5. tif2jpg2000.pl

Script (for unix/linux) to convert all tif images in a directory to jpg images and copy the .tfw to .jgw.

Unix usage: perl tif2jpg2000.pl

```
#!/usr/bin/perl –s
$ifile = "list";
system("ls -1 *.tif > list");
```

```
open(LST,"<$ifile");
while ($input=<LST>)
   {
   chomp($input);
   $cubname = substr($input, 0, 12);
   system("cp $cubname.tfw $cubname.jgw");
   $output = "$cubname.jpg";
   $return = system("convert $input -compress JPEG2000 $output");
   }
close(LST);
system("rm --force list");
```

A.6. divdataset.pl

Divides a dataset into X*X parts, using the georeference information from the worldfiles. It creates a directory per part and uses the windows 'move' program to move the images. Uses the Image::Size package (http://search.cpan.org/~rjray/Image-Size-3.0/Size.pm). Windows usage: perl divdataset.pl X

```
#!/usr/bin/perl –s
use Image::Size qw(:all);

$griddiv = $ARGV[0];
$init = 1;
$ifile = "jpg";
$to = "infotable";
system("dir/b *.jpg>jpg");
open(LST,"<$ifile");
open(TO,'>'.$to);
while ($input=<LST>)
      {
      chomp($input);
      $imgname = substr($input,0,-4);
      $jgw = $imgname.".jgw";
      $i = 1;
      open(JGWFILE,"<$jgw");
                  while ($jgwlist=<JGWFILE>)
                  {
                  chomp($jgwlist);
                  if($i == 1)
                              {
                              $pixsize = $jgwlist;
                              }
                  if($i == 5)
                              {
                              $xcoordlu = $jgwlist;
                              }
                  if($i == 6)
                              {
                              $ycoordlu = $jgwlist;
                              }
                  $i++;
                  }
      close(JGWFILE);
      ($x, $y) = imgsize($input);
```

```
	# Specific for polar stereographic projection:
	$xcoordc = $xcoordlu + (($x/2)*$pixsize);
	$ycoordc = $ycoordlu - (($y/2)*$pixsize);
	if($init == 1)
		{
		$xcoordmax = $xcoordc;
		$xcoordmin = $xcoordc;
		$ycoordmax = $ycoordc;
		$ycoordmin = $ycoordc;
		$init = 0;
		}
	if($xcoordc > $xcoordmax)
		{
		$xcoordmax = $xcoordc;
		}
	if($xcoordc < $xcoordmin)
		{
		$xcoordmin = $xcoordc;
		}
	if($ycoordc > $ycoordmax)
		{
		$ycoordmax = $ycoordc;
		}
	if($ycoordc < $ycoordmin)
		{
		$ycoordmin = $ycoordc;
		}
	print TO "$imgname,$xcoordlu,$xcoordc,$ycoordlu,$ycoordc,$pixsize,$x,$y\n";
	}
close(LST);
close(TO);

# Set up the grid
$xlength = $xcoordmax - $xcoordmin;
$ylength = $ycoordmax - $ycoordmin;
$gridx = $xlength/$griddiv;
$gridy = $ylength/$griddiv;
$xdone = $griddiv + 1;
$ydone = $griddiv + 1;
$leftx = $xcoordmin;
$xpart = 1;
until($xpart == $xdone)
	{
	$rightx = $leftx + $gridx;
	$uppery = $ycoordmax;
	$ypart = 1;
	until($ypart == $ydone)
		{
		$lowery = $uppery - $gridy;
		system("md $xpart.$ypart");
		open (IT,"<infotable");
		while (<IT>)
			{
			($imgname,$xcoordlu,$xcoordc,$ycoordlu,$ycoordc,$pixsize,$x,$y)	=
split(',',$_);
```

```
                        if(($xcoordc < $rightx) && ($xcoordc > $leftx) && ($ycoordc < $uppery)
&& ($ycoordc > $lowery))
                                {
                                print "$imgname lies within grid part $xpart x $ypart\n";
                                system("move $imgname.* $xpart.$ypart");
                                }
                        }
                close(IT);
                $ypart++;
                $uppery = $lowery;
                }
        $xpart++;
        $leftx = $rightx;
        }
```

A.7. arcgis2lst.pl

A perl script to extract the .cub filenames from a text file generated by the ArcMap arcscript 'List MXD Sources'.

Usage: perl arcgis2lst.pl infile outfile

```
#!/usr/bin/perl –s

$from = $ARGV[0];
$to = $ARGV[1];
open(INFILE,'<'.$from);
my $thmfind;
read INFILE,$thmfind,-s $from;
close INFILE;
open(OUTFILE,'>'.$to);
while($thmfind=~/(\\\\\b.*?.jpg)/isg)
        {
        my $thmnr=$1;
        $thmnr= substr($thmnr, 2, -4);
        print OUTFILE "$thmnr.irmc.cub\n";
        }
close OUTFILE;
```

A.8. mosaicird.pdf

Mosaicking for IR day. The script has to be run on the ISIS tae command line. It uses a list textfile created from the Table of Contents within ArcMap (mc.lst). This textfile lists all the irmc.cub or vismc.cub files in the correct mosaicking order. The temp.pdf routine creates irmc.cub.l4 or vismc.cub.l4 files. Therefore l4.lst has to be created from mc.lst listing the .l4 files in their correct mosaicking order.

The LAT and LON arguments contain the latitude (A and B) and longitude (C and D) ranges for the mosaic. I used lonsys = 180 and therefore the longitude has to be given in this system (330 then becomes –30).

```
procedure
body

b4equal FROMLIST=mc.lst MODE=SD
equalizer FROMLIST=mc.lst
```

```
temp
ush perl mc2l4.pl mc.lst l4.lst
noseam FROMLIST=l4.lst TO=mosaic.cub LAT=(A,B) LON=(C,D) LINE=11 SAMP=11

ush dform.pl -t -gis=YES mosaic.cub
ush convert mosaic.tif -compress JPEG2000 mosaic.jpg
ush cp mosaic.tfw mosaic.jgw

end-proc
.end
```

A.9. mc2l4.pl

For usage see Appendix A.7.

```
#!/usr/bin/perl -s

$from = $ARGV[0];
$to = $ARGV[1];
open(MCIN,'<'.$from);
open(L4OUT,'>'.$to);
      while($input = <MCIN>)
      {
                  chomp($input);
                  $url = "$input.l4\n";
                  print L4OUT $url;
      }
close MCIN;
close L4OUT;
```

A.10. mosaicirn.pdf

Mosaicking for IR night. The script has to be run on the ISIS tae command line. It uses a list textfile created from the Table of Contents within ArcMap (mc.lst). This textfile lists all the irmc.cub files in the correct mosaicking order.

A, B, C and D are the latitude and longitude ranges, respectively for the mosaic. I used lonsys = 180 and therefore the longitude has to be given in this system (330 then becomes –30).

```
procedure
body

ush perl mosaic.pl mc.lst A B C D
ush dform.pl -t -gis=YES mosaic.cub
ush convert mosaic.tif -compress JPEG2000 mosaic.jpg
ush cp mosaic.tfw mosaic.jgw

end-proc
.end
```

A.11. mosaic.pl

For usage see Appendix A.9.

```
#!/usr/bin/perl –s
```

```
$ifile = $ARGV[0];
$lat1 = $ARGV[1];
$lat2 = $ARGV[2];
$lon1 = $ARGV[3];
$lon2 = $ARGV[4];
$init = "y";

open(LST,"<$ifile");

while ($input=<LST>)
{
chomp($input);
system("mosaic from=$input to=mosaic.cub init=$init lat=\($lat1,$lat2\) lon=\($lon1,$lon2\)");
$init = "n";
}
close(LST);
```

A.12. vicarstart.sh

This shell script started the VICAR environment so that VICAR programs could be used. The path names should be changed to the locations of all the files on your system.

```
#!/bin/tcsh
source /usr/local/vicar/estec_setup.csh
setenv MARSDTM /usr/local/vicar/data/mars_5km.dtm
setenv LEAPSECONDS /usr/local/vicar/kernel/NAIF0008.tls
setenv CONSTANTS   /usr/local/vicar/kernel/p_constants.ker
setenv SUNKER      /usr/local/vicar/kernel/de405s.bsp
setenv HWSPICE_TF  /usr/local/vicar/kernel/MEX_v08.TF
setenv HWSPICE_TI  /usr/local/vicar/kernel/MEX_HRSC_V03.TI
setenv HWSPICE_BC /usr4/users/joosthoe/kernels/data/ck/ATNM_PTR00334_050828_001.BC
setenv HWSPICE_BSP /usr4/users/joosthoe/kernels/data/spk/ORMM_050901000000_00165.BSP
setenv HWSPICE_TSC /usr4/users/joosthoe/kernels/data/sclk/MEX_060112_STEP.TSC
alias xvd 'xvd -xrm "*enableDirectColor: false"'
```

A.13. hrsc2jpg.pl

Perl script to create map projected jpeg images of HRSC data.
Usage: perl hrsc2jpg.pl projection_type listfile

```
$trantype = $ARGV[0];
$ifile = $ARGV[1];
$HWLIB = $ENV{"HWLIB"};

open(LST,"<$ifile");

while ($input=<LST>)
      {
      chomp($input);
      if($trantype == "1")
                  {
                  $output = $input . ".simp";
                  system("$HWLIB/dlrmaptran inp=$input out=$output mp_type=cylindrical_e_a
cen_lat=0 cen_long=0 outmax=10240");
```

```
                system("vtiff2 INP=$input OUT=$input.tif");
                system("convert $input.tif -compress JPEG2000 $input.jpg");
                }
        if($trantype == "2")
                {
                $output = $input . ".pola";
                system("$HWLIB/dlrmaptran inp=$input out=$output mp_type=stereographic
cen_lat=-90 cen_long=0 outmax=10240");
                system("vtiff2 INP=$input OUT=$input.tif");
                system("convert $input.tif -compress JPEG2000 $input.jpg");
                }
   }
close(LST);
```

A.14. hrscworld.pl

Perl script to grab information from the HRSC data headers to create world files (after a script by Trent Hare).

Usage: perl hrscworld.pl listfile

```
# After Trent Hare
$ifile = $ARGV[0];
open(LST,"<$ifile");
while ($hrscfile=<LST>)
        {
        chomp($hrscfile);
        open(FIL,'<'.$hrscfile);
        my $data;
        read(FIL,$data,10000);
        close FIL;
        @data = split /  /, $data;
        $c[1]="MAP_SCALE";
        $c[2]="LINE_PROJECTION_OFFSET";
        $c[3]="SAMPLE_PROJECTION_OFFSET";

        foreach $c (@data)
        {
        ($var, $val) = split /=/,$c;
        $h{$var}=$val;
        }

        $xydim = $h{$c[1]} * 1000;
        $ydim = $xydim * -1;
        $ulxmap = ($h{$c[3]} * $xydim * -1);
        $ulymap = ($h{$c[2]} * $xydim);

        $newworld = $hrscfile.".jgw";
        open OUTWORLD, "> $newworld ";
        print OUTWORLD "$xydim\n";
        print OUTWORLD "0.0\n";
        print OUTWORLD "0.0\n";
        print OUTWORLD "$ydim\n";
        print OUTWORLD "$ulxmap \n";
        print OUTWORLD "$ulymap \n";
        close OUTWORLD;
```

```
    }
close(LST);
```

A.15. hrscsplit.pl

Perl script to split HRSC data prior to projecting and .jpg conversion.
Usage: perl hrscsplit listfile number (number is the amount of pixels, default is 20000)

```
$ifile = $ARGV[0];
$pixels = $ARGV[1];
if($ARGV[1] == 0)
    {
    $pixels = 20000;
    }

$HWLIB = $ENV{"HWLIB"};

open (LST,"<$ifile");
while ($input=<LST>)
    {
    chomp($input);
    open(HRSCDATA,'<'.$input);
    my $hrsc;
    read(HRSCDATA,$hrsc,10000);
    close HRSCDATA;
    if($hrsc=~/(NL=\b.*? )/isg)
            {
            $nlines=$1;
            $nlines = substr($nlines, 3, -1);
            print "The number of lines of $input: '$nlines'\n";
            }
    if($hrsc=~/(NS=\b.*? )/isg)
            {
            $nsamples=$1;
            $nsamples = substr($nsamples, 3, -1);
            print "The number of samples of $input: '$nsamples'\n";
            }
    $d = round($nlines/$pixels);
    $g = round($nsamples/$pixels);
    if(($d == 1) && ($g == 1))
            {
            $d = 2;
            $g = 2;
            }
    if($d < 1)
            {
            $d = 1;
            }
    if($g < 1)
            {
            $g = 1;
            }
    print "Creating matrix columns*rows: $g*$d\n";
    $e = $d + 1;
    $h = $g + 1;
    $part = round($nlines/$d);
```

```
	$sl = 1;
	$x = 1;
	until ($x == $e)
		{
		$samp = round($nsamples/$g);
		$ss = 1;
		$y = 1;
		until ($y == $h)
			{
			$aa = $samp+$ss-1;
			if($aa>$nsamples)
				{
				$samp = $nsamples - $ss + 1;
				}
			$bb = $part+$sl-1;
			if($bb>$nlines)
				{
				$part = $nlines - $sl + 1;
				}
			print "DLRMAPTRAN from $input to $input.l$x.s$y\n  Starting line = $sl, number of lines = $part\n  Starting sample = $ss, number of samples = $samp\n";
			system("$HWLIB/dlrmaptran inp=$input out=$input.l$x.s$y sl=$sl nl=$part ss=$ss ns=$samp outmax=10240");
			print "Creating tiff...\n";
			system("vtiff2 inp=$input.l$x.s$y out=$input.l$x.s$y.tif");
			print "Converting tiff to jpg...\n";
			system("convert $input.l$x.s$y.tif -compress JPEG2000 $input.l$x.s$y.jpg");
			print "Processing of $input completed.\n\n";
			$y++;
			$ss = $ss + $samp;
			}
		$x++;
		$sl = $sl + $part;
		}
	}
close LST;
system("ls -1 *.l?-s?>num");
system("perl hrscworld.pl num");
system("rm --force num");

sub round {
	my($number) = shift;
	return int($number + .5);
}
```

A.16. hrsc2arcgis.pl

This perl script processes PSA downloaded HRSC .IMG files and creates sinusoidally projected ArcGIS ready .bsq data. It does not work yet for polar data with a Stereographic projection.

Usage: perl hrsc2arcgis.pl

```
use Win32::OLE;
use Cwd;
```

```
$dir = getcwd;

$ifile = $ARGV[0];
if($#ARGV < 0)
	{
	system("dir/b *.IMG>IMG");
	$ifile = "IMG";
	}

open (LST,"<$ifile");
while ($input=<LST>)
	{
		chomp($input);
		$output=substr($input,0,-4);
		open(HRSCDATA,'<'.$input);
		my $idata;
		read(HRSCDATA,$idata,10000);
		close HRSCDATA;

		# header creation
		$first=$idata;
		if($first=~/(MAP_SCALE\b.*?\n)/isg)
			{
			$a=$1;
			$a = substr($a,34,-12);
			}
		$second=$idata;
		if($second=~/(LINE_PROJECTION_OFFSET\b.*?\n)/isg)
			{
			$b=$1;
			$b = substr($b,34,-1);
			}
		$third=$idata;
		if($third=~/(SAMPLE_PROJECTION_OFFSET\b.*?\n)/isg)
			{
			$c=$1;
			$c = substr($c,34,-1);
			}
		$fourth=$idata;
		if($fourth=~/(FILE_RECORDS\b.*?\n)/isg)
			{
			$d=$1;
			$d = substr($d,34,-1);
			}
		$fifth=$idata;
		if($fifth=~/(LINES\b.*?\n)/isg)
			{
			$e=$1;
			$e = substr($e,34,-1);
			}
		$sixth=$idata;
		if($sixth=~/(LINE_SAMPLES\b.*?\n)/isg)
			{
			$f=$1;
			$f = substr($f,34,-1);
			}
```

```
                $seventh=$idata;
                if($seventh=~/(CENTER_LONGITUDE\b.*?\n)/isg)
                        {
                        $g=$1;
                        $g = substr($g,34,-1);
                        }
                $xydim = $a * 1000;
                $ydim = $xydim * -1;
                $ulxmap = ($c * $xydim * -1);
                $ulymap = ($b * $xydim);

                # create header
                print "Writing header for $input...\n";
                $header = $output.".hdr";
                open OUTHEADER, '>'.$header;
                print OUTHEADER "nrows $e\n";
                print OUTHEADER "ncols $f\n";
                print OUTHEADER "nbands 1\n";
                print OUTHEADER "nbits 8\n";
                print OUTHEADER "byteorder I\n";
                print OUTHEADER "layout BSQ\n";
                print OUTHEADER "skipbytes $d\n";
                print OUTHEADER "ulxmap $ulxmap\n";
                print OUTHEADER "ulymap $ulymap\n";
                print OUTHEADER "xdim $xydim\n";
                print OUTHEADER "ydim $xydim\n";
                close OUTHEADER;

                # create projection
                $proj = $output.".prj";
                open OUTPROJ, '>'.$proj;
                print                                                                   OUTPROJ
"PROJCS[\"Mars_Sinusoidal_clon$g\",GEOGCS[\"GCS_Mars_2000_Sphere\",DATUM[\"D_Ma
rs_2000_Sphere\",SPHEROID[\"Mars_2000_IAU_IAG_Sphere\",3396190.0,0.0]],PRIMEM[\"Re
ference_Meridian\",0.0],UNIT[\"Degree\",0.0174532925199433]],PROJECTION[\"Sinusoidal\"],
PARAMETER[\"False_Easting\",0.0],PARAMETER[\"False_Northing\",0.0],PARAMETER[\"C
entral_Meridian\",$g],UNIT[\"Meter\",1.0]]";
                close OUTPROJ;

                # rename .IMG
                print "Renaming $input $output.bsq...\n";
                system("rename $input $output.bsq");

                # create and execute python script to assign projection to image.
                print "Creating auxilary file (.aux) using python...\n";
                my $class = "esriGeoprocessing.GpDispatch.1";
                my $gp = Win32::OLE->new($class) || die "Could not create a COM $class object";
                $gp->defineprojection_management("$dir\\$output.bsq", "$proj");
                unlink($proj);
                print "Building pyramids...\n";
                # This takes some time, if you don't want it, place # in front of the following line:
                $gp->BuildPyramids_management("$dir\\$output.bsq");
        }
close LST;
unlink($ifile);
```

A.17. hrscanag.pl

Perl script to create two HRSC images which can be combined to form an anaglyph. It uses the following DLR VICAR routines: hrfill, dlrto8, hrortho and vtiff2. It also uses the ImageMagick 'convert' program to create jpeg2000 files. I used this script on a unix machine where the VICAR DLR routines were installed. All programs except vtiff2 are available in the minivicar package (http://pds-imaging.jpl.nasa.gov/data/mex/mex/hrsc/mexhrsc_0001/software/).

Unix usage: perl hrscanag.pl transformation_type

```
$ORI_MODE = "EXT";
$ANAG_MPSCALE = 0.1;
$ANCH_ANA_L3 = 100;
$START_L = 1;
$NOF_L = 0;
$MAXOUTSIZE = 10240;

$trantype = $ARGV[0];
if($trantype == "1")
      {
      $MP_TYPE = "cylindrical_e_a";
      $MP_CENLAT = 0;
      $MP_CENLON = 0;
      }
if($trantype == "2")
      {
      $MP_TYPE = "stereographic";
      $MP_CENLAT = -90;
      $MP_CENLON = 0;
      }
if($trantype == "3")
      {
      $MP_TYPE = "sinusoidal";
      $MP_CENLAT = 0;
      $MP_CENLON = "--";
      }
$HWLIB = $ENV{"HWLIB"};

system("ls -1 *.s12.??>s12");

open(LST,"<s12");
while ($input=<LST>)
      {
      chomp($input);
      $i = $input;
      $j = substr($input, 0,11)."nd2".substr($input,14,3);
      system("$HWLIB/hrfill inp=$i out=$i.filled");
      system("$HWLIB/hrfill inp=$j out=$j.filled");
      if(-e "$i.filled")
                  {
                  system("$HWLIB/dlrto8 inp=$i.filled out=$i.8bit DNMIN=-1 DNMAX=-1");
                  }
      else
                  {
                  system("$HWLIB/dlrto8 inp=$i out=$i.8bit DNMIN=-1 DNMAX=-1");
```

```
		}
	if(-e "$j.filled")
		{
		system("$HWLIB/dlrto8 inp=$j.filled out=$j.8bit DNMIN=-1 DNMAX=-1");
		}
	else
		{
		system("$HWLIB/dlrto8 inp=$j out=$j.8bit DNMIN=-1 DNMAX=-1");
		}
	system("$HWLIB/hrortho inp=$i.8bit ori=$ORI_MODE ext=$i"."_ext"."  out=$i.lev3
sl_i=$START_L nl_i=$NOF_L anch=$ANCH_ANA_L3 OUTMAX=$MAXOUTSIZE rep=yes
dtm=0 mp_type=$MP_TYPE cen_lat=$MP_CENLAT cen_long=$MP_CENLON
mp_sca=$ANAG_MPSCALE -usemp");
	system("$HWLIB/hrortho inp=$j.8bit ori=$ORI_MODE ext=$j"."_ext"."  out=$j.lev3
sl_i=$START_L nl_i=$NOF_L anch=$ANCH_ANA_L3 OUTMAX=$MAXOUTSIZE rep=yes
dtm=0 fitto=$i.lev3");
	}
close(LST);

system("ls -1 *.lev3>lev3");
open(LST,"<lev3");
while ($input=<LST>)
	{
	chomp($input);
	system("vtiff2 INP=$input OUT=$input.tif");
	system("convert $input.tif -compress JPEG2000 $input.jpg");
	}
close(LST);
```

A.18. hrscdtm2arcgis.pl

This perl script is windows only and you need ArcGIS 9.1 with Spatial Analyst.
Usage: hrscdtm2arcgis.pl listfile

```
#!/usr/bin/perl

use Cwd;
use Win32::OLE;
$dir = getcwd;
$ifile = $ARGV[0];
my $class = "esriGeoprocessing.GpDispatch.1";
my $gp = Win32::OLE->new($class) || die "Could not create a COM $class object";
$gp->CheckOutExtension("Spatial");

open(LST,"<$ifile");
while ($dtmfile=<LST>)
	{
	print "Grabbing label from $dtmfile\n";
	chomp($dtmfile);
	open(DTM,'<'.$dtmfile);
	my $dtmlabel;
	read(DTM,$dtmlabel,10000);
	close DTM;

	@dtmlabel = split /  /, $dtmlabel;
```

```
$c[1]="MAP_SCALE";
$c[2]="LINE_PROJECTION_OFFSET";
$c[3]="SAMPLE_PROJECTION_OFFSET";
$c[4]="LBLSIZE";
$c[5]="NL";
$c[6]="NS";
$c[7]="POSITIVE_LONGITUDE_DIRECTION";
$c[8]="CENTER_LONGITUDE";
$c[9]="STOP";

foreach $c (@dtmlabel) {
($var, $val) = split /=/,$c;
$h{$var}=$val;
};

if($h{$c[7]} =~ /EAST/)
        {
        $sinlon = $h{$c[8]};
        }
if($h{$c[7]} =~ /WEST/)
        {
        $sinlon = -$h{$c[8]};
        }
$xydim = $h{$c[1]} * 1000;
$ulxmap = ($h{$c[3]} * $xydim * -1);
$ulymap = ($h{$c[2]} * $xydim);
$righe = $h{$c[5]};
$colonne = $h{$c[6]};
$skip = $h{$c[4]};

$newfile = substr($dtmfile, 0, 10);
$bsqfile = $newfile.".bsq";
$hdrfile = $newfile.".hdr";
print "Writing header...\n";
open OUTWORLD, "> $hdrfile ";
print OUTWORLD "nrows $righe\n";
print OUTWORLD "ncols $colonne\n";
print OUTWORLD "nbands 1\n";
print OUTWORLD "nbits 16\n";
print OUTWORLD "byteorder I\n";
print OUTWORLD "layout BSQ\n";
print OUTWORLD "skipbytes $skip\n";
print OUTWORLD "ulxmap $ulxmap\n";
print OUTWORLD "ulymap $ulymap\n";
print OUTWORLD "xdim $xydim\n";
print OUTWORLD "ydim $xydim\n";
close OUTWORLD;

print "Renaming $dtmfile to $bsqfile\n";
system("ren $dtmfile $bsqfile");
$Expression = "select ( merge ( setnull ( $dir/$bsqfile > 32767 , $dir/$bsqfile ) , ( $dir/$bsqfile - 65536 ) ) , 'value <> -32768' )";
$gp->SingleOutputMapAlgebra_sa($Expression, "$dir/$newfile");

print "Assigning projection...\n";
$proj = $newfile.".prj";
```

```
    open OUTPROJ, '>'.$proj;
    print OUTPROJ
"PROJCS[\"Mars_Sinusoidal_clon$sinlon\",GEOGCS[\"GCS_Mars_2000\",DATUM[\"D_Mars_
2000\",SPHEROID[\"Mars_2000_IAU_IAG\",3396190.0,169.8944472236118]],PRIMEM[\"Refe
rence_Meridian\",0.0],UNIT[\"Degree\",0.0174532925199433]],PROJECTION[\"Sinusoidal\"],P
ARAMETER[\"False_Easting\",0.0],PARAMETER[\"False_Northing\",0.0],PARAMETER[\"Ce
ntral_Meridian\",$sinlon],UNIT[\"Meter\",1.0]]";
    close OUTPROJ;
    $gp->defineprojection_management("$dir/$newfile", "$proj");
    unlink($proj);
    }
close(LST);
```

A.19. moc2arcgis.pl

A perl script to reproject MOC images. It uses the gdal_translate program from GDAL and the geoprocessor from ArcGIS. It needs a moclatlons.txt file generated from SPICE and MOLA datasets by Shane Byrne. It also uses wget to download the MOC images. I assume the direction of the Mars Global Surveyor was NNEward when the MOC image was taken. A small amount of MOC images are NNW.

Usage: moc2arcgis.pl ArcGIS_Attribute_Table_Export_file

```
#!/usr/bin/perl -s

# pre stuff
use Image::Size qw(:all);
use Cwd;
use Math::Trig;
use warnings;
use Win32::OLE;
$dir = getcwd;
$from = $ARGV[0];
$pi = atan2(1,1) * 4;

# Data input
open(MOCLIST,'<'.$from);
my $moc;
read MOCLIST,$moc,-s $from;
close MOCLIST;
open(MOCDATA,'<'."moclatlons.txt");
my $mocdata;
read MOCDATA,$mocdata,-s "moclatlons.txt";
close MOCDATA;

# Do for every image
while($moc=~/(http\b.*?,)/isg)
    {
    my $mocid=$1;
    # conversion from wr.usgs website to msss.com website
    $mocid = uc(substr($mocid,35,-7));
    $mocid1 = substr($mocid,0,1);
    $mocid2 = substr($mocid,1,2);
    $mocid3 = substr($mocid,0,3);
    $url1 = "http://www.msss.com/moc_gallery/";
    if(substr($mocid2,0,1)=="0")
```

```
        {
        $mocid2=substr($mocid2,1,2);
        }
if((substr($mocid,0,2) =~ /SP/) || (substr($mocid,0,2) =~ /AB/))
        {
        $url2 = "ab1_m04";
        }
if($mocid1 =~ /M/)
        {
        if($mocid2 <= "4")
                {
                $url2 = "ab1_m04";
                }
        if(($mocid2 >= "7") && ($mocid2 <= "12"))
                {
                $url2 = "m07_m12";
                }
        if(($mocid2 >= "13") && ($mocid2 <= "18"))
                {
                $url2 = "m13_m18";
                }
        if($mocid2 >= "19")
                {
                $url2 = "m19_m23";
                }
        }
if($mocid1 =~ /E/)
        {
        if($mocid2 <= "6")
                {
                $url2 = "e01_e06";
                }
        if(($mocid2 >= "7") && ($mocid2 <= "12"))
                {
                $url2 = "e07_e12";
                }
        if(($mocid2 >= "13") && ($mocid2 <= "18"))
                {
                $url2 = "e13_e18";
                }
        if($mocid2 >= "19")
                {
                $url2 = "e19_r02";
                }
        }
if($mocid1 =~ /R/)
        {
        if($mocid2 <= "2")
                {
                $url2 = "e19_r02";
                }
        if(($mocid2 >= "3") && ($mocid2 <= "9"))
                {
                $url2 = "r03_r09";
                }
        if(($mocid2 >= "10") && ($mocid2 <= "15"))
```

```
                        {
                        $url2 = "r10_r15";
                        }
                if(($mocid2 >= "16") && ($mocid2 <= "21"))
                        {
                        $url2 = "r16_r21";
                        }
                if($mocid2 >= "22")
                        {
                        $url2 = "r22_s04";
                        }
                }
        if($mocid1 =~ /S/)
                {
                if($mocid2 <= "4")
                        {
                        $url2 = "r22_s04";
                        }
                if(($mocid2 >= "5") && ($mocid2 <= "10"))
                        {
                        $url2 = "s05_s10";
                        }
                }
        # download map or non map projected
        print "Attempting to download map-projected image...\n";
        $urlmap = "$url1$url2/full_jpg\_map/$mocid3/$mocid.jpg\n";
        system("wget --passive-ftp --tries=1 -nc -nv $urlmap");
        $map = 0;
        if(-e "$mocid.jpg")
                {
                $map = 1;
                }
        if($map == 0)
                {
                print "Unsuccesfull, attempting to download map-projected image...\n";
                $urlnonmap = "$url1$url2/full_jpg\_non_map/$mocid3/$mocid.jpg\n";
                system("wget --passive-ftp --tries=1 -nc -nv $urlnonmap");
                }
        # start processing
        if(-e "$mocid.jpg")
                {
                print "Deriving image corner latitude/longitudes...\n";
                # derive info from moclatlons.txt
                $mocdata0=$mocdata;
                $mocid0 = uc($mocid);
                ($x, $y) = imgsize("$mocid.jpg");
                if($mocdata0=~/($mocid0\b.*?\n)/isg)
                        {
                        $all=$1;
                        ($mocid,$ione,$itwo,$ithree,$ifour,$ifive,$isix,$iseven,$ieight)                =
split(',',$all);
                        # conversion of 0 > 360 east longitude to -180 > 180 east longitude.
                        if($ione > 180)
                                {
                                $ione = $ione - 360;
                                }
```

```
                        if($ithree > 180)
                                {
                                $ithree = $ithree - 360;
                                }
                        if($ifive > 180)
                                {
                                $ifive = $ifive - 360;
                                }
                        if($iseven > 180)
                                {
                                $iseven = $iseven - 360;
                                }
                        }
                if($map == 0)
                        {
                        $fa1 = ($ione - $ithree)**2;
                        $fa2 = ($itwo - $ifour)**2;
                        $fb1 = ($ione - $iseven)**2;
                        $fb2 = ($itwo - $ieight)**2;
                        $fa = sqrt($fa1 + $fa2);
                        $fb = sqrt($fb1 + $fb2);
                        $factorx = $x / $fa;
                        $factory = $y / $fb;
                        $zeropointx = $ifive;
                        $zeropointy = $ieight;
                        $x1 = ($ione - $zeropointx) * $factorx;
                        $y1 = ($itwo - $zeropointy) * $factory;
                        $x2 = ($ithree - $zeropointx) * $factorx;
                        $y2 = ($ifour - $zeropointy) * $factory;
                        $x3 = ($iseven - $zeropointx) * $factorx;
                        $y3 = ($ieight - $zeropointy) * $factory;
                        $x4 = ($ifive - $zeropointx) * $factorx;
                        $y4 = ($isix - $zeropointy) * $factory;
                        $newx = $x1;
                        $newy = abs($y2);
                        # start gdal and arcgis processing
                        print "Converting and rescaling image to tiff using gdal_translate...\n";
                        system("gdal\\gdal_translate -outsize $newx $newy $mocid.jpg temp.tif");
                        unlink("$mocid.jpg");
                        my $class = "esriGeoprocessing.GpDispatch.1";
                        my $gp = Win32::OLE->new($class) || die "Could not create a COM $class
object";
                        my $SourcePoints = "0 0; $x1 0; 0 $y2; $x1 $y2";
                        my $TargetPoints = "$x4 $y4; $x3 $y3; $x2 $y2; $x1 $y1";
                        print "Warping image...\n";
                        $gp->Warp_management("$dir\\temp.tif",  $SourcePoints,  $TargetPoints,
"$dir\\temp2.tif", "POLYORDER1");
                        $gp->CheckOutExtension("Spatial");
                        print "Converting 255 to NODATA...\n";
                        $asciidata = "2552NODATA.txt";
                        open AD, '>'.$asciidata;
                        print AD "255\tNODATA";
                        close AD;
                        $gp->ReclassByASCIIFile_sa("$dir\\temp2.tif",           "$dir\\$asciidata",
"$dir\\$mocid.tif", "DATA");
                        unlink($asciidata);
```

```
                        unlink("temp.tif");
                        unlink("temp.aux");
                        unlink("temp2.tif");
                        unlink("temp2.aux");
                        unlink("temp2.rrd");
                        unlink("temp2.tif.xml");
                        unlink("temp2.tif");
                        unlink($mocid.".aux");
                        unlink($mocid.".rrd");
                        unlink($mocid.".tif.xml");
                        print "Converting back to jpeg using gdal_translate...\n";
                        system("gdal\\gdal_translate -a_nodata 1 -of jpeg $mocid.tif $mocid.jpg");
                        unlink("$mocid.tif");
                        # create worldfile
                        print "Creating worldfile...\n";
                        $yscale = (1 / $factory) * (($pi * 3396190.0) / 180);
                        $xscale = (1 / $factorx) * (($pi * 3396190.0) / 180);
                        $ulymap = $zeropointy * (($pi * 3396190.0) / 180);
                        $ulxmap = $zeropointx * (($pi * 3396190.0) / 180);
                        $newworld = $mocid.".jgw";
                        open OUTWORLD, '>'.$newworld;
                        print OUTWORLD "$xscale\n";
                        print OUTWORLD "0.0\n";
                        print OUTWORLD "0.0\n";
                        print OUTWORLD "-$yscale\n";
                        print OUTWORLD "$ulxmap \n";
                        print OUTWORLD "$ulymap \n";
                        close OUTWORLD;
                        # create and assign projection
                        print "Assigning projection...\n";
                        $proj = $mocid.".prj";
                        open OUTPROJ, '>'.$proj;
                        print                                                   OUTPROJ
"PROJCS[\"Mars_Equicylindrical_clon=0\",GEOGCS[\"GCS_Mars_2000\",DATUM[\"D_Mars_
2000\",SPHEROID[\"Mars_2000_IAU_IAG\",3396190.0,0.0]],PRIMEM[\"Reference_Meridian\"
,0.0],UNIT[\"Degree\",0.0174532925199433]],PROJECTION[\"Equidistant_Cylindrical\"],PARA
METER[\"False_Easting\",0.0],PARAMETER[\"False_Northing\",0.0],PARAMETER[\"Central_
Meridian\",0.0],UNIT[\"Meter\",1.0]]";
                        close OUTPROJ;
                        $gp->defineprojection_management("$dir\\$mocid.jpg", "$proj");
                        unlink($proj);
                        print "Building pyramids...\n";
                        $gp->BuildPyramids_management("$dir\\$mocid.jpg");
                        }
                else
                        {
                        # image is already map projected so only create worldfile
                        print "Creating worldfile...\n";
                        $yscale = abs($ieight - $ifour) * (($pi * 3396190.0) / 180) / $y;
                        $xscale = abs($ifive - $ione) * (($pi * 3396190.0) / 180) / $x;
                        $ulymap = ((($pi * 3396190.0) / 180) * $ieight);
                        $ulxmap = -(abs($ifive - $ione) * (($pi * 3396190.0) / 180)) / 2;
                        $newworld = $mocid.".jgw";
                        open OUTWORLD, '>'.$newworld;
                        print OUTWORLD "$xscale\n";
                        print OUTWORLD "0.0\n";
```

```
                        print OUTWORLD "0.0\n";
                        print OUTWORLD "-$yscale\n";
                        print OUTWORLD "$ulxmap \n";
                        print OUTWORLD "$ulymap \n";
                        close OUTWORLD;
                        # create and assign projection
                        $proj = $mocid.".prj";
                        open OUTPROJ, '>'.$proj;
                        $sinlon = ($ifive + $ione) / 2;
                        print OUTPROJ
"PROJCS[\"Mars_Sinusoidal_clon$sinlon\",GEOGCS[\"GCS_Mars_2000_Sphere\",DATUM[\"D
_Mars_2000_Sphere\",SPHEROID[\"Mars_2000_IAU_IAG_Sphere\",3396190.0,0.0]],PRIMEM[
\"Reference_Meridian\",0.0],UNIT[\"Degree\",0.0174532925199433]],PROJECTION[\"Sinusoida
l\"],PARAMETER[\"False_Easting\",0.0],PARAMETER[\"False_Northing\",0.0],PARAMETER[
\"Central_Meridian\",$sinlon],UNIT[\"Meter\",1.0]]";
                        close OUTPROJ;
                        print "Assigning projection...\n";
                        my $class = "esriGeoprocessing.GpDispatch.1";
                        my $gp = Win32::OLE->new($class) || die "Could not create a COM $class
object";
                        $gp->defineprojection_management("$dir\\$mocid.jpg", "$proj");
                        unlink($proj);
                        print "Building pyramids...\n";
                        $gp->BuildPyramids_management("$dir\\$mocid.jpg");
                        }
                print "\n";
                }
        else
                {
                print "Unsuccesfull, $mocid.jpg cannot be found!..\n\n";
                }
        }
```

A.20. MOLA2arcgis.pl

Usage: perl MOLA2arcgis.pl MOLA.TAB MOLA.TXT

When you add the data to ArcMap via Tools > Add XY Data make sure you change the projection to MOLAproj.prj.

---------- beginning of MOLAproj,prj ----------

PROJCS["Equirectangular projection using MOLA sphere",GEOGCS["MOLA_Sphere",DATUM["D_MOLA_Sphere",SPHEROID["MOLA_Sphere",3396000.0,0.0]],PRIMEM["Reference_Meridian",0.0],UNIT["Degree",0.0174532925199433]],PROJECTION["Equidistant_Cylindrical"],PARAMETER["False_Easting",0.0],PARAMETER["False_Northing",0.0],PARAMETER["Central_Meridian",0.0],PARAMETER["Standard_Parallel_1",0.0],UNIT["Meter",1.0]]

---------- end of MOLAproj,prj ----------

```
#!/usr/bin/perl -s
# MOLA2arcgis.pl

$ifile = $ARGV[0];
$to = $ARGV[1];
$line = 1;
```

```
open(PNTLST,'>'.$to);
print PNTLST "X,Y,LON,LAT,Z,ORBIT\n";
open(LST,"<$ifile");
while ($input=<LST>)
      {
      chomp($input);
   if ($line > 2){
      $lon = substr($input,0,9);
      $lat = substr($input,10,7);
      $z = substr($input,22,8);
      $orbit = substr($input,67,5);
      if(substr($lat,0,1) =~ / /)
                {
                $lat = substr($lat,1,(length($lat)-1))
                }
      if(substr($lat,0,1) =~ / /)
                {
                $lat = substr($lat,1,(length($lat)-1))
                }
      if(substr($lon,0,1) =~ / /)
                {
                $lon = substr($lon,1,(length($lon)-1))
                }
      if(substr($lon,0,1) =~ / /)
                {
                $lon = substr($lon,1,(length($lon)-1))
                }
      if(substr($orbit,0,1) =~ / /)
                {
                $orbit = substr($orbit,1,(length($orbit)-1))
                }
      if(substr($orbit,0,1) =~ / /)
                {
                $orbit = substr($orbit,1,(length($orbit)-1))
                }
      # conversion of 0 > 360 east longitude to -180 > 180 east longitude.
      if($lon > 180)
                {
                $lon = $lon - 360;
                }
      # Latitude is OCentric so can be directly related to the Y belonging to 180 degrees:
      $pi = atan2(1,1) * 4;
      $y = (3396000 * $pi / 180) * $lat;
      $x = (3396000 * $pi / 180) * $lon;
      print PNTLST "$x,$y,$lon,$lat,$z,$orbit\n";
      }
   $line++;
      }
close LST;
close PNTLST;
print "Saved to '$to'.";
```

A.21. OMEGAsplit.pl

Usage: perl OMEGAsplit.pl

```
$ifile = $ARGV[0];
use Cwd;
my $dir = getcwd;

open (OC, '> omegasplit.pro');
open (LST,"<$ifile");
while ($input=<LST>)
      {
      chomp($input);
      print OC "ENVI_OPEN_FILE, '$dir/$input', r_fid=ac_all\n";
      print OC "envi_file_query, ac_all, ns=ns, nl=nl\n";
      print OC "dims = [-1,0,ns-1,0,nl-1]\n";
      print OC "pos = lindgen(128)\n";
      print OC "ENVI_OUTPUT_TO_EXTERNAL_FORMAT, /ENVI, fid=ac_all, pos=pos,
dims=dims, OUT_NAME='$dir/$input-IR-C'\n";
      print OC "pos = lindgen(128) + 128\n";
      print OC "ENVI_OUTPUT_TO_EXTERNAL_FORMAT, /ENVI, fid=ac_all, pos=pos,
dims=dims, OUT_NAME='$dir/$input-IR-L'\n";
      print OC "pos = lindgen(96) + 256\n";
      print OC "ENVI_OUTPUT_TO_EXTERNAL_FORMAT, /ENVI, fid=ac_all, pos=pos,
dims=dims, OUT_NAME='$dir/$input-VIS'\n";
      print OC "\n\n";
      }
print OC "close\n";
print OC "END\n";
close (OC);
close (LST);
```

A.22. writeOMEGAproj.pl

Perl script to write the projection IDL code for all the kdat OMEGA data in the directory.
Usage: perl writeOMEGAproj.pl

```
#!/usr/bin/perl -s

$ifile = "orbs";

# UNIX:
# system("ls -1 *kdat > orbs");
# DOS:
system("dir/s/b *kdat > orbs");

open(LST,"<$ifile");
open (OC, '> OMEGAproj.pro');

while ($omegalst=<LST>)
      {
      chomp($omegalst);
      $ORB = substr($omegalst, 0, -5);
      print OC "ENVI_OPEN_FILE, '$ORB\_lonlat', r_fid=lonlat\n";
      print OC "ENVI_OPEN_FILE, '$ORB\_kdat', r_fid=kdat\n";
      print OC "params = [3396190.0, 0.0, 0.0, 0.0, 0.0]\n";
      print OC "name = 'Mars Equirectangular Sphere'\n";
      print OC "datum = 'D_Mars_2000'\n";
      print OC "envi_file_query, kdat, nb=nb\n";
```

```
      print OC "pos  = lindgen(nb)\n";
      print OC "AreoLatLong = ENVI_PROJ_CREATE(/geographic, datum=datum)\n";
      print OC "AreoAramChaos = ENVI_PROJ_CREATE(type=17, name=name, datum=datum,
params=params)\n";
      print OC "ENVI_DOIT, 'ENVI_GLT_DOIT', I_PROJ=AreoLatLong,
O_PROJ=AreoAramChaos, OUT_NAME='$ORB\_GLT', R_FID=orbglt, X_FID=lonlat,
X_POS=0, Y_FID=lonlat, Y_POS=1\n";
      $return = print OC "ENVI_DOIT, 'ENVI_GEOREF_FROM_GLT_DOIT',
BACKGROUND=0 , FID=kdat, GLT_FID=orbglt, POS=pos, OUT_NAME='$ORB\_PROJ'\n\n";
      }
close(LST);
print OC "close\n";
print OC "END\n";
close (OC);
```

A.23. *'Divide_By_Spectrum' IDL function*
This script was created by Harald van der Werff.
Usage within IDL command line: RESULTS = Divide_By_Spectrum(image,spectrum)

```
function Divide_By_Spectrum,image,spectrum

 ns = N_ELEMENTS(image[*,0,0])
 nl = N_ELEMENTS(image[0,*,0])
 nb = N_ELEMENTS(image[0,0,*])

 output = FLTARR(ns,nl,nb)

 for x = 0, ns-1 do begin
   for y = 0, nl-1 do begin
     output[x,y,*] = image[x,y,*]/float(spectrum)
   endfor
 endfor

 return, output

end
```

A.24. Concentricity / Radiality
VBA script to calculate the Concentricity and Radiality of a selection of lineaments relative to a specific point (with Xcenter/Ycenter coordinates).

```
Dim Pi As Double
Dim Angle As Double
Dim Dx As Double
Dim Dy As Double
Dim Xcenter As Double
Dim Ycenter As Double
Dim RadAngle As Double
Dim RadialAngle As Double
Dim Concentricity As Double

Xcenter = VALUEX
Ycenter = VALUEY
```

```
Pi = 3.14159265358979323846264338327950288419 72

Dx = Xcenter - [Easting]
Dy = Ycenter - [Northing]
RadAngle = 90 - ( atn (Dy / Dx) * ( 180 / Pi ))

If ( [GEOANGLE] > 180) Then
  Angle = [GEOANGLE]  - 180
ElseIf ( [GEOANGLE] < 180) Then
  Angle = [GEOANGLE]
End If

RadialAngle = Angle - RadAngle

If ( abs (RadialAngle) > 90) Then
  Concentricity = 180 - abs (RadialAngle)
ElseIf ( abs (RadialAngle) < 90) Then
  Concentricity = abs (RadialAngle)
End If
```

Appendix B – Mars Simple Cylindrical Projection

The projection parameters can be saved in a file with a .prj extension. This projection uses an ellipse and the zero degree longitude as central meridian (clon=0).

```
PROJCS["Mars Simple Cylindrical (Ellipse, clon=0)",
    GEOGCS["GCS_Mars_2000",
        DATUM["<custom>",
            SPHEROID["<custom>",3396190.0,169.8944472236118]],
        PRIMEM["Reference_Meridian",0.0],
        UNIT["Degree",0.0174532925199433]],
    PROJECTION["Equidistant_Cylindrical"],
        PARAMETER["False_Easting",0.0],
        PARAMETER["False_Northing",0.0],
        PARAMETER["Central_Meridian",0.0],
        PARAMETER["Standard_Parallel_1",0.0],
        UNIT["Meter",1.0]]
```